

# NATURAL, SYNTHETIC, AND RECYCLED POLYMERS IN COMPOSITE MATERIALS

GUEST EDITORS: GONZALO MARTÍNEZ-BARRERA, OSMAN GENÇEL,  
CARMINA MENCHACA-CAMPOS, AND ENRIQUE VIGUERAS-SANTIAGO





---

# **Natural, Synthetic, and Recycled Polymers in Composite Materials**

International Journal of Polymer Science

---

## **Natural, Synthetic, and Recycled Polymers in Composite Materials**

Guest Editors: Gonzalo Martínez-Barrera, Osman Gencel,  
Carmina Menchaca-Campos, and Enrique Viguera-Santiago



---

Copyright © 2013 Hindawi Publishing Corporation. All rights reserved.

This is a special issue published in "International Journal of Polymer Science." All articles are open access articles distributed under the Creative Commons Attribution License, which permits unrestricted use, distribution, and reproduction in any medium, provided the original work is properly cited.

## Editorial Board

Harald W. Ade, USA  
Christopher Batich, USA  
David G. Bucknall, USA  
Yoshiki Chujo, Japan  
Marek Cypryk, Poland  
Li Ming Dai, USA  
Yulin Deng, USA  
Ali A. Entezami, Iran  
Benny D. Freeman, USA  
Peng He, USA  
Jan-Chan Huang, USA  
Tadashi Inoue, Japan

Avraam I. Isayev, USA  
Koji Ishizu, Japan  
Patric Jannasch, Sweden  
Saad Khan, USA  
Wen-Fu Lee, Taiwan  
Jose Ramon Leiza, Spain  
Haojun Liang, China  
Giridhar Madras, India  
Evangelos Manias, USA  
Jani Matisons, Australia  
Dinesh K. Mishra, Korea  
Geoffrey Mitchell, UK

Qinmin Pan, Canada  
Zhonghua Peng, USA  
Miriam Rafailovich, USA  
B. L. Rivas, Chile  
Hj Din Rozman, Malaysia  
E. Sancaktar, USA  
Robert Shanks, Australia  
Mikhail Shtilman, Russia  
Masaki Tsuji, Japan  
Hideto Tsuji, Japan  
Yakov Vygodskii, Russia  
Qijin Zhang, China

## Contents

**Cellulose-Based Polymer Composite with Carbon Black for Tetrahydrofuran Sensing,**

Susana Hernández-López, Enrique Viguera-Santiago, Miriam Mendoza Mora, José Rurik Farias Mancilla, and Erasto Armando Zaragoza Contreras

Volume 2013, Article ID 381653, 7 pages

**Effects of the Addition of *Ortho*- and *Para*-NH<sub>2</sub> Substituted Tetraphenylporphyrins on the Structure of Nylon 66,** Luis A. Díaz-Alejo, E. Carmina Menchaca-Campos, J. Uruchurtu Chavarín, R. Sosa-Fonseca, and Miguel A. García-Sánchez

Volume 2013, Article ID 323854, 14 pages

**Ultrasonic, Molecular and Mechanical Testing Diagnostics in Natural Fibre Reinforced,**

**Polymer-Stabilized Earth Blocks,** C. Galán-Marín, C. Rivera-Gómez, and F. Bradley

Volume 2013, Article ID 130582, 10 pages

**Polypropylene Fibers as Reinforcements of Polyester-Based Composites,** Gonzalo Martínez-Barrera,

Enrique Viguera Santiago, Susana Hernández López, Osman Gencel, and Fernando Ureña-Nuñez

Volume 2013, Article ID 143894, 6 pages

**Electrochemical Evaluation of a Recycled Copolymer Coating for Cultural Heritage Conservation**

**Purposes,** Marco Hernández-Escampa, Fausto Rodríguez-Acuña, Franco Millán-Cruz, Pilar Rodríguez-Rojas, Miguel Hernández-Gallegos, Alba Covelo, Carmina Menchaca-Campos, and Jorge Uruchurtu

Volume 2013, Article ID 751056, 9 pages

**Processing and Performance of Polymeric Transparent Conductive Composites,** Parul Jain,

Ranjani Muralidharan, Jennifer Sedloff, Xiao Li, Norma A. Alcantar, and Julie P. Harmon

Volume 2013, Article ID 845432, 13 pages

**Nylon/Graphene Oxide Electrospun Composite Coating,** Carmina Menchaca-Campos,

César García-Pérez, Iván Castañeda, Miguel A. García-Sánchez, René Guardián, and Jorge Uruchurtu

Volume 2013, Article ID 621618, 9 pages

**Synthesis and Characterization of Polyphosphazenes Modified with Hydroxyethyl Methacrylate and**

**Lactic Acid,** Evelyn Carolina Martínez Ceballos, Ricardo Vera Graziano, Gonzalo Martínez Barrera, and Oscar Olea Mejía

Volume 2013, Article ID 645869, 7 pages

**Effects of Crumb Rubber Size and Concentration on Performance of Porous Asphalt Mixtures,**

Altan Cetin

Volume 2013, Article ID 789612, 10 pages

**Synthesis, Electrical Conductivity, and Dielectric Behavior of Polyaniline/V<sub>2</sub>O<sub>5</sub> Composites,**

Shama Islam, G. B. V. S. Lakshmi, Azher M. Siddiqui, M. Husain, and M. Zulfequar

Volume 2013, Article ID 307525, 7 pages

**Effect of Gamma-Irradiated Recycled Low-Density Polyethylene on the High- and Low-Temperature Properties of Bitumen,** Perviz Ahmedzade, Alexander Fainleib,

Taylan Günay, Olga Starostenko, and Tetyana Kovalinska

Volume 2013, Article ID 141298, 9 pages

**Silica Aerogel Improves the Biocompatibility in a Poly- $\epsilon$ -Caprolactone Composite Used as a Tissue Engineering Scaffold**, Jianhua Ge, Musen Li, Qingguo Zhang, Christopher Z. Yang, Paul H. Wooley, Xiaofeng Chen, and Shang-You Yang  
Volume 2013, Article ID 402859, 7 pages

**Effects on Mechanical Properties of Recycled PET in Cement-Based Composites**, Liliana Ávila Córdoba, Gonzalo Martínez-Barrera, Carlos Barrera Díaz, Fernando Ureña Nuñez, and Alejandro Loza Yañez  
Volume 2013, Article ID 763276, 6 pages

**The Effect of Polymer-Cement Stabilization on the Unconfined Compressive Strength of Liquefiable Soils**, Ali Ateş  
Volume 2013, Article ID 356214, 8 pages

**Facile Solventless Synthesis of a Nylon-6,6/Silver Nanoparticles Composite and Its XPS Study**, Raúl A. Morales-Luckie, Víctor Sánchez-Mendieta, Oscar Olea-Mejia, Alfredo R. Vilchis-Nestor, Gustavo López-Téllez, Víctor Varela-Guerrero, L. Huerta, and Jesús Arenas-Alatorre  
Volume 2013, Article ID 235850, 8 pages

**Comparison of Cement-Based and Polymer-Based Concrete Pipes for Analysis of Cost Assessment**, Orhan Bozkurt and Mehmet İslamoğlu  
Volume 2013, Article ID 921076, 6 pages

**Manufacture of Partially Biodegradable Composite Materials Based on PLA-Tires Powder: Process and Characterization**, Carlos Rolando Rios-Soberanis, Shuchi Wakayama, Takenobo Sakai, José de los Ángeles Rodríguez-Laviada, and Emilio Pérez-Pacheco  
Volume 2013, Article ID 514951, 8 pages

## Editorial

# Natural, Synthetic, and Recycled Polymers in Composite Materials

**Gonzalo Martínez-Barrera,<sup>1</sup> Osman Gencel,<sup>2</sup>  
Carmina Menchaca-Campos,<sup>3</sup> and Enrique Viguera-Santiago<sup>1</sup>**

<sup>1</sup> *Laboratorio de Investigación y Desarrollo de Materiales Avanzados (LIDMA), Facultad de Química, Universidad Autónoma del Estado de México, Km 12 de la Carretera Toluca-Atlacomulco, 50200 San Cayetano, MEX, Mexico*

<sup>2</sup> *Civil Engineering Department, Faculty of Engineering, Bartin University, 74100 Bartin, Turkey*

<sup>3</sup> *Centro de Investigación en Ingeniería y Ciencias Aplicadas (CIICAp), Universidad Autónoma del Estado de Morelos, 62210 Cuernavaca, MOR, Mexico*

Correspondence should be addressed to Gonzalo Martínez-Barrera; [gonzomartinez02@yahoo.com.mx](mailto:gonzomartinez02@yahoo.com.mx)

Received 1 September 2013; Accepted 1 September 2013

Copyright © 2013 Gonzalo Martínez-Barrera et al. This is an open access article distributed under the Creative Commons Attribution License, which permits unrestricted use, distribution, and reproduction in any medium, provided the original work is properly cited.

Mechanical and management improvements in composite materials require the use of new ways to produce them. The actual tendencies and global developments of novel materials include the introduction of natural, synthetic, and recycled polymers into the composite materials. Recently, composite materials have been used for certain applications, which depend on several conditions such as materials' nature, concentrations, and methodology for their elaboration. Nevertheless, certain properties are not reachable with traditional components; thus, different materials are needed as fillers for reinforce and improve such properties. A worldwide tendency is to use recycled or natural materials and evaluate their influence after adding them to the composite materials. In this sense, polymers are used in a very large variety of composite materials, mainly as fillers or reinforcements. Their chemical structure and physical morphology have been modified by using different kind of energies, including thermal, chemical, and radiation energy. The perspectives are to obtain new materials with improved properties at low cost by using easy technologies and chemically sustainable for the environment.

The knowledge and understanding of such composite materials are therefore of great importance for our living. In this issue, some investigations related to composite materials

are shown, covering different topics, including improvement of the biocompatibility of polycaprolactone and silica aerogel composites used as tissue engineering scaffolds or modifications of polymers (polyphosphazenes) by using some chemicals; polymeric composites with electrical and dielectric properties, including polyaniline conductive compounds and  $V_2O_5$ , whose routes of synthesis are made in situ, where the energy band gap is controlled by the amount of particles; the outstanding use of recycled polyolefins for improvement of bitumen materials and recycled PET of water bottles and its use as filler material of concrete; polymer fibers as reinforcement of polymer composites, especially of polyester-based concretes; the use of recycling copolymers from the automotive industry and their conversion into corrosion protection coatings for metal artifact cultural heritage conservation purposes, highlighting their properties when comparing to a commercial varnish used in conservation. Moreover, the topics also include composite coatings manufactured by electrospinning method for applications in fuel cells, energy storage, and coatings against corrosion; control of the mechanical properties of polymer-cement composites, focusing on comparison of cement-based and polymer-based concrete pipes; natural rubber used in the porous asphalt mixtures, or tire rubber in the manufacture of

biodegradable composites; studies of polymer/nanoparticles composites synthesized by facile solventless procedure; polymeric compounds derived from renewable sources for the detection of solvents, where detection sensitivity is controlled by the layer thickness.

*Gonzalo Martínez-Barrera*  
*Osman Gencel*  
*Carmina Menchaca-Campos*  
*Enrique Viguera-Santiago*

## Research Article

# Cellulose-Based Polymer Composite with Carbon Black for Tetrahydrofuran Sensing

Susana Hernández-López,<sup>1</sup> Enrique Viguera-Santiago,<sup>1</sup> Miriam Mendoza Mora,<sup>1</sup> José Rurik Farias Mancilla,<sup>2</sup> and Erasto Armando Zaragoza Contreras<sup>3</sup>

<sup>1</sup> Laboratorio de Investigación y Desarrollo de Materiales Avanzados (LIDMA), Facultad de Química, Universidad Autónoma del Estado de México, Campus Rosedal, Paseo Colón Esquina con Paseo Tollocan s/n, 50000 Toluca, MEX, Mexico

<sup>2</sup> Universidad Autónoma de Ciudad Juárez, Avenida del Charro 450 Norte, 32310 Ciudad Juárez, CHIH, Mexico

<sup>3</sup> Centro de Investigación en Materiales Avanzados, S.C. Miguel de Cervantes No. 120, Complejo Industrial Chihuahua, 31109 Chihuahua, CHIH, Mexico

Correspondence should be addressed to Susana Hernández-López; [shernandezl@uaemex.mx](mailto:shernandezl@uaemex.mx)

Received 21 May 2013; Revised 14 August 2013; Accepted 15 August 2013

Academic Editor: Gonzalo Martínez-Barrera

Copyright © 2013 Susana Hernández-López et al. This is an open access article distributed under the Creative Commons Attribution License, which permits unrestricted use, distribution, and reproduction in any medium, provided the original work is properly cited.

This work focused on studying the sensing efficiency of tetrahydrofuran (THF) by composite films made of thin layers of a cellulose-based polymer and carbon black. We analyze the reproducibility, durability, desorption time, and the sensitivity percent as a function of the amount of solvent. Two types of experiments were conducted, (1) progressive sensing test (PST) which consisted of progressively increasing the amount of solvent from 0.1 mL increments up to 1.0 mL and (2) multiple sensing test (MST) where the layers were subjected to consecutive pulses of the same amount of solvent, with a minimum of 0.1 mL and a maximum of 0.4 mL. The response and desorption times were a few seconds, and the sensitivity percent ranged from 1% to 170% and was dependent on the solvent quantity.

## 1. Introduction

The polymer/carbon particles composites using carbon black (CB) and carbon nanotubes (CNT) have been extensively investigated for detecting an array of solvent vapors [1–20]. These materials function at room temperature, and it is possible to detect a wide variety of compounds through the appropriate choice of polymer and conductive particles.

The most critical characteristics of these compounds, for use in sensors, are the sensibility, response and desorption times, and durability. Controlling of these parameters in polymer matrices made from renewable sources is of great interest, and there are many potential applications for use in vapor sensing devices.

Cellulose is the most abundant natural product, in addition to being biodegradable and renewable. It is a colorless polymer, insoluble in water, dilute acids and alkalis and in the

most of organic solvents. In addition, cellulose can, via esterification and etherification reactions in pendant hydroxyl groups, yield a wide variety of derivatives. Cellulose esters and ethers can be easily dissolved in aqueous and/or organic solvents. Acrylamidomethyl cellulose acetate butyrate (ACAB) is an ester derived from cellulose obtained by reacting cellulose acetate butyrate (CAB) with N-methylacrylamide (NMA) in an aqueous phase and in the presence of sulfuric acid catalyst. The product, a white powder, is used to produce copolymers with optimum processing properties [21] used in the fabrication of composite materials. Figure 1 shows the chemical structure and composition of ACAB.

In a previous paper [21], we studied the electrical properties of ACAB composites with carbon black. The composites exhibited a critical concentration of 3 wt.% CB. This property and ease of processing make ACAB an attractive material for sensing organic solvent vapors. In this work, we studied

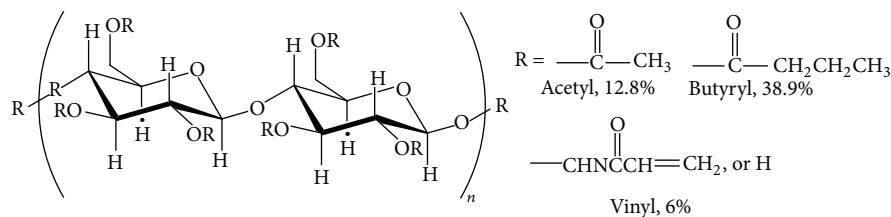


FIGURE 1: Structural representation and composition of commercial ACAB.

the THF vapor detection efficiency using thin layers of an ACAB/10 wt.% CB composite. Sensitivity percent, response, relaxation times, and the durability were studied as a function of the amount of solvent. These parameters were evaluated in two types of experiments: (1) in the first experiment, progressive sensing test (PST), samples were subjected to pulses in which the amount of solvent was progressively increasing from 0.1 mL in 0.1 mL up to complete 1 mL. This methodology was useful in determining the electrical behavior of the composite as a function of solvent level. This testing also served to establish the minimum and maximum limits of detection in the range of 0.1 to 1.0 mL. (2) The second type of experiment, multiple sensing testing (MST), consisted of subjecting the composite layers to the same amount of solvent repeatedly until deterioration ensued. The fixed amounts established for this second experiment (0.1 and 0.4 mL) were determined in accordance with the reproducibility of the results obtained in the PST experiment. Sensing experiments were carried out in an in-house designed chamber. The sample was placed in the chamber, conditioned via a flow of moisture-free air, and then exposed to controlled solvent amounts while the electrical resistance was monitored.

## 2. Experimental Part

**2.1. Reactants.** Acrylamidomethyl cellulose acetate butyrate (ACAB) was obtained from Sigma-Aldrich, Chemical Company. The number-average molecular weight,  $M_n$ , is about 10,000 as determined by GPC. The material is soluble in a variety of acrylic monomer. Other properties include: density of 1.31 g/mL at 25°C, viscosity of 60 cp at 25°C,  $T_g$  of 118°C, and  $T_m$  of 146°C. Carbon Black Vulcan XC72 was donated by Cabot Co. The particle size is in the range of 32 nm, and conductivity is 10–10<sup>2</sup> S/m. HPLC grade tetrahydrofuran (THF) was obtained from Sigma-Aldrich, Chemical Company Inc. It is a solvent with medium polarity that allows an optimum dispersion of carbon black [21–23] and dissolves ACAB. The molecular weight is 72.11 g/mol, the bp 66°C, vapor pressure 19.3 kPa at 20°C, and density 0.88 g/cm<sup>3</sup>. Silver Paint was provided by Electron Microscopy Sciences. It is a colloidal silver liquid with 72% in solids and a contact resistance of 1 Ω.

**2.2. Preparation of the Polymer Composites.** The polymer composites were prepared in accordance with the methodology reported in [21]. Layers of polymer composite were deposited on glass substrates of 2.5 × 2.5 cm, at a speed of 1000 rpm in a spin coating system. Each layer of polymer was obtained by 10 consecutive deposits of ACAB/10 wt.% CB

dissolution, leaving a time of approximately 3 min between each deposit.

The layers were put in a vacuum for 24 hr in order to remove the residual solvent. Electrical contacts were put on the layer composite by painting two parallel lines of silver paint with a distance of 1.5 cm of separation. The layers were selected in accordance with the range of their electrical resistance (a few MΩ in order of magnitude) for each group of experiments.

**2.3. Sensing Tests.** THF vapors were detected using a system in which the electrical resistance of the layer is monitored with a multimeter STEREN MUL model 600 coupled to a computer. The layer first is subjected to a flow of moisture-free air and oil at a rate of 1 L/min. After that, the air is infused with controlled amounts of THF pulses. Each pulse is applied by injecting the respective amount of THF using graduate syringes. Between pulse and pulse, a 10 to 15 min is left so that the resistance returns to a stable value. The layer in relation to the air flow is always placed at a right angle as shown in Figure 2.

**2.3.1. Progressive Sensing Test (PST).** In this type of experiment, the layers were exposed to a progressive increasing of THF pulses in 5 samples with the same range of resistance, from 1 to 2 MΩ. Pulses were applied from 0.1 to 1 mL with increments of 0.1 mL. After the completion of all the pulses, the sample is put in a vacuum for 24 hr to remove the residual solvent, and again it is exposed to the same process. This cycle is made repeatedly (5 times) in order to get a statistics.

**2.3.2. Multiple Sensing Test (MST).** This experiment used layers with the same range of resistance, from 2 to 3.5 MΩ for multiple sensing using 0.1 mL of solvent, and from 5 to 6.5 MΩ for using 0.4 mL. Layers were subjected to repetitive pulses of the same amount of THF until deterioration of the sample was detected. In all cases, this deterioration was identified by an interruption of the electrical signal or because the resistance values were not reproducible, outside of the average of the previous measurements.

## 3. Results and Discussion

**3.1. Tests Progressive Sensing.** The initial characteristics of the used samples are shown in Table 1.

Figure 3 illustrates a typical PST experiment. Each signal is produced in response to a pulse of solvent in quantities that increment from 0.1 to 0.1 up to 1 mL, starting with 0.1 mL.

TABLE 1: Original resistance ( $R_0$ ) for the layers used in each test before any THF pulse.

For PST		For MST at 0.1 mL		For MST at 0.4 mL	
Sample	$R_0$ (M $\Omega$ )	Sample	$R_0$ (M $\Omega$ )	Sample	$R_0$ (M $\Omega$ )
PST 1	1.637	MST 1a	3.539	MST 1b	5.499
PST 2	1.181	MST 2a	3.328	MST 2b	6.190
PST 3	1.553	MST 3a	3.090	MST 3b	6.559
PST 4	1.108	MST 4a	2.109	MST 4b	6.288
PST 5	1.765	MST 5a	4.44	MST 5b	6.190

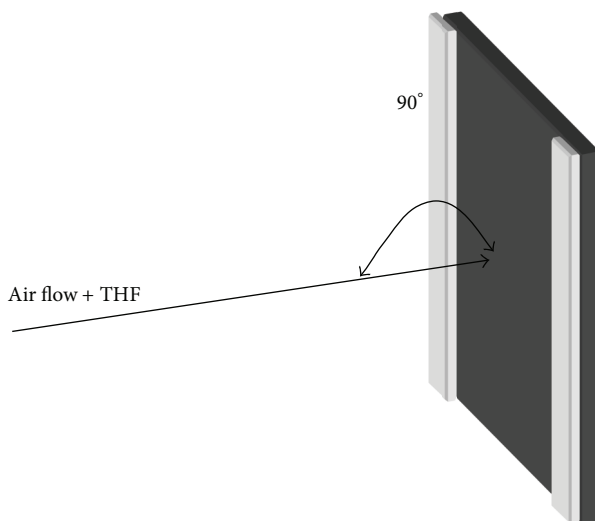


FIGURE 2: Experimental arrangement for sensing test.

The sensitivity percent, response, and desorption times were determined according to the definitions given in [24]. The resistance after a pulse never returns the  $R_0$  value, being  $R_0$  the original resistance before any pulse. The sensitivity of each pulse was calculated using the  $R_i$  value corresponding to the value at which the resistance returns from the previous pulse. Figure 3 shows how  $R_i$  value increases as the amount of solvent increases, and this is usually higher than the initial  $R_0$  value. This effect could be the result of the fact that some solvent is retained by the layer and/or there is a modification of the initial configuration of the conductive networks derived from the swelling of the polymer matrix in contact with the solvent. A similar effect takes place in thin layers of polymer composites when they are exposed to several cycles of heat treatment [23]. The average value of the sensitivity percent is shown in Table 2.

As the amount of solvent increases, the detection sensitivity percent also increases. For a pulse of 1 mL, the sensitivity percent is nearly 180 times greater than the sensitivity for a pulse of 0.1 mL. In the PST experiment, the increase in sensitivity is almost linear between pulse and pulse, from 0.1 to 0.4 mL. The percent of higher sensitivity is presented for THF volumes from 0.5 to 1.0 mL; however, the error in the changes of sensitivity is higher than for volumes from 0.1 to 0.4 mL. For all the THF volumes, the sensitivity percent is greater than the unit, which is an indication, as mentioned before, that the compound of ACAB with CB is a sensitive sensor to THF.

TABLE 2: Sensitivity average (SA), error percent, and response time for the progressive sensing tests.

THF pulse (mL)	SA (%)	Error (%)	$t_R$ (s)
0.1	1.53	$\pm 1.34$	11
0.2	2.10	$\pm 3.32$	13
0.3	4.50	$\pm 22.23$	13
0.4	15.70	$\pm 98.21$	24
0.5	33.93	$\pm 43.00$	11
0.6	57.65	$\pm 11.45$	15
0.7	105.83	$\pm 37.42$	9
0.8	131.95	$\pm 33.74$	8
0.9	143.78	$\pm 7.58$	4
1	178.83	$\pm 17.68$	2

The response time is defined as the time that it takes until the detector reaches the 90% of the maximum resistance [24]. The average of the response time in the PST experiments is shown in Table 2. In this type of experiments, the response times of the ACAB with CB composite to THF in the range of 0.1–1.0 mL take no longer than 24 s, and this is very good for sensors derived from polymeric composites. The response times have a tendency to decrease with the amount of THF. This indicates that THF has to be absorbed via diffusion and swelling of the polymer matrix. This swelling produces a separation of the conductive particles and, in turn, a variation

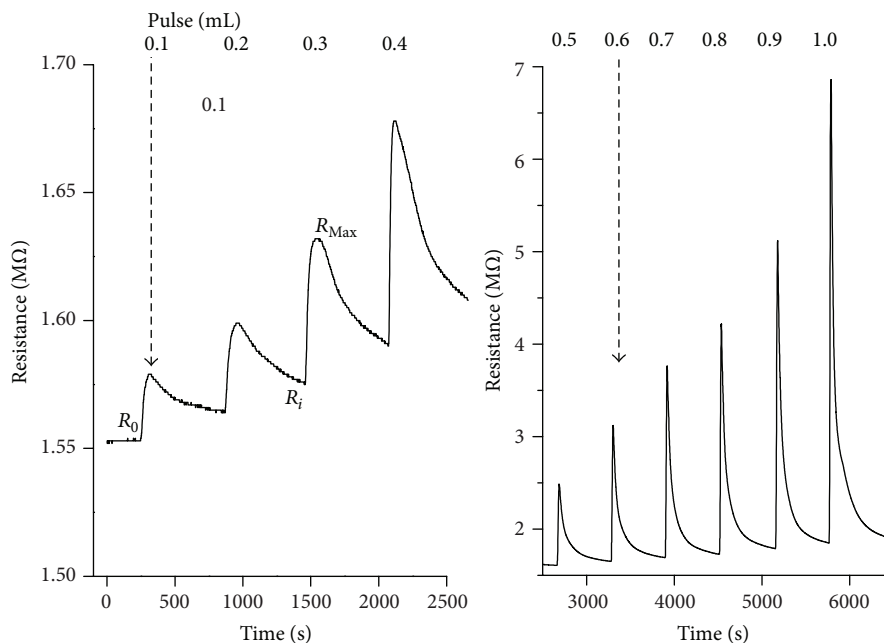


FIGURE 3: Progressive sensing test from 0.1 to 1 mL of THF for PST 3 sample.

in the electrical response or resistance. With a small amount of solvent, there is a slight penetration of the surface of the layer, and the change in resistance is not significant. As the amount of solvent increases, absorption and swelling are greater, and the response to the detection is incremental. In this case, the response is detected in the first few seconds that the composite material comes in contact with the solvent.

The desorption time is the time taken for the layer composite to release the absorbed solvent at a specific resistance value. This value corresponds to that at which the resistance has reached the 10% of its saturation value after it has decreased from the maximum value [24]. It is noticed that as the solvent amount increases there is a reduction in desorption times. A part of the solvent remains absorbed in the layer (as evidenced by the greater initial resistance in each subsequent pulse). When low amounts of solvent are used, most remains absorbed by the layer and desorption of minute amounts of it is a very slow process. For higher solvent amounts, some vapor also persists but the rest is desorbed immediately, making the desorption process faster.

**3.2. Multiple Sensing Test (MST).** The purpose of this experiment was to evaluate the reproducibility of the composite by applying a consecutive series of pulses using the same THF quantity. 0.1 and 0.4 mL quantities of THF were studied. The values of initial resistance for the composite layers are shown in Table 1. The results of the multiple sensing tests are shown in Figure 4(a). Each peak represents the response to an injected pulse of 0.1 mL THF. The average of the sensitivity percent of five samples subjected to 20 pulses of 0.1 mL in this MST experiment is displayed in Table 3.

The sensitivity percent is shown in Figure 4(b), and it is compared with the average value that is 1.77. The percent error with respect to the media is  $\pm 5.64\%$ . Thirty-five percent are

TABLE 3: Sensitivity average for the MST experiments to 0.1 and 0.4 mL THF.

Test number	SA (%) for 0.1 mL	SA (%) for 0.4 mL
1	1,783	17.400
2	1,859	19.300
3	1,662	19.250
4	1,799	19.700
5	1,593	18.900
6	1,873	16.600
7	1,843	18.950
8	1,674	18.100
9	1,619	16.800
10	1,560	18.700
11	1,862	—
12	1,825	—
13	1,815	—
14	1,773	—
15	1,770	—
16	1,593	—
17	1,943	—
18	1,940	—
19	1,937	—
20	1,757	—
Average	1,774	18.370

outside of the range of error; therefore, 65% of the pulses are accepted as the reproducibility sensing percent, with a continuous average service of 9.3 hr for each layer, equivalent to 20 pulses. In the same way as in the previous test, five layers were evaluated for pulses of 0.4 mL. The same methodology

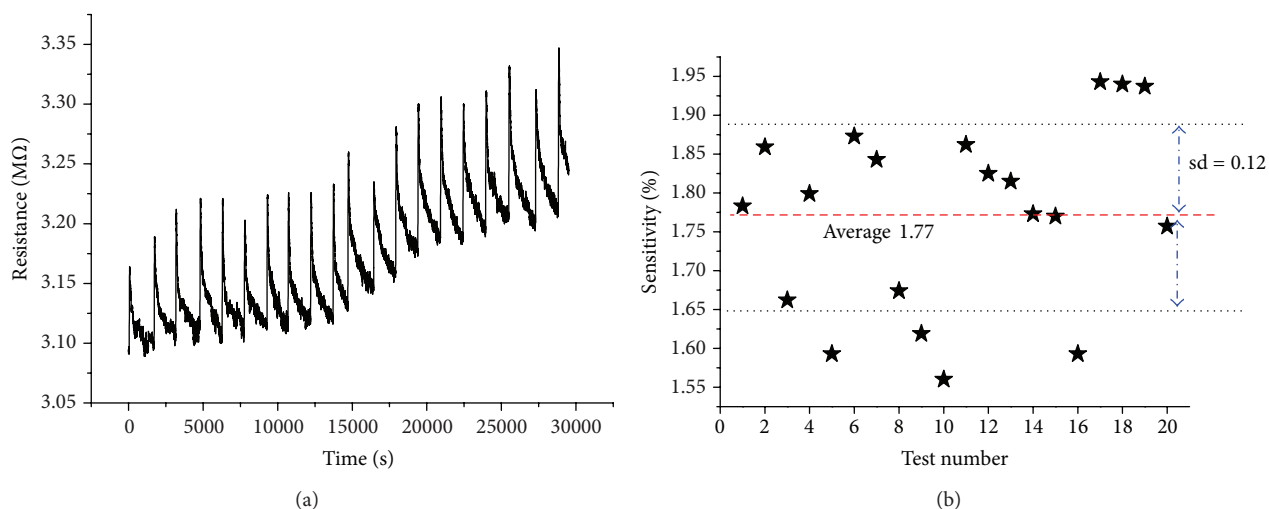


FIGURE 4: For the MST-3a sample: (a) MST experiment to 0.1 mL THF and (b) reproducibility to the MST experiment at 0.1 mL THF.

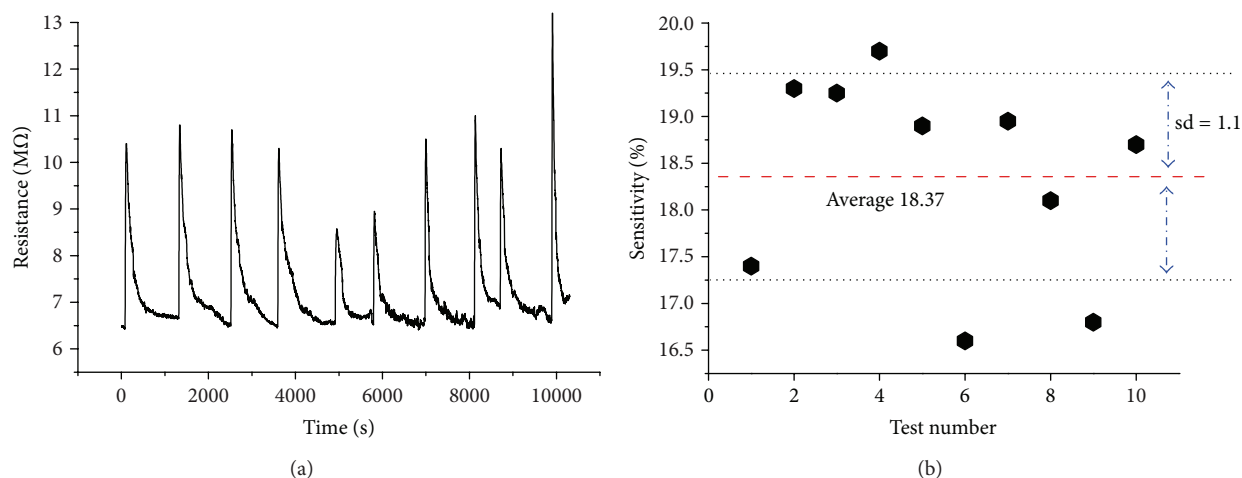


FIGURE 5: For the MST-3c sample: (a) MST experiment to 0.4 mL THF and (b) reproducibility to the MST experiment at 0.4 mL of THF for the same sample.

was used to evaluate five layers with pulses of 0.4 mL. The original resistance of the layers is shown in Table 1.

A multiple sensing test using 0.4 mL THF is shown in Figure 5(a). It is noted that the sensitivity is higher for pulses of 0.4 mL than for 0.1 mL; however, at high volumes the deterioration of the sensor layer is faster. This is detected by the lower number of pulses of 0.4 mL THF in which the layer senses before it is damaged. The average sensitivity of the five evaluated layers is shown in Table 3. The number of performed tests was, on average, 10 pulses with an error of  $\pm 5.08\%$  in comparison with the average value (18.37%). The results are shown in Figure 5(b), where the average sensitivity is the dotted line; the solid lines represent the range of acceptable error for reproducibility. Thirty percent of the injected pulses are outside of this range, and therefore 70% of the pulses are reproducible with 3.5 hr of continuous sensing. While with 0.1 mL it is possible to detect 20 successive pulses, with 0.4 mL, the error is  $\pm 5\%$ . This

deviation can be due to a change in the accommodation of the conductive networks produced by the carbon black particles in the polymer matrix. The carbon black particles undergo a modification of their initial or previous pulse. It can be seen that the response and desorption times depend on the THF concentration. For quantities lower than 0.5 mL, the response times tend to be greater than 2–10 s. The sensitivity percent is greater for higher THF quantities, on the order of 180%, and the desorption times tend to be greater than 5 min. Low THF concentrations tend to be retained with higher intensity, and this is evidenced by long desorption times.

It can be seen that the response and desorption times depend on the THF concentration. For concentrations lower than 0.5 mL, the response times tend to be greater than 2–10 s for amounts above 0.5 mL THF. The sensitivity percent is greater than the unit for lower THF quantities, but for higher concentrations than 0.4 mL the sensitivity percent is in

the order of 180%, and the desorption time similarly tends to be greater than 5 min. Small THF concentrations tend to be retained with higher intensity, which is evidenced by the long desorption times.

Some authors, such as Kaur et al. [25], note that a short response time in a chemiresistor is 45 s; Chen et al. [26] noted that a sensor of WPU/3.5 wt.% CB exposed to 10 ppt (parts per trillion) of acetone exhibits response times from 150 to 400 s, and a short desorption time for the same sensor ranges from 50 to 100 s. Ding et al. [27] reported a desorption time (less than or equal to 7 s) in a gas sensor based on nanofibers manufactured via electrospinning. There is not a precise time designed to define a short or long response. However, one might conclude that the same compound exhibits a range in the parameters depending on the type of sensor and on the specific application.

#### 4. Conclusions

Conductive layers of modified cellulose and 10 wt.% CB composites were prepared by spinning. Their ability to detect THF vapors was evaluated by determining parameters: sensitivity percent, response and desorption times, reproducibility, and durability in two types of experiments, PST and MST. The sensitivity percent from PST experiments allowed evaluation of the potential to effectively sense THF in the range from 0.1 to 1.0 mL. Sensing effectiveness increased as the amount of THF increased, reaching a maximum of 180% at 1.0 mL THF. The response times for the same experiment were in the range of 2–24 s while desorption times decreased from 12 to 2.3 min. MST experiments were undertaken to determine reproducibility and durability at constant THF volumes, 0.1 and 0.4 mL. For both volumes, the reproducibility was around 65%, and the durability decreased at a half from 20 to 10 pulses when the amount of solvent increases from 0.1 to 0.4 mL. Those results indicate that ACAB with 10 wt.% CB composites effectively detects THF.

#### Conflict of Interests

The authors of the paper do not have a direct financial relation or conflict of interests with the commercial identities mentioned in this paper. The commercial trademarks, Sigma-Aldrich and Chemical and Electron Microscopy Sciences mentioned in this paper, are only for guaranteeing the reproducibility of the experiments, not leading to a conflict of interests for any of the authors.

#### Acknowledgment

The authors gratefully acknowledge financial support by PROMEP-SEP for “Red de Compuestos Poliméricos, Propiedades y Aplicaciones.”

#### References

- [1] M. Castro, B. Kumar, J. F. Feller, Z. Haddi, A. Amari, and B. Bouchikhi, “Novel e-nose for the discrimination of volatile organic biomarkers with an array of carbon nanotubes (CNT) conductive polymer nanocomposites (CPC) sensors,” *Sensors and Actuators B*, vol. 159, no. 1, pp. 213–219, 2011.
- [2] M. S. Freund and N. S. Lewis, “A chemically diverse conducting polymer-based ‘electronic nose,’” *Proceedings of the National Academy of Sciences of the United States of America*, vol. 92, pp. 2652–2656, 1995.
- [3] B. J. Doleman and N. S. Lewis, “Comparison of odor detection thresholds and odor discriminabilities of a conducting polymer composite electronic nose versus mammalian olfaction,” *Sensors and Actuators B*, vol. 72, no. 1, pp. 41–50, 2001.
- [4] A. V. Shevade, M. A. Ryan, M. L. Homer, A. M. Manfreda, H. Zhou, and K. Manatt, “Molecular modeling of polymer composite-analyte interactions in electronic nose sensors,” *Sensors and Actuators B*, vol. 93, no. 1–3, pp. 84–91, 2003.
- [5] A. V. Shevade, M. L. Homer, C. J. Taylor et al., “Correlating polymer-carbon composite sensor response with molecular descriptors,” *Journal of the Electrochemical Society*, vol. 153, no. 11, Article ID 026611JES, pp. H209–H216, 2006.
- [6] M. A. Ryan, H. Zhou, M. G. Buehler et al., “Monitoring space shuttle air quality using the jet propulsion laboratory electronic nose,” *IEEE Sensors Journal*, vol. 4, no. 3, pp. 337–347, 2004.
- [7] S. V. Patel, M. W. Jenkins, R. C. Hughes, W. G. Yelton, and A. J. Ricco, “Differentiation of chemical components in a binary solvent vapor mixture using carbon/polymer composite-based chemiresistors,” *Analytical Chemistry*, vol. 72, no. 7, pp. 1532–1542, 2000.
- [8] N. Tsubokawa, Y. Shirai, M. Okazaki, and K. Maruyama, “A novel gas sensor from crystalline polymer-grafted carbon black: responsibility of electric resistance of composite from crystalline polymer-grafted carbon black against solvent vapor,” *Polymer Bulletin*, vol. 42, no. 4, pp. 425–431, 1999.
- [9] E. J. Severin, B. J. Doleman, and N. S. Lewis, “An investigation of the concentration dependence and response to analyte mixtures of carbon black/insulating organic polymer composite vapor detectors,” *Analytical Chemistry*, vol. 72, no. 4, pp. 658–668, 2000.
- [10] J. R. Li, J. R. Xu, M. Q. Zhang, and M. Z. Rong, “Carbon black/polystyrene composites as candidates for gas sensing materials,” *Carbon*, vol. 41, no. 12, pp. 2353–2360, 2003.
- [11] M. C. Burl, B. C. Sisk, T. P. Vaid, and N. S. Lewis, “Classification performance of carbon black-polymer composite vapor detector arrays as a function of array size and detector composition,” *Sensors and Actuators B*, vol. 87, no. 1, pp. 130–149, 2002.
- [12] E. G. Berrios, T. Gao, D. Walker, B. S. Brunschwig, and N. S. Lewis, “Composites of carboxylate-capped TiO<sub>2</sub> nanoparticles and carbon black as chemiresistive vapor sensors,” *Sensors and Actuators B*, vol. 158, p. 17, 2011.
- [13] M. Matsuguchi, K. Asahara, and T. Mizukami, “Highly sensitive toluene vapor sensors using carbon black/amino-functional copolymer composites,” *Journal of Applied Polymer Science*, vol. 127, no. 4, pp. 2529–2535, 2013.
- [14] E. S. Tillman and N. S. Lewis, “Mechanism of enhanced sensitivity of linear poly(ethylenimine)-carbon black composite detectors to carboxylic acid vapors,” *Sensors and Actuators B*, vol. 96, no. 1–2, pp. 329–342, 2003.
- [15] B. J. Doleman, R. D. Sanner, E. J. Severin, R. H. Grubbs, and N. S. Lewis, “Use of compatible polymer blends to fabricate arrays of carbon black-polymer composite vapor detectors,” *Analytical Chemistry*, vol. 70, no. 13, pp. 2560–2564, 1998.
- [16] B. C. Sisk and N. S. Lewis, “Vapor sensing using polymer/carbon black composites in the percolative conduction regime,” *Langmuir*, vol. 22, no. 18, pp. 7928–7935, 2006.

- [17] G. Sakale, M. Knite, V. Teteris, V. Tupureina, S. Stepina, and E. Liepa, "The investigation of sensing mechanism of ethanol vapour in polymer-nanostructured carbon composite," *Central European Journal of Physics*, vol. 9, no. 2, pp. 307–312, 2011.
- [18] M. C. Lonergan, E. J. Severin, B. J. Doleman, S. A. Beaber, R. H. Grubbs, and N. S. Lewis, "Array-based vapor sensing using chemically sensitive, carbon black-Polymer resistors," *Chemistry of Materials*, vol. 8, no. 9, pp. 2298–2312, 1996.
- [19] L. Niu, Y. Luo, and Z. Li, "A highly selective chemical gas sensor based on functionalization of multi-walled carbon nanotubes with poly(ethylene glycol)," *Sensors and Actuators B*, vol. 126, no. 2, pp. 361–367, 2007.
- [20] C. Wei, L. Dai, A. Roy, and T. B. Tolle, "Multifunctional chemical vapor sensors of aligned carbon nanotube and polymer composites," *Journal of the American Chemical Society*, vol. 128, no. 5, pp. 1412–1413, 2006.
- [21] S. H. Lopez and E. V. Santiago, "Acrylated-epoxidized soybean oil-based polymers and their use in the generation of electrically conductive polymer composites," in *Soybean—Bio-Active Compounds*, H. A. El-Shemy, Ed.
- [22] R. San Juan-Farfán, S. Hernández-López, G. Martínez-Barrera, M. A. Camacho-López, and E. Viguera-Santiago, "Electrical characterization of polystyrene-carbon black composites," *Physica Status Solidi*, vol. 2, no. 10, pp. 3762–3765, 2005.
- [23] S. H. López, E. V. Santiago, M. M. Rojas, and D. R. Contreras, "Changes in the electrical resistivity of thin-films for polymer composites induced by heating-cooling cycles," *Journal of Materials Science and Engineering B*, vol. 2, no. 12, pp. 601–6010, 2012.
- [24] M. Kaur, D. K. Aswal, and J. V. Yakhmi, "Chemiresistor gas sensors: materials, mechanisms and fabrication," in *Science and Technology of Chemiresistor Gas Sensors*, chapter 2, pp. 33–93, 2007.
- [25] M. Kaur, D. K. Aswal, and J. V. Yakhmi, "Chemiresistor gas sensors: materials, mechanisms and fabrication," in *Science and Technology of Chemiresistor Gas Sensors*, pp. 33–93, 2007.
- [26] S. G. Chen, J. W. Hu, M. Q. Zhang, M. Z. Rong, and Q. Zheng, "Improvement of gas sensing performance of carbon black/waterborne polyurethane composites: effect of crosslinking treatment," *Sensors and Actuators B*, vol. 113, no. 1, pp. 361–369, 2006.
- [27] B. Ding, M. Wang, J. Yu, and G. Sun, "Gas sensors based on electrospun nanofibers," *Sensors*, vol. 9, no. 3, pp. 1609–1624, 2009.

## Research Article

# Effects of the Addition of *Ortho*- and *Para*-NH<sub>2</sub> Substituted Tetraphenylporphyrins on the Structure of Nylon 66

Luis A. Díaz-Alejo,<sup>1</sup> E. Carmina Menchaca-Campos,<sup>2</sup> J. Uruchurtu Chavarín,<sup>2</sup>  
R. Sosa-Fonseca,<sup>3</sup> and Miguel A. García-Sánchez<sup>1</sup>

<sup>1</sup> Departamento de Química, Universidad Autónoma Metropolitana-Iztapalapa, San Rafael Atlixco 186, Colonia Vicentina, 09340 Mexico City, DF, Mexico

<sup>2</sup> Centro de Investigación en Ingeniería y Ciencias Aplicadas (CIICAp), Universidad Autónoma del Estado de Morelos (UAEM), Avenida Universidad 1001, Colonia Chamilpa, 62209 Cuernavaca, MOR, Mexico

<sup>3</sup> Departamento de Física, Universidad Autónoma Metropolitana-Iztapalapa, San Rafael Atlixco 186, Colonia Vicentina, 09340 Mexico City, DF, Mexico

Correspondence should be addressed to Miguel A. García-Sánchez; mags@xanum.uam.mx

Received 30 March 2013; Revised 27 June 2013; Accepted 16 July 2013

Academic Editor: Enrique Viguera Santiago

Copyright © 2013 Luis A. Díaz-Alejo et al. This is an open access article distributed under the Creative Commons Attribution License, which permits unrestricted use, distribution, and reproduction in any medium, provided the original work is properly cited.

The synthetic tetrapyrrole macrocycles, such as porphyrins (H<sub>2</sub>P) and phthalocyanines (H<sub>2</sub>Pc), exhibit interesting physicochemical properties suitable to be used in modern technology. For many applications, those species should be trapped or fixed inside graphite, hydrotalcites, silica, TiO<sub>2</sub>, or polymers. Methodologies for the optimization of the properties of porphyrins, trapped or fixed inside polymers, have been barely developed. Our research works in the development of methodologies for the optimization of incorporation and display of properties of tetrapyrrole macrocycles inside inorganic, polymeric, or hybrid networks. This paper shows some results about the effect of the spatial disposition of the amine (–NH<sub>2</sub>) groups attached on the periphery of substituted tetraphenylporphyrins, on the Nylon 66 structure and on the display of the physicochemical properties of the trapped macrocycles. Nylon 66 was synthesized from adipoyl chloride and hexamethylenediamine in presence of tetraphenylporphyrins substituted with –NH<sub>2</sub> groups localized at the *ortho*- or *para*-positions of the phenyls. Cobalt complexes formation was used to quantify the amount of porphyrins in the polymer fibers. Characterization results show that the spatial position of amine groups of the porphyrins has important structural and textural effect on the Nylon 66 fibers and on the fluorescence of the porphyrins integrated into the fibers.

## 1. Introduction

Porphyrins are tetrapyrrole macrocyclic compounds playing a transcendental role in nature as one of the principal components of molecules such as (i) chlorophyll, (ii) the *heme* group in blood and cytochromes and (iii) cyanocobalamin (Vitamin B<sub>12</sub>) [1–3]. Formally, porphyrins are modified or substituted aromatic tetrapyrrole macrocyclic compounds derived from porphin (Figure 1), which consists of four pyrrole rings bonded through *methine* (=CH) bridges in order to form a planar and highly conjugated macrocycle. In the free bases of porphyrins, the two *pyrrolic* hydrogens can be substituted by a cation, and the remaining two nitrogens tend to easily coordinate with a metal nucleus as to form

a stable metalloporphyrin. Synthetic porphyrinic complexes, involving practically all metallic elements of the periodic table, have been synthesized already [2–4]. The central space of porphyrins can only accommodate ions having an atomic radius smaller than 0.201 nm [2–4]; thus, causing that in the porphyrinic complexes containing the larger ions, the metallic element must be located outside of the molecular plane. Similar to the size of the cation, the presence of massive axial ligands can either induce the loss of planarity or the structural deformation of the macrocycle. Furthermore, both peripheral and remaining pyrrole hydrogens as well as those allocated on the *methine* bridges can be exchanged by different chemical substituents to render an extraordinary family of compounds (Figure 1(b)).

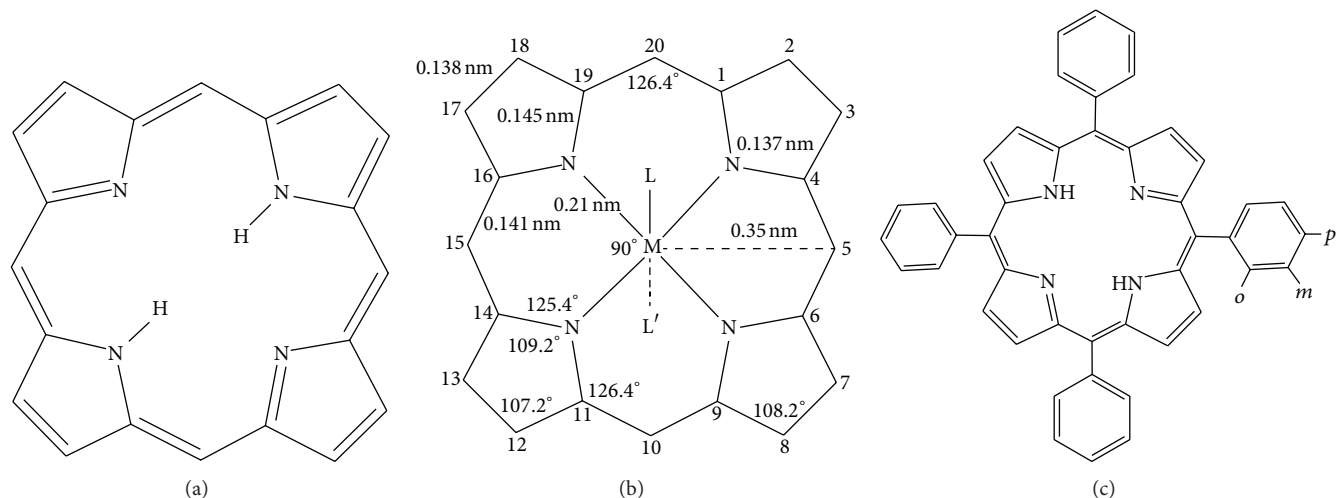


FIGURE 1: (a) Structure of the tetrapyrrolic porphyrin macrocycle; (b) bond lengths, bond angles, and positions (1 to 20) of possible peripheral substituents in the respective metallic complex; and (c) *ortho*-, *meta*-, and *para*-positions in a tetraphenylporphyrin ( $H_2T(o-, m-, p-S)PP$ ).

The extensively delocalized  $\pi$ -electron systems of these centrosymmetric compounds confer upon them, besides chemical and thermal stability, some other interesting spectroscopic, optical, and electrical properties that allow a great number of applications in fields such as optics [5, 6], electrochemistry [7], catalysis [8], and sensing [9, 10]. The free bases of porphyrins exhibit a red fluorescence in the range from 600 to 730 nm, and it is known that light of wavelength between 620 and 690 nm penetrates about 1.0 cm into biological tissues [11]. However, at both the far red or near infrared radiation regions (650 to 1,500 nm), a better tissue penetration occurs [12]. Furthermore, some substituted porphyrins are selectively adsorbed by malignant tissues when singlet oxygen ( $^1O_2$ ) atoms are generated under red light illumination [2–4, 13–15]. Due to these properties, porphyrins have been extensively probed and used in Photodynamic Therapy (PDT) of cancer [16] and in the inactivation of some kinds of bacteria [17].

In *meso*-porphyrins, either one or several methylene hydrogens can be substituted by *alkyl* or *aryl* groups, as, for instance, phenyl rings in tetraphenylporphyrins ( $H_2TPP$ ). In tetraphenylporphyrins, the substituents are commonly located at the *para*-positions of phenyls (Figure 1(c)); that is, these groups are situated on the same molecular plane [8, 18, 19]. It has been demonstrated that there exists a relationship among (i) the presence of electroattracting substituents, (ii) the basicity of the central nitrogens, and (iii) the *redox* and photophysical properties of  $H_2TPP$  molecules [20]. Reactivity differences have been discovered among the *ortho*-, *meta*-, and *para*-substituted isomers of tetrakis-(*N*-methylpyridinium)-porphyrin,  $H_2TMPyP^{2+}$  [21, 22]. In this molecule, the *ortho*-isomer results to be a very acid porphyrin ( $pK_a = -0.9$ ), and it is a very well-known example of a stable porphyrin in acid medium (1 M), the  $H_2TMPyP^{4+}$  dicationic form of which can be observed at high acid concentration (up of 10 M). Great differences in the *redox* and photophysical properties have been discovered among the *ortho*-, *meta*-, and

*para*-halide substituted traphenylporphyrins,  $H_2T(o, m \acute{o} p-X)PP$ , and this kind of phenomenon has been termed as the “*ortho-effect*” [21–25].

The electroattracting character of the substituents present in *meso*-tetraphenylporphyrins diminish the intensity of UV-Vis absorption [21, 22, 26, 27], but this effect results are more evident in the emission spectra [23–25, 28]. Related to this, a shallow, but persistent shift is observed with respect of the principal bands (i.e., the Soret and Q bands) in the UV-Vis spectra of *para*-, *meta*-, and *ortho*- $H_2TMPyP$  isomers. Yet, these changes occur differently for *ortho*- and *para*-isomers than for the *meta*-isomers. However, larger differences in the UV-Vis spectra are detected for the *ortho*, *meta*, and *para* isomers of protonated forms of  $H_2TPP$  and  $H_2TMPyP$  species.

For some of the above mentioned applications, porphyrins require to be trapped or fixed inside diverse substrates such as carbon, zeolites, and inorganic oxides [29]. However, the development of pertinent methods for preserving the physicochemical and luminescent properties of porphyrins trapped or fixed within polymer networks has been scarcely explored during the past decades [30–32]. In view of the transcendental role played by tetrapyrrole macrocycles in nature and because of the properties inherent in their synthetic analogues, during the last decade an increased interest has aroused for the synthesis of new materials based on the use of these compounds [4, 33–49]. At this concern, new polymeric systems were synthesized; the important point being that porphyrins could be trapped, fixed as a ramification, or inserted as part of the polymeric chain. The materials so obtained showed interesting physicochemical properties suitable to be used in technological areas and devices such as catalysis [4, 37, 38], electrocatalysis [31, 32], solar cells [4, 39, 40], electronics [4, 41], optics [4, 42, 43], permeable membranes [44], medical appliances [45, 46], and sensors [47–49].

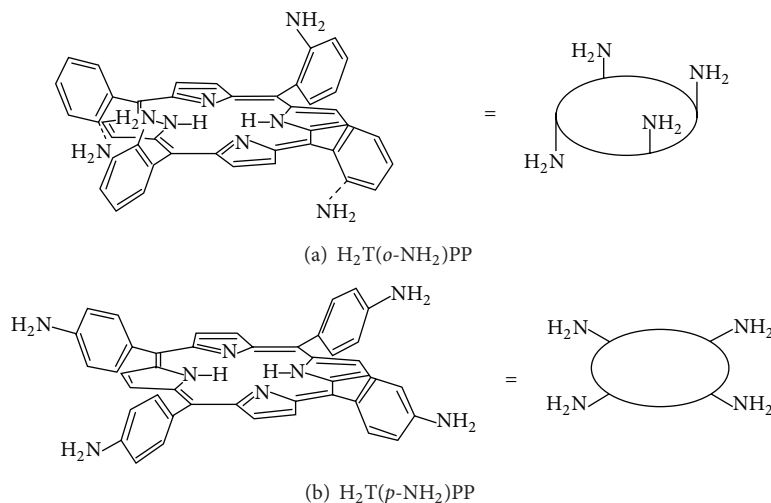


FIGURE 2: Structural representation of: (a) *ortho*-amino,  $H_2T(o-NH_2)PP$ , and (b) *para*-amino,  $H_2T(p-NH_2)PP$ , isomers of substituted tetraphenylporphyrins.

In the present work, we have explored the structural effect of structurally attaching different isomers of tetraphenylporphyrins over polymer fibers that grow from polyamine Nylon 66-like polymers when the isomers of *ortho*- and *para*-amine substituted tetraphenylporphyrins, that is, ( $H_2T(o-NH_2)PP$  and  $H_2T(p-NH_2)PP$ ) (Figure 2), were included in the synthesis. The formation of the respective cobalt complexes of porphyrins was used as a way to confirm and quantify the presence of it in the polyamide chains. The miscellaneous properties showed by porphyrins and their potential integration to Nylon 66 fibers could be used in the design of new and interesting hybrid materials, suitable to be employed in assorted technological areas.

## 2. Experimental

**2.1. Synthesis of Porphyrin Free Bases.** Free bases of *ortho*- (*o*) and *para*- (*p*) substituted tetraphenylporphyrins,  $H_2T(o$ - or  $p$ -S)PP (Figure 1(b)), were synthesized by the Rothmund reaction and the Adler Method [50–52], from their respective substituted *ortho*- or *para*-nitro benzaldehyde, together with pyrrole, and zinc acetate,  $Zn(Ac)_3$ , under reflux in propionic acid (Figure 3). Once the reaction mixture was cooled to ambient conditions, an equivalent volume of chloroform was added to the mixture, which was kept under stirring for 12 hours. The resultant solid was filtered and washed with chloroform and methanol until the filtered liquid was clear. In a second step, the nitro groups ( $-NO_2$ ) were reduced with a  $SnCl_2 \cdot 2H_2O$ , HCl solution while maintaining the temperature at around  $65-70^\circ C$  for 25 minutes. After this period, the mixture was neutralized with a 30 vol.%  $NH_4OH$  solution. The reddish precipitate was extracted with chloroform, which was later evaporated. The solid obtained was washed with a diluted ammonia solution. Purified  $H_2T(o-NH_2)PP$  or  $H_2T(p-NH_2)PP$  solids were obtained by filtration through a chromatographic silica gel column employing chloroform as eluent. The resultant purple solids were characterized by

elemental chemical analysis, FTIR, UV-Vis, and fluorescence spectroscopies.

**2.2. Synthesis of Nylon 66 with Chemically Attached *Ortho*- or *Para*- $NH_2$  Substituted Porphyrins (Ny 66-*o*- $NH_2$  or Ny 66-*p*- $NH_2$ ).** To synthesize Nylon 66 fibers containing free bases of porphyrins as part of the polyamide structure, 0.8 g of hexamethylene diamine was dissolved in 12 mL of a 0.625 M NaOH solution. This dissolution was added under continuous stirring to a second mixture consisting of 1 mL of adipoyl chloride and 11.1 mL of a solution of either  $1.63 \times 10^{-4}$  M of  $H_2T(o-NH_2)PP$  or  $H_2T(p-NH_2)PP$ , in chloroform, while kept under ice inside a water bath (Figure 4). The polyamide solid formed this way was filtered and washed with methanol and chloroform, dried at room temperature overnight, and left reacting for one more night at  $75^\circ C$ . For simplicity, the samples were labeled as Ny 66-*o*- $NH_2$  or Ny 66-*p*- $NH_2$ ; additionally, a pure Nylon 6 sample was synthesized in the absence of porphyrins to be employed as a blank specimen. All polyamides were characterized by FTIR, UV-Vis, fluorescence, SEM, and EDS mapping.

**2.3. Synthesis of the Ny 66-Co-*o*- $NH_2$  or Ny 66-Co-*p*- $NH_2$  Cobalt Complexes.** The Ny 66-Co-*o*- $NH_2$  or Ny 66-Co-*p*- $NH_2$  cobalt complexes were synthesized from a 0.100 g mixture of the respective Ny 66-*o*- $NH_2$  or Ny 66-*p*- $NH_2$  samples dissolved in methanol and 0.4 g of  $CoCl_2$ ; this reactant system was kept under reflux for 12 h. After this time, the solids were filtered and washed sequentially with methanol, chloroform, and water to eliminate any unreacted cobalt. The dried solids were characterized by FTIR, UV-Vis, and fluorescence spectroscopies, as well as by HRSEM and EDS mapping.

**2.4. Instrumentation.** UV-vis-NIR characterization was carried out in a Cary-Varian 500 E spectrophotometer from

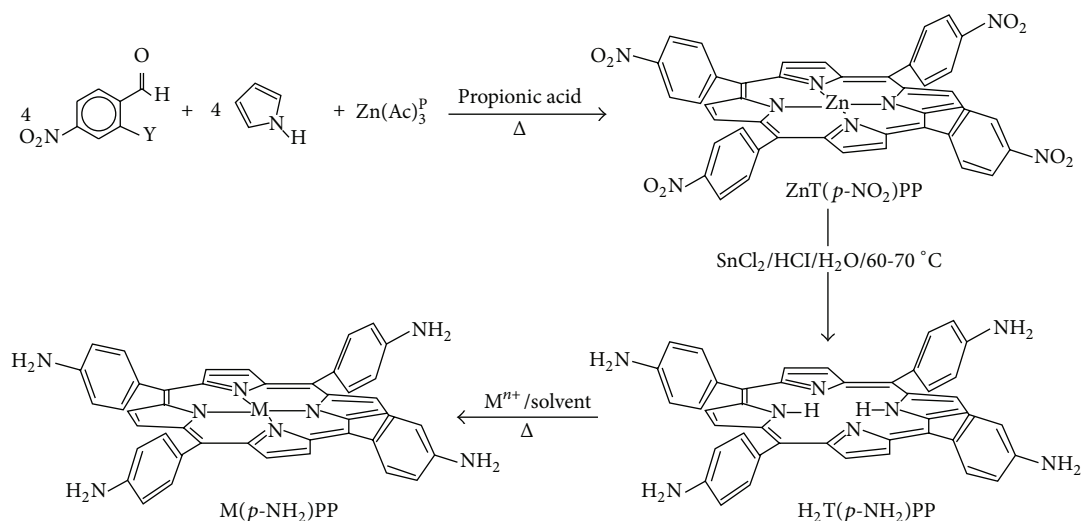


FIGURE 3: Synthesis route of  $H_2T(p-NH_2)PP$  species through the production of  $Zn(p-NO_2)PP$ , zinc tetra-nitro-phenyl porphyrin, intermediary. Starting from the  $H_2T(p-NH_2)PP$  free base, it is possible to synthesize complexes with some other cations ( $M^{n+}$ ), including cobalt.

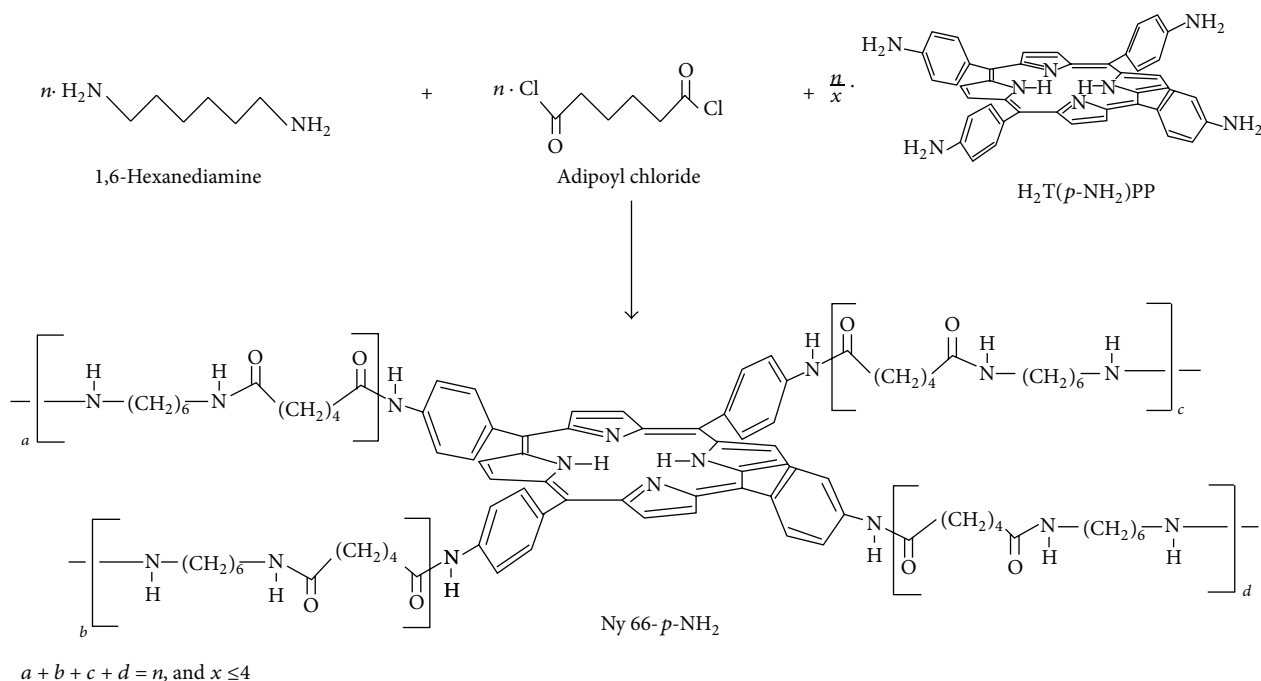


FIGURE 4: Synthesis route for the incorporation of the  $H_2T(o- \text{ or } p-NH_2)PP$  species into the Nylon 66 network; the  $a$ ,  $b$ ,  $c$ , and  $d$  subindexes are related to the lateral chains formed over the amine groups of porphyrin, which could attain the same or different sizes.

200 to 800 nm (UV-vis) and from 1000 nm to 2500 nm ( $100,000$  to  $4,000 \text{ cm}^{-1}$ ) (NIR). Infrared spectra (FTIR) were obtained from a Perkin-Elmer GX FTIR spectrometer. The fluorescence of solutions was measured at  $25^\circ\text{C}$  in a PC1 spectrofluorometer from ISS (Champaign, IL), equipped with a water-jacketed cell holder for temperature control. Fluorescence emission of the hybrid solids was obtained at room temperature, between 200 and 800 nm (UV-vis), by means of a Perkin-Elmer 650-10S spectrofluorometer fitted with a 150 W xenon lamp. The XRD diffractograms were obtained

with powders Diffractometer Siemens D-5000 with graphite monochromator of  $\lambda(\text{CuK}\alpha) = 1.5418 \text{ \AA}$ . HRSEM images were obtained from a JEOL 7600F Instrument, including an Oxford Instruments INCA EDS detector.

### 3. Results and Discussion

The UV-visible spectra of free porphyrins are characterized by an intense band at around 420–430 nm (i.e., the Soret or B band) and four small Q bands in the range from 500

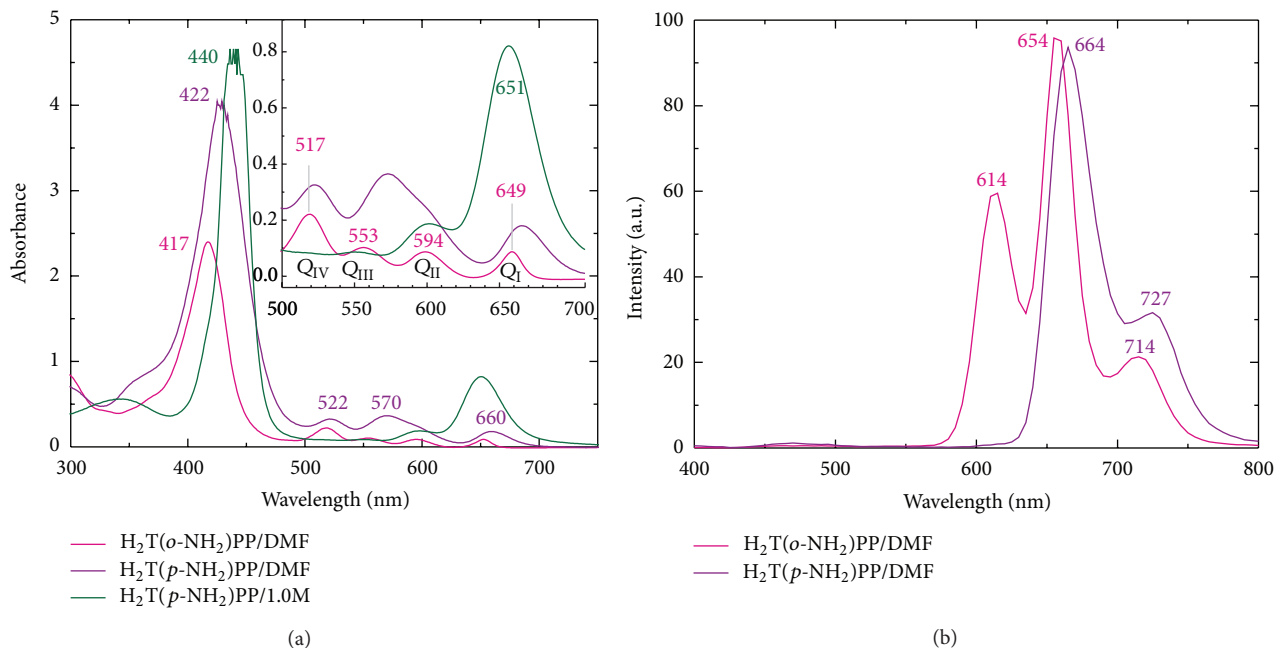


FIGURE 5: (a) UV-Vis and (b) fluorescence spectra ( $\lambda_{\text{exc}} = 3270 \text{ nm}$ ) of  $\text{H}_2\text{T}(o\text{-NH}_2)\text{PP}$  and  $\text{H}_2\text{T}(p\text{-NH}_2)\text{PP}$  free bases and  $\text{H}_4\text{T}(p\text{-NH}_2)\text{PP}^{2+}$  dicationic species in solution.

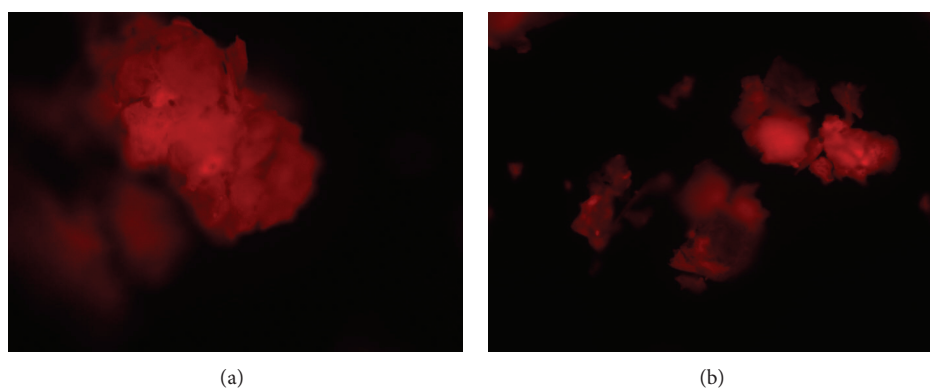


FIGURE 6: Microscopy images ( $\times 10$ ) of the fluorescent: (a) Ny 66- $o\text{-NH}_2$  and (b) Ny 66- $p\text{-NH}_2$  samples.

to 700 nm; these last signals are assigned to the  $a_{2u} \rightarrow e_g$  and  $a_{1u}, a_{2u} \rightarrow e_g$  transitions, respectively [2, 3]. In acid solution, free porphyrins can be protonated to form the  $\text{H}_4\text{P}^{2+}$  dicationic species. The UV-visible spectrum of this species shows a bathochromic-shifted Soret band (20–40 nm); the  $\text{Q}_{\text{IV}}$  and  $\text{Q}_{\text{III}}$  bands disappear, while the  $\text{Q}_1$  signal grows and masks the  $\text{Q}_{\text{II}}$  band [2, 3, 53]. Further changes evidence an increment in the resonance interaction between phenyl and pyrrole rings followed by a slight projection out of the molecular plane of the compound [54].

For the particular case of  $\text{H}_2\text{T}(o\text{-NH}_2)\text{PP}$  species in solution, the Soret band is observed at 417 nm together with four Q bands at 517, 553, 594, and 649 nm (Figure 5(a)), respectively. In the case of the  $\text{H}_2\text{T}(p\text{-NH}_2)\text{PP}$  species, the Soret band is located at 622 nm, while three other bands

appear at 522, 570, and 660 nm, the  $\text{Q}_{\text{II}}$  signal being a broad band at around 590 nm. In acid solution, the purple-red solution of these compounds turns green as a consequence of porphyrin protonation. The protonation of the central nitrogens of the porphyrin macrocycle leads to the formation of  $\text{H}_4\text{T}(o\text{-NH}_2)\text{PP}^{2+}$  or  $\text{H}_4\text{T}(p\text{-NH}_2)\text{PP}^{2+}$  dicationic species, the UV-vis spectra of which show bathochromic-shifted Soret bands, and lonely  $\text{Q}_1$  bands that mask the remaining Q bands. In the particular case of  $\text{H}_2\text{T}(p\text{-NH}_2)\text{PP}$  species, the Soret band is observed at 440 nm and the  $\text{Q}_1$  band at 651 nm. As it was mentioned in Section 1, many of the free bases of porphyrins and some of their complexes show fluorescence in the visible region, principally in the red part of the spectrum [8, 18, 19]. In turn,  $\text{H}_2\text{T}(o\text{-NH}_2)\text{PP}$  or  $\text{H}_2\text{T}(p\text{-NH}_2)\text{PP}$  solutions show fluorescence spectra with a principal

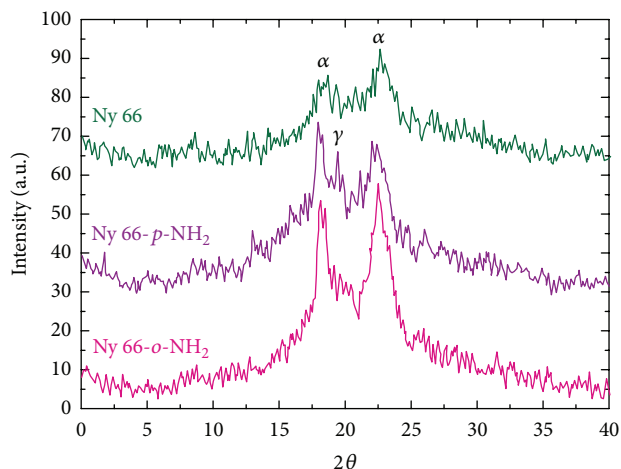


FIGURE 7: X-ray diffraction spectra of the Nylon 66, Ny 66-*o*-NH<sub>2</sub>, and Ny 66-*p*-NH<sub>2</sub> samples.

band located at around 650 to 660 nm and a lesser intense band at around 710–730 nm (Figure 5(b)). Moreover, the H<sub>2</sub>T(*o*-NH<sub>2</sub>)PP species show an additional band at around 614 nm.

The optimization of the above mentioned methodology can render new materials suitable to be used in diverse technological fields as optics, catalysis, sensor, medicine, or inclusively in electronics if conductive polymers are incorporated.

After the synthesis and purification of Nylon 66 fibers containing *ortho*- or *para*-amine substituted porphyrins, the Ny 66-*o*-NH<sub>2</sub> and Ny 66-*p*-NH<sub>2</sub> final samples were obtained. These specimens were amorphous, granular, and yellowish solids. In these samples, it was possible to observe the characteristic red fluorescence of porphyrins after being subjected to UV irradiation (Figure 6).

The X-ray diffraction patterns (Figure 7) of the Nylon 66, Ny 66-*o*-NH<sub>2</sub>, and Ny 66-*p*-NH<sub>2</sub> samples showed the same diffraction pattern of a predominant amorphous material with some crystallinity amount. In this sense, the bands at around 20.5° and 24.5° correspond to the reflection of (100) and (010, 110) doublet of the  $\alpha$  phase of Nylon 66 crystals oriented in a triclinic cell, and the less intense band observed at around 21.6° in the diffractogram of the Ny 66-*p*-NH<sub>2</sub> could be assigned to the presence of  $\gamma$  phase in this sample [55–57]. The couple of bands attributed to the  $\alpha$  phase were more intense for the Ny 66-*o*-NH<sub>2</sub> and Ny 66-*p*-NH<sub>2</sub> samples than for the pristine Nylon 66. This difference and the existence of  $\gamma$  phase in the Ny 66-*p*-NH<sub>2</sub> sample could be attributed to a slight crystallinity increment induced by the incorporation of the porphyrins in the polyamide network.

As for the FTIR spectrum of H<sub>2</sub>T(*p*-NH<sub>2</sub>)PP free base species (Figure 8), one band can be seen at around 3300 cm<sup>-1</sup> and another one at 960 cm<sup>-1</sup>; these signals can be ascribed to the NH bond stretching and bending frequencies of NH<sub>2</sub> substituents and of the central nitrogens of the porphyrin free base. The bands located in the range from 2850 to 3150 cm<sup>-1</sup> are attributed to C–H bond vibrations of the benzene and pyrrole rings. The band located at around 1490 to 1650 cm<sup>-1</sup>

can be assigned to C=C vibrations and that located at around 1350 and 1272 cm<sup>-1</sup> can be due to –C=N and C–N stretching vibrations. The signals at around 1800 to 1900 cm<sup>-1</sup> as well as the bands at about 800 cm<sup>-1</sup> and 750 cm<sup>-1</sup> are ascribed to C–H bond bending vibrations of *para*-substituted phenyls.

In the FTIR spectra of pure Nylon 66, it can be observed that the bands at 3314 and 3221 cm<sup>-1</sup> and those arising at 1450 cm<sup>-1</sup> and 750 cm<sup>-1</sup> can be assigned to the stretching, deformation, and wagging vibrations of N–H bonds. The bands at 3089 and 3020 cm<sup>-1</sup> are due to the asymmetric and symmetric stretching vibrations of C–H bonds. The bands at 2946 and 2867 cm<sup>-1</sup> are associated to the CH<sub>2</sub> stretching vibrations. In turn, the C=O stretching vibrations can be observed at around 1717 cm<sup>-1</sup>. The stretching, asymmetric deformation, and wagging of NH amide groups are observed at 1654, 1547, and 1376 cm<sup>-1</sup>, respectively. The bands located at around 1140 cm<sup>-1</sup> can be attributed to CO–CH symmetric bending vibration combined with CH<sub>2</sub> twisting. The bands at 936 and 600 cm<sup>-1</sup> are associated with the stretching and bending vibrations of C–C bonds, and the band at 583 cm<sup>-1</sup> can be due to O=C–N bending. The bands appearing at 936 and 1140 cm<sup>-1</sup> are associated to the crystalline and amorphous structures of Nylon 66, respectively [58]. In the spectra of polymers containing *ortho*- or *para*-isomers of porphyrin, that is, Ny 66-*o*-NH<sub>2</sub> and Ny 66-*p*-NH<sub>2</sub>, the bands in the range from 3100 to 3600 cm<sup>-1</sup> are slightly narrower than those observed in Nylon 66 spectra, suggesting a lower amount of physisorbed water. The bands located at around 3150 and 3300 cm<sup>-1</sup> suggest the presence of a very low amount of macrocycle molecules in the solid samples. Furthermore, the band at around 940 cm<sup>-1</sup> appears to have a lower intensity in the Ny 66-*o*-NH<sub>2</sub> system, thus suggesting a lower crystalline structure than that of the Ny 66-*p*-NH<sub>2</sub> sample. Because of the low concentration of macrocyclic species that are incorporated into the polymer network, the last result may not be conclusive at this point.

In the UV-vis spectra of Nylon 66 synthesized altogether with the H<sub>2</sub>T(*o*-NH<sub>2</sub>)PP, H<sub>2</sub>T(*p*-NH<sub>2</sub>)PP species (samples labelled as Ny 66-*o*-NH<sub>2</sub> and Ny 66-*p*-NH<sub>2</sub>), the band at around 250 nm and the shoulder at 290 nm, assigned to the Nylon 66 [59], are observed to depict a lower intensity than those due to the intense  $\pi$ - $\pi^*$  transitions of porphyrins. By this reason, the UV-Vis analysis is centred to the signals of the macrocyclic species. In the Ny 66-*o*-NH<sub>2</sub> and Ny 66-*p*-NH<sub>2</sub> samples, the observed Soret bands were wider than those obtained from solutions of these macrocycles and located at 437 and 426 nm, respectively (Figure 9). Both samples show the four Q bands, characteristic of porphyrin free base, however, the red-shifted Soret band together with the Q<sub>1</sub> band (at 656 nm) in the spectrum of Ny 66-*o*-NH<sub>2</sub> suggests the existence of a very small concentration of protonated porphyrin, that is, and likely, a higher interaction with the polyamide chains. The shift of the Soret band in the case of Ny 66-*p*-NH<sub>2</sub> was of only 4 nm, thus suggesting a low interaction of the macrocycle with the polyamide chains.

In the fluorescence spectra of Nylon 66 synthesized together with H<sub>2</sub>T(*o*-NH<sub>2</sub>)PP or H<sub>2</sub>T(*p*-NH<sub>2</sub>)PP species,

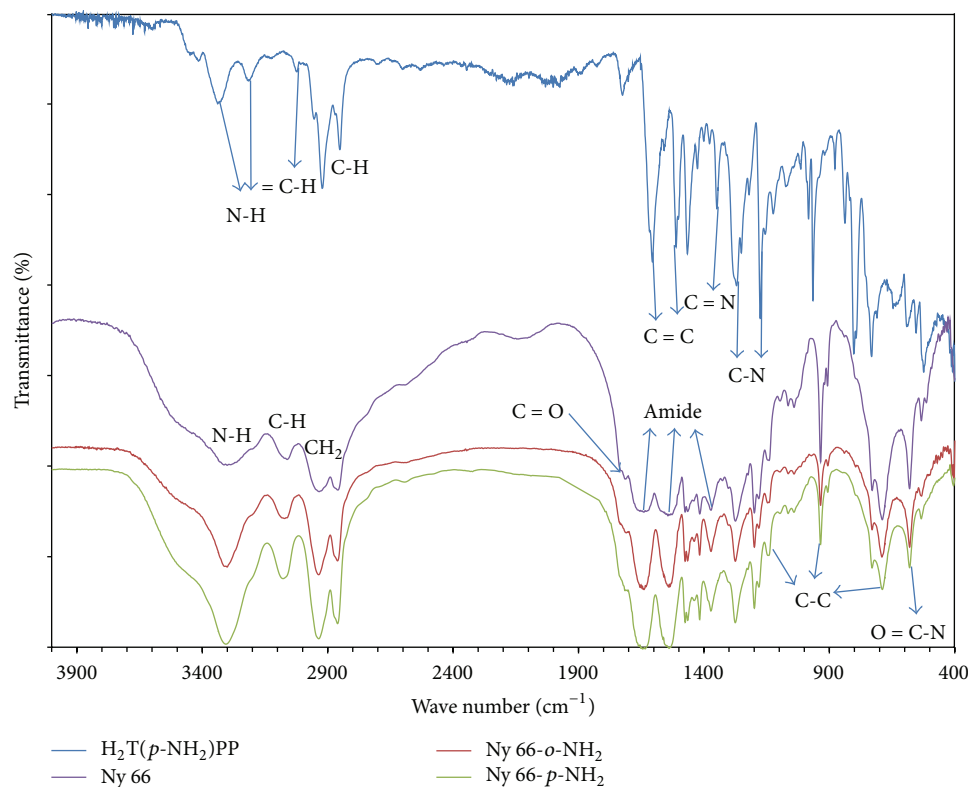


FIGURE 8: FTIR spectra of pure Nylon 66 (blank) and of Ny 66-*o*-NH<sub>2</sub> and Ny 66-*p*-NH<sub>2</sub> hybrid species as compared with the FTIR spectrum of the H<sub>2</sub>T(*p*-NH<sub>2</sub>)PP free base.

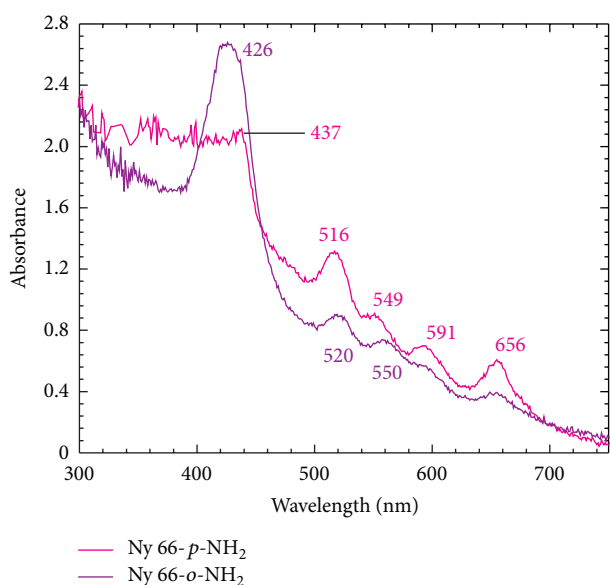


FIGURE 9: UV-Vis spectra of dry Ny 66-*o*-NH<sub>2</sub> and Ny 66-*p*-NH<sub>2</sub> samples.

obtained by excitation at 370 nm ( $\lambda_{exc} = 370$  nm), two set of signals can be observed (Figure 10(a)); the bands located at around 661 and 674 nm can be due to the fluorescent red emission of H<sub>2</sub>T(*o*-NH<sub>2</sub>)PP and H<sub>2</sub>T(*p*-NH<sub>2</sub>)PP free bases, respectively [60–62]. As it was demonstrated for Nylon 66, both, samples show fluorescence and phosphorescence;

these phenomena can be attributed to the presence of chromophoric structures or oxidation impurities created during the synthesis of the polymers [63–67]. Then, the bands seen in the range from 380 to 600 nm with maxima appearing at 461, 471, and 532 nm can be the result of the emissions of polyamide alone [63–67] or from its interaction with the macrocycle species. When these spectra are obtained by using an exciting light of 420 nm, that is, in the range of maximum absorbance, the signals appearing in the interval from 430 to 600 nm are observed to depict a lower intensity than those signals located from 600 to 750 nm (Figure 10(b)). This means that bands displayed from 600 to 750 nm are emissions that can only be associated to the macrocyclic species, while the emissions of pure polyamide, or its interaction with the macrocycle, can only be observed when the systems are irradiated with light of a higher energy of shorter wavelength (i.e.,  $\lambda_{exc} \approx 370$  nm). Additionally, this last observation means that, in the synthesized systems, macrocyclic species and polyamide chains remain in the proximity of one another.

Even if the shape and localization of the bands in these last spectra are very similar to those observed for porphyrins in solution (Figure 5(b)), in the case of the Ny 66-*o*-NH<sub>2</sub> sample, the maximum band at 661 nm is red-shifted by about 7 nm and the band at 724 nm is red-shifted by 10 nm with respect to those observed in solution (Figure 5(b)). Furthermore, in this sample, the third band appearing at 614 nm, in the spectra of the H<sub>2</sub>T(*o*-NH<sub>2</sub>)PP solution, appears very weakly and at the same position as for the Ny 66-*o*-NH<sub>2</sub> sample.

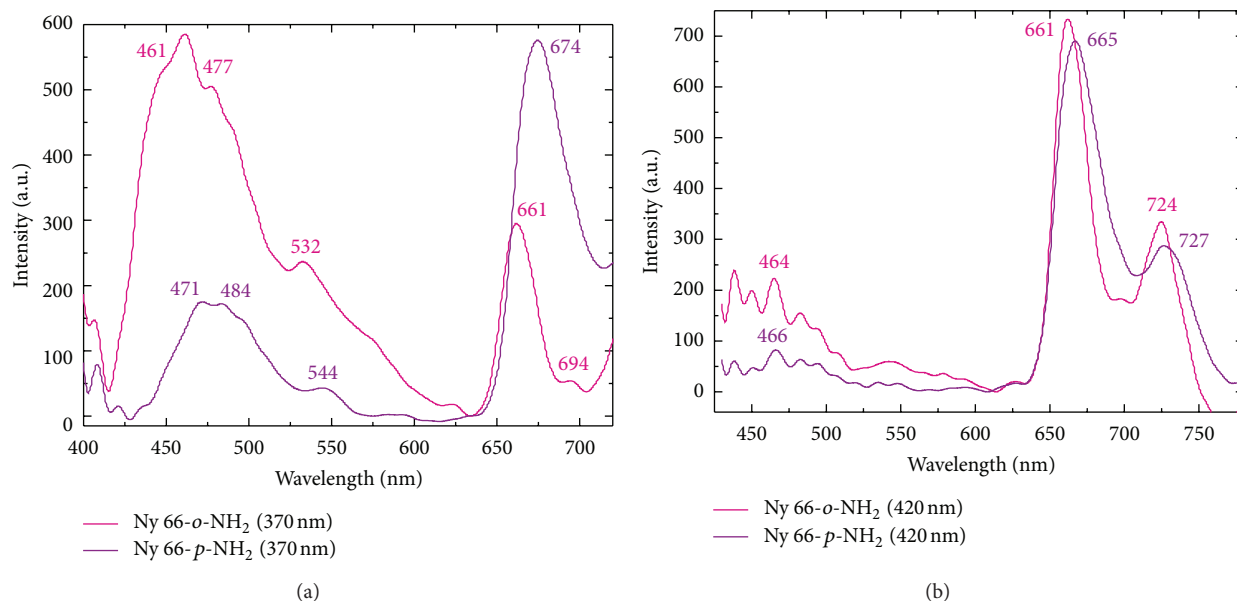


FIGURE 10: Fluorescence spectra obtained with excitation radiation of 370 nm (a) or 420 nm (b) of the Ny 66-*o*-NH<sub>2</sub> and Ny 66-*p*-NH<sub>2</sub> samples.

The bands in the fluorescence spectra of the Ny 66-*p*-NH<sub>2</sub> sample remain practically at the same positions as those observed for the porphyrin in solution, that is, located at 665 and 727 nm. The last observations suggest that, in the Ny 66-*p*-NH<sub>2</sub> sample, porphyrin remains immersed under a physicochemical environment that is practically not affecting its emission process. Comparatively, the fluorescence spectra of the Ny 66-*o*-NH<sub>2</sub> sample suggest that, in this network, the luminescent process of porphyrin is slightly affected by the proximity of the polyamide chains formed up and down of the macrocycle plane, then causing that the emissions occur at longer wavelengths than those found in solution. That is, under these conditions, the emission of the H<sub>2</sub>T(*o*-NH<sub>2</sub>)PP species takes place after dispersing some amount of energy through vibration, something that is facilitated by the presence of polyamide chains.

The examination of the characteristic UV-Vis and fluorescence bands in the spectra of the Ny 66-*o*-NH<sub>2</sub> and Ny 66-*p*-NH<sub>2</sub> samples confirms the incorporation of a low amount of the respective H<sub>2</sub>T(*o*-NH<sub>2</sub>)PP and H<sub>2</sub>T(*p*-NH<sub>2</sub>)PP species into the structure of the polyamide network.

In the SEM images of Nylon 66, synthesized as a blank, both layered and radial structures can be observed of approximately the same diameters of about 7 μm (Figures 11(a) and 11(b)). In contrast, the images of polyamide synthesized in the presence of the H<sub>2</sub>T(*o*-NH<sub>2</sub>)PP species show lamellar and curved structures in which the radial structures, observed in the blank sample, cannot be further detected (Figures 11(c) and 11(d)). Additionally, in the polymer synthesized in the presence of the H<sub>2</sub>T(*p*-NH<sub>2</sub>)PP species, there exists a rougher but more homogeneous, compact, and complex structure. This structure consists of a sequence of continuous and folded layers inside a network with, apparently, a higher amount of smaller pores

(Figures 11(e) and 11(f)). Evidently, in the cases of these systems, the presence of porphyrin isomers induces particular textural effects.

As it is well known, porphyrin macrocycles are tetradentate agents which form complexes with practically all metallic elements of the periodic table [2–4]. In order to probe the existence and evaluate the amount of porphyrin macrocycle integrated to the structure of polyamide, the preparation of the respective cobalt complexes was performed. For example, the UV-Vis spectra of the CoT(*p*-NH<sub>2</sub>)PP complex in solution (Figure 12(a)) show an intense Soret band, shifted to longer wavelengths located at 438 nm. In the region of Q bands, the Q<sub>III</sub> and Q<sub>II</sub> bands remain situated at around 555 and 597 nm. The last pathway of signals is characteristic of porphyrinic complexes [2–4]. In the respective UV-Vis spectra of samples of Nylon 66 synthesized with H<sub>2</sub>T(*o*-NH<sub>2</sub>)PP or H<sub>2</sub>T(*p*-NH<sub>2</sub>)PP and obtained after the reaction with CoCl<sub>2</sub>, signals of porphyrinic complexes formation are observed. In both cases, the detected Soret bands are of a high intensity, broad, red-shifted, and located at 442 and 451 nm for the samples labeled as Ny 66-Co-*o*-NH<sub>2</sub> and Ny 66-Co-*p*-NH<sub>2</sub>, respectively (Figure 12(b)). In the spectrum of the last sample, only the Q<sub>III</sub> and Q<sub>II</sub> bands are observed at around 550 and 592 nm. For the case of Ny 66-Co-*o*-NH<sub>2</sub> sample, the Q<sub>III</sub> and Q<sub>II</sub> bands are observed as shoulders at around 549 nm. The bands displayed in the spectra of the two systems confirm the formation of the respective complexes by substitution of the two central hydrogens of porphyrin by cobalt ions. However, the deformation of the pathway of these bands may be attributed to the interactions of cobalt porphyrins with polyamide chains. The amount of cobalt integrated to the polymeric systems results is lower for the system synthesized with the H<sub>2</sub>T(*o*-NH<sub>2</sub>)PP species, while this same amount was higher for the polymer containing the H<sub>2</sub>T(*p*-NH<sub>2</sub>)PP species.

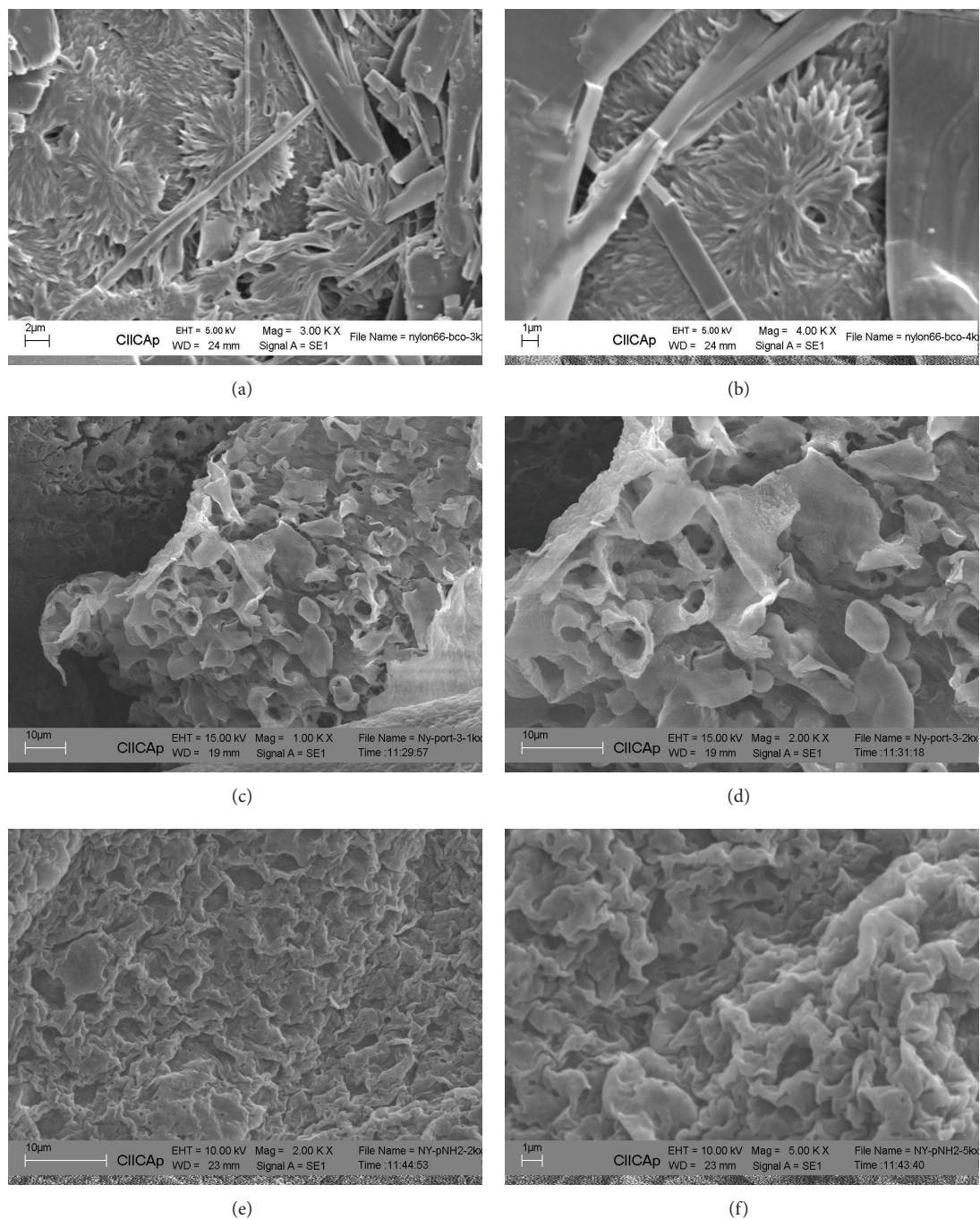


FIGURE 11: SEM images of Nylon-66 ((a) and (b)), Ny 66-*o*-NH<sub>2</sub> ((c) and (d)) and, Ny 66-*p*-NH<sub>2</sub> ((e) and (f)) samples.

From the EDS analysis of Ny 66-Co-*o*-NH<sub>2</sub>, a uniform distribution of carbon (Figure 13(b)) is evident; contrastingly, the nitrogen distribution (Figure 13(c)) follows a pathway that coincides with the borders of the curved layers observed in the SEM micrograph (Figure 13(a)). The carbon distribution can be associated to the six carbons existing in adipic acid and hexane diamine chains that are present in the polyamide chains and also with the carbon skeleton of porphyrins. However, the nitrogen distribution can only be associated to the nitrogens of amide groups, to the four central porphyrinic

nitrogens, and to the four peripheral nitrogens, attached at the *ortho*- or *para*-positions of phenyls in the macrocycle.

The amount of cobalt detected in the Ny 66-Co-*o*-NH<sub>2</sub> and Ny 66-Co-*p*-NH<sub>2</sub> systems is very low (Table 1); nevertheless, it allows to calculate the approximated amount of monomer units present in every material. Having that in mind, the cobalt complex formed with a porphyrin macrocycle has the molecular formula CoC<sub>44</sub>H<sub>32</sub>N<sub>8</sub>, and four chains of the same length can be formed from the *ortho*- or *para*-NH<sub>2</sub> groups attached at the periphery of macrocycle;

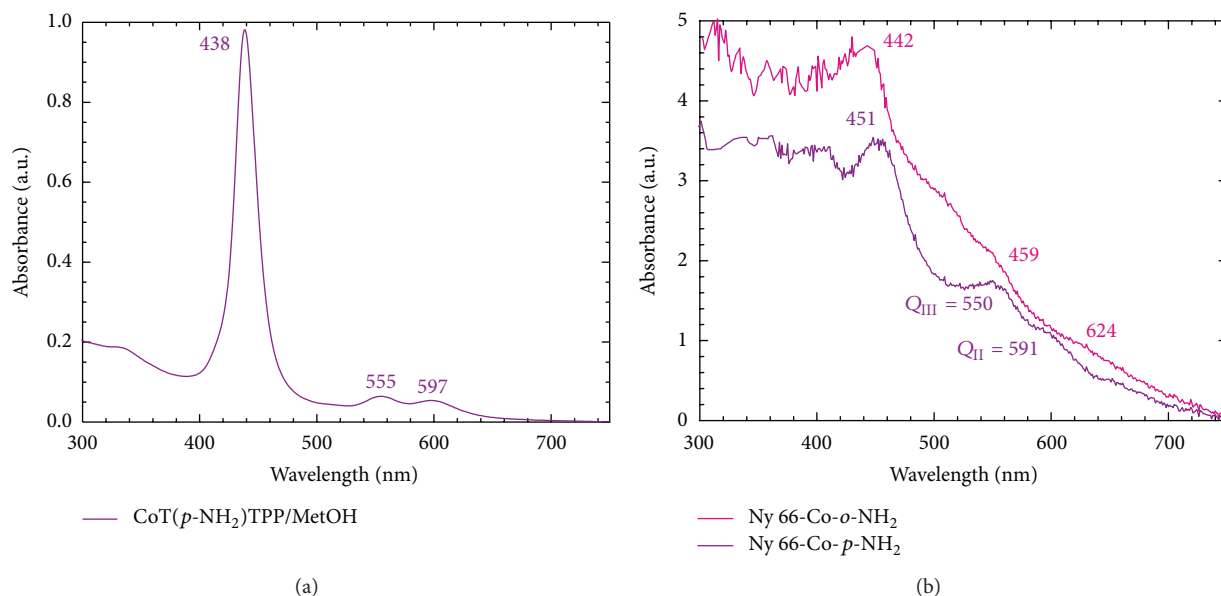


FIGURE 12: (a) UV-Vis spectra of CoT(*p*-NH<sub>2</sub>)PP in solution and of the (b) Ny 66-Co-*o*-NH<sub>2</sub> and Ny 66-Co-*p*-NH<sub>2</sub> polymers.

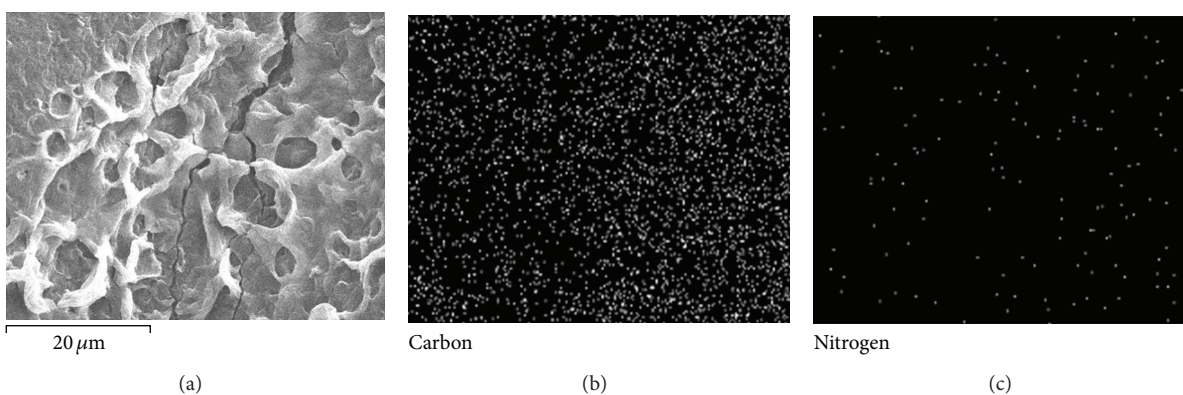
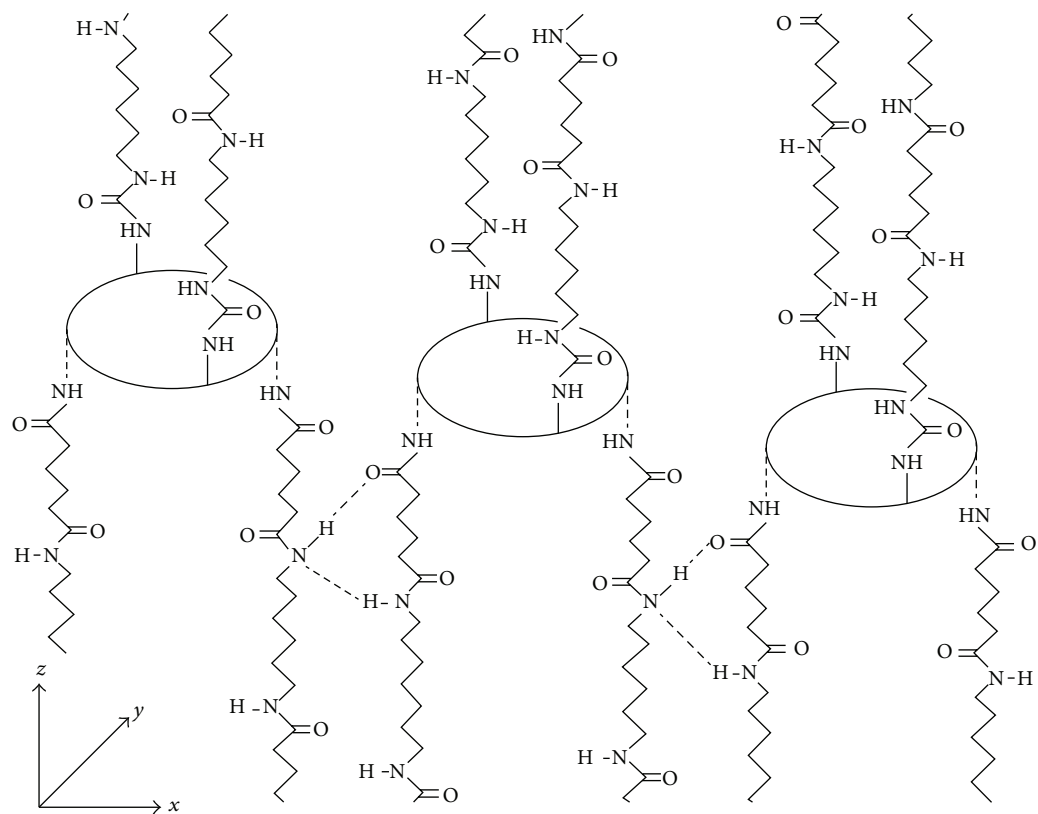


FIGURE 13: (a) SEM image and EDS distributions of (b) Carbon and (c) Nitrogen on the surface of the Ny 66-Co-*o*-NH<sub>2</sub> sample.

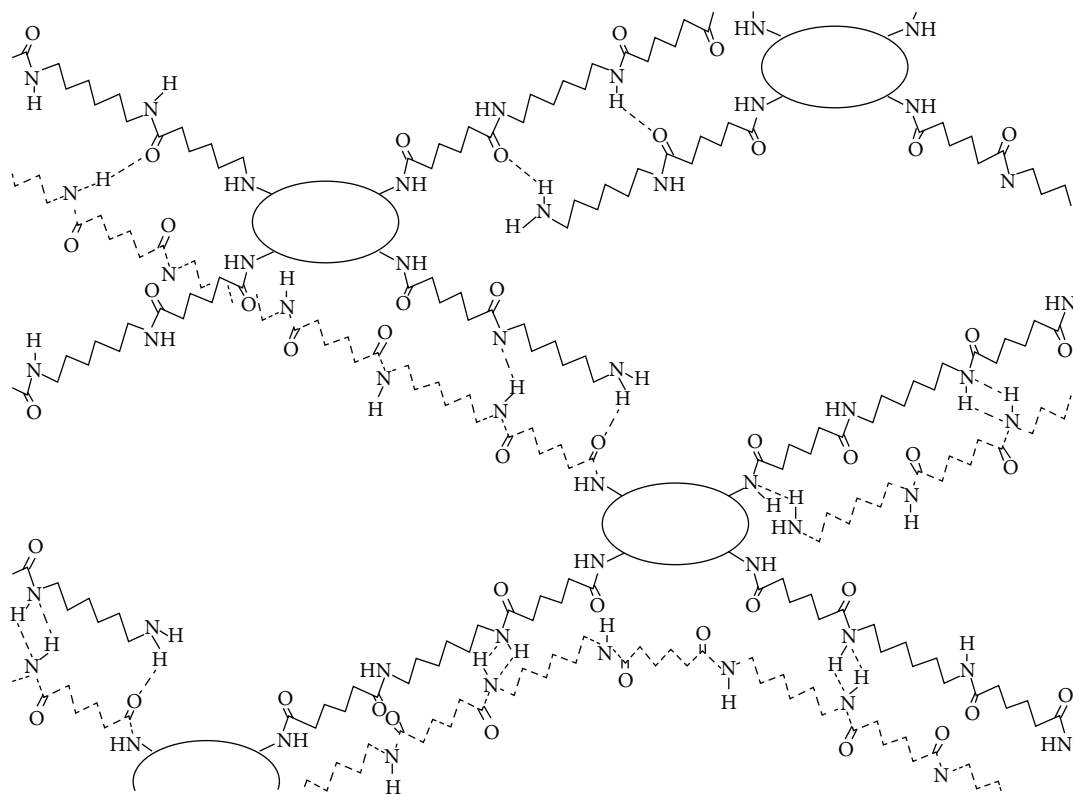
the weight percent evaluated from the EDS analysis allows to determine that four chains are formed each consisting of 93 to 94 monomer units around every CoT(*o*-NH<sub>2</sub>)PP macrocycle. These chains are formed by around 78 monomeric units, in the case of CoT(*p*-NH<sub>2</sub>)PP (Table 1).

Because of the lower basicity of the -NH<sub>2</sub> groups attached in the H<sub>2</sub>T(*o*-NH<sub>2</sub>)PP and H<sub>2</sub>T(*p*-NH<sub>2</sub>)PP species, compared with the basicity of the hexanediamine, the formation of the Nylon 66 takes place faster and in a more easy way. However, the above mentioned results suggest that, in presence of the porphyrins, the formation of polyamide chains occurs easily with the H<sub>2</sub>T(*o*-NH<sub>2</sub>)PP species, in which there exist two amine groups above and two other below the molecular plane. The integration of the porphyrins to the polyamide chains occurs began, or ending, on the -NH<sub>2</sub> groups, with the interactions between the two polyamide chains arising as in pristine Nylon 66. This situation makes the incorporation of additional porphyrin macrocycles between the same two chains difficult (Figure 14(a)), which probably takes place only with one of the two chains that grows at every side

of the molecular plane of the H<sub>2</sub>T(*o*-NH<sub>2</sub>)PP species. By these effects resulting rare the incorporation of another porphyrin with two shared chains of the four polyamide chains grow from every H<sub>2</sub>T(*o*-NH<sub>2</sub>)PP species. By the same reasons, the length of the lateral chains formed around the H<sub>2</sub>T(*o*-NH<sub>2</sub>)PP species is longer and has a low porphyrin concentration than those evaluated in the Ny 66-*p*-NH<sub>2</sub> sample. The polymerization of the four polyamide chains begins from the H<sub>2</sub>T(*p*-NH<sub>2</sub>)PP species which occurs with lower steric hindrance existing around the four peripheral -NH<sub>2</sub> groups attached and localized in the same molecular plane of porphyrin (Figure 14(b)). The hydrogen and dipole-dipole interactions of amide groups are the principal responsible of the macroscopic structure of the formed polyamide network, with the H<sub>2</sub>T(*o*-NH<sub>2</sub>)PP or H<sub>2</sub>T(*p*-NH<sub>2</sub>)PP species determining only the initial growing and particular spatial disposition of polyamide chains. Perhaps, by this reason, the macroscopic structure of polyamide contained in H<sub>2</sub>T(*p*-NH<sub>2</sub>)PP results to be rougher, denser, and with smaller pores



(a)



(b)

FIGURE 14: The spatial position of amine groups in *ortho*- or *para*-NH<sub>2</sub> substituted tetraphenyl porphyrins induces the growth of different pathways on Nylon 66 fibers.

TABLE I: Weight % of carbon, oxygen, and cobalt evaluated by EDS on the surface of Ny 66-Co-*o*-NH<sub>2</sub> and Ny 66-Co-*p*-NH<sub>2</sub> samples.

Sample	% w/w Carbon	% w/w Oxygen	% w/w Cobalt	Monomer units ( <i>n</i> )	Number of units bilateral chain*
Ny 66-Co- <i>o</i> -NH <sub>2</sub>	83.24	16.67	0.09	376	94
Ny 66-Co- <i>p</i> -NH <sub>2</sub>	77.57	21.33	0.10	312	78

\* Lateral chains are formed by *a*, *b*, *c*, or *d* units rendering a total of *n* units in each porphyrin.

than those obtained with H<sub>2</sub>T(*o*-NH<sub>2</sub>)PP (Figures 11(b) and 11(c)).

All the above mentioned evidence suggests that the spatial localization of amine groups in the *ortho*- and *para*-amine substituted tetraphenylporphyrins induces important effects on the length, spatial disposition, and on the crossing and linking of polyamine chains. Furthermore, the polymerization occurs in such way that starts or ends over the -NH<sub>2</sub> groups of the H<sub>2</sub>T(*o*-NH<sub>2</sub>)PP or H<sub>2</sub>T(*p*-NH<sub>2</sub>)PP species. In the case of the H<sub>2</sub>T(*o*-NH<sub>2</sub>)PP species, the polyamide chains can be formed above and below of the molecular plane (along the *z*-axis direction in Figure 14(a)). In the case of H<sub>2</sub>T(*p*-NH<sub>2</sub>)PP, these chains can be formed at the periphery of the macrocycle (i.e., the *x-y* plane in Figure 14(b)). In the two cases, hydrogen bonds and dipole-dipole interactions between polyamide chains are responsible for the macroscopic structure of the polymer.

UV-Vis and fluorescence spectra suggest that polyamide chains interact stronger with the H<sub>2</sub>T(*o*-NH<sub>2</sub>)PP species than with the H<sub>2</sub>T(*p*-NH<sub>2</sub>)PP species. Additionally, the formation of cobalt complexes is more effective and in a higher amount, in the case of the network synthesized from H<sub>2</sub>T(*p*-NH<sub>2</sub>)PP, thus suggesting the existence of weak inhibiting effects over the central window of the macrocycle to coordinate cobalt or other cations. The last results suggest that the preferred direction for the growing of polyamide chains is initially determined by the position of the -NH<sub>2</sub> groups on the porphyrin. That is, the porphyrin macrocycle functions as a nucleation point (knot) that reinforces the Nylon structure and inhibits the formation of very long polyamide chains, but without creating a great interference with hydrogen bonds and dipole-dipole intermolecular interactions.

The above results suggest the incorporation of only a low amount of porphyrin molecules but still enough to display a notable fluorescence emission (Figures 6 and 10) and to form detectable amounts of cobalt atoms coordinated to the porphyrin structure. However, the possibility of increase the basicity of the -NH<sub>2</sub> groups of the H<sub>2</sub>T(*o*-NH<sub>2</sub>)PP or H<sub>2</sub>T(*p*-NH<sub>2</sub>)PP species exist for optimiz its integration to the polyamide chains. In a deeper investigation of the effect of using *ortho*- or *para*-substituted porphyrins on the structure of polyamides, our research group is now exploring the consequences of employing other porphyrin substituents or of other polyamide monomers, such as aromatic diamines or dicarboxyls. This possibilities suggest that the method can be optimized to a higher degree in order to synthesize new materials suitable to be used in optics, catalysis, sensors, membranes, medicine, and, if conductive polymers are included, in photoelectronic.

## 4. Conclusions

The results of the present document show that the incorporation of tetrapyrrole macrocyclic species is possible, such as the substituted porphyrins, in the structure of known polymeric chains such as Nylon 66. The integration of substituted porphyrinic molecules with spatial functional groups for the growing of polyamide chains induces beneficial structural and textural effects on the Nylon 66 matrix.

The number and spatial position of the amine groups (-NH<sub>2</sub>) at the *ortho*- and *para*-positions of phenyls of tetraphenylporphyrins, incorporated to the polymerization reaction of adipoyl chloride and hexanediamine, produce two different modified Nylon networks. The use of H<sub>2</sub>T(*p*-NH<sub>2</sub>)PP species apparently induces the formation of a more homogeneous but rougher porous matrix than that of the H<sub>2</sub>T(*o*-NH<sub>2</sub>)PP species. However, the existence of four central nitrogens in the porphyrin macrocycle makes the synthesis of the respective cobalt complexes possible; these systems are suitable of be used with other cations such as transition metals, lanthanides, and actinides.

The optimization of the above mentioned methodology can render new materials suitable to be used in diverse technological fields as optics, catalysis, sensor, medicine, or inclusively in electronics if conductive polymers are incorporated.

## Acknowledgments

The authors wish to thank the CONACyT for the scholarship 252086 and the Ministry of Education (SEP-PROMEPE) for the support provided to the Academic Body "Fisicoquímica de Superficies" (UAM-I CA-031) and to the Academic Network "Diseño Nanoscópico y Textural de Materiales Avanzados". The authors are grateful to Patricia Castillo for her timely and professional assessment at different stages of this investigation and Dr. Fernando Rojas-González for the review and comments of the different versions of the manuscript.

## References

- [1] R. L. Milgrom, *The Colour of Life: An Introduction to the Chemistry of Porphyrins and Related Compounds*, Oxford University Press, Oxford, UK, 1997.
- [2] K. M. Smith, *Porphyrins and Metalloporphyrins*, Elsevier Scientific Publishing, Amsterdam, The Netherlands, 1976.
- [3] D. Dolphin, *The Porphyrins, Physical Chemistry, Part A and B*, Academic Press, New York, NY, USA, 1979.

- [4] K. Kadish, K. M. Smith, and R. Guilard, *The Porphyrin Handbook*, vol. 6, Academic Press, San Diego, Calif, USA, 2003.
- [5] J. Friedrich, H. Wolfrum, and D. Haarer, "Photochemical holes: a spectral probe of the amorphous state in the optical domain," *The Journal of Chemical Physics*, vol. 77, no. 5, pp. 2309–2316, 1982.
- [6] J. Friedrich, H. Wolfrum, and D. Haarer, "Direct measurements of nonlinear absorption and refraction in solutions of phthalocyanines," *Applied Physics B*, vol. 54, no. 1, pp. 46–51, 1992.
- [7] Y. Liu, K. Shigehara, and A. Yamada, "Preparation of Bis(phthalocyaninato)lutetium with various substituents and their electrochemical properties," *Bulletin of the Chemical Society of Japan*, vol. 65, pp. 250–257, 1992.
- [8] J. R. Darwent, P. Douglas, A. Harriman, G. Porter, and M.-C. Richoux, "Metal phthalocyanines and porphyrins as photosensitizers for reduction of water to hydrogen," *Coordination Chemistry Reviews*, vol. 44, no. 1, pp. 83–126, 1982.
- [9] A. D. F. Dunbar, S. Brittle, T. H. Richardson, J. Hutchinson, and C. A. Hunter, "Detection of volatile organic compounds using porphyrin derivatives," *Journal of Physical Chemistry B*, vol. 114, no. 36, pp. 11697–11702, 2010.
- [10] H. Zhang, Y. Sun, K. Ye, P. Zhang, and Y. Wang, "Oxygen sensing materials based on mesoporous silica MCM-41 and Pt(II)-porphyrin complexes," *Journal of Materials Chemistry*, vol. 15, no. 31, pp. 3181–3186, 2005.
- [11] S. Wan, J. A. Parrish, R. R. Anderson, and M. Madden, "Transmittance of nonionizing radiation in human tissues," *Photochemistry and Photobiology*, vol. 34, no. 6, pp. 679–681, 1981.
- [12] J. P. A. Marijnissen and W. M. Star, "Quantitative light dosimetry *in vitro* and *in vivo*," *Lasers in Medical Science*, vol. 2, no. 4, pp. 235–242, 1987.
- [13] A. Harriman, "Luminescence of porphyrins and metalloporphyrins—part 1: zinc(II), nickel(II) and manganese(II) porphyrins," *Journal of the Chemical Society, Faraday Transactions 1*, vol. 76, pp. 1978–1985, 1980.
- [14] A. Harriman, "Luminescence of porphyrins and metalloporphyrins—part 2: copper(II), chromium(III), manganese(III), iron(II) and iron(III) porphyrins," *Journal of the Chemical Society, Faraday Transactions 1*, vol. 77, no. 2, pp. 369–377, 1981.
- [15] A. Harriman, "Luminescence of porphyrins and metalloporphyrins—part 3: heavy-atom effects," *Journal of the Chemical Society, Faraday Transactions 2*, vol. 77, no. 7, pp. 1281–1291, 1981.
- [16] E. Weizman, C. Rothmann, L. Greenbaum et al., "Mitochondrial localization and photodamage during photodynamic therapy with tetraphenylporphyrins," *Journal of Photochemistry and Photobiology B*, vol. 59, no. 1–3, pp. 92–102, 2000.
- [17] E. Reddi, M. Cecon, G. Valduga et al., "Photophysical properties and antibacterial activity of meso-substituted cationic porphyrins," *Photochemistry and Photobiology*, vol. 75, no. 5, pp. 462–470, 2002.
- [18] A. Harriman, G. Porter, and P. Walters, "Photo-oxidation of metalloporphyrins in aqueous solution," *Journal of the Chemical Society, Faraday Transactions 1*, vol. 79, no. 6, pp. 1335–1350, 1983.
- [19] A. Harriman, G. Porter, and M.-C. Richoux, "Photosensitized reduction of water to hydrogen using water-soluble zinc porphyrins," *Journal of the Chemical Society, Faraday Transactions 2*, vol. 77, no. 5, pp. 833–844, 1981.
- [20] J. Turay and P. Hambright, "Activation parameters and a mechanism for metal-porphyrin formation reactions," *Inorganic Chemistry*, vol. 19, no. 2, pp. 562–564, 1980.
- [21] P. Hambright, T. Gore, and M. Burton, "Synthesis and characterization of new isomeric water-soluble porphyrins. Tetra(2-N-methylpyridyl)porphine and tetra(3-N-methylpyridyl)porphine," *Inorganic Chemistry*, vol. 15, no. 9, pp. 2314–2315, 1976.
- [22] J. B. Reid and P. Hambright, "Kinetics of copper incorporation into tetra(2-N-methylpyridyl)porphine. Effects of basicity on rate," *Inorganic Chemistry*, vol. 16, no. 4, pp. 968–969, 1977.
- [23] J. B. Kim, J. J. Leonard, and F. R. Longo, "A mechanistic study of the synthesis and spectral properties of meso-tetraphenylporphyrin," *Journal of the American Chemical Society*, vol. 94, no. 11, pp. 3986–3992, 1972.
- [24] D. J. Quimby and F. R. Longo, "Luminescence studies on several tetraarylporphyrins and their zinc derivatives," *Journal of the American Chemical Society*, vol. 97, no. 18, pp. 5111–5117, 1975.
- [25] G. D. Egorova, V. N. Knyukshto, K. N. Solovev, and M. P. Tsvirko, "Intramolecular spin-orbital perturbations in ortho- and meta-halogeno-derivatives of tetraphenylporphyrin," *Optics and Spectroscopy*, vol. 48, no. 6, pp. 602–607, 1980.
- [26] S. Sugata, S. Yamanouchi, and Y. Matsushima, "Meso tetrapyrrolylporphyrins and their metal complexes. Syntheses and physico chemical properties," *Chemical and Pharmaceutical Bulletin*, vol. 25, no. 5, pp. 884–889, 1977.
- [27] M. Meot-Ner and A. D. Adler, "Substituent effects in noncoplanar  $\pi$  systems. ms-porphyrins," *Journal of the American Chemical Society*, vol. 97, no. 18, pp. 5107–5111, 1975.
- [28] G. D. Egorova, V. N. Knyukshto, K. N. Solovev, and M. P. Tsvirko, *Optics and Spectroscopy*, vol. 48, p. 1101, 1980.
- [29] S.-K. Lee and I. Okura, "Optical sensor for oxygen using a porphyrin-doped sol-gel glass," *Analyst*, vol. 122, no. 1, pp. 81–84, 1997.
- [30] S. Salhi, M. Vernières, C. Bied-Charreton, J. Faure, and A. Revillon, "New polymeric materials: porphyrins attached to preformed polystyrene," *New Journal of Chemistry*, vol. 18, no. 7, p. 783, 1994.
- [31] D. A. Buttry and F. C. Anson, "New strategies for electrocatalysis at polymer-coated electrodes. Reduction of dioxygen by cobalt porphyrins immobilized in nafion coatings on graphite electrodes," *Journal of the American Chemical Society*, vol. 106, no. 1, pp. 59–64, 1984.
- [32] J. E. Bennett and T. Malinski, "Conductive polymeric porphyrin films: application in the electrocatalytic oxidation of hydrazine," *Chemistry of Materials*, vol. 3, no. 3, pp. 490–495, 1991.
- [33] X. Shi, K. M. Barkigia, J. Fajer, and C. M. Drain, "Design and synthesis of porphyrins bearing rigid hydrogen bonding motifs: highly versatile building blocks for self-assembly of polymers and discrete arrays," *Journal of Organic Chemistry*, vol. 66, no. 20, pp. 6513–6522, 2001.
- [34] J. A. A. W. Elemans, R. van Hameren, R. J. M. Nolte, and A. E. Rowan, "Molecular materials by self-assembly of porphyrins, phthalocyanines, and perylenes," *Advanced Materials*, vol. 18, no. 10, pp. 1251–1266, 2006.
- [35] F. de Loos, I. C. Reynhout, J. J. L. Cornelissen, A. E. Rowan, and R. J. M. Nolte, "Construction of functional porphyrin polystyrene nano-architectures by ATRP," *Chemical Communications*, vol. 1, pp. 60–62, 2005.
- [36] P. A. J. De Witte, M. Castriciano, J. J. L. M. Cornelissen, L. M. Scolaro, R. J. M. Nolte, and A. E. Rowan, "Helical polymer-anchored porphyrin nanorods," *Chemistry—A European Journal*, vol. 9, no. 8, pp. 1775–1781, 2003.

- [37] B. G. Choi, R. Song, W. Nam, and B. Jeong, "Iron porphyrins anchored to a thermosensitive polymeric core-shell nanosphere as a thermotropic catalyst," *Chemical Communications*, no. 23, pp. 2960–2962, 2005.
- [38] J. Chen, P. Wagner, L. Tong, G. G. Wallace, D. L. Officer, and G. F. Swiegers, "A porphyrin-doped polymer catalyzes selective, light-assisted water oxidation in seawater," *Angewandte Chemie—International Edition*, vol. 51, no. 8, pp. 1907–1910, 2012.
- [39] M. G. Walter, A. B. Rudine, and C. C. Wamser, "Porphyrins and phthalocyanines in solar photovoltaic cells," *Journal of Porphyrins and Phthalocyanines*, vol. 14, no. 9, pp. 759–792, 2010.
- [40] N. Xiang, Y. Liu, W. Zhou et al., "Synthesis and characterization of porphyrin-terthiophene and oligothiophene  $\pi$ -conjugated copolymers for polymer solar cells," *European Polymer Journal*, vol. 46, no. 5, pp. 1084–1092, 2010.
- [41] V. Cleave, G. Yahioglu, P. le Barny et al., "Transfer processes in semiconducting polymer-porphyrin blends," *Advanced Materials*, vol. 13, no. 1, pp. 44–47, 2001.
- [42] H. Chen, J. Zeng, F. Deng, X. Luo, Z. Lei, and H. Li, "Synthesis and photophysical properties of porphyrin-containing polymers," *Journal of Polymer Research*, vol. 19, pp. 9880–9889, 2012.
- [43] B. Li, X. Xu, M. Sun et al., "Porphyrin-cored star polymers as efficient nondoped red light-emitting materials," *Macromolecules*, vol. 39, no. 1, pp. 456–461, 2006.
- [44] J. L. O'Donnell, N. Thaitrong, A. P. Nelson, and J. T. Hupp, "Liquid/liquid interface polymerized porphyrin membranes displaying size-selective molecular and ionic permeability," *Langmuir*, vol. 22, no. 4, pp. 1804–1809, 2006.
- [45] C. Hsu, M. Nieh, and P. Lai, "Facile self-assembly of porphyrin-embedded polymeric vesicles for theranostic applications," *Chemical Communications*, vol. 48, no. 75, pp. 9343–9345, 2012.
- [46] C. Xing, Q. Xu, H. Tang, L. Liu, and S. Wang, "Conjugated polymer/porphyrin complexes for efficient energy transfer and improving light-activated antibacterial activity," *Journal of the American Chemical Society*, vol. 131, no. 36, pp. 13117–13124, 2009.
- [47] A. Modak, M. Nandi, J. Mondal, and A. Bhaumik, "Porphyrin based porous organic polymers: novel synthetic strategy and exceptionally high CO<sub>2</sub> adsorption capacity," *Chemical Communications*, vol. 48, no. 2, pp. 248–250, 2012.
- [48] T. Mathew and S. Kuriakose, "Cobalt(II) porphyrins supported on crosslinked polymer matrix as model compounds," *Journal of Porphyrins and Phthalocyanines*, vol. 3, no. 4, pp. 316–321, 1999.
- [49] M. Schäferling and P. Bäuerle, "Porphyrin-functionalized oligo- and polythiophenes," *Journal of Materials Chemistry*, vol. 14, no. 7, pp. 1132–1141, 2004.
- [50] A. D. Adler, F. R. Longo, J. D. Finarelli, J. Goldmacher, J. Assour, and L. Korsakoff, "A simplified synthesis for meso-tetraphenylporphyrin," *Journal of Organic Chemistry*, vol. 32, no. 2, p. 476, 1967.
- [51] P. Rothmund, "Formation of porphyrins from pyrrole and aldehydes," *Journal of the American Chemical Society*, vol. 57, pp. 2010–2011, 1935.
- [52] P. Rothmund, "A new porphyrin synthesis. The synthesis of porphin," *Journal of the American Chemical Society*, vol. 58, no. 4, pp. 625–627, 1936.
- [53] G. D. Dorrough, J. R. Miller, and F. M. Huennekens, "Spectra of the metallo-derivatives of  $\alpha,\beta,\gamma,\delta$ -tetraphenylporphine," *Journal of the American Chemical Society*, vol. 73, no. 9, pp. 4315–4320, 1951.
- [54] A. Stone and E. B. Fleischer, "The molecular and crystal structure of porphyrin diacids," *Journal of the American Chemical Society*, vol. 90, no. 11, pp. 2735–2748, 1968.
- [55] H. H. Chang, S.-Ch. Chen, D. Lin, and L. Cheng, "Preparation of bi-continuous Nylon-66 porous membranes by coagulation of incipient dopes in soft non-solvent baths," *Desalination*, vol. 313, pp. 77–86, 2013.
- [56] M. Herrero, P. Benito, F. M. Labajos et al., "Structural characterization and thermal properties of polyamide 6.6/Mg, Al/adipate-LDH nanocomposites obtained by solid state polymerization," *Journal of Solid State Chemistry*, vol. 183, no. 7, pp. 1645–1651, 2010.
- [57] D.-J. Lin, C.-L. Chang, C.-K. Lee, and L.-P. Cheng, "Fine structure and crystallinity of porous Nylon 66 membranes prepared by phase inversion in the water/formic acid/Nylon 66 system," *European Polymer Journal*, vol. 42, no. 2, pp. 356–367, 2006.
- [58] H. W. Starkweather and R. E. Moynihan Jr., "Density, infrared absorption, and crystallinity in 66 and 610 nylons," *Journal of Polymer Science*, vol. 22, no. 102, pp. 363–368, 1956.
- [59] A. M. Liquori, A. Mele, and V. Carelli, "Ultraviolet absorption spectra of polyamides," *Polymer Chemistry*, vol. 10, no. 5, pp. 510–512, 1953.
- [60] M. A. García-Sánchez, S. R. Tello-Solís, R. Sosa-Fonseca, and A. Campero, "Fluorescent porphyrins trapped in monolithic SiO<sub>2</sub> gels," *Journal of Sol-Gel Science and Technology*, vol. 37, no. 2, pp. 93–97, 2006.
- [61] M. A. García-Sánchez, V. de la Luz, M. L. Estrada-Rico et al., "Fluorescent porphyrins covalently bound to silica xerogel matrices," *Journal of Non-Crystalline Solids*, vol. 355, no. 2, pp. 120–125, 2009.
- [62] M. A. García-Sánchez, V. de la Luz, M. I. Coahuila-Hernández, F. Rojas-González, S. R. Tello-Solís, and A. Campero, "Effects of the structure of entrapped substituted porphyrins on the textural characteristics of silica networks," *Journal of Photochemistry and Photobiology A*, vol. 223, no. 2-3, pp. 172–181, 2011.
- [63] N. S. Allen, J. F. McKellar, and C. B. Chapman, "Formation of luminescent impurities during the polymerization of nylon 66," *Applied Polymer Science*, vol. 20, no. 6, pp. 1717–1719, 1976.
- [64] N. S. Allen, J. F. McKellar, and G. O. Phillips, "Luminescence from thermally oxidized model amides in relation to nylon 66 degradation," *Journal of Polymer Science A*, vol. 12, no. 11, pp. 2623–2629, 1974.
- [65] N. S. Allen, J. F. McKellar, and D. Wilson, "Quenching of chromophoric species in nylon-6,6 by halide ions," *Journal of Photochemistry*, vol. 6, no. 1, pp. 73–74, 1976–1977.
- [66] N. S. Allen, J. F. McKellar, and D. Wilson, "Identification of the phosphorescent species in nylon 66," *Journal of Polymer Science A*, vol. 15, no. 11, pp. 2793–2795, 1977.
- [67] Ch. M. Stellman, K. S. Booksh, and M. Myrick, "Multivariate fluorescence imaging of gel on nylon 66 production pack screens," *Applied Spectroscopy*, vol. 49, no. 11, pp. 1545–1549, 1995.

## Research Article

# Ultrasonic, Molecular and Mechanical Testing Diagnostics in Natural Fibre Reinforced, Polymer-Stabilized Earth Blocks

C. Galán-Marín,<sup>1</sup> C. Rivera-Gómez,<sup>1</sup> and F. Bradley<sup>2</sup>

<sup>1</sup> *Departamento Construcciones Arquitectónicas I, Escuela Técnica Superior de Arquitectura, University of Seville, Avda. Reina Mercedes, 2, 41012 Seville, Spain*

<sup>2</sup> *Department of Architecture, Faculty of Engineering, University of Strathclyde, 16 Richmond Street, Glasgow G11XQ, UK*

Correspondence should be addressed to C. Galán-Marín; [cgalan@us.es](mailto:cgalan@us.es)

Received 25 March 2013; Revised 10 July 2013; Accepted 11 July 2013

Academic Editor: Gonzalo Martínez-Barrera

Copyright © 2013 C. Galán-Marín et al. This is an open access article distributed under the Creative Commons Attribution License, which permits unrestricted use, distribution, and reproduction in any medium, provided the original work is properly cited.

The aim of this research study was to evaluate the influence of utilising natural polymers as a form of soil stabilization, in order to assess their potential for use in building applications. Mixtures were stabilized with a natural polymer (alginate) and reinforced with wool fibres in order to improve the overall compressive and flexural strength of a series of composite materials. Ultrasonic pulse velocity (UPV) and mechanical strength testing techniques were then used to measure the porous properties of the manufactured natural polymer-soil composites, which were formed into earth blocks. Mechanical tests were carried out for three different clays which showed that the polymer increased the mechanical resistance of the samples to varying degrees, depending on the plasticity index of each soil. Variation in soil grain size distributions and Atterberg limits were assessed and chemical compositions were studied and compared. X-ray diffraction (XRD), X-ray fluorescence spectroscopy (XRF), and energy dispersive X-ray fluorescence (EDXRF) techniques were all used in conjunction with qualitative identification of the aggregates. Ultrasonic wave propagation was found to be a useful technique for assisting in the determination of soil shrinkage characteristics and fibre-soil adherence capacity and UPV results correlated well with the measured mechanical properties.

## 1. Introduction

The development of building systems has been inextricably linked throughout history with the evolution of construction materials and the technological advancements related to harvesting and exploiting our planet's natural resources [1]. In recent years, the construction sector has been under increasing pressure to reduce its CO<sup>2</sup> emissions and the volume of natural resources which it is responsible for consuming. Environmental concerns relating to the specification of contemporary materials which often involve energy-intensive and oil-dependent processes have become increasingly recognised [2] and with buildings, cities, and their associated infrastructure playing such a significant role in depleting our global resources, it is vital that material utilisation within buildings is specified with care in order to reduce the impact on our planet's resources and delicate ecosystems.

The purpose of this research was to explore the potential for developing a low embodied energy construction materials

obtained where possible from natural, renewable resources. The main barrier to the use of natural materials at present, particularly in developed countries, is their perceived poor mechanical properties and durability in comparison with synthetic materials such as steel, concrete, and other ceramics. This study therefore explores the mechanical properties of an innovative, natural, unfired, composite brick designed to reduce both embodied energy values and CO<sup>2</sup> emissions.

Earth construction is not only cost effective, as a result of the inclusion of low-cost raw materials, but it also uses locally sourced, benign materials. As a building system, it is considered to be highly energy efficient due to the excellent thermal properties which earthen materials exhibit and it also possesses a low embodied energy when raw clay is utilised [3]. Adobe blocks, for example, do not undergo any energy-intensive firing processes since they are simply sun-dried and therefore harness solar energy directly. To put this in context, the energy required to produce an adobe block is only 5 (kWh)/cubic meter compared to about 1000 (kWh)/cubic

metre for a fired brick and 400–500 (kWh)/cubic metre for concrete [4].

Earth construction is therefore becoming an increasingly valued natural building material and its durability benefits and minimization of pollution and waste characteristics—particularly in industrial countries—are also being progressively recognised [5]. With regards to unfired earth construction, Heath et al. [6] have recently shown that there is structural potential for utilizing commercially manufactured unfired bricks but concluded that additional research needs to be carried out into structural behaviour and methods for minimizing moisture susceptibility. This project therefore examines an innovative, sustainable, natural earth product to assess its initial performance against an extensive series of mechanical and analytical laboratory tests [7].

Chemical soil stabilization involves changing the properties of a soil by adding chemicals or additives. This occurs either by creating a matrix, which binds or coats the grains, or by means of a physiochemical reaction between the grains and the additive materials. Cement is one of the most widely used chemical stabilizers for compressed earth blocks (CEBs) and adding it before compaction improves the characteristics of the material, particularly its resistance to water [8–13]. A proportion of at least 5–6% of cement is generally needed to obtain satisfactory results [14]. When compaction of moist soil is used in combination with cement stabilisation, it not only improves compressive strength and water resistance compared to earth construction techniques such as “adobe,” but also improves dimensional stability and tolerances improving construction quality and integrity [15].

Another method of stabilizing soil is with nonhydraulic lime (quicklime or slaked lime). This technique is commonly used for road construction, although it is mainly adopted in temporary roads. The use of this type of stabilizer is not recommended, however, for the manufacture of CEBs as these bricks require a fairly low moisture content and a soil with a relatively high sand content. For stabilization purposes the amounts generally used range from 6 to 12% that is equivalent to the proportion of cement used [16]. The disadvantage of using lime alone is its negative impact on durability as described in [17].

Cementing and waterproofing cohesive soils can be achieved with small amounts of natural or synthetic polymers proportionally less than 2% by dry weight of soil. Typical polymers used in soils comprise cement-resin mixes such as polymer cements or organic resins. These range from epoxy, acrylic, polyacrylate, polyurethane, polymers derived from tomato pulp to alginate, which is an extract from seaweed [18]. There are other recently researched methods relating to the stabilization of clay bricks described in [19] and a variety of techniques and compositions currently under investigation relating to fired and unfired bricks. This research work, however, focuses on 100% natural material ingredients, namely, clay, lignin, wool, and alginate.

## 2. Materials and Methods

The main objectives of this research were to analyse the effect on the mechanical properties of alginate added to

TABLE 1: Physical characteristics, grain size, and Atterberg limits of the three soils.

Physical characteristics	Errol	Ibstock	Raeburn
Sand content	22.50%	27.50%	35.00%
Silt content	45.00%	47.50%	40.00%
Clay content	32.00%	25.00%	25.00%
Classification I.S.S.S.	Silty clay loam	Silt loam	Loam
Liquid limit	34.8%	25.9%	25.9%
Plastic limit	19.1%	16.4%	16.8%
Plasticity index	15.7%	9.5%	9.1%



FIGURE 1: Photograph of the three soil types used.

hand-moulded bricks stabilized with natural fibre and to determine an optimal ratio for wool and alginate within three different soil types. The samples and methods that were selected are described in this section. X-ray diffraction (XRD), energy dispersive X-ray fluorescence (EDXRF), ultrasonic pulse velocity (UPV), and compression and bending tests were all conducted to provide a wide spectrum of data for analysis.

**2.1. Soil.** The materials used in these experiments were three different types of clay soils, alginate, wool, and lignin. The physical properties and Atterberg limits of the three different types of alluvial soils used in this experimental investigation are described in Table 1. All the soils were supplied by Scottish brick manufacturers; Errol (from the East Coast of Scotland) and Ibstock and Raeburn from Glasgow (see Figure 1). All three soils had different colours and textures but importantly their particle-size distributions were all within the maximum limits specified for utilisation within CEBs.

The moisture content (in mass percentage) at which clays and silts pass from semisolid into plastic states and then into a liquid state is defined by the Atterberg limits, which are empirical divisions between the solid, plastic, and liquid limits of a clay. The upper and lower limits of the range of water content over which soils exhibit plastic behaviour are defined by liquid and plastic limits and the water content range between these values is termed the plasticity index [20]. The Errol soil has a much higher liquid limit compared to the other soils as can be seen in Table 1. The clay in each soil sample acts like cement in concrete, binding all the larger

particles in the soil whereas the silt and sand particles behave as filters in the soil matrix in a similar manner to aggregates.

Errol soil is described as a silty clay loam and contains a significantly higher proportion of clay compared to either an Ibstock or Raeburn soil. The Ibstock soil is classified as a silt loam and the Raeburn soil is classified as a loam [20]. With regards to their plasticity indexes, it is interesting to note the quite remarkable variation (see Table 1). All soils were additionally analysed and characterized by utilizing X-ray diffraction (XRD) and X-ray fluorescence (EDXRF) tests.

**2.2. Alginate.** Seaweed is abundant within the coastal waters of countries across the globe and during the last two centuries has been used for a wide variety of products from food and medical products to soda ash production for soap and glass production. In terms of its chemical composition, alginic acid, also called algin or alginate, is a polysaccharide or carbohydrate molecule and it is obtained by extracting alginate salts from the cell walls of brown seaweeds. These alginate salts make up between 20 and 60% of the dry matter of the algae and take the form of different compounds including sodium alginate, calcium alginate, and magnesium alginate. The physical and chemical properties of alginates are nowadays being increasingly investigated and the polymer composition of this natural molecule is increasingly being understood to have a structural function within the cell walls and intercellular mucilage of seaweed [21]. The alginate matrix therefore contributes to the flexibility and mechanical strength of algae [22] in a similar manner to the way that cellulose and pectin components affect land-based plants [23]. Different algal species as well as geographical and environmental conditions influence alginate matrices which gives rise to the variations in properties that different alginates can exhibit.

Alginates are extremely versatile and exhibit important gelling properties as well as high water holding characteristics. Importantly in this research, they have the ability to act as a natural binding matrix within composite systems. Their natural propensity for improving viscosity and stabilizing emulsions has facilitated their widespread use today within the medical, pharmaceutical, and food industries where they are widely used as dental impression materials and gelling agents. Their colours range from white to yellowish brown and they are sold in a variety of forms including filamentous, granular, powdered, or gel forms.

Within the geotechnical engineering sector it, patents have been approved for the use of alginates within in situ stabilization of contaminated and non-contaminated soils [24] and a few previous tests such as those of Friedemann et al. [25] and Galán-Marín et al. [18, 26] have also been carried out incorporating alginate into building materials.

The initial selected proportions of the composite materials was derived from work previously carried out at the Laboratory of the Building Construction Department at the University of Seville and has been the subject of a patent [27]. The alginate used in our research was supplied by FMC Biopolymer, Girvan, Scotland (UK), under the name of seaweed extract and contained sodium alginate, sodium carbonate, and inorganic salt. In these experiments, we used

an alginate paste (gluey, brown liquid), which is a product of the first stage of alginate extraction from seaweed.

**2.3. Fibre.** Traditionally, natural fibres have been used as soil reinforcement where available, to improve certain engineering properties of the soil. Vegetal fibres, derived from plants such as coir, jute, sisal, bamboo, wood, palm leaf, coconut leaf truck, cotton, hemp, and grass, have been tested as reinforcing materials not only for soils, but also within various polymer matrix composites [28] for utilisation within various industries.

Vegetal fibres such as coir can come in different varieties and the individual fibre cells are narrow and hollow, with thick walls made of cellulose. Coir is a relatively waterproof fibre and is one of the few natural fibers resistant to damage by salt water. Jute, in contrast, is a long, soft, shiny vegetable fibre similar to industrial hemp and flax (linen) and can be spun into coarse, strong threads and when woven is called hessian or burlap [29]. Another natural fibre that has recently been utilised in CEB research has been produced from cassava peels [17] and sugarcane bagasse ash [30] so there are a wide variety of vegetal fibres currently being examined in clay composites with regards to strength and flexural properties. Organic products containing cellulose fibres do however have several drawbacks such as an incompatibility with hydrophobic polymer matrices [31] and a propensity to show little resistance to prolonged moisture. For this reason this project has examined the behaviour of animal fibres which to date have tended to be overlooked as a constituent in unfired brick reinforcement.

Wool fibre is composed of a protein known as keratin. Generally, wool fibres measure 40–127 mm in length and 14–40  $\mu$  in width. Their cross-sectional shape is oval in form and the fibre grows in the form of a wave with a certain amount of twist. Its mechanical properties include a tensile strength 120–174 MPa, an elasticity component of 25–35% elongation at break and Young's modulus of 2.3–3.4 MPa [32]. Alternative figures listed in CES Edupak (2012) [29] give a tensile strength of between 40 Mpa and 200 Mpa and Young's modulus values between 3.9 MPa and 5.2 Mpa. Different species of sheep produce quite different types of wool with varied fibre length, diameter, and other differing physical characteristics. The molecular structure of wool fibres is interesting in that they comprise two different types of cell. Internal cells are referred to as the cortex and then outside these cells are external cuticle cells (or scales) that form a sheath around the fibre, overlapping like roof tiles. This structure gives wool its uniqueness compared to the variety of other fibres being used within natural composites today.

For the tests carried out in this project, wool fibre was added as the natural reinforcement within earth blocks, totally untreated and taken straight from the animal fleece so that no artificial additives were introduced. In addition, the wool was hand-cut, by trimming the top 10 mm strand of fibre, as longer fibres would have been too long to create a homogenous mix. All the specimens for this study were prepared and manufactured with the addition randomly oriented of a small amount (0.5–0.25%) of this raw, unprocessed wool according to recommendations from previous

TABLE 2: Mixes used (by weight).

Soil mix no.	Proportions	Soil	Alginate	Lignum	Wool	Water
1	Unstabilized soil	80.0%	—	0.5%	—	19.5%
2	Soil + alginate	79.5%	19.75%	0.5%	—	0.25%
3	Soil + 0.25% wool	79.5%	—	0.5%	0.25%	19.75%
4	Soil + alginate + 0.50% wool	79.0%	19.5%	0.5%	0.50%	0.50%
5	Soil + alginate + 0.25% wool	79.5%	19.5%	0.5%	0.25%	0.25%

TABLE 3: Mass percentages of each mineral and clay proportions.

Soil	Calcite	Quartz	Phyllosilicates	Feldspars	Illite	Kaolinite	Chlorite
Errol	<5	41	52	Traces	50	38	12
Ibstock	—	39	59	Traces	36	64	Traces
Raeburn	—	34	62	<5	27	69	4

research which looked at the impact of various proportions [18].

**2.4. Lignin.** Lignin is a treacle-like resin extracted from wood during the production of cellulose. Lignosulfonate and lignin products are therefore derived from a natural raw material. In all three mixes 0.5% of lignin sulfonate (under name of Additive A, Traffaid 45 by Borregaard LignoTech) was added to improve the workability of the soil mixture because it greatly facilitates the mixing of clay with low proportions of water. This additive is commonly used in the manufacturing processes for unfired bricks.

### 3. Sample Manufacturing Process

Material preparation was carried out manually in the laboratory of the University of Seville. Machine mixing was carried out using hand compaction and no extra compression was added. The mixtures adopted a proportion of close to 80:20 soil: (water + stabilizer) ratio after making necessary adjustments to previously carried out corrective dosages [26]. It was decided to choose a water/soil ratio of 19.5/80% (adding 0.5% of lignum) to get a normal consistency and low total shrinkage for mixes without the addition of alginate. Ratios of 0.25–0.5% of wool were added to mixes, where alginate was added to the mix and 0.25% only where no alginate was present (see Table 2). Soil Mixes numbered 1, 2, and 3 were used as contrast dosages to compare the effect of either the fibre or the polymer alone. Soil Mixes numbered 4 and 5 were manufactured to detect the appropriate quantity of fibre reinforcement. Reinforcing wool fibres were cut to the required length, soaked in water for 24 hours, to improve mixing, and then added randomly, but in a homogeneous way, to the moist soil using a 5 litre mixer until a completely homogeneous composite was achieved. All the brick samples used in this study were prismatic specimens (160 × 40 × 40 mm) in accordance with the European standards format for the mechanical testing of mortar tests for masonry [33].

In this research study three different soils were tested and five different mix combinations. For each batch, seven specimens were tested. All specimens were first placed in

an oven at 50°C to dry for 24 hours and subsequently dried at room temperature for 48 hours before unmolding. Specimens were cured in the uncontrolled laboratory environment at 20–25°C and about 65% RH. A different consistency and workability was observed during the manufacturing process, for the Errol mixes. This was due to the higher percentages of illite within the Errol soil compared to Raeburn or Ibstock, which allowed more water to be absorbed within the crystal matrix.

**3.1. X-Ray Diffraction (XRD).** In order to identify and quantify the presence of the different mineral components within the clays and the phyllosilicates in each soil, the researchers followed a standard protocol, set out in a standard preparation protocol procedure, entitled PNT07LRX0044 [34]. The experiments were carried out in the laboratory within the University of Seville and the protocol determined the percentage composition of the small illite, kaolinite, and chlorite grains within each sample, using the oriented aggregates method which led to the proportions described in Table 3.

The oriented aggregates study included dissolving the samples in ethylene glycol and then subjecting them to a heat treatment between 350 degrees and 550 degrees. Figures 2, 3, and 4 show the phyllosilicate and quartz fractions over the majority of each soil type and the percentage and proportion of each mineral is shown in Table 2. Testing and analysis was performed in this way relating to all the different groups of clays prevailing within each soil.

**3.2. X-Ray Fluorescence Spectroscopy (XRF).** XRF is mostly a quantitative technique—the peak-height for any element being directly related to the concentration of that element within the sampling volume. However, extreme care must be taken because two or more elements can interact with each other, resulting in contamination and thus skewing results. XRF tests showed (see Table 4) the chemical composition of three soils (samples dried at 110°C).

**3.3. Energy Dispersive X-Ray Fluorescence (EDXRF).** Energy dispersive X-ray fluorescence is one of two general types of X-ray fluorescence techniques used for elemental analysis

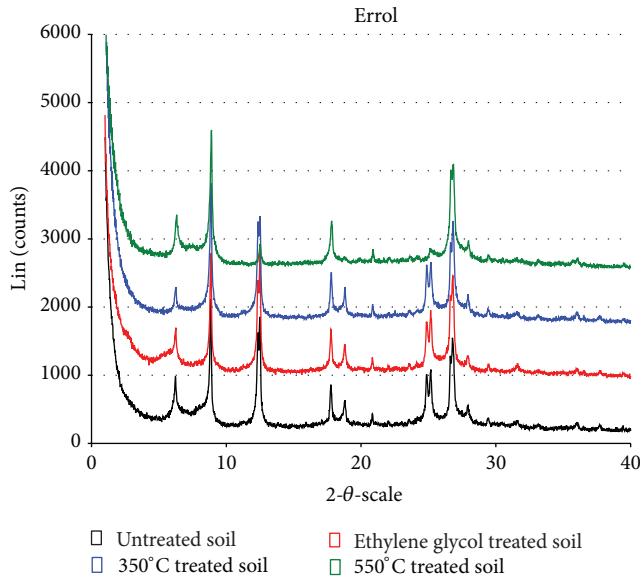


FIGURE 2: XRD patterns of the Errol soil oriented aggregates.

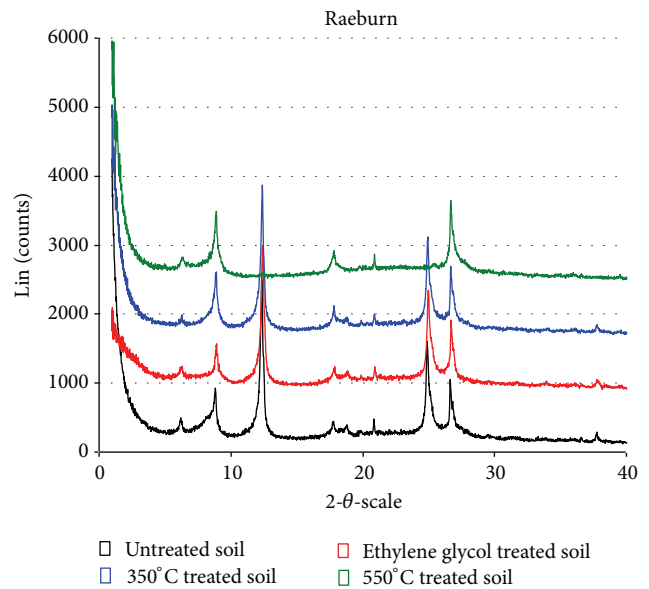


FIGURE 4: XRD patterns of the Raeburn soil oriented aggregates.

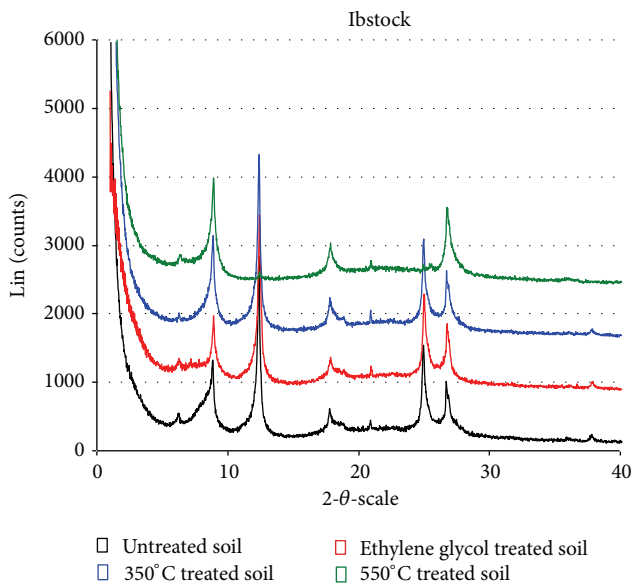


FIGURE 3: XRD patterns of the Ibstock soil oriented aggregates.

TABLE 4: Chemical composition of three soils.

		Errol	Ibstock	Raeburn
SiO <sub>2</sub>	%	56,53	56,93	51,72
Al <sub>2</sub> O <sub>3</sub>	%	17,02	19,57	20,19
Fe <sub>2</sub> O <sub>3</sub>	%	7,09	4,81	6,51
MnO	%	0,10	0,06	0,10
MgO	%	2,71	1,21	1,50
CaO	%	2,07	0,60	0,74
Na <sub>2</sub> O	%	1,53	0,23	0,28
K <sub>2</sub> O	%	3,18	2,31	2,22
TiO <sub>2</sub>	%	0,95	1,02	0,95
P <sub>2</sub> O <sub>5</sub>	%	0,15	0,12	0,18
SO <sub>3</sub>	%	0,03	0,02	0,03
PC	%	6,02	10,59	13,34
TOTAL	%	97,39	97,47	97,77

applications. These tests show the chemical composition of the three soils (samples dried at 110°C), their main elements, and traces (see Table 5).

3.4. *Ultrasonic Pulse Velocity Testing (UPV)*. Application of ultrasonic methods for the testing of materials including polymer composites has a long-lasting tradition. In this context, ultrasound’s physical nature as a mechanical wave is used and knowledge of sound wave propagation characteristics in a tested medium allows for a theoretical analysis of a phenomenon.

On the basis of wave parameters on the boundary of an area, conclusions can be drawn concerning geometric

properties and the distribution of physical properties within a medium—in this case unfired natural bricks.

Ultrasonic tests were carried out with the ultrasonic model brand BPV Krautkramer. This equipment gives the delay time from when a transmitted wave leaves the probe until the wave is received back by the probe. It is measured by a liquid crystal five digit display which measures the reading time in microseconds. The accuracy is ±0.1 μs. Measurements were recorded by cylindrical transducers and the emission frequency of the probes was 50 KHz. A single ultrasonic head was used and the time of a sound wave transition through tested samples (τ), was expressed in microseconds. The sound wave velocity (V) through a sample was then calculated using the following formula:

$$V = \frac{h}{\tau}, \tag{1}$$

TABLE 5: Chemical composition of three soils (main elements and traces).

	Cl ppm	Sc ppm	V ppm	Cr ppm	Co ppm	Ni ppm	Cu ppm	Zn ppm	Ga ppm	Ge ppm	As ppm	Se ppm	Br ppm
Errol	32	15	106	111	16	53	38	86	22	N.D.	14	N.D.	N.D.
Ibstock	35	12	83	102	15	51	28	61	23	N.D.	4	0	N.D.
Raeburn	34	12	83	101	17	57	29	68	24	N.D.	6	0	N.D.
	Rb ppm	Sr ppm	Y ppm	Zr ppm	Nb ppm	Mo ppm	Ag ppm	Cd ppm	Sn ppm	Sb ppm	Te ppm	I ppm	Cs ppm
Errol	106	152	24	178	15	1	N.D.	N.D.	4	2	N.D.	N.D.	3
Ibstock	111	184	28	188	17	1	N.D.	N.D.	4	3	N.D.	N.D.	5
Raeburn	102	217	28	167	15	1	N.D.	N.D.	4	4	N.D.	N.D.	5
	Ba ppm	La ppm	Ce ppm	Nd ppm	Sm ppm	Yb ppm	Hf ppm	Ta ppm	Tl ppm	Pb ppm	Bi ppm	Th ppm	U ppm
Errol	582	40	72	33	3	1	4	N.D.	0	22	N.D.	11	1
Ibstock	400	45	78	35	6	3	4	N.D.	0	23	0	13	2
Raeburn	402	41	81	37	7	2	4	0	N.D.	24	N.D.	14	2

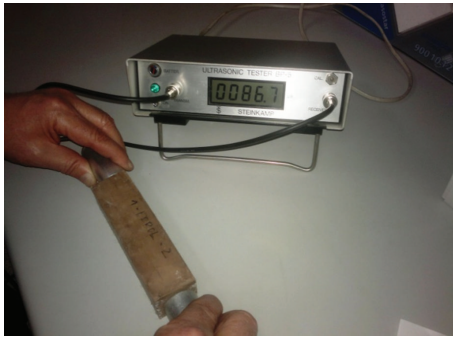


FIGURE 5: Ultrasonic tests.

where  $h$  was the sample thickness. All the UPV tests were carried out on the prism specimens as per the guidelines of UNE-EN 583-1/A1 [32]. Test pieces with dimensions  $160 \text{ mm} \times 40 \text{ mm} \times 40 \text{ mm}$  were tested perpendicularly to the  $40 \text{ mm} \times 40 \text{ mm}$  plane as shown in Figure 5 and the results are shown in Figure 6. A comparison between a series of mechanical and UPV test results for all soils and mixes is shown in Table 6.

## 4. Mechanical Test Results

**4.1. Compression Tests.** After breaking samples roughly in half, three-point bending strength tests were used to determine compressive strength and a total of 210 compressive strength tests were carried out (see Table 6 and Figure 7).

**4.2. Flexural Tests.** Bending strengths were determined by carrying out a three-point bending test on the specimens, in agreement with the specifications of UNE-EN 1015-11:2000 European standards. This standard is for the determination of bending strength of mortars used for rough castings and mortar linings, but it was decided to adopt this standard in the absence of other specific regulations. Several papers including

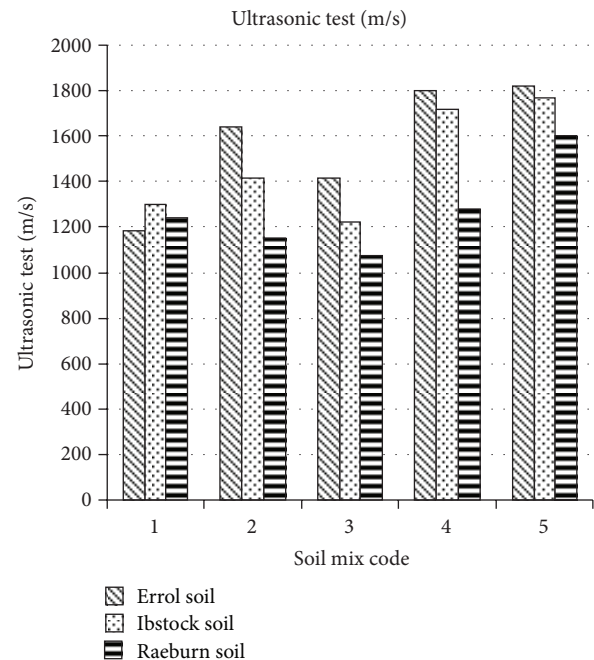


FIGURE 6: Graphical comparison of the UPV results on the five different mixes of the three types of soils.

the study carried out by Raut et al. [19] have illustrated the wide range of testing and curing regimes currently being carried out in different laboratories as well as the range of sizes of earth brick samples. Furthermore and Heath et al. [6] have additionally discussed the current limitations in Eurocode 6: Design of masonry structures (BS EN 1996-2:2006) and the fact that it does not currently have a section referring to earth masonry. Within this context, it was felt that UNE-EN1015-11:2000 was an appropriate standard to adopt.

All the flexural tests were conducted at room temperature ( $20^\circ\text{C}$ ) on a Codein S.L., MCO-30/139 machine (maximum

TABLE 6: Mechanical and UPV tests results of three soils.

Mix code	01	02	03	04	05
	Unstabilized soil	Soil + alginate	Soil + 0.25% wool	Soil + alginate + 0.50% wool	Soil + alginate + 0.25% wool
<b>Errol soil</b>					
Compressive strength (MPa)	2,23	3,77	3,05	4,37	4,44
Flexural strength (MPa)	1,12	1,06	1,1	1,08	1,45
Ultrasonic testing (m/s)	1182	1637	1416	1798	1818
<b>Ibstock soil</b>					
Compressive strength (MPa)	2,06	2,49	1,89	3,43	3,59
Flexural strength (MPa)	0,97	0,98	0,96	1,28	1,61
Ultrasonic testing (m/s)	1298	1413	1222	1720	1769
<b>Raeburn soil</b>					
Compressive strength (MPa)	2,44	2,24	1,88	2,69	3,75
Flexural strength (MPa)	1,12	1,1	0,93	1,11	1,24
Ultrasonic testing (m/s)	1240	1153	1075	1280	1604

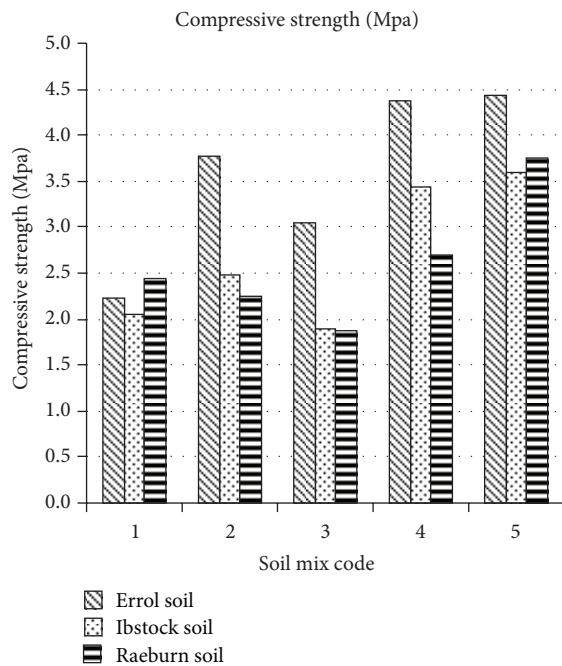


FIGURE 7: Graphical comparison of the compressive strength results on the five different mixes of the three types of soils.

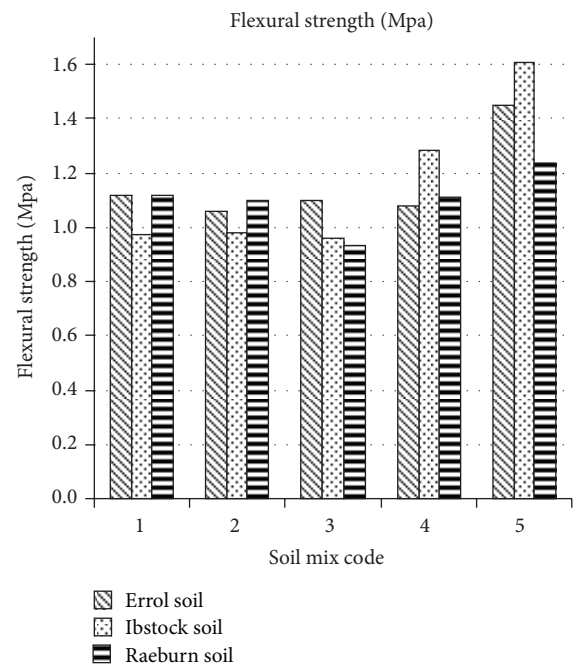


FIGURE 8: Graphical comparison of the flexural strength results on the five different mixes of the three types of soils.

load 10 kN) in a three-point bending configuration. The support length was adapted to the size of sample, and at least seven specimens were tested for each mix under study. A total of 105 tensile tests were therefore conducted both with the fibrous and non-fibrous samples and the mechanical properties determined from these tests included the flexural modulus, the ultimate stress, and the ultimate strain (see Table 6 and Figure 8).

### 5. Results and Discussion

It is generally accepted that incorporation of fibres increases flexural strength. Our tests have not shown the expected improved flexural strength, indeed sometimes just the opposite, as is shown in Figure 8 for the Ibstock soil. In fact the addition of just fibre to soils, without the presence of alginate (as indicated in the comparison between mixes 03 and 01), does not increase flexural strength. Additionally, compressive

strength in samples with no alginate and only fibres is increased only in the soil with the high plasticity index, namely, Errol. Indeed, both the flexural and compressive strengths of the Raeburn and Ibstock soils decreased in the mixture only containing wool fibres without the polymer.

In contrast, adding wool into the soil mixed with alginate always increased flexural resistance, especially if a proportion of 0.25% of wool was added. The incremental strength improvement was particularly significant (65%), for the Ibstock soil specimens, where flexural resistance changed from 0.97 MPa (plain soil specimens) to 1.60 MPa (0.25% wool + soil + alginate mixes).

As the XRD analytical results show, higher percentages of illite can be found in the Errol soil (compared to Raeburn or Ibstock). This phyllosilicate appears to allow more water to be absorbed within the crystal matrix giving rise to a drier mix and this finding is consistent with the plasticity indexes obtained for the different soils showed in Table 1. The consequences of this drier and therefore stiffer consistency can be observed in the mechanical results.

UPV measurements (see Figure 6) demonstrated that Errol specimens, in most of the mixes tested, provided much higher compactness and with regards to mechanical tests, Errol specimens reached higher resistance values in the compression tests compared with the other soils. Flexural tests, however were less conclusive, with Errol providing higher flexural strengths in mix 3, Raeburn in mix 2, and Ibstock in mixes 4 and 5. Flexural strength values were equal in the Raeburn and Errol soils in mix 1 and the UPV results showed a pulse velocity increase for mixes 4 and 5 compared to mixtures 1, 2, and 3. Specimens of any type of soil tested for mix 5 (the mix with the lower quantities of wool reinforcement) showed higher UPV values than mix 4. This was particularly the case with the Raeburn soil which had the lowest plasticity index. This compactness decrease could be caused by the fact that the shrinkage values for the fibre were much higher than the soil shrinkage.

Lower compressive and flexural resistance values were obtained when larger quantities of fibre were used in mix 4. This could be explained as follows: the development of strength properties in the fibre/soil mixes mostly depends on the formation of fibre-matrix bonds as has been shown in previous studies [35]. Bonding is affected by fibre dimensions, surface textures, and the number of fibres present in a given volume of material. Increasing wool fibre quantities gives rise to fibre agglomeration and folding of fibres (balling) and this can result in a decrease in the bond strength within the specimens, which in turn leads to lower compressive strength values. In addition to the XRD, XRF, and EDXRF results, the ultrasonic results were incorporated into this study's testing regime in order to indicate the prevalence of voids and compare the relative material densities. The results of these tests within each sample confirm that mix 5 had the best overall engineering properties and it is suggested that this was due to the quality of bonding within the composite matrix and the overall homogeneity of the mixture.

The highest compressive strength, in all three soil types, was obtained with the composite specimens including both alginate and wool reinforcement and better results were

obtained with the reduced quantity of wool, that is, the 0.25% mix 04. By adding wool to the mix, the Ibstock soil specimens stabilized with alginate improved their compressive strengths by 74% whilst the Raeburn soil specimens improved their compressive strengths by 54%.

Various research papers have shown that hygrometric shrinkage and its associated cracking of earth-based materials can be greatly reduced by introducing fibres into the mixture and this study confirmed these findings by demonstrating that shrinkage due to the drying process was significantly reduced with the inclusion of natural fibres into the soil mix. As would be expected, specimens of plain soil had a very quick (and almost without warning), brittle failure mode. In contrast, fibre-reinforced mixes deformed, after the ultimate load was reached and fine cracks could be seen on the surface giving warning before failure.

## 6. Conclusions

Soil characterization through XRD, XRF, and EDXRF tests has proved to be very important in order to understand the different mechanical behaviour of the different stabilised soils (with the same fibre and stabilizer content) and therefore the effect of the stabilization itself.

Mixes 2, 4, and 5 (those that included the alginate polymer as a stabilizer) showed better results in UPV tests in every type of soils, especially though the Errol soil and these results are consistent with the compression test results. As would be expected, flexural resistance values generally increased in mixes 4 and 5, where alginate and fibre were used simultaneously.

The use of UPV, in this study, has added an interesting additional data set with results which closely align with the mechanical compressive strength results. Errol soil, due to its higher content of illite, contains a crystalline structure that facilitates a higher level of water absorption compared to the Raeburn and Ibstock kaolinite crystalline structures. Improved results were therefore obtained with the Errol soil due to the higher plasticity index related to a higher proportion of illite within the clay fraction.

The addition of short wool fibres (10 mm long) randomly oriented to the mixes leads to a decrease in bulk density which correspondingly decreases the compressive strength of the specimens. Therefore UPV measurements were useful in determining the resultant final porosity of the dried mix, after the shrinkage process.

Fibre water adsorption and soil-fibre surface friction, due to the drying shrinkage characteristics of a fibre, depend on the available water and this in turn depends on the characteristics of the soil plasticity for different types of clay. The higher plasticity index obtained for the Errol soil seems to be responsible for its different behaviour observed in the various tests compared with the Ibstock and Raeburn soils, in mixtures with similar water proportions.

As a result of the range of data presented within this paper, it has therefore been shown that it is possible to prepare 100% green composites from natural fibres and natural polymers with mechanical performance results within ranges compatible with producing unfired bricks. Further research

is currently under development to investigate methods for improving composite bonding and interaction and ultimately durability.

## Acknowledgments

The authors wish to acknowledge the IUACC “Instituto Universitario de Arquitectura y Ciencias de la Construcción” for the necessary support to develop this research. They would also wish to acknowledge the CITIUS “Centro de Investigación, Tecnología e Innovación” of the University of Seville, X-Ray Laboratory, where these tests were carried out.

## References

- [1] J. M. Saiter, L. Dobircan, and N. Leblanc, “Are 100% green composites and green thermoplastics the new materials for the future?” *International Journal of Polymer Science*, vol. 2012, Article ID 280181, 7 pages, 2012.
- [2] M. F. Ashby, *Materials and the Environment: Eco-Informed Material Choice*, Elsevier, Oxford, UK, 2009.
- [3] P. McHenry, *Adobe and Rammed Earth Construction. Adobe, Build It Yourself*, 1994.
- [4] A. Debnath, S. V. Singh, and Y. P. Singh, “Comparative assessment of energy requirements for different types of residential buildings in India,” *Energy and Buildings*, vol. 23, no. 2, pp. 141–146, 1995.
- [5] J. O. Arumala and T. Gondal, *Compressed Earth Building Blocks for Affordable Housing*, RICS, COBRA, London, UK, 2007.
- [6] A. Heath, D. Maskell, P. Walker, M. Lawrence, and C. Fourie, “Modern earth masonry: structural properties and structural design,” *Structural Engineering*, vol. 90, no. 4, pp. 38–44, 2012.
- [7] E. A. Adam and P. J. Jones, “Thermophysical properties of stabilised soil building blocks,” *Building and Environment*, vol. 30, no. 2, pp. 245–253, 1995.
- [8] D. A. Adesanya, “Evaluation of blended cement mortar, concrete and stabilized earth made from ordinary Portland cement and corn cob ash,” *Construction and Building Materials*, vol. 10, no. 6, pp. 451–456, 1996.
- [9] L. K. Aggarwal, “Bagasse-reinforced cement composites,” *Cement and Concrete Composites*, vol. 17, no. 2, pp. 107–112, 1995.
- [10] V. Agopyan, H. Savastano Jr., V. M. John, and M. A. Cincotto, “Developments on vegetable fibre-cement based materials in São Paulo, Brazil: an overview,” *Cement and Concrete Composites*, vol. 27, no. 5, pp. 527–536, 2005.
- [11] E. A. Basha, R. Hashim, H. B. Mahmud, and A. S. Muntohar, “Stabilization of residual soil with rice husk ash and cement,” *Construction and Building Materials*, vol. 19, no. 6, pp. 448–453, 2005.
- [12] P. R. Blankenhorn, B. D. Blankenhorn, M. R. Silsbee, and M. DiCola, “Effects of fiber surface treatments on mechanical properties of wood fiber-cement composites,” *Cement and Concrete Research*, vol. 31, no. 7, pp. 1049–1055, 2001.
- [13] R. S. P. Coutts, “Fibre-matrix interface in air-cured wood-pulp fibre-cement composites,” *Journal of Materials Science Letters*, vol. 6, no. 2, pp. 140–142, 1987.
- [14] R. Bahar, M. Benazzoug, and S. Kenai, “Performance of compacted cement-stabilised soil,” *Cement and Concrete Composites*, vol. 26, no. 7, pp. 811–820, 2004.
- [15] J.-C. Morel, A. Pkka, and P. Walker, “Compressive strength testing of compressed earth blocks,” *Construction and Building Materials*, vol. 21, no. 2, pp. 303–309, 2007.
- [16] J. R. Prusinski and S. Bhattacharja, “Effectiveness of portland cement and lime in stabilizing clay soils,” *Transportation Research Record*, vol. 1, no. 1652, pp. 215–227, 1999.
- [17] M. Villamizar, V. Araque, C. Reyes, and R. Silva, “Effect of the addition of coal-ash and cassava peels on the engineering properties of compressed earth blocks,” *Construction and Building Materials*, vol. 36, pp. 276–286, 2012.
- [18] C. Galán-Marín, C. Rivera-Gómez, and J. Petric-Gray, “Effect of animal fibres reinforcement on stabilized earth mechanical properties,” *Journal of Biobased Materials and Bioenergy*, vol. 4, no. 2, pp. 121–128, 2010.
- [19] S. P. Raut, R. V. Ralegaonkar, and S. A. Mandavgane, “Development of sustainable construction material using industrial and agricultural solid waste: a review of waste-create bricks,” *Construction and Building Materials*, vol. 25, no. 10, pp. 4037–4042, 2011.
- [20] R. F. Craig, *Craig’s Soil Mechanics*, Spon Press, New York, NY, USA, 7th edition, 2004.
- [21] I. D. Hay, Z. U. Rehman, and B. H. Rehm, “Membrane topology of outer membrane protein AlgE which is required for alginate production in pseudomonas aeruginosa. Identification of two aflatrem biosynthesis gene loci in aspergillus flavus and metabolic engineering of penicillium paxilli to elucidate their function,” *The American Society For Microbiology*, vol. 76, no. 6, pp. 1806–1812, 2010.
- [22] I. L. Andresen, O. Skipnes, O. Smidsrod, K. Ostgaard, and P. C. Hemmer, “Some biological functions of matrix components in benthic algae in relation to their chemistry and the composition of seawater,” *ACS Symposium Series of the American Chemical Society*, vol. 48, pp. 361–381, 1977.
- [23] I. Donati and S. Paoletti, “Materials properties of alginates,” in *Alginates: Biology and Applications*, B. H. A. Rehm, Ed., pp. 1–54, Springer, Berlin, Germany, 2009.
- [24] G. L. Schneider, “Method of stabilizing soils,” USA Patent 4,002,633, 1977.
- [25] K. Friedemann, F. Stallmach, and J. Kärger, “NMR diffusion and relaxation studies during cement hydration-A non-destructive approach for clarification of the mechanism of internal post curing of cementitious materials,” *Cement and Concrete Research*, vol. 36, no. 5, pp. 817–826, 2006.
- [26] C. Galán-Marín, C. Rivera-Gómez, and J. Petric, “Clay-based composite stabilized with natural polymer and fibre,” *Construction and Building Materials*, vol. 24, no. 8, pp. 1462–1468, 2010.
- [27] C. Galán-Marín and G. Rivera-Gómez, “Method for stabilising clay soils with natural organic polymers reinforced with animal fibre,” Patent WO2012/101299, 2012.
- [28] N. Uddin and R. R. Kalyankar, “Manufacturing and structural feasibility of natural fiber reinforced polymeric structural insulated panels for panelized construction,” *International Journal of Polymer Science*, vol. 2011, Article ID 963549, 7 pages, 2011.
- [29] G. Design and M. F. Ashby, *CES Edupak: Material Selector*, 2012.
- [30] S. Lima, H. Varim, A. Sales, and V. Neto, “Analysis of the mechanical properties of compressed earth block masonry utilizing the sugarcane bagash ash,” *Construction and Building Materials*, vol. 35, pp. 829–837, 2012.
- [31] A. L. Martínez-Hernández, C. Velasco-Santos, M. de-Icaza, and V. M. Castaño, “Dynamical-mechanical and thermal analysis of polymeric composites reinforced with keratin biofibres from chicken feathers,” *Composites B*, vol. 38, pp. 405–410, 2007.

- [32] “UNE-EN 583-1/A1. Non-destructive testing. Ultrasonic examination. Part 1: general principles,” AENOR, European Committee for Standardization, 2004.
- [33] “UNE-EN, 1015-11:2000/A1. Methods of test for mortar for masonry. Part 11: determination of flexural and compressive strength of hardened mortar,” AENOR, European Committee for Standardization, 2000.
- [34] reparation Protocol System PNT 07LRX0044, CITIUS, “Centro de Investigación, Tecnología e Innovación” (Research Center for Technology and Innovation) of the University of Seville, 2011.
- [35] C. Galán-Marín, C. Rivera-Gómez, and F. Bradley, “The mechanical properties and molecular bonding characteristics of clay-based natural composites reinforced with animal fibres,” *Journal of Biobased Materials and Bioenergy*, vol. 7, pp. 143–151, 2013.

## Research Article

# Polypropylene Fibers as Reinforcements of Polyester-Based Composites

**Gonzalo Martínez-Barrera,<sup>1</sup> Enrique Viguera Santiago,<sup>1</sup> Susana Hernández López,<sup>1</sup> Osman Gencel,<sup>2</sup> and Fernando Ureña-Nuñez<sup>3</sup>**

<sup>1</sup> *Laboratorio de Investigación y Desarrollo de Materiales Avanzados (LIDMA), Facultad de Química, Universidad Autónoma del Estado de México, Km. 12 de la Carretera Toluca-Atlacomulco, 50200 San Cayetano, Mexico*

<sup>2</sup> *Civil Engineering Department, Faculty of Engineering, Bartin University, 74100 Bartin, Turkey*

<sup>3</sup> *Instituto Nacional de Investigaciones Nucleares, Carretera México-Toluca S/N, 52750 La Marquesa Ocoyoacac, Mexico*

Correspondence should be addressed to Gonzalo Martínez-Barrera; [gonzomartinez02@yahoo.com.mx](mailto:gonzomartinez02@yahoo.com.mx)

Received 27 March 2013; Revised 18 June 2013; Accepted 23 June 2013

Academic Editor: Carmina Menchaca-Campos

Copyright © 2013 Gonzalo Martínez-Barrera et al. This is an open access article distributed under the Creative Commons Attribution License, which permits unrestricted use, distribution, and reproduction in any medium, provided the original work is properly cited.

Effects of gamma radiation and the polypropylene fibers on compressive properties of polymer concrete composites (PC) were studied. The PCs had a composition of 30 wt% of unsaturated polyester resin and 70 wt% of marble particles which have three different sizes (small, medium, and large). The PCs were submitted to 200, 250, and 300 kGy of radiation doses. The results show that the compressive properties depend on the combination of the polypropylene fiber concentration and the applied radiation dose. The compressive strength value is highest when using medium particle size, 0.1 vol% of polypropylene fibers and 250 kGy of dose; moreover, the compressive modulus decreases when increasing the particle size.

## 1. Introduction

Polymer concrete (PC) is a composite material formed by combining mineral aggregates with a thermoset resin. In its elaboration several parameters must be taken into account, such as resin type, initiator, and accelerator concentrations. The unsaturated polyester resin (UPR) is the most widely used due to their balanced mechanical and chemical characteristics, its ease of handling, and low cost; for its polymerization, 2 wt% of methyl-ethyl-ketone peroxide (MEKP), as initiator, and 0.5 wt% of cobalt naphthenate as accelerator are normally used, with at least 40 wt% of styrene.

The composition of polymer concrete is determined by its applications especially loading stress levels and ability to resist corrosive environment. PC is increasingly being used as an alternative to ordinary Portland cement concrete (PCC) in many applications, such as finishing work in cast-in-place applications, precast products, highway pavements, bridge decks, waste water pipes, and even decorative construction panels. In the last 40 years polymer concrete has made tremendous progress and continues to be very promising

materials for a wide range of new and innovative applications. Moreover, the use of polymers should be well considered to guarantee better performance and improved sustainability [1–3]. Improvement on mechanical strength and chemical resistance is basic advantages of polymer concrete in comparison to ordinary Portland cement concrete (PCC). Three to five times on the compressive strength, high values for tensile strength (20 MPa), and flexural strength (50 MPa) are still an outstanding advantage of polymer concrete [3, 4].

Mechanical properties of polymer concrete depend on the type of resin and mineral aggregates. In the case of the last, higher specific surface means higher mechanical values, for example, (a) polymer concrete with clean sand have higher values than those with foundry sand [5]; (b) for concrete elaborated with epoxy resin, silica sand, hematite, and colemanite, the mechanical properties depend on the resin and hematite-colemanite concentrations; larger improvement for hematite is done [6]; (c) for concrete with waste marble as aggregate the splitting tensile strength decreases, and improvement on the elasticity modulus is produced [7].

Polymer concrete has relatively low tensile strength compared to its compressive strength. This limits its usefulness for load-bearing applications. Sudden and brittle failures occur in planes where tensile stresses exceed the tensile strength of the polymer concrete. Thus, reinforcement either by synthetic or natural fibers is one option to increasing its strength capacity, ductility, and toughness [5]. For example, glass fibers have been used for reinforcement of polyester polymer concrete, particularly for increasing flexural strength and strain at peak stress. An improvement of 80% in the flexural strength is obtained with respect to unreinforced polymer concrete. The toughness is increased by more than 1440% when 6 wt% of glass fibers is added. The glass fibers were 3 mm long and 0.013 mm of diameter, with a tensile strength of 2.5 GPa and a modulus of 70 GPa [8].

Carbon and glass fibers (1% and 2%, resp.) added to epoxy polymer concrete showed different behaviors. The carbon fibers increase the fracture energy by 340% while glass fibers by 140% when comparing to plain polymer concrete. Nevertheless, the fibers induce failure due to poor adhesion between them and polymer resin including the break of the fibers when compressive test is evaluated [9]. Chopped glass fibers were with random size, while chopped carbon fibers (made from a poly-acrylic-nitrile precursor material) were on average 6 mm.

The fracture behavior of concrete elaborated with polyester resin (18%) and sand and glass fibers (82%) was studied. Stable crack growth prior to peak load was found when adding 4% of glass fibers (13 mm long) [10]. In the case of polymer concrete with polypropylene fibers the compressive strength, splitting tensile strength, and especially flexural strength and elasticity modulus increase while the weight diminishes [11].

Some studies concerned with the use of gamma radiation on polymer/mineral composites have been carried out. The effects of gamma radiation on pure polyester resin and polyester resin/gypsum composites show that the rupture stress is higher for pure resin than that for the composite (6.5 MPa versus 2.0 MPa, at 20 kGy). At highest dose (320 kGy) the values increase up to 9.0 MPa for pure resin and 3.6 MPa for the composite. Such difference is due to the lower tensile strength of gypsum (filler) when comparing to those for resin. Moreover, only the polymer chains (but not the inorganic filler particles) would build cross-links between the chains [12]. In other results, a minimal variation on the hardness is observed at different doses: 91% and 92% for the composite and 89% and 88% for pure resin (at 20 and 320 kGy, resp.) [12].

As it is known, the cross-linking reaction of unsaturated polyester resins (UP) is usually initiated by a thermal or redox initiator, but sometimes the full conversion is not fully achieved, due to the difficulty of mixing with initiators and/or promoters, which reduces the conversion, especially at room temperature [13]. The release of residual styrene of the UP resins creates problems to the environment and is the source of odor in many applications. One alternative route of curing UP resins is by radiation processing [14, 15]. Some differences are found when polyester resin with or without initiators is irradiated. At low dose (11.1 kGy), polyester resin with

initiator shows a larger increase in the maximum load (30 N) higher than that for resin without initiator (20 N). Notorious is this value at higher dose (33.3 kGy), 320 N for resin with initiator and 200 N for resin without initiator [16].

## 2. Materials and Methods

*2.1. Specimen Preparation.* Before preparing the polymer concrete composites, one set of polypropylene atactic fibers (CONSA, Distrito Federal, Mexico) whose diameters vary from 50 to 60  $\mu\text{m}$  were cut to 10 mm length on the average. For preparing the polymer concrete specimens, marble from a local company (GOSA, Atizapan, Mexico), as the fine aggregate, polypropylene fibers at concentrations of 0.1, 0.2, or 0.3% by volume, and a commercial unsaturated preaccelerated polyester resin (Polylite 32494-00, Reichhold, Atlacomulco, Mexico) were used. The proportion of the polyester resin in the PC was 30% by weight, and the PP fibers were distributed hazardingly within the polymer matrix.

Polymer concrete specimens were prepared to be subjected to three different irradiation doses. After mixing, the polymer concrete cubic specimens (5  $\times$  5  $\times$  5 cm) were placed in a controlled temperature room at  $23.0 \pm 3.0^\circ\text{C}$  for 24 hours. Polymer concrete specimens were prepared and subjected to three different irradiation doses (200, 250, and 300 kGy).

*2.2. Mechanical Tests.* Compressive tests of the polymer concrete specimens were carried out in an Universal Testing Machine model 70-S17C2 (Controls, Cernusco, Italy), located at Laboratory of Research and Development in Advanced Materials (LIDMA) of the Autonomous University of the State of Mexico (UAEM), according to the ASTM C-109M standard.

*2.3. Morphological Characterization.* First, the fibers were vacuum-coated with carbon (thickness between 3 to 10 nm) with the aid of a Vacuum Evaporator (E. F. Fullam) at 50 mTorr. Then, the fiber surfaces were analyzed by scanning electron microscopy (SEM) in a JEOL model JSM-6510LV microscope in the secondary-electron mode, at 20 keV.

*2.4. Irradiation Procedure.* Atactic PP fibers and the polymer concrete composites were exposed at various gamma radiation doses using a  $^{60}\text{Co}$  source. The fibers were placed in packets of 50 in a capillarity tube. The dosages were 200, 250, and 300 kGy at the dose rate of 3.5 kGy/h; the experiments were performed in air at room temperature. The irradiation was provided by a 651 PT Gammabeam Irradiator manufactured by NORDION (Chalk River, Ontario) and located at the Institute of Nuclear Sciences of the National Autonomous University of Mexico.

## 3. Results and Discussion

*3.1. Compressive Strength.* The PCs were fabricated containing different marble-particle sizes and different polypropylene-fiber concentrations. The selection of the particle sizes was in function of the availability of the commercial mesh (sieve), in our case 25, 14, and 8, which correspond to

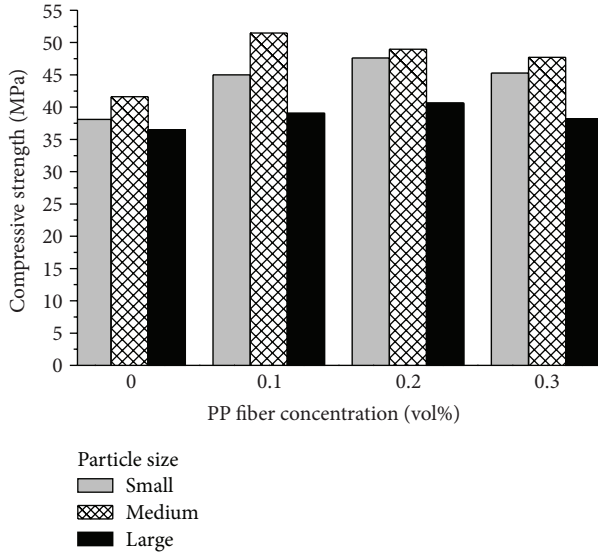


FIGURE 1: Compressive strength of polymer concrete with different marble particle sizes and fiber concentrations.

an average particle size of 0.71, 1.4, and 2.36 mm, respectively. Thus, we have approximately 1 : 2 : 3 as the ratio. Through the article we will use the terms small (S), medium (M) or large (L) size, for 0.71, 1.4 and 2.36 mm, respectively.

It can be seen in Figure 1 the compressive strength ( $\sigma_c$ ) values for PC elaborated with different particle sizes and polypropylene-fiber concentrations. The  $\sigma_c$  value is highest when using medium particle size and 0.1 vol% of polypropylene fibers, namely, 51 MPa. Conversely, the lowest value (36 MPa) is for those with large particle size and nonpolypropylene fibers.

For plain polymer concrete (without fibers), the  $\sigma_c$  values are in the range from 36 to 41 MPa, while for fiber-reinforced PCs from 38 to 51 MPa; thus, an improvement of 24% is obtained when using PP fibers. Moreover, a high-to-low sequence in the  $\sigma_c$  values for PC with respect to the particle size is as follows: (medium) > (small) > (large), independent of the fiber concentrations.

When comparing the present  $\sigma_c$  values with other PCs, we can see similar results. The  $\sigma_c$  values of the present communication are from 36 to 51 MPa; similar results were obtained as PC with silica sand (49 MPa) [17], but lower than for PC with  $\text{CaCO}_3$  (86 MPa) [18], or with silica sand +  $\text{CaCO}_3$  (106 MPa) [19].

The effect of the gamma irradiation is observed in Figure 2. The highest  $\sigma_c$  value is 70 MPa, that is, 58% of improvement in comparison with plain concrete. The present  $\sigma_c$  values are from 46 to 59 MPa.

According to the irradiation dose, different behaviors are well defined for the  $\sigma_c$  values: (a) the highest  $\sigma_c$  values are always obtained at 250 kGy, for all specimens, independent of the fiber concentration and particle size; (b) two well-defined stages are seen for each particle size; the first one consists of an increase of  $\sigma_c$  according to gamma radiation increase up to 250 kGy; then for higher dose the  $\sigma_c$  values decrease; an explanation for such behavior seems related to the radiation

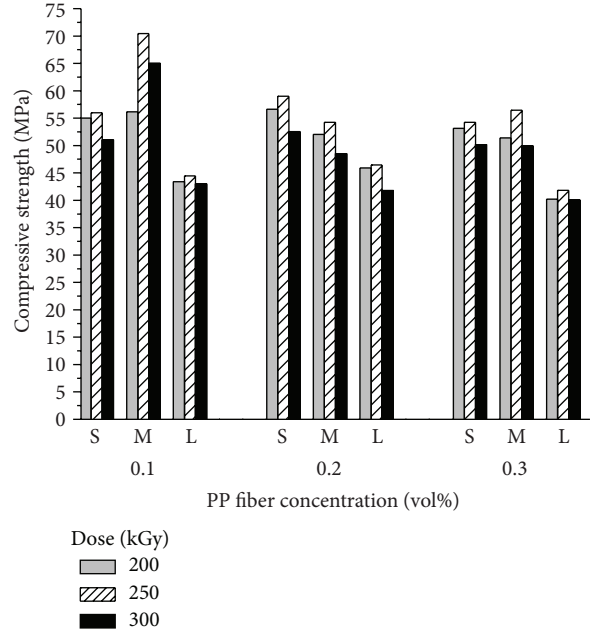


FIGURE 2: Compressive strength of irradiated-polymer concrete with different marble particle sizes and fiber concentrations.

effects on the polyester resin; as already noted, the irradiation causes chain scission, but it also produces some crosslinking, chain relaxation, and cage breaking [20, 21].

(c) The maximum values are achieved when using medium particle sizes, and a high-to-low sequence in the  $\sigma_c$  values with respect to the particle size is as follows: (medium) > (small) > (large), independent of the fiber concentrations except for PC with 0.2% of fibers, where (small) > (medium) > (large) sequence is established.

Small size marble particles provide more obstacles to crack propagation in a given amount of concrete. Apparently the use of large particle sizes causes detrimental results due to poor adhesion between the polyester resin and the marble particles. Our PC had 70 wt% of marble particles.

In the case of irradiated PCs, there are significant differences. The present  $\sigma_c$  values were from 40 to 70 MPa and lower than for PC with silica sand (62–86 MPa) [17], with silica sand +  $\text{CaCO}_3$  (104–112 MPa), [19] or with  $\text{CaCO}_3$  (126–135 MPa) [18].

Along these lines, the ionizing energy generates more contact points and in consequence larger contact areas between the components: fibers, polyester resin, and marble particles [19, 22]. In turn, an increased number of contact points in the concrete will resist larger loads oriented at various angles relative to the longitudinal axes of the fibers. Eventually, the concrete will split approximately parallel to the dominant axis of the fibers, and the resulting crack will propagate out to the surface. In other words, the energy transfer drops rapidly unless reinforcement is provided to restrain the opening of the splitting crack.

3.2. *Compressive Strain at Yield Point.* In Figure 3 compressive strain values at yield point are shown. For plain polymer

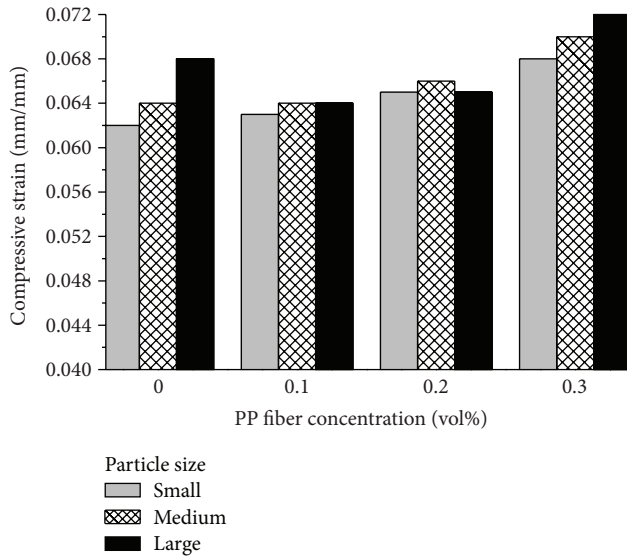


FIGURE 3: Compressive strain of polymer concrete with different marble particle sizes and fiber concentrations.

concrete the values vary from 0.062 to 0.068 mm/mm. The highest values are for PC with 0.3 vol% of fibers (0.068 to 0.073 mm/mm); this means a minimal 7% of difference with respect to polymer concrete without fiber.

The compressive strain increases as the fiber concentration increases. Moreover, the sequence of high-to-low values in terms of the particle sizes is: (large) > (medium) > (small), except for polymer concrete with 0.2 vol% of fibers.

Different behaviors of the compressive strain for irradiated-polymer concrete were observed in Figure 4. (a) the high-to-low sequence on the values in terms of the fiber concentration is (0.1% by volume) > (0.3% by volume) > (0.2% by volume). Thus, an optimal concentration is 0.1% by volume for getting a more ductile concrete and 0.2% by volume, for getting a hard concrete. (b) For all specimens the compressive strain increases when gamma radiation dose increases.

The highest value (0.076 mm/mm) was obtained for polymer concrete with medium particle size and irradiated at 300 kGy; this means 11% of improvement with respect to nonirradiated polymer concrete.

**3.3. Compressive Modulus of Elasticity.** The compressive modulus of elasticity  $E_c$  for nonirradiated PCs showed values ranging from 0.71 to 1.26 GPa (Figure 5). Such values exhibit the same behaviour for all specimens: the modulus diminishes as the particle sizes increase, following the sequence: (small) > (medium) > (large); thus a statement can be formulated: the compressive modulus decreases when increasing the particle size. Apparently small particles—while providing good protection against crack propagation—provide more reinforcement than the medium or large ones.

A maximum for PC with small particles size and 0.1 vol% of PP fibers was identified, namely, 1.26 GPa; conversely a minimal value was obtained for PC with large particle size and 0.3 vol% of fibers (0.71 GPa).

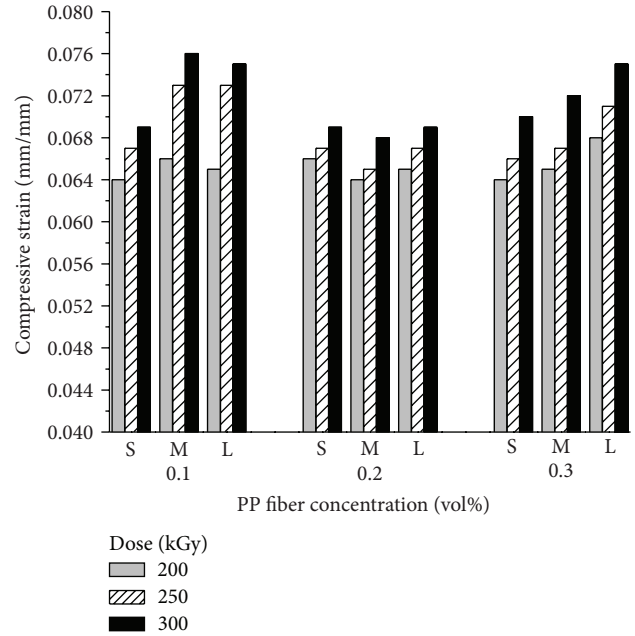


FIGURE 4: Compressive strain of irradiated-polymer concrete with different marble particle sizes and fiber concentrations.

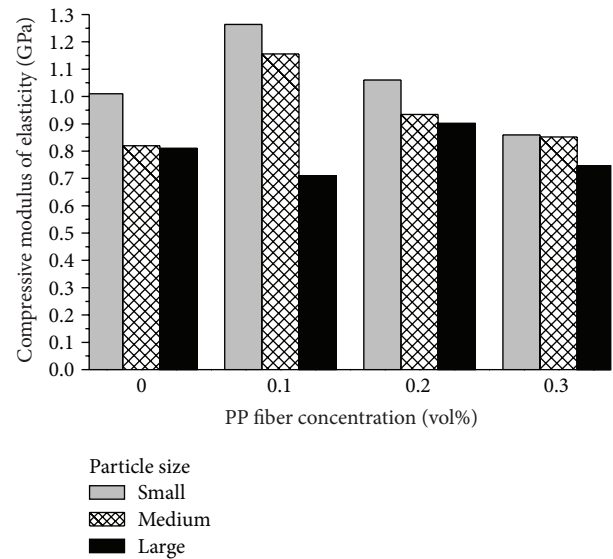


FIGURE 5: Compressive modulus of elasticity of polymer concrete with different marble particle sizes and fiber concentrations.

When comparing the  $E_c$  values for nonirradiated PCs with other PCs elaborated with different mineral aggregates, it was observed that the present value 1.88 GPa is lower than for PC with silica sand +  $\text{CaCO}_3$  (5.2 GPa) [19], or silica sand + polypropylene fibers (5.7 GPa) [23], or PC with marble + calcium bentonite (6.8 GPa) [22], or for PC with silica sand (7.3 GPa) [17], or PC with  $\text{CaCO}_3$  (7.6 GPa) [18].

In the case of  $E_c$  values for irradiated PCs, several behaviors were observed. The present values are in the range from 0.99 to 1.88 GPa (Figure 6); it means 49% of improvement

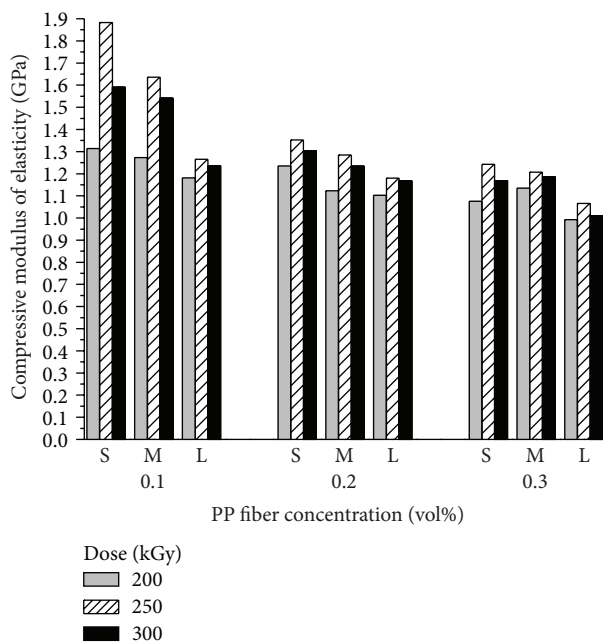


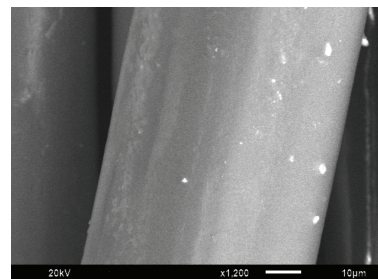
FIGURE 6: Compressive modulus of elasticity of irradiated-polymer concrete with different marble particle sizes and fiber concentrations.

with respect to  $E_c$  values of nonirradiated PCs. In terms of PP fiber concentration, higher values were observed when adding 0.1 vol% of fibers and lower values when adding 0.3 vol% of fibers. Thus, the values follow the sequence: (0.1 vol%) > (0.2 vol%) > (0.3 vol%), and it is established that the compressive modulus decreases when increasing the PP fiber concentration.

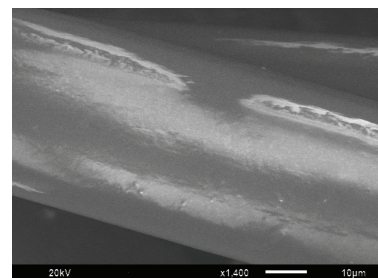
With respect to particles size, the  $E_c$  values follow the rule: when increasing the particle size, the compressive modulus diminishes; same behavior was observed for nonirradiated PCs. Finally, following the radiation dose, for each particle size a premise is observed: the  $E_c$  values show two well-defined stages; the Young modulus increases when the radiation dose increases up to 250 kGy, and after this dose the Young modulus decreases. At 250 kGy the highest value is obtained.

When comparing with another  $E_c$  reported in the literature, the highest  $E_c$  value (1.88 GPa) is lower than for PC with two mineral aggregates of marble + calcium bentonite (6.3 GPa) [22], or for PC with silica sand +  $\text{CaCO}_3$  (8.0 GPa) [19], or for PC with silica sand + polypropylene fibers (9.6 GPa) [23], including PCs with one aggregate: silica sand (16.3 GPa) [17] or with  $\text{CaCO}_3$  (16.1 GPa) [18].

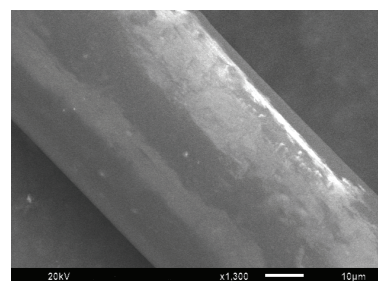
As it was studied the compressive strength and strain as well as compressive modulus depend on: particle size, PP fiber concentration, and gamma dose. The last one involves the modifications of the surface morphology caused by radiation on the polypropylene fibers. SEM images for irradiated fibers at 200, 250, and 300 kGy are shown in Figure 7. Small pieces of scrap of material and well-defined lines at irradiation dose of 200 kGy (Figure 7(a)) can be seen. When increasing the radiation dose at 250 kGy, roughness



(a)



(b)



(c)

FIGURE 7: SEM images of irradiated polypropylene fibers at (a) 200 kGy, (b) 250 kGy, and (c) 300 kGy.

and deteriorated regions are observed (Figure 7(b)). Such deteriorated regions increase at 300 kGy dose, and more small particles are formed on the surface.

## 4. Conclusions

As expected, mechanical behavior depends on the combination of polypropylene fiber concentration and the applied radiation dose. Compressive strength values are higher for polymer concrete with medium particle sizes and irradiated at 250 kGy and the lowest elasticity modulus with large particle sizes. Such last behavior suggests generation of a ductile material. Moreover, depending on the latter combination of particle sizes, the polymer concrete needs low or high radiation doses to obtain high deformability with moderate compressive strength.

## Conflict of Interests

The authors declare that none of them have a direct financial relationship with the commercial trademarks mentioned in

this paper (CONSA, Controls, and GOSA) that might lead to a conflict of interests for any of the authors.

## Acknowledgments

Financial support of the Autonomous University of the State of Mexico (UAEM) by Grant UAEM 9017/2013 CAFF and help of Mr. Francisco García Flores for the sample irradiation performed at the Institute of Nuclear Sciences of the National Autonomous University of Mexico (UNAM) are acknowledged.

## References

- [1] J. M. Laredo Dos Reis, "Mechanical characterization of fiber reinforced Polymer Concrete," *Materials Research*, vol. 8, no. 3, pp. 357–360, 2005.
- [2] D. Van Gemert, L. Czarnecki, M. Maultzsch et al., "Cement concrete and concrete-polymer composites: two merging worlds: a report from 11th ICPIC Congress in Berlin, 2004," *Cement & Concrete Composites*, vol. 27, no. 9-10, pp. 926–933, 2005.
- [3] L. Czarnecki, "Concrete-polymer composites: trends shaping and future," *International Journal of the Society of Materials Engineering for Resources*, vol. 15, no. 1, pp. 1–5, 2007.
- [4] J. M. L. dos Reis, "Effect of textile waste on the mechanical properties of polymer concrete," *Materials Research*, vol. 12, no. 1, pp. 63–67, 2009.
- [5] A. J. M. Ferreira, C. Tavares, and C. Ribeiro, "Flexural properties of polyester resin concretes," *Journal of Polymer Engineering*, vol. 20, no. 6, pp. 459–468, 2000.
- [6] O. Gencil, W. Brostow, G. Martínez-Barrera, and M. S. Gok, "Mechanical properties of polymer concretes containing different amount of hematite or colemanite," *Polimery*, vol. 57, no. 4, pp. 276–283, 2012.
- [7] O. Gencil, C. Ozel, F. Koksall, E. Erdogmus, G. Martínez-Barrera, and W. Brostow, "Properties of concrete paving blocks made with waste marble," *Journal of Cleaner Production*, vol. 21, no. 1, pp. 62–70, 2012.
- [8] C. Vipulanandan and S. Mebarkia, "Flexural strength, toughness, and fracture properties of polyester composites," *Journal of Applied Polymer Science*, vol. 50, no. 7, pp. 1159–1168, 1993.
- [9] J. M. L. Reis and A. J. M. Ferreira, "A contribution to the study of the fracture energy of polymer concrete and fibre reinforced polymer concrete," *Polymer Testing*, vol. 23, no. 4, pp. 437–440, 2004.
- [10] N. Dharmarajan and C. Vipulanandan, "Fracture toughness of particle filled fiber reinforced polyester composites," *Journal of Applied Polymer Science*, vol. 42, no. 3, pp. 601–607, 1991.
- [11] O. Gencil, C. Ozel, W. Brostow, and G. Martínez-Barrera, "Mechanical properties of self-compacting concrete reinforced with polypropylene fibres," *Materials Research Innovations*, vol. 15, no. 3, pp. 216–225, 2011.
- [12] Z. Ajji, "Preparation of polyester/gypsum/composite using gamma radiation, and its radiation stability," *Radiation Physics and Chemistry*, vol. 73, no. 3, pp. 183–187, 2005.
- [13] T. Jurkin and I. Pucic, "Post-irradiation crosslinking of partially cured unsaturated polyester resin," *Radiation Physics and Chemistry*, vol. 75, no. 9, pp. 1060–1068, 2006.
- [14] G. Martínez-Barrera and W. Brostow, "Fiber-reinforced polymer concrete: property improvement by gamma irradiation," in *Gamma Radiation Effects on Polymeric Materials and Its Applications*, C. Barrera-Díaz and G. Martínez-Barrera, Eds., pp. 27–44, Research Signpost, Kerala, India, 2009.
- [15] G. Martínez-Barrera, C. Menchaca Campos, and F. Ureña-Nuñez, "Gamma radiation as a novel technology for development of new generation concrete," in *Gamma Radiation*, F. Adrovic, Ed., pp. 91–114, InTech, Rijeka, Croatia, 2012.
- [16] M. Levitt, D. J. McGahan, and P. R. Hills, "Comparison of concrete polymer composites produced by high energy radiation," *Journal of the Precast/Prestressed Concrete Institute*, vol. 18, no. 3, pp. 35–41, 1973.
- [17] G. Martínez-Barrera, U. Texcalpa-Villarruel, E. Viguera-Santiago, S. Hernández-López, and W. Brostow, "Compressive strength of Gamma-irradiated polymer concrete," *Polymer Composites*, vol. 29, pp. 1210–1217, 2008.
- [18] G. Martínez-Barrera, M. E. Espinosa-Pesqueira, and W. Brostow, "Concrete + polyester + CaCO<sub>3</sub>: mechanics and morphology after gamma irradiation," *e-Polymers*, Article ID 083, 2007.
- [19] E. A. Bobadilla-Sánchez, G. Martínez-Barrera, W. Brostow, and T. Datashvili, "Effects of polyester fibers and gamma irradiation on mechanical properties of polymer concrete containing CaCO<sub>3</sub> and silica sand," *Express Polymer Letters*, vol. 3, no. 10, pp. 615–620, 2009.
- [20] T. Nishiura, S. Nishijima, and T. Okada, "Creep behavior of epoxy resin during irradiation at cryogenic temperature," *Radiation Physics and Chemistry*, vol. 56, no. 5-6, pp. 605–609, 1999.
- [21] I. Pucic and F. Ranogajec, "Phase separation during radiation crosslinking of unsaturated polyester resin," *Radiation Physics and Chemistry*, vol. 67, no. 3-4, pp. 415–419, 2003.
- [22] G. Martínez-Barrera, L. F. Giraldo, B. L. López, and W. Brostow, "Effects of  $\gamma$  radiation on fiber-reinforced polymer concrete," *Polymer Composites*, vol. 29, no. 11, pp. 1244–1251, 2008.
- [23] G. Martínez-Barrera, A. L. Martínez-Hernández, C. Velasco-Santos, and W. Brostow, "Polymer concretes improved by fiber reinforcement and gamma irradiation," *e-Polymers*, vol. 103, pp. 1–14, 2009.

## Research Article

# Electrochemical Evaluation of a Recycled Copolymer Coating for Cultural Heritage Conservation Purposes

**Marco Hernández-Escampa,<sup>1</sup> Fausto Rodríguez-Acuña,<sup>2</sup>  
Franco Millán-Cruz,<sup>3</sup> Pilar Rodríguez-Rojas,<sup>3</sup> Miguel Hernández-Gallegos,<sup>1</sup>  
Alba Covelo,<sup>2</sup> Carmina Menchaca-Campos,<sup>3</sup> and Jorge Uruchurtu<sup>3</sup>**

<sup>1</sup> *Facultad de Ingeniería, Universidad Nacional Autónoma de México, Circuito Exterior s/n Ciudad Universitaria, 04510 Mexico, DF, Mexico*

<sup>2</sup> *Facultad de Química, Universidad Nacional Autónoma de México, Circuito Exterior s/n Ciudad Universitaria, 04510 Mexico, DF, Mexico*

<sup>3</sup> *CIICAp, Universidad Autónoma del Estado de Morelos, Avenida Universidad 1001, Col. Chamilpa, 62209 Cuernavaca, MOR, Mexico*

Correspondence should be addressed to Fausto Rodríguez-Acuña; [faustic99@yahoo.com](mailto:faustic99@yahoo.com)

Received 28 March 2013; Revised 19 June 2013; Accepted 25 June 2013

Academic Editor: Enrique Viguera Santiago

Copyright © 2013 Marco Hernández-Escampa et al. This is an open access article distributed under the Creative Commons Attribution License, which permits unrestricted use, distribution, and reproduction in any medium, provided the original work is properly cited.

Acrylonitrile-butadiene-styrene (ABS) is a well-known discard product from the industry. This copolymer can be dissolved in organic solvents, and thin films can be created by immersion. Two requirements for coatings used for cultural heritage conservation purposes are transparency and reversibility, both fulfilled by ABS films. The aim of this work was to characterize the copolymer and to evaluate the electrochemical properties of ABS coatings applied to copper. Such performance was compared to that of a commercial varnish commonly used in conservation. The results indicate high protection values of the ABS film, generating a potential application for this waste material. The electrochemical techniques included electrochemical noise, impedance spectroscopy, and potentiodynamic polarization.

## 1. Introduction

Cultural heritage conservation constitutes a relevant field of research which frequently relies on material science to solve the challenges posed by the degradation of artifacts, architectural structures, and ornaments [1–5]. Historic, artistic, and archaeological items are frequently built of metals. Through the ages, copper and its alloys constitute a particular set of metals widely used in such manufactures [6]. Even when these materials tend to form protective patinas due to their interactions with the environment, such natural protective layers may fail, especially in highly polluted atmospheres [7]. Therefore, the application of coatings to both clean and patina covered metallic surfaces has proved to be useful to preserve cultural heritage [8]. Two highly desirable conditions of

conservation-oriented coatings are transparency in order not to affect the aesthetical traits of the artifacts and reversibility, which refers to an easy removal process [9].

On the other hand, acrylonitrile-butadiene-styrene (ABS) waste and residues represent a well-known discard product from the automotive industry. Since law usually forbids the recycling of this material because all pieces must be brand new, considerable amounts of ABS become unused waste and a nuisance to dispose due to environmental restrictions. Therefore, research has been done trying to find usable recycling applications with added value to this and other polymer discards. Due to the finite reserve of hydrocarbon in the world, a proposal has been obtaining degradation oils from plastics, potentially useful as fuel [10]. However, such processes cannot avoid the presence

of heteroatoms such as chlorine from poly(vinyl chloride) (PVC) or nitrogen from ABS. These heteroatoms relate to corrosion of machinery parts and participate in the formation of dangerous compounds such as cyanic products, SO<sub>x</sub> or NO<sub>x</sub>, in the combustion process [11, 12].

The mechanical and chemical properties of ABS have been studied demonstrating its durability, elongation to break, and impact resistance. However, thermooxidative processes can degrade this polymer due to hydrogen abstraction by oxygen [13]. Two models explain the ABS degradation: heat aging or physical aging [14–17]. It is well known that this polymer can be dissolved in organic solvents; also, thin layers become practically transparent. Therefore, an ABS coating potentially fulfills some of the major requirements for coatings used in cultural heritage conservation. Hence, a combination of adequate properties and ecological values due to waste recycling might be implied in the utilization of this coating for the stated purpose.

The aim of this work was to evaluate the protective properties of recycled ABS applied to copper surfaces, compared to the behavior of an aliphatic commonly used commercial coating, for conservation purposes. In order to achieve this goal, an experimental procedure was designed which allowed to (1) create coatings recurring to the dissolution properties of ABS in acetone and (2) simulate the degradation of the coatings in highly corrosive ambient. The techniques used included electrochemical noise, impedance spectroscopy, and potentiodynamic polarization. The obtained results constitute a potential contribution to the cultural heritage conservation field because an alternate coating for copper substrates is proposed. Copper and its alloys are found in a vast array of archaeological and historical artifacts around the world.

## 2. Materials and Methods

**2.1. Coating Preparation.** The ABS wastes were cut into small pieces, and afterwards 60 grams of this polymer was added to 1 liter of acetone under constant stirring for 10 minutes at room temperature. This way, the obtained solution is ready for the metal samples to be coated (ABS coating) by immersion.

**2.2. Polymer Characterization.** The recycled ABS was characterized in two states: in raw form and in solution as mentioned previously.

**Thermal Analysis.** Thermal analysis were carried out in a Perkin Elmer Thermal Analyzer TGA/DTA, from 30 to 500°C, with a heating rate of 20°C/min, in normal atmosphere, using aluminum disposable holders. The samples were cut into small pieces and placed into the holder.

**Infrared Spectroscopy.** To evaluate the ABS structure, Fourier Transformed Infrared Spectroscopy (FTIR) was used. Infrared analysis is an extremely reliable and well-recognized fingerprinting method. A Perkin Elmer Fourier Transformed Infrared Spectroscopy (FTIR) with Attenuated Total Reflectance (ATR) accessory was used.

**2.3. Coating Thickness Measurements.** Metallic plates were immersed, one (ABS-1), two (ABS-2), and three (ABS-3), for 30 seconds per immersion in the ABS solution. Scanning electronic microscope (SEM) LEO 1450VP was used to determine the thickness of the coatings for each case. Samples were attached with carbon sticky tape to the microscope holders and covered with a thin layer of Au/Pd to prevent electrostatic charge accumulation. The images were observed at 15 kV and secondary electrons emission.

**2.4. Electrochemical Evaluation.** Commercial copper coupons with an exposed area of 1.1 cm<sup>2</sup> were embedded in acrylic resin. The coupons were polished with 600, 800, and 1200 emery paper. Afterwards, the metal samples were immersed in the coating solution for 30 seconds and then removed, to allow the solvent to evaporate. The samples were placed in a desiccator for 24 hours to be ready for testing.

A first group of samples was used as blank to evaluate the electrochemical properties of the base material in two different solutions. The first solution, Na<sub>2</sub>SO<sub>4</sub> 0.1 M, is mildly aggressive while the second one, Na<sub>2</sub>SO<sub>4</sub> 0.1 M + 3% weight NaCl, presents highly corrosive properties and simulates an aggressive urban-marine atmosphere. As reference, a second group of coupons was coated with commercial aliphatic polyurethane (varnish). The application consisted of a single layer using a small brush, simulating the manual procedure frequent in conservation. These coupons were evaluated electrochemically as a function of time, for two weeks, immersed in the highly corrosive solution.

A third group of coupons was coated by immersion in the ABS solution (ABS-1, ABS-2, and ABS-3). Electrochemical evaluation in the highly aggressive solution was performed for the three ABS coatings for comparative purposes. Coupons with three immersion cycles were evaluated electrochemically as a function of time for two weeks.

All electrochemical evaluations performed in this work included electrochemical noise measurement, impedance spectroscopy, and potentiodynamic polarization. All measurements reported were made using a three-electrode arrangement, and potentials were quoted versus silver/silver chloride reference electrode. Electrochemical values are all corrected for the area of the working electrode.

**2.4.1. Electrochemical Noise Measurement.** The experimental setup used for electrochemical noise data recording consists of a working electrode, the tip of a platinum wire, and the reference electrode. The potential and current electrochemical noise oscillations were obtained simultaneously at a sampling rate of 1 point per second for 2048 seconds in each test, using an auto-ZRA ACM instrument connected to a personal computer. Removal of the DC trend from the raw noise data was the first step in the noise analysis. To accomplish this, a least squares fitting was used. The DC trend had to be eliminated because this could originate large distortions in subsequent statistical noise data processing [18].

The noise resistance ( $R_{\text{noise}}$ ) was obtained by statistical analysis of voltage and current noise records as follows:

$$R_{\text{noise}} = \frac{\sigma [V (\Delta t)]}{\sigma [i (\Delta t)]}, \quad (1)$$

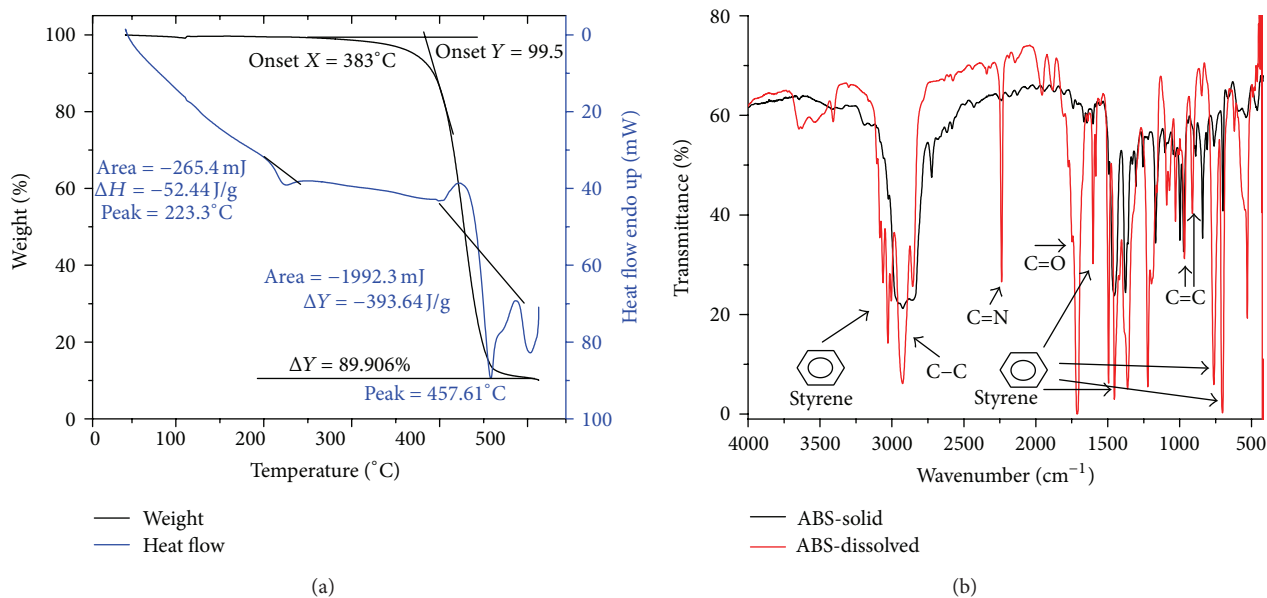


FIGURE 1: ABS characterization: (a) thermal analysis and (b) infrared spectroscopy.

where  $\sigma[V(\Delta t)]$  is the standard deviation of voltage noise in time interval  $\Delta t$  and  $\sigma[i(\Delta t)]$  is the standard deviation of current noise in the same time interval  $\Delta t$ . The noise resistance was presented and obtained as a function of time. These measurements were performed to evaluate the protective properties of the coupons polymeric coating and its evolution in time.

**2.4.2. Electrochemical Impedance Spectroscopy.** The electrochemical impedance spectroscopy (EIS) used a sine wave. Classical three-electrode arrangement experimental set-up was used for EIS tests. The electrochemical signals were monitored by AC Gill potentiostat connected to a personal computer. The equipment was previously calibrated in accordance with the standard [19]. An alternating current (AC) signal, with a 10 mV amplitude signal, was applied in the frequency range of 100 mHz to 10 kHz. A silver/silver chloride electrode connected through a lugging probe was used as a reference electrode and graphite as counter electrode. These measurements were performed in the described times to evaluate different protective measurements and their evolution in time.

**2.4.3. Potentiodynamic Polarization.** Electrochemical polarization curve measurements were made with a scan rate of 60 mV/min. Coupons were immersed in the unstirred solutions. The stabilization period before polarization was 10 minutes. The cathodic branch was performed  $-1000$  mV from the rest potential and the anodic branch went up to 2000 mV from that same rest potential.

### 3. Results and Discussion

**3.1. Polymer Characterization.** Figure 1(a) shows the TGA/DTA measurement results for recycling ABS, as it is discarded. The TG curve shows one stage weight decrease

between 300 and 500°C, due to thermal decomposition with the onset in 400°C, remaining just 10% at 500°C, which corresponds to additives, fillers, and other aggregates present in the copolymer because of the application for which it was tailored. At the same time, the DT curve shows two main peaks, a small one around 220°C due to melting of the elastic butadiene and a bigger one that initiates at 420°C corresponding to the ABS decomposition.

The IR spectra of ABS in raw and in solution are shown in Figure 1(b). Both present characteristic peaks of the three main components, but in solution they are clearly seen: the nitrile band of acrylonitrile at 2237  $\text{cm}^{-1}$ , the aromatic ring of styrene at 1602, 1494, 761, and 699  $\text{cm}^{-1}$  [20–22], and the double bond of butadiene at 967  $\text{cm}^{-1}$  trans and 911  $\text{cm}^{-1}$  vinyl. The rest of nonidentified peaks in the spectra correspond to acetone major absorptions.

**3.2. Coating Thickness Measurements.** Figure 2(a) presents the coating thickness after one immersion with an interval between 14 and 22  $\mu\text{m}$ , looking not very compact and disbanded. After the first immersion, the procedure was repeated twice for 30 s (Figures 2(b) and 2(c)). The coating looks compact but maintains a thickness around 13 to 16  $\mu\text{m}$ . These results suggest that immersion cycles did not increase the coating thickness, but rather pores present after the first immersion are sealed and the compactness was improved (see Figure 2). Also during the second and third immersions, the ABS solution promotes partial removal of the top of the coating due to the action of the solvent.

**3.3. Electrochemical Evaluation.** Figure 3 shows the polarization curves of the copper coupons used as blank in  $\text{Na}_2\text{SO}_4$  0.1M and  $\text{Na}_2\text{SO}_4$  0.1M + 3% weight NaCl solutions. It also includes the curve corresponding to the varnish coated coupons in the aggressive solution. The corrosion rates of

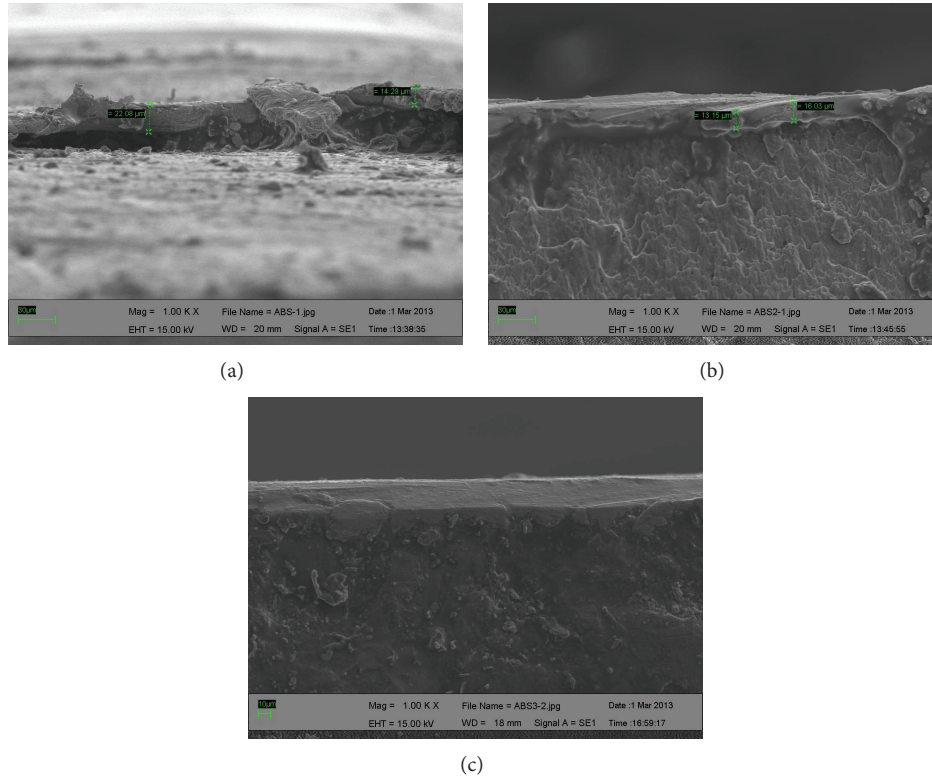


FIGURE 2: Coating thickness measurement by SEM: (a) ABS-1, (b) ABS-2, and (c) ABS-3.

copper increase two orders of magnitude in comparison to the mild solution. In contrast, the copper coated with varnish decreases the corrosion rates as much as three orders of magnitude compared to the uncoated copper in the aggressive solution, demonstrating the protectiveness of the coating. The performance of the varnish was considered as reference to compare the protectiveness of the polymer coating under evaluation.

Figure 4 shows the polarization curves of the varnish coated coupons in aggressive solution for different times of immersion (0 hours up to two weeks). As time elapses, the corrosion rates increase suggesting the degradation of the coating. This is coherent with the presence of passivation zones after 24 to 48 hours due to the oxidation of the base material as the solution reaches it through the coating pores or cracks.

Figure 5 presents the electrochemical noise and impedance measurements for the varnish coated copper coupons. The Bode impedance diagrams show that the total impedance values decrease in time, although there is an increment after two weeks which once again can be related to the corrosion products formed as the coating deteriorates. Such oxidation can start as early as 24 to 48 hours according to the polarization curves. The electrochemical noise resistance values show similar behavior to the impedance measurements, although an increase can be seen since week one. Therefore, the results of the three electrochemical

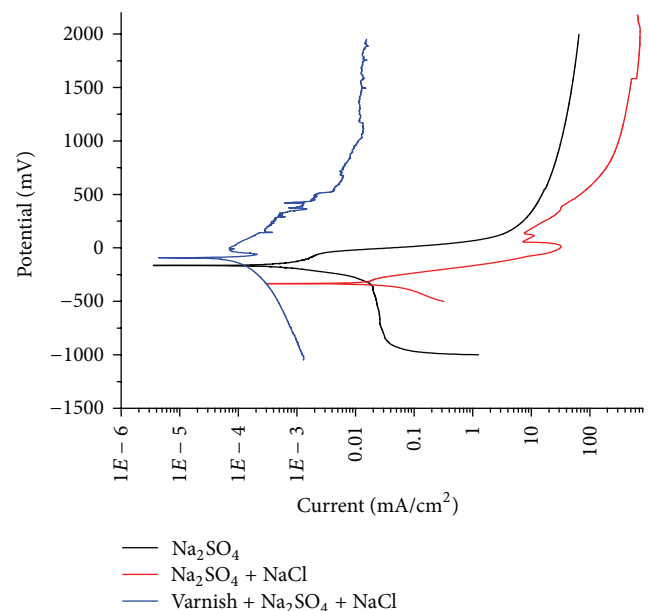


FIGURE 3: Polarization curves of blanks. Copper in  $\text{Na}_2\text{SO}_4$  solution, copper in  $\text{Na}_2\text{SO}_4 + 3 \text{ wt}\% \text{ NaCl}$  solution, copper coated with varnish in  $\text{Na}_2\text{SO}_4 + 3 \text{ wt}\% \text{ NaCl}$  solution.

techniques are coherent to each other since they show similar trends.

TABLE 1: Values of the equivalent circuits for the ABS-3 copper coupons in  $\text{Na}_2\text{SO}_4 + 3 \text{ wt\% NaCl}$  solution in time.

ABS-3	Rsol. (ohm $\text{cm}^2$ )	Rpo (ohm $\text{cm}^2$ )	Cc (F)	Dep angle	Rcor (ohm $\text{cm}^2$ )	Ccor (F)	Dep angle
0 h	52	$6.32E5$	$1.13E-9$	11.89	$1.13E6$	$1.32E-6$	64.78
24 h	50	$1.41E5$	$1.65E-8$	40.86	$2.60E5$	$1.60E-5$	71.51
48 h	53	$1.48E4$	$8.53E-5$	29.73	$2.21E4$	$9.60E-5$	32.27
1 w	51	$2.23E3$	$2.92E-9$	7.03	$6.42E3$	$2.60E-5$	41.74
2 w	50	$2.03E4$	$9.29E-5$	48.81	$2.61E4$	$1.25E-4$	38.47

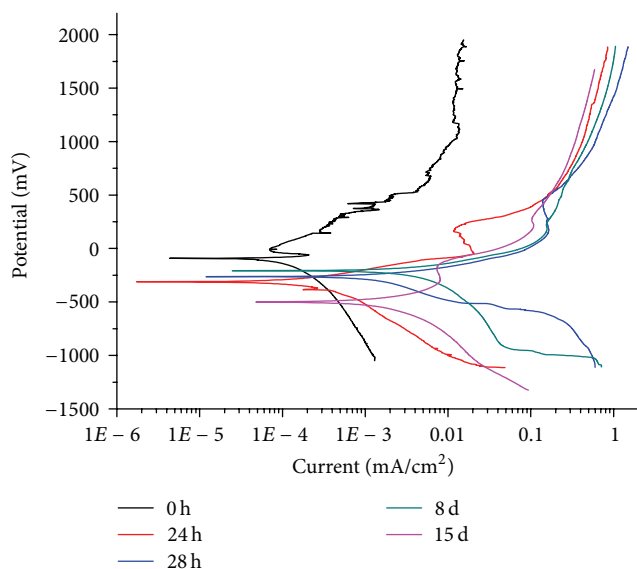
FIGURE 4: Polarization curves of copper coated with varnish in  $\text{Na}_2\text{SO}_4 + \text{NaCl}$  solution, as a function of time.

Figure 6 shows the Bode diagrams for each of the three cases: ABS-1, ABS-2, and ABS-3. Even when no significant increase of thickness was achieved with the consecutive immersions, the total impedance increased as a function of the number of immersion. This can be related to the fact that each immersion sealed the pores of the polymer layer. The total impedance values of the ABS-3 coupons reached similar values compared to the varnish coated coupons.

Figure 7 shows the polarization curves of the ABS-3 copper coupons. In the initial time there is well-defined passivation zone suggesting corrosion processes in the surface of the base material. As time elapses, the passivation zones tend to diminish and the corrosion rates increase as the coating deteriorates. Corrosion potentials become more negative in time indicating surface activation of the metal.

Figure 8 presents the impedance and electrochemical noise measurements in time for the ABS-3 copper coupons. The Bode impedance diagrams show that the total impedance values decrease in time without any increment as observed in the case of the varnish. The electrochemical noise resistance values also show a general decrease, compared with the initial

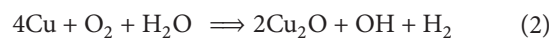
time of immersion. However, there is an increase in noise resistance values after one week. This behavior is similar to the one observed for the varnish.

Figure 9 shows the equivalent electric circuit for the corrosion process in the evaluated system. The values of the corresponding elements of the circuit are presented in Table 1. The electrochemical impedance simulation results obtained and presented reflect the coating degradation process occurring in the electrolyte as a function of time of immersion.

Figure 10 compares the total impedance ( $Z_t$ ) and noise resistance ( $R_n$ ) values in time for both the varnish and ABS-3 copper coupons. In both cases, the behavior decreases as time goes by and the coatings deteriorate. The resulting values are very similar in magnitude compared to each other, and hence it is possible to suggest that the protective performance of the coatings is comparable. In the case of  $Z_t$ , the ABS coating stays with higher protective values during a considerable time.  $R_n$  values indicate a similar behavior, even when initially, the protection of the ABS coating is slightly below in relation to the performance of the varnish. At some point in time, the parameter values are inverted and both coatings reach very similar values. With the noise resistance being independent of the frequency, the values obtained and presented in the noise impedance spectra are related totally to the coating performance [23].

Figure 11 compares the macroscopic aspect of coupons coated with varnish and ABS-3 after two weeks in the aggressive solution. The coupon protected with varnish shows blue-green corrosion products while the one coated with ABS-3 stayed in the copper color range. This suggests that the pores and/or failures in the varnish allow diffusion of bigger ions in solution such as sulfates reaching the metallic surface, which combined with chloride and oxygen may form  $\text{CuSO}_4$ , as compared to those in the ABS coating. In the latter, probably smaller pores allow diffusion only of oxygen, generating a highly adherent and protective copper oxide ( $\text{Cu}_2\text{O}$  and  $\text{CuO}$ ) patina whose properties combine with those of the ABS-3 coating. Also, the difference observed in both samples corroborates the suggestion made as to the immersion cycles and pore sealing presented and discussed in Figure 2.

Atmospheric corrosion of copper reaction is [24]



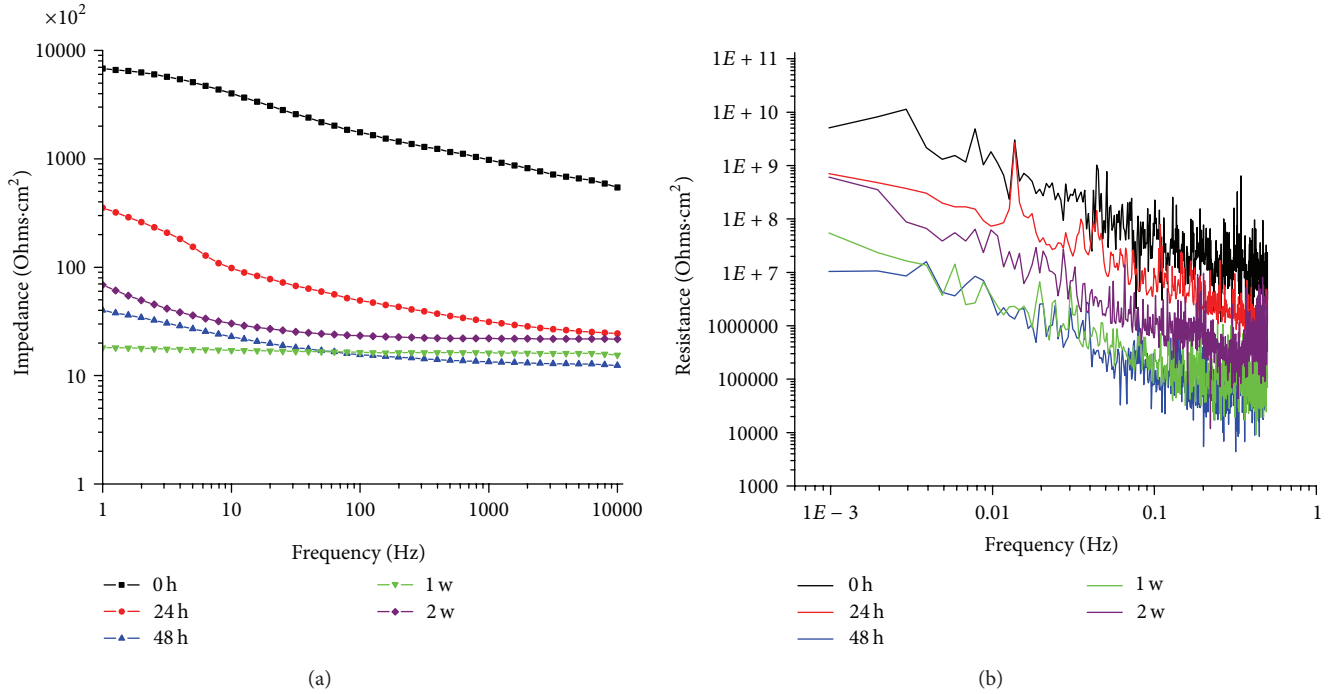


FIGURE 5: Copper coated with varnish in  $\text{Na}_2\text{SO}_4 + 3 \text{ wt}\% \text{ NaCl}$  solution in time: (a) Bode impedance diagrams and (b) electrochemical resistance noise.

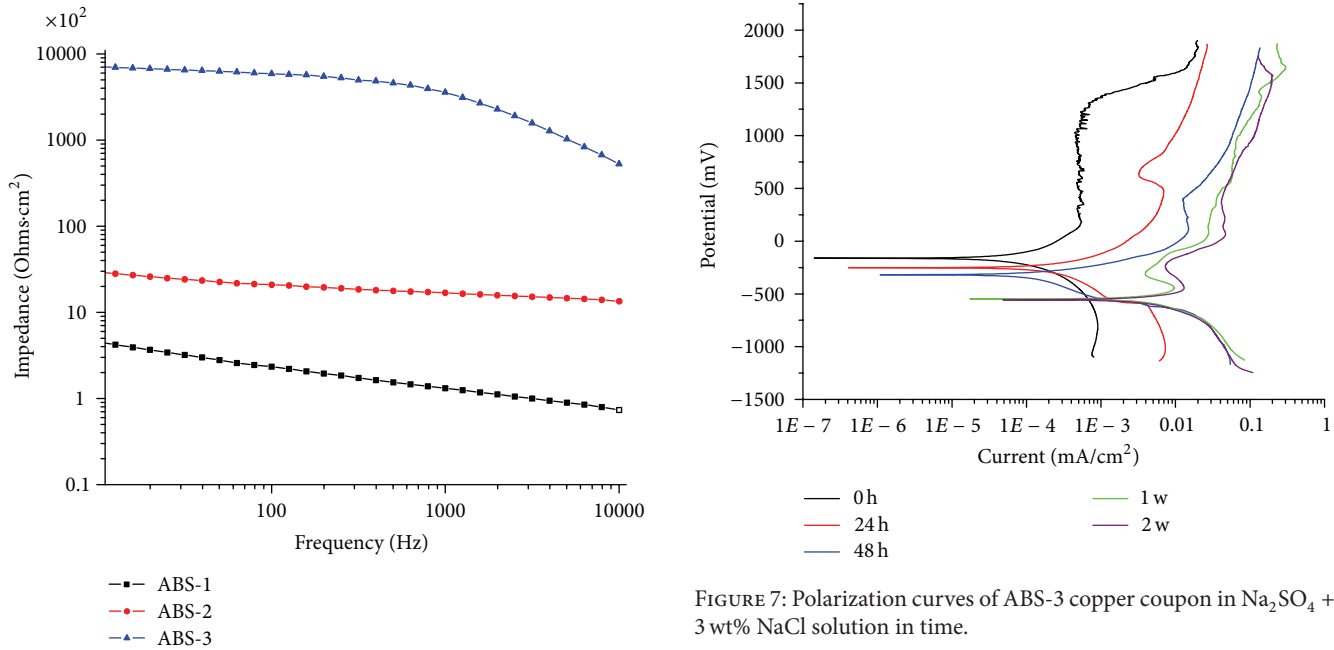
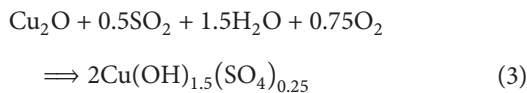


FIGURE 6: Bode impedance diagrams of ABS-3 copper coated in  $\text{Na}_2\text{SO}_4 + 3 \text{ wt}\% \text{ NaCl}$  solution.

FIGURE 7: Polarization curves of ABS-3 copper coupon in  $\text{Na}_2\text{SO}_4 + 3 \text{ wt}\% \text{ NaCl}$  solution in time.

under polluted conditions



Corrosion of copper and its alloys forms complex patinas over the surface, being more or less protective depending upon the environmental conditions and the nature of the pollutants present. In the atmosphere the range of corrosion rates is in the order of less than  $0.1 \mu\text{m}/\text{year}$  for rural atmospheres up to approximately  $5.6 \mu\text{m}/\text{year}$  for industrial-marine environments [24, 25]. Electrochemical measurements immersed in neutral solution on samples with patinas formed after long exposures under different atmospheres

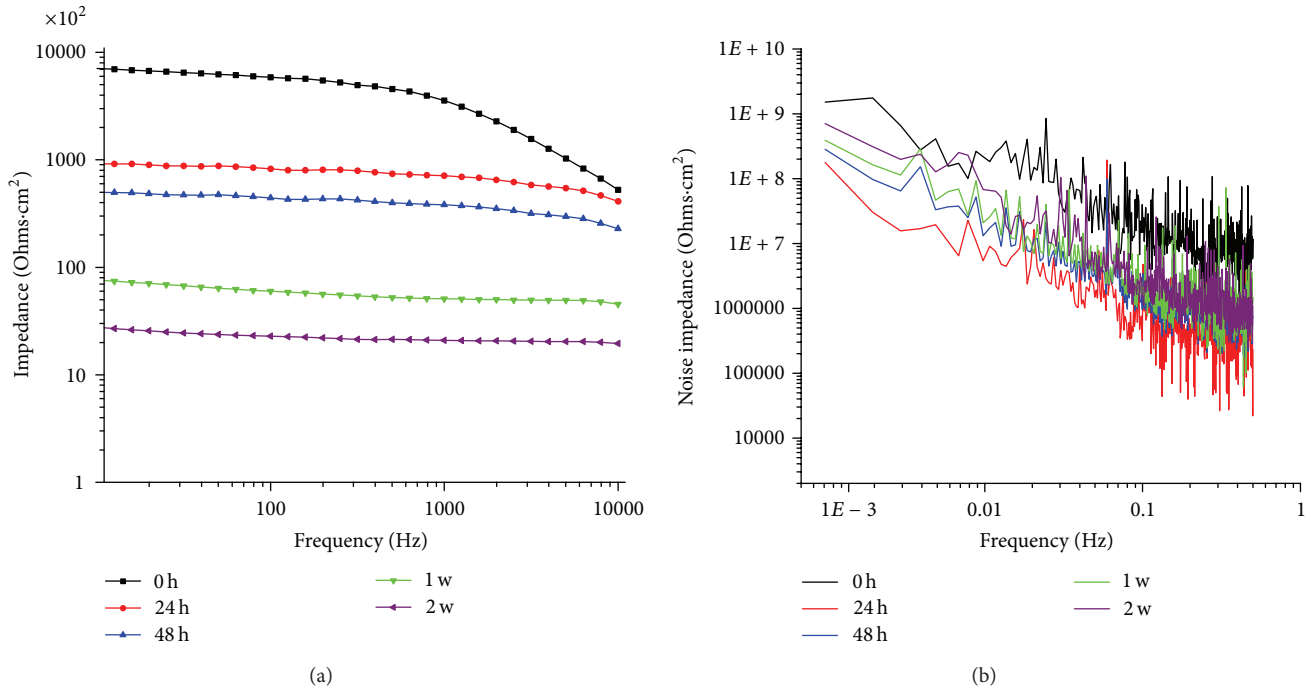


FIGURE 8: ABS-3 copper coupons in Na<sub>2</sub>SO<sub>4</sub> + 3 wt% NaCl solution in time: (a) Bode impedance diagrams and, (b) electrochemical resistance noise.

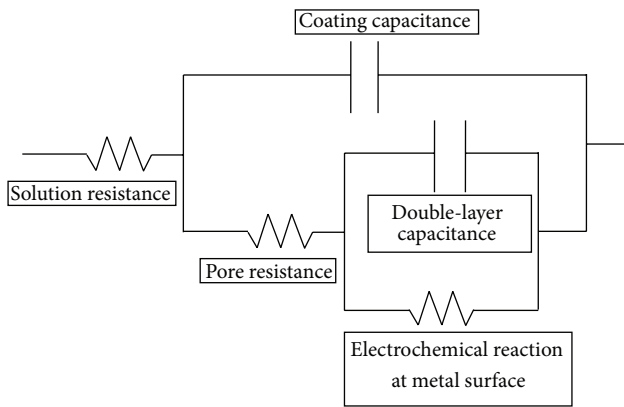


FIGURE 9: Equivalent circuit for the ABS-3 copper coupons in Na<sub>2</sub>SO<sub>4</sub> + 3 wt% NaCl solution obtained by the electrochemical impedance technique.

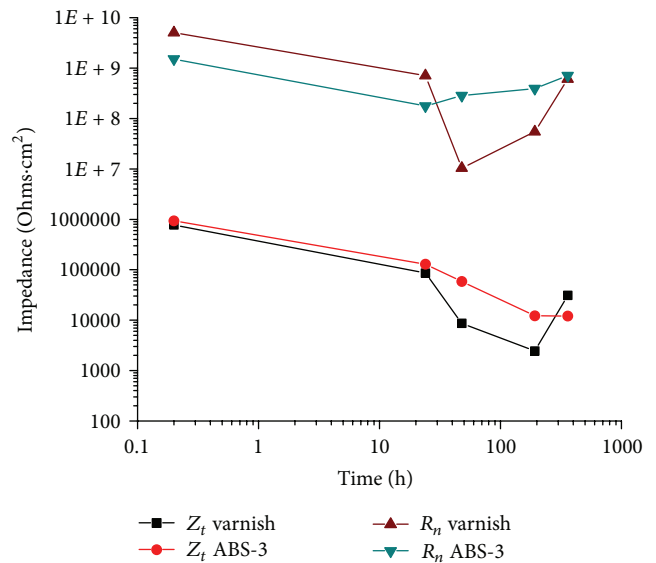


FIGURE 10: Comparative curves of Z<sub>t</sub> and R<sub>n</sub> in time for varnish and polymer ABS coatings as a function of time.

rendered polarization resistance values of 5.4 kohms·cm<sup>2</sup> for rural atmospheres up to 35.2 kohms·cm<sup>2</sup> for industrial-marine polluted atmospheres. For comparison, bare copper presents polarization resistance values in the range of 1.5 to 6 kohms·cm<sup>2</sup> [24].

In comparison under similar experimental conditions, for copper samples coated with a commercial alkyd varnish used for restoration and conservation of pieces of works of art of cultural and historic heritage, polarization resistance values obtained were 10 to 100 kohms·cm<sup>2</sup> [25]. Results obtained

and presented in this work compare favorably with the results previously reported for this type of coatings. When using a copper corrosion inhibitor such as benzotriazole forming a polymeric oxide and reported [26], the polarization resistance values obtained for chloride solution were around 50 kohms·cm<sup>2</sup>. According to the results obtained

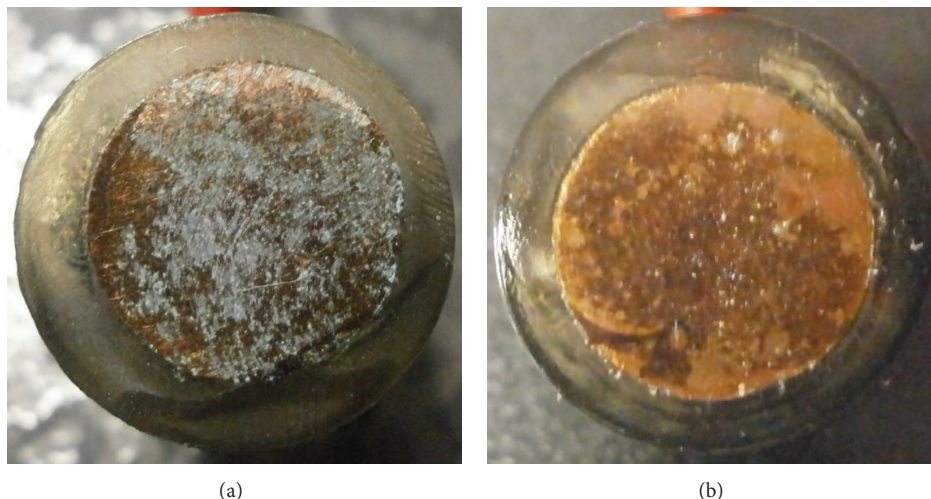


FIGURE 11: Macroscopic aspect of coupons coated after two weeks in the aggressive solution: (a) varnish and (b) ABS-3.

in this work, this coating presents good performance when compared to other corrosion protection systems [27, 28].

#### 4. Conclusions

The ABS films fulfill two major requirements for cultural heritage conservation purposes. Both transparency and reversibility, by dissolution in organic solvents such as acetone, combine with a highly acceptable protective capacity of the material. Furthermore, the film can be easily applied, even in field conditions providing adequate temporal or long-term protection to copper artifacts, as required. This proposed application for conservation adds value to an industrial waste and contributes to finding recycling alternatives for this discard polymer, hence collaborating not only with the conservation science, but also with the ecological concerns and needs. The results indicate high performance of the coating; however, further studies are needed to characterize and optimize the system.

#### Acknowledgments

The authors wish to thank the Ministry of Education (SEP-PROMEPE) for the support provided both to the Academic Body “Desarrollo y Análisis de Materiales Avanzados” (UAEMOR-CA-43) and to the Academic Network “Diseño Nanoscópico y Textural de Materiales Avanzados.” The authors are grateful to Dr. Miguel Ángel García-Sánchez (UAM-I) and Dr. René Guardían-Tapia (UAEM-CIICAp) for their timely and professional assessment at different stages of this investigation. Finally, the authors thank CONACyT for the grants received during this work.

#### References

- [1] G. Torraca, *Porous Building Materials: Materials Science for Architectural Conservation*, Iccrom, Rome, Italy, 1982.
- [2] G. W. Scherer, R. Flatt, and G. Wheeler, “Materials science research for the conservation of sculpture and monuments,” *MRS Bulletin*, vol. 26, no. 1, pp. 44–50, 2001.
- [3] F. Rodríguez-Acuña, J. Genescá, and J. Uruchurtu, “Electrochemical evaluation of patinas formed on nineteenth century bronze bells,” *Journal of Applied Electrochemistry*, vol. 40, no. 2, pp. 311–320, 2010.
- [4] M. Hernandez-Escampa, J. Gonzalez, and J. Uruchurtu-Chavarin, “Electrochemical assessment of the restoration and conservation of a heavily corroded archaeological iron artifact,” *Journal of Applied Electrochemistry*, vol. 40, no. 2, pp. 345–356, 2010.
- [5] J. A. M. Salgado, J. U. Chavarin, and D. M. Cruz, “Observation of copper corrosion oxide products reduction in metallic samples by means of digital image correlation,” *International Journal of Electrochemical Science*, vol. 7, no. 2, pp. 1107–1117, 2012.
- [6] H. H. Coghlan, E. Voce, and T. K. Penniman, “Notes on the prehistoric metallurgy of copper and bronze in the Old World,” *Occasional Papers on Technology*, no. 4, pp. 1–131, 1951.
- [7] C. Chiavari, K. Rahmouni, H. Takenouti, S. Joiret, P. Vermaut, and L. Robbiola, “Composition and electrochemical properties of natural patinas of outdoor bronze monuments,” *Electrochimica Acta*, vol. 52, no. 27, pp. 7760–7769, 2007.
- [8] M. Pilz and H. Römich, “Sol-gel derived coatings for outdoor bronze conservation,” *Journal of Sol-Gel Science and Technology*, vol. 8, no. 1-3, pp. 1071–1075, 1997.
- [9] B. Appelbaum, “Criteria for treatment: reversibility,” *Journal of the American Institute for Conservation*, vol. 26, no. 2, pp. 65–73, 1987.
- [10] Y. Sakata, A. Uddin, A. Muto et al., “Thermal and catalytic degradation of municipal waste plastics into fuel oil,” *Polymer Recycling*, vol. 2, no. 4, pp. 309–315, 1996.
- [11] S. Ozdogan, S. Uygur, and N. Egrican, “Formation and dispersion of toxic combustion byproducts from small-scale combustion systems,” *Energy*, vol. 22, no. 7, pp. 681–692, 1997.

- [12] F. Radtke, R. Köppel, and A. Baiker, "Formation of undesired by-products in deNO<sub>x</sub> catalysis by hydrocarbons," *Catalysis Today*, vol. 26, no. 2, pp. 159–167, 1995.
- [13] M. D. Wolkowicz and S. K. Gaggar, "Effect of thermal aging on impact strength acrylonitrile-butadiene-styrene (ABS) terpolymer," *Polymer Engineering and Science*, vol. 21, no. 9, pp. 571–575, 1981.
- [14] B. D. Gesner, "Environmental surface effects on ABS resins," *Journal of Applied Polymer Science*, vol. 9, no. 11, Article ID 10.1002/app.1965.070091117, pp. 3701–3706, 1965.
- [15] J. Shimada and K. Kabuki, "The mechanism of oxidative degradation of ABS resin. Part II: the mechanism of photooxidative degradation," *Journal of Applied Polymer Science*, vol. 12, no. 4, pp. 671–682, 1968.
- [16] M. G. Wyzgoski, "Effects of oven aging on ABS, poly (acrylonitrile-butadiene-styrene)," *Polymer Engineering and Science*, vol. 16, no. 4, pp. 265–269, 1976.
- [17] S. R. Salman and N. D. Al-Shama'a, "Effect of thermal aging on the optical properties of ABS plastics," *Polymer-Plastics Technology and Engineering*, vol. 30, no. 4, pp. 343–349, 1991.
- [18] J. Uruchurtu-Chavarin and J. M. Malo, "Electrochemical noise as a powerful electrochemical technique for corrosion studies," *Trends in Corrosion Research*, vol. 2, pp. 49–58, 1997.
- [19] "Standard practice for verification of algorithm and equipment for electrochemical impedance measurements," ASTM G 106-89, 2004.
- [20] <http://jp.fujitsu.com/group/fql/en/services/analysis/method/ft-ir/>.
- [21] R. Krache and I. Debbah, "Some mechanical and thermal properties of PC/ABS blends," *Materials Sciences and Applications*, vol. 2, pp. 404–410, 2011.
- [22] G. Reena, S. Sangita, and K. Verinder, "Ft-ir studies of e-plastic obtained from obsolete computers," *Journal of Chemical and Pharmaceutical Research*, vol. 3, no. 5, pp. 660–667, 2011.
- [23] M. Hernández, J. Genescá, J. Uruchurtu, and A. Barba, "Correlation between electrochemical impedance and noise measurements of waterborne coatings," *Corrosion Science*, vol. 51, no. 3, pp. 499–510, 2009.
- [24] M. Morcillo, M. E. M. Almeida, B. M. Rosales, M. Marrocos, and J. Uruchurtu, *Corrosión y Protección de Metales en las Atmosferas de Iberoamérica*, CYTED, Madrid, Spain, 1999.
- [25] L. Mariaca-Rodríguez, J. Genesca-Llongueras, J. Uruchurtu-Chavarin, and L. S. Hernández, *Corrosividad Atmosférica (MICAT-México)*, Plaza y Valdes, México, Mexico, 1999.
- [26] C. Menchaca, I. Castañeda, A. Soto-Quintero et al., "Characterization of a "smart" hybrid varnish electrospun nylon benzotriazole copper corrosion protection coating," *International Journal of Corrosion*, vol. 2012, Article ID 925958, 10 pages, 2012.
- [27] T. Kosec, D. K. Merl, and I. Milošev, "Impedance and XPS study of benzotriazole films formed on copper, copper-zinc alloys and zinc in chloride solution," *Corrosion Science*, vol. 50, no. 7, pp. 1987–1997, 2008.
- [28] M. Finšgar and I. Milošev, "Inhibition of copper corrosion by 1,2,3-benzotriazole: a review," *Corrosion Science*, vol. 52, no. 9, pp. 2737–2749, 2010.

## Research Article

# Processing and Performance of Polymeric Transparent Conductive Composites

Parul Jain,<sup>1</sup> Ranjani Muralidharan,<sup>1</sup> Jennifer Sedloff,<sup>1</sup> Xiao Li,<sup>1</sup>  
Norma A. Alcantar,<sup>2</sup> and Julie P. Harmon<sup>1</sup>

<sup>1</sup> Department of Chemistry, University of South Florida, 4202 East Fowler Avenue, CHE 205, Tampa, FL 33620-5250, USA

<sup>2</sup> Department of Chemical Engineering, University of South Florida, 4202 East Fowler Avenue, ENB 118, Tampa, FL 33620-5250, USA

Correspondence should be addressed to Julie P. Harmon; [harmon@usf.edu](mailto:harmon@usf.edu)

Received 11 April 2013; Revised 18 June 2013; Accepted 27 June 2013

Academic Editor: Carmina Menchaca-Campos

Copyright © 2013 Parul Jain et al. This is an open access article distributed under the Creative Commons Attribution License, which permits unrestricted use, distribution, and reproduction in any medium, provided the original work is properly cited.

Recent advances in microelectronic and optoelectronic industries have spurred interest in the development of reticulate doped polymer films containing “metallic” charge transfer complexes. In this study, such reticulate doped polymer films were prepared by exposing solid solutions of bis(ethylenedioxy) tetrathiafulvalene (BEDO-TTF) in polycarbonate (PC) to iodine, forming conductive charge transfer complexes. The resulting films exhibited room temperature conductivities ranging from  $6.33$  to  $90.4 \times 10^{-5} \text{ S} \cdot \text{cm}^{-1}$ . The colored iodine complexes in the film were reduced by cyclic voltammetry yielding conductive, colorless, transparent films. We were intrigued to examine the dielectric properties of BEDO-TTF in solid solution in PC prior to formation of the charge transfer complex as no such studies appear in the literature. Dielectric analysis (DEA) was used to probe relaxations in neat PC and BEDO-TTF/PC. BEDO-TTF plasticized the PC and decreased the glass transition temperature. Two secondary relaxations appeared in PC films, whereas the transitions merged in the BEDO-TTF/PC film. DEA also evidenced conductivity relaxations above  $180^\circ\text{C}$  which are characterized via electric modulus formalism and revealed that BEDO-TTF increased AC conductivity in PC.

## 1. Introduction

In the last few decades, there has been growing interest in conductive polymers and composites due to an array of potential applications in biological and chemical sensors, separations, microelectronics circuit boards, biomedical, coatings, and optical displays [1–5]. The ability to prepare thin, flexible, transparent films is an asset in applications requiring nanostructuring and miniaturization [6]. Conductivity is a general property of metals, but some polymers in combination with organic charge moieties exhibit metallic behavior [7]. After the discovery of the first organic superconductor,  $(\text{TMTSeF})_2\text{PF}_6$ , a growing number of organic charge transfer complexes and conductive salts have been investigated [8]. These salts exhibit a charge transfer between a donors and acceptors in the solid state; the donors and acceptors molecules form segregated stacked sheets of cations

and anions, respectively [9–11]. These materials also have low critical temperatures,  $T_c$ s (the temperature below which material is superconducting).  $(\text{TMTSeF})_2\text{PF}_6$  was subsequently replaced by another class of organic superconductors with BEDT-TTF (bis(ethylenedithio)tetrathiafulvalene) donors (Figure 1(a)) containing sulfur heterocycles [9]. The peripheral sulfur atoms allow better orbital overlap between donor stacks, forming a two-dimensional network. Suzuki et al. proposed that the substitution of sulfur or selenium atoms by lighter atoms, such as oxygen, would increase the  $T_c$  of organic superconductors. They synthesized an oxygen analogue of BEDT-TTF, bis(ethylenedioxy)tetrathiafulvalene (BEDO-TTF) (Figure 1(b)) in which outer sulfur atoms are replaced by oxygen atoms [12, 13]. BEDO-TTF was synthesized postulating that  $\pi$  donation from oxygen atoms into tetrathiafulvalene ring would lower the first ionization energy and make it an easily oxidized donor molecule [14]. In its

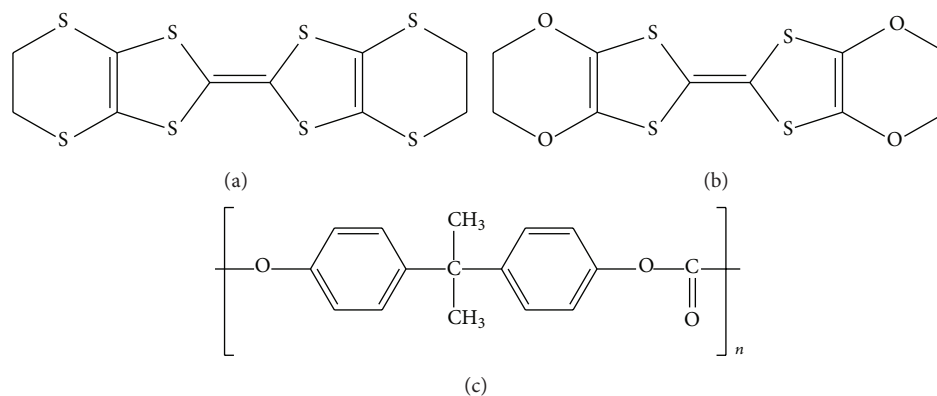


FIGURE 1: Molecular structure of (a) BEDT-TTF, (b) BEDO-TTF, and (c) polycarbonate.

partially oxidized state, the BEDO-TTF molecule has a tendency to self-aggregate via interactions in its peripheral heteroatoms. This results in the formation of a two-dimensional electronic structure, with metallic properties [15–19]. BEDO-TTF is of great interest in the design of organic superconductors, semiconductors, Langmuir-Blodgett films, crystalline organic metals, metal-like composites, biosensors, and soft electrodes [17, 20–23].

Surface conductive reticulate doped polymer (RDP) films are easily processed. The BEDO-TTF (donor) is an orange crystalline substance [13]. It is soluble in bisphenol A polycarbonate (PC) (Figure 1(c)) and easily processed into films. Bisphenol A polycarbonate, based on 2,2'-bis(4-hydroxyphenyl) propane, is a nonconductive amorphous polymer with optimum mechanical properties, optical properties, thermal stability, corrosion resistance, low density, and low cost [24, 25]. Jeszka and coworkers prepared films with BEDO-TTF/PC complexed with iodine and bromine to yield charge transfer complexes with conductive surfaces [26]. Both exhibited metallic properties; however, the Br doped films were clear, while the iodine films were dark colored and did not transmit light. Additionally, BEDO-TTF/PC iodine films were metallic down to 10 K, whereas BEDO-TTF/PC bromine films were metallic to about 100 K. Both of these films exhibited surface conductivity higher than  $10^{-3}$  S/sq [26]. Work by all of these researchers spurred us to investigate reticulate doped PC films with BEDO-TTF/halogen charge transfer complexes for use in the construction of sensors designed to detect nitroaromatic compounds [27]. Hopefully, sensors can be designed to detect via changes in current specific to the type and concentration of the nitroaromatics detected. An additional desired property is transparency which has the potential of allowing any changes in spectroscopic properties that accompany binding of the nitroaromatics to be detected. This paper describes the processing of a series of RDP charge transfer complexes. It also reports on electrochemical methodology used to control the oxidation state of iodine species and to induce transparency in the BEDO-TTF/iodine films [28]. In the course of this investigation, we thought that it is important to further delve into the properties of BEDO-TTF dissolved in PC prior to

complexation with halogens. We use dielectric spectroscopy to characterize the effect of BEDO-TTF on the relaxation behavior of PC as well as to characterize the conductive nature of BEDO-TTF in the PC matrix. To date, no DEA analysis has been undertaken on these interesting systems.

## 2. Materials and Methods

**2.1. Materials.** Poly (bisphenol-A carbonate) with molecular weight 45,000 was obtained from Arcos (Fair Lawn, NJ, USA). BEDO-TTF was purchased from Synchem OHG (Felsberg, Hesse, Germany). Methylene chloride (DCM), iodine and potassium iodide were purchased from Sigma-Aldrich (St. Louis, MO, USA). Double distilled water ( $18.2 \text{ M}\Omega\text{-cm}$ ) was purified using cascada BIO-water system (Port Washington, NY, USA).

**2.2. Purification of Polycarbonate Resin.** PC resin was dissolved in DCM at room temperature, precipitated in methanol, and dried for 2-3 days under a vacuum.

**2.3. Film Casting.** PC and BEDO-TTF/PC films were prepared by solution casting 1 wt% PC in DCM. Neat PC and PC containing 2 wt% BEDO-TTF were dissolved in DCM. Solutions were stirred until dissolution was complete, cast on a glass surfaces, and evaporated at room temperature for 24 hours. The films were subsequently dried in a vacuum oven at  $40^\circ\text{C}$  for 72 hrs. The neat films obtained by this method were colorless and transparent, whereas BEDO-TTF/PC films were pink and transparent.

Surface conductive reticulate iodine doped BEDO-TTF/PC films were prepared by dissolving iodine in DCM and pouring the solution into a vial with a level rim. BEDO-TTF/PC films mounted on the glass slide were placed 5 mm above the solvent level. Iodine exposure resulted in oxidation of BEDO-TTF and formation of BEDO-TTF/PC-Iodine salts on the surface of films [26]. Optimum conditions were obtained by varying the exposure time and concentration of iodine to minimize surface resistivity. Depending on the exposure time and concentration, BEDO-TTF/PC films

exhibit color ranging from shiny purple to dark green. Light purple to olive green films with metallic sheen are conductive. The metallic sheen increased as the optimum conductivity was reached. BEDO-TTF/PC films exposed for a longer period of time to iodine vapors exhibited dull green to dark purple color with no metallic sheen, thereby resulting in nonconductive films. Long exposure time led to changes in the oxidation state of BEDO-TTF, resulting films with nonconductive surfaces [26].

## 2.4. Characterization

**2.4.1. Differential Scanning Calorimetry.** Calorimetric experiments were carried out using TA Instruments DSC 2920. The amount of sample used was about 5 mgs, and the heating rate was maintained at 10°C/min. Samples were scanned in the range from 25 to 300°C and were encapsulated in hermetically sealed aluminum pans under a nitrogen purge rate of 70–80 mL/min. Temperature calibrations were performed with indium as a standard. All data analysis was performed using the TA instruments universal analysis program, version 3.9A. Two scans were performed for films: the first scan erased thermal history, and the second scan was used to determine the glass transition temperature.

**2.4.2. Dielectric Analysis.** Note that dielectric analysis was conducted on neat PC and BEDO-TTF/PC films. The iodine complexes conduct electricity and are not suitable for DEA. Dielectric measurements were performed with the TA instruments DEA 2970 using single surface electrodes. The samples were heated to 225°C to embed the sample into the channels of the single surface and then cooled to –120°C with liquid nitrogen. A maximum force of 250 N was exerted on the samples to achieve a minimum spacing of 0.25 mm, which ensures good contact between the samples and the sensors. The experiments were performed with the temperature range from –120 to 225°C, with 4°C increments through a frequency range of 1 Hz to 100 kHz. A dry helium atmospheric purge of 500 mL/min was used to create an inert atmosphere. Capacitance and conductance were measured as a function of time, temperature, and frequency to obtain the dielectric constant or permittivity ( $\epsilon'$ ), dielectric loss ( $\epsilon''$ ), and loss tangent ( $\tan \delta = \epsilon''/\epsilon'$ ).

**2.4.3. UV-Vis Spectroscopy.** UV-Vis films and solutions measurements were performed using a Perkin Elmer Lambda 40 UV-Vis-NIR double beam spectrophotometer with scan range from 190 nm to 800 nm. The UV-vis spectra of PC, BEDO-TTF, and BEDO-TTF/PC solutions in dichloromethane were recorded using quartz cell with 1 cm path length and dichloromethane as reference solution. PC and BEDO-TTF/PC and BEDO-TTF/PC-Iodine doped films were scanned with quartz slide.

**2.4.4. Optical Images.** Surface morphology of the BEDO-TTF/PC-Iodine films was studied using a Leica optical microscope in the reflection mode.

**2.4.5. Four-Point Probe.** The four-point probe method was used for the resistivity measurements on BEDO-TTF/PC-Iodine films. The probe consists of four linearly arranged and equally spaced electrodes, which remain in contact with a sample. The current,  $I$ , was supplied to the material through two outside probes with the help of a Keithley 6221 DC and AC current source, and steady voltage across the other two inside probes,  $V$ , was determined by Keithley 6514 system electrometer. Resistivity of BEDO-TTF/PC-Iodine films was measured randomly at different locations on the film's surface. Voltages were measured in volts and current in milliamperes. Electrical conductivity,  $\sigma$ , was obtained by simply inverting the corresponding values of the surface resistivity.

**2.4.6. Electrochemistry.** The electrochemical modifications on BEDO-TTF/PC-Iodine film (0.095 mol · L<sup>-1</sup>, exposed for 2 minutes) were carried out using a CH 760 electrochemistry workstation (CH Instrument, TX, USA). An Ag/AgCl electrode (BASi) was used as the reference electrode, and a platinum wire was used as the counter electrode. The electrolyte was 0.1 M KI solution in water.

## 3. Results and Discussion

**3.1. UV-Vis Spectroscopy.** UV-vis spectra for solutions and films are shown in Figure 2. In solution, BEDO-TTF exhibits strong absorption peaks at 314 nm and 334 nm and a weaker absorption peak around 518 nm. These absorption bands have been observed in the molecular absorption of neutral BEDO-TTF (undoped) earlier [26]. PC in DCM exhibits an absorption peak at 235 nm and another at 265 nm with a shoulder around 271 nm. These absorptions are characteristic of the bisphenol A unit which exhibits a main absorbance band at 226 nm with a secondary band at 276 nm [29].

PC films with and without BEDO-TTF were scanned as well. The purpose was to note any scatter at wavelengths above the electronic transition bands. The films were approximately 50 microns thick. At this thickness the absorbance was over 3.0 at wavelengths below 390 nm. However, the baseline at wavelengths above the absorption maxima indicates a lack of any appreciable scattering, and this indicates that the BEDO-TTF did not fall out of solution in the PC matrix. BEDO-TTF/PC-Iodine doped films were not transparent and became more metallic in appearance as the conductivity increased.

**3.2. Optical Images.** Figure 3 shows surface morphology of BEDO-TTF/PC-Iodine films at different iodine concentrations, where the conductivity is maximum. The surface exhibits fine regular grooves on optimized BEDO-TTF/PC-Iodine films. Longer exposure times and lower iodine concentrations results yield more pronounced surface topology, which, as shown in the next section, correlates with increased conductivity.

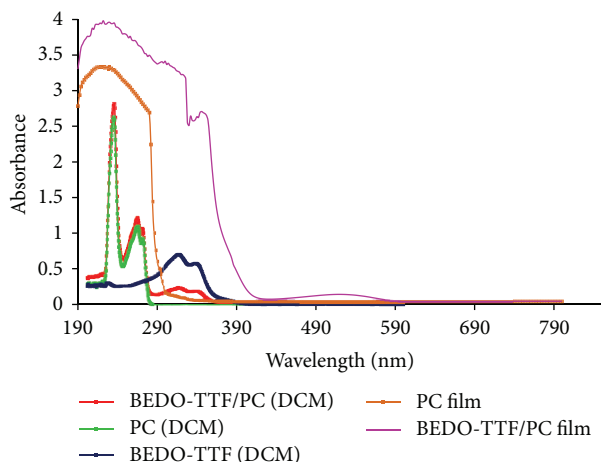


FIGURE 2: UV-Vis spectra of BEDO-TTF/PC, PC and BEDO-TTF dissolved in DCM and UV-Vis spectra of PC film and BEDO-TTF/PC film.

### 3.3. Electrical Properties

**3.3.1. Four-Point Probe.** Table 1 shows, as expected, that the surface of the BEDO-TTF/PC-Iodine films becomes conductive as a result of complex formation between acceptor iodine and donor species BEDO-TTF. This correlates with the surface topology viewed via light microscopy. The opposite side of the films are, of course, nonconductive [26]. It has been shown that there is a window of optimum exposure time, wherein the conductivity maximizes [26]. Beyond this time, films are nonconductive due to a change in the oxidation state of BEDO-TTF. Table 1 shows the calculated average resistivity and conductivity of these BEDO-TTF/PC-Iodine films. The exposure time required to reach minimum resistivity for each BEDO-TTF/PC-Iodine film increases with a decrease in iodine concentration. The surface resistivity values measured at three locations on the surface of the film were clustered closely around one central value. Standard deviations of surface resistivity for films when exposed for 2, 4, and 10 min are  $\pm 1.0 \text{ K}\Omega/\text{sq}$ ,  $\pm 0.02 \text{ K}\Omega/\text{sq}$ , and  $\pm 0.005 \text{ K}\Omega/\text{sq}$ , respectively.

**3.3.2. Electrochemical Properties.** Figure 4 shows the cyclic voltammogram of BEDO-TTF/PC-Iodine film in 0.1 M KI solution. The oxidation peak at 0.5 V in the anodic scan corresponds to the oxidation of iodide to iodine, and the reduction peak at  $-0.15 \text{ V}$  in the reverse scan is due to reduction of iodine to iodide [30, 31]. The oxidation and reduction of iodine at these potentials is also confirmed by the visual observation of the coloration of the film at high potentials and discoloration at low potentials. It is interesting to note that while the reversible oxidation/reduction peak of BEDO or TTF was reported ca. 0.4–0.6 V in organic solvents [14, 32], no distinguishable peak for BEDO-TTF was observed on the film in aqueous solution. This is due to the presence of iodine in the film which can react with BEDO-TTF [33]. Furthermore, the electrochemical method can be used to control the oxidation state of iodine species in the film. For

instance, by holding the potential at  $-0.4 \text{ V}$ , the iodine species in the film was reduced to iodide. Then, the conductivity of the reduced film was measured to ascertain the effect of iodine on the conductivity of the film. The discoloration gives rise to transparent film with 10% loss in conductivity. This finding encourages further studies on optimizing these systems.

**3.3.3. Differential Scanning Calorimetry.** The DSC thermograms for PC and BEDO-TTF/PC films are shown in Figure 5. The glass transition temperature for PC and BEDO-TTF/PC films are  $148.5^\circ\text{C}$  and  $142.7^\circ\text{C}$ , respectively [34–36]. The glass transition temperature of the BEDO-TTF/PC film decreased by about  $6^\circ\text{C}$  as compared to the neat film, indicating that the BEDO-TTF dissolves in and plasticizes the film.

**3.3.4. Dielectric Analysis.** The summary of dielectric analysis is provided for readers interested in a brief review. DEA is a thermal analysis technique well suited to the study of relaxations in polar polymers. In dielectric experiments, a sample is exposed to an alternating electric field, which generates an alternating electric polarization. The polarization causes the output current to lag behind the applied electric field by a phase shift angle,  $\theta$ . DEA helps in determining the capacitance and conductance as  $f(t, T, f)$  [37]. The capacitance and conductance of a material are measured over a range of temperatures and frequencies and are related to dielectric permittivity,  $\epsilon'$ , and dielectric loss factor,  $\epsilon''$ , respectively. The dielectric permittivity,  $\epsilon'$ , represents the amount of dipole alignment (both induced and permanent), and the dielectric loss factor,  $\epsilon''$ , measures the amount of energy required to align the dipoles or move ions. The complex permittivity,  $\epsilon^*$ , is defined as follows [38]:

$$\epsilon^* = \epsilon' - i\epsilon''$$

$$\epsilon' = \epsilon'_{\text{induced dipole}} + \epsilon'_{\text{alignment of dipole}} \quad (1)$$

$$\epsilon'' = \epsilon''_{\text{dipole loss factor}} + \epsilon''_{\text{ionic conductance}}$$

where  $\epsilon'$  and  $\epsilon''$  are the real and imaginary components of the dielectric complex permittivity  $\epsilon^*$ .  $\epsilon'$ , dielectric constant or permittivity, represents the amount of dipole alignment both induced and permanent in the sample. The permittivity of a dielectric material is measured relative to that of a vacuum ( $\epsilon_0 = 8.85 \times 10^{-12} \text{ F}\cdot\text{m}^{-1}$ ) [39]. Plots of  $\epsilon''$  versus temperature maximize at temperatures that increase with frequency,  $f$ . Plots of  $\ln f$  versus  $1/T_{\text{max}}$  are used to characterize transitions in polymers. Linear plots indicate secondary relaxations due to small scale motion such as side group rotation in the backbone. The large scale segmental motion accompanying the glass transition results in nonlinear plots discussed later.

However, at high temperatures conductivity often obscures the maxima noted in  $\epsilon''$  versus temperature. The Maxwell-Wagner-Sillars (MWS) effect created in a heterogeneous environment due to accumulation of charge, electrode polarization, impurities, and so forth masks relaxation behavior [40–43].

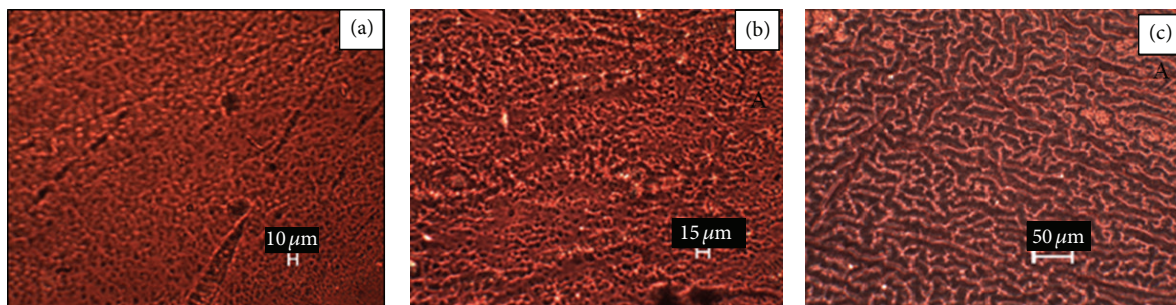


FIGURE 3: Optical images of BEDO-TTF/PC-Iodine film surface obtained using the transmission mode of a Leica microscope at (20X) with different exposure times and  $I_2$  concentration (a) 0.095 mol/L-2 min, (b) 0.063 mol/L-4 min, and (c) 0.033 mol/L-10 min.

TABLE 1: Surface resistivity and conductivity of BEDO-TTF/PC-Iodine films.

BEDO-TTF (wt%) in PC	Iodine conc. in DCM (mol L <sup>-1</sup> )	Exposure time (mins)	Surface resistivity (KΩ/sq)	Conductivity (S cm <sup>-1</sup> )
2	0.095	2	15.82 ± 1.0	6.33E - 05
2	0.063	4	1.47 ± 0.02	6.80E - 04
2	0.033	10	1.10 ± 0.005	9.04E - 04

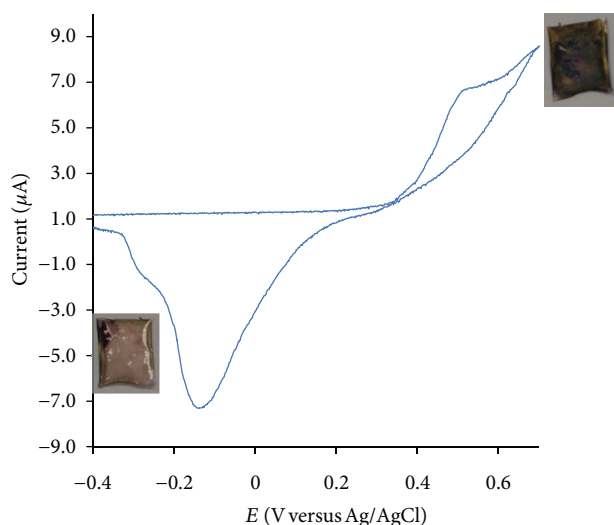


FIGURE 4: Cyclic voltammogram of BEDO-TTF/Iodine film with 0.095 mol/L (2 mins) in 0.1 M KI aqueous solution. Starting potential is 0.2 V, and scan rate is 5 mV/s.

McCrum et al. formulated a mathematical treatment of the complex permittivity,  $\epsilon^*$ , and defined electric modulus ( $M^*$ ) as the inverse of the complex permittivity ( $\epsilon^*$ ) as follows [38]:

$$M^* = \frac{1}{\epsilon^*} = M' + iM'' = \frac{\epsilon'}{\epsilon'^2 + \epsilon''^2} + i \frac{\epsilon''}{\epsilon'^2 + \epsilon''^2}, \quad (2)$$

where  $M^*$  is the complex electric modulus,  $M'$  is the electric storage modulus, and  $M''$  is the electric loss modulus.

The dielectric loss spectra ( $\epsilon''$ ) versus temperature provide information on different relaxations, whereas loss modulus ( $M''$ ) versus temperature reveal viscoelastic and ionic conductivity region. Figures 6(a) and 7(a) are plots of  $\epsilon''$  versus temperature for PC and BEDO-TTF/PC. Figures 6(b) and

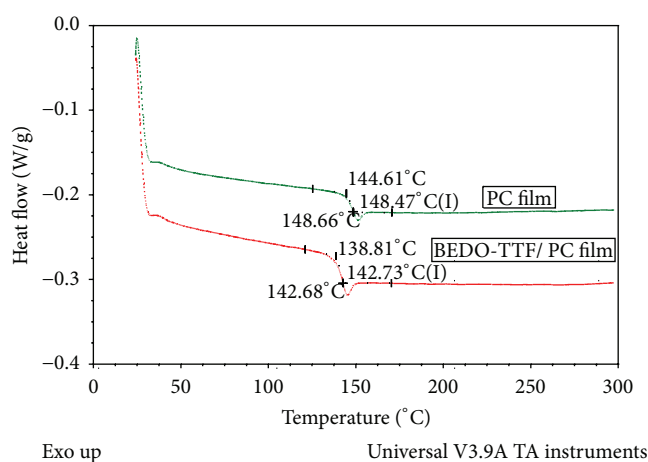


FIGURE 5: DSC thermograms for (a) PC film and (b) BEDO-TTF/PC film.

7(b) are plots for  $M''$  versus temperature for PC and BEDO-TTF/PC. The secondary  $\beta$  relaxation is enlarged in the insets of the  $\epsilon''$  plots. The glass transition region also exhibits clear maxima in  $\epsilon''$  versus temperature plots. Many other polymers exhibit conductivity effects that obscure the glass transition region. However, when electric modulus formalism is used, the glass transition region is again visible, but in addition, a high temperature relaxation, the conductivity relaxation, is noted. This region is important because it provides information for calculating AC and DC conductivities, as well as activation energies for ion translation [44]. Each relaxation region is further discussed in detail.

(1) *Secondary Relaxation*. The secondary relaxation,  $\beta$ , in PC has been widely studied by a host of techniques such as NMR [45–48], neutron scattering [49], molecular dynamic simulations [50], dynamic mechanical spectroscopy [51–54], dielectric analysis [55, 56], depolarized Rayleigh scattering

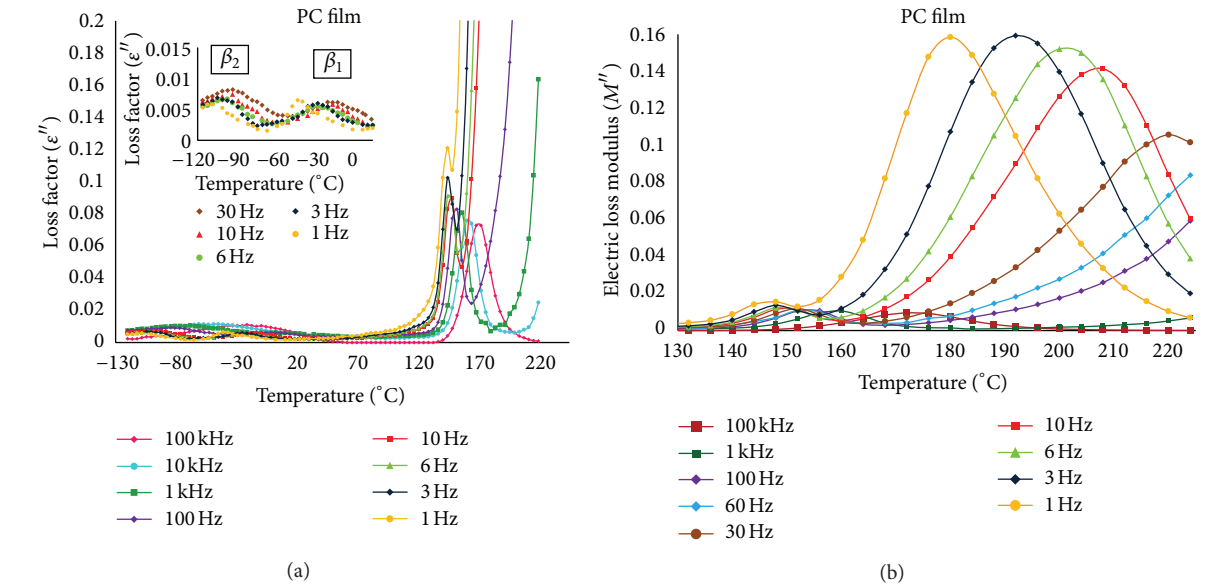


FIGURE 6: (a)  $\epsilon''$  versus temperature ( $^{\circ}\text{C}$ ) and (b)  $M''$  versus temperature ( $^{\circ}\text{C}$ ) plots for PC film.

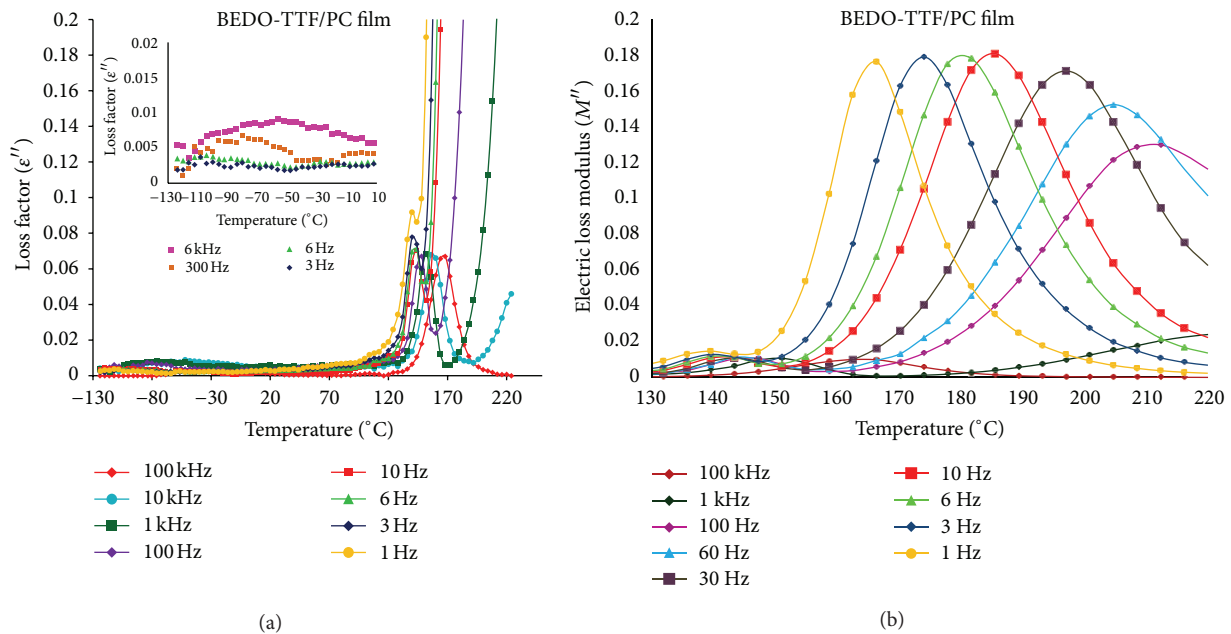


FIGURE 7: (a)  $\epsilon''$  versus temperature ( $^{\circ}\text{C}$ ) and (b)  $M''$  versus temperature ( $^{\circ}\text{C}$ ) plots for BEDO-TTF/PC film.

[57], light scattering [58, 59], and thermally stimulated discharge current (TSC) [60]. Different explanations of the origin of beta relaxation have been proposed over the last few decades. Earlier investigations on PC ascertained that beta relaxation is a single, unresolved relaxation that involves rotation of carbonate groups [51, 55]. Later several studies were performed on beta relaxation over a broad frequency range and at the wide temperatures where the secondary transition separated into two or three regions resulting from phenyl ring motion, carbonate group motion, and coupled

phenyl ring and carbonate motion [61–66]. Our DEA studies for PC reveal a broad  $\beta$  relaxation observed at higher frequencies (1 kHz–100 kHz). The inset in Figure 6(a) shows that the broad  $\beta$  relaxation process was further resolved prominently into two prominent components at lower frequencies (1 Hz–30 Hz). The relaxation occurring at higher temperature is termed as  $\beta_1$  relaxation, whereas other peaks at lower temperatures are termed as  $\beta_2$  relaxation. In comparison to PC, the BEDO-TTF/PC film exhibits only one secondary relaxation in the frequency range 1 Hz–100 kHz.

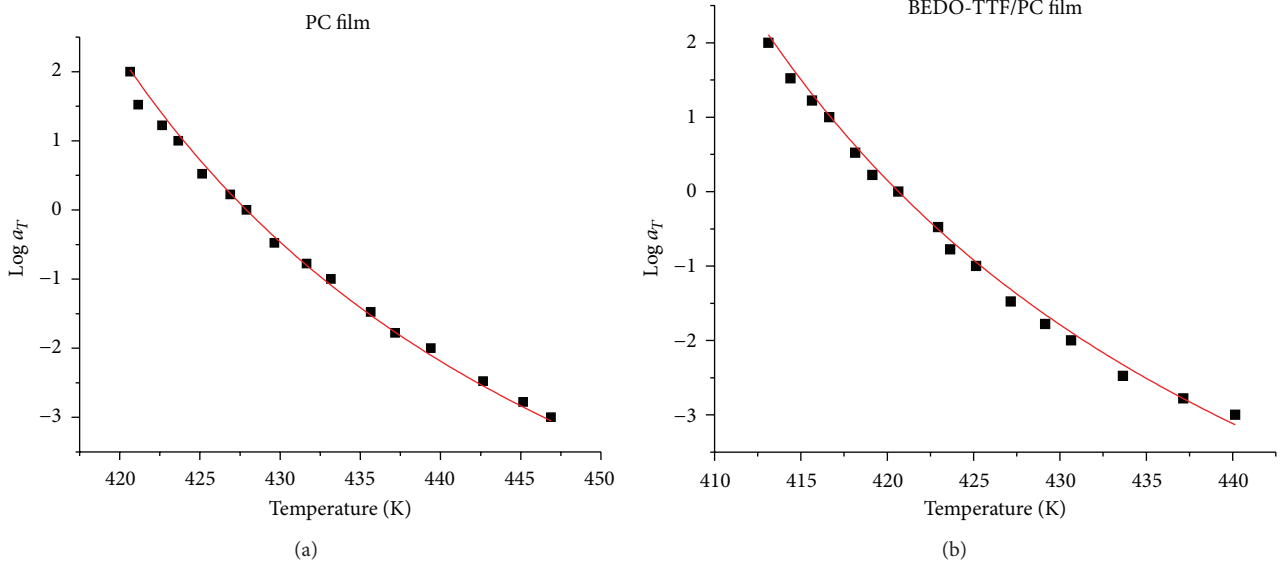


FIGURE 8: WLF plot for glass transition of (a) PC and (b) BEDO-TTF/PC films.

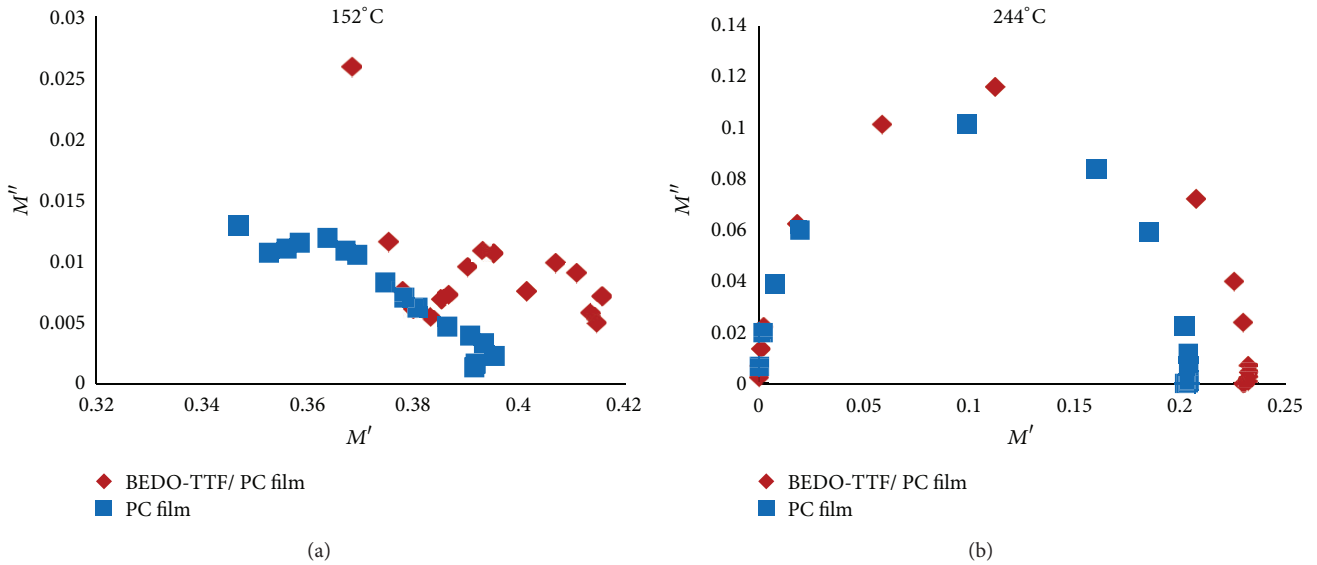


FIGURE 9: Argand plots derived from the conductivity relaxation region at different temperatures (152 and 224°C).

Peak maxima for each of the relaxation processes were assigned, and the slope of line obtained from Arrhenius plots of  $\ln$  frequency versus reciprocal of temperature was used to calculate activation energies. The activation energies for  $\beta_1$  and  $\beta_2$  processes in PC in frequency range 1 Hz–30 Hz were found to be 44 and 54 kJ/mol, whereas for PC, it was determined to be 47 kJ/mole in frequency range 1 kHz–100 kHz. The activation energy for BEDO-TTF/PC in frequency range 1 kHz–100 kHz is 38 kJ/mole, respectively.

(2) *Primary Relaxation.* In PC, the alpha transition or glass transition involves micro-Brownian motion in the main chain and conformational changes in the phenyl groups [67,

68]. The  $\alpha$  relaxation is discernible in  $\epsilon''$  versus temperature plots. The maxima in  $\epsilon''$  for Tg occur from 148 to 174°C for PC and from 140 to 168°C for BEDO-TTF/PC. The William-Landel-Ferry (WLF) equation (3) was used to characterized relaxation behavior [69, 70]. Plots of  $\log a_T$  versus temperature were constructed as shown in Figure 8 Consider

$$\ln a_T = \log \frac{\tau(T)}{\tau(T_0)} = -\log \frac{\omega}{\omega_0} = \frac{-C_1(T - T_0)}{C_2 + (T - T_0)}, \quad (3)$$

where  $a_T$  is the shift factor that corresponds to frequency,  $T$  is a given temperature,  $T_0$  is the reference temperature,  $\tau$  is the relaxation time, and  $\omega_0$  is the angular frequency at

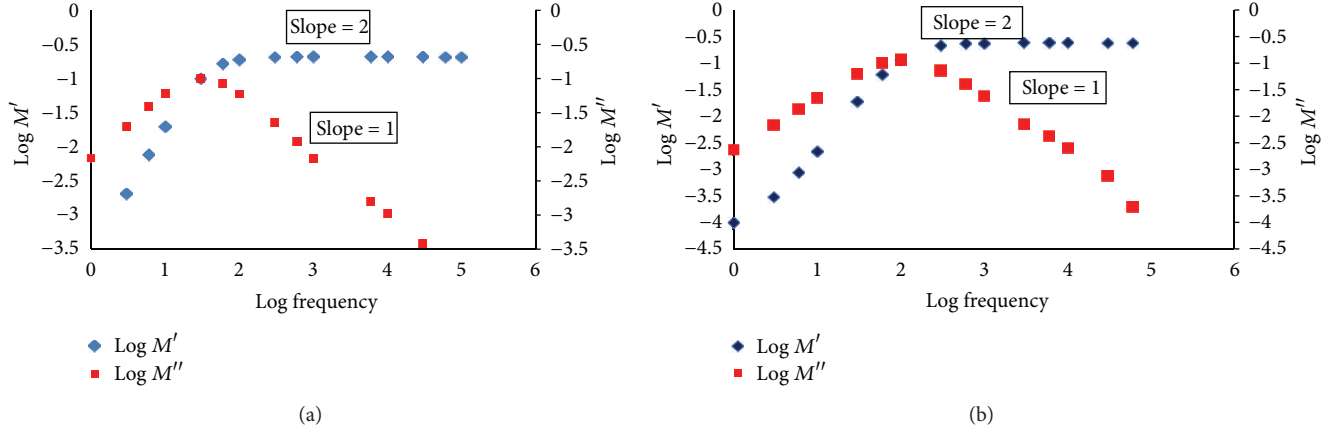


FIGURE 10: (a) Dependence of the real ( $M'$ ) and imaginary ( $M''$ ) parts of the electric modulus on frequency in the region of the conductivity for PC and (b) BEDO-TTF/PC films, respectively.

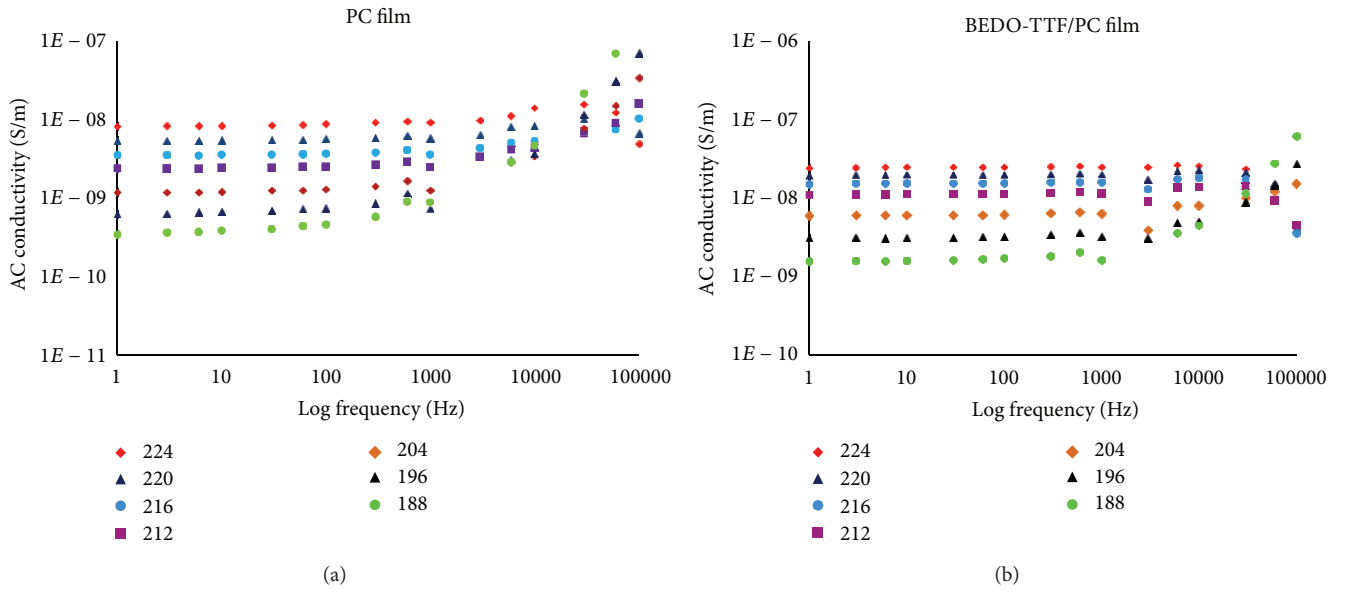


FIGURE 11: Frequency dependence of AC conductivity  $\sigma_{AC}$  (S/m) for (a) PC and (b) BEDO-TTF/PC film (2 wt%), respectively, above  $T_g$  temperature.

$T_0$ ,  $C_1$ ,  $C_2$ , and  $T_0$  are WLF constants that are determined by curve fitting the data to the WLF equation using Origin software as shown in Figures 8(a) and 8(b). The values of  $C_1$ ,  $C_2$ , and  $T_0$  were found to be 9.8, 42.7 K, and 427.9 K within a temperature range of 148–174°C for PC and 10.1, 43.8 K, and 420.6 K within a temperature range of 140–167°C for BEDO-TTF/PC, respectively. The WLF constants  $C_1$  and  $C_2$  reveal information related to fractional free volume ( $f_g$ ) and thermal expansion ( $\alpha_f$ ) parameters through.

$$f_g = \frac{B}{(2.303 * C_1)}, \quad (4)$$

$$\alpha_f = \frac{f_g}{C_2},$$

where  $f_g$  is an unoccupied (free) volume in the structure and  $B$  is taken as unity according to Doolittle equation. The  $f_g$  for PC and BEDO-TTF/PC are 0.044 and 0.042, respectively, whereas the thermal expansion for PC and BEDO-TTF/PC is  $1.03 \times 10^{-3}$  and  $0.958 \times 10^{-3}$ , respectively. The apparent activation energy ( $\Delta H$ ) values for PC and BEDO-TTF/PC were calculated accordingly to the Catsiff and Tobolsky equation [71]:

$$\Delta H = 2.303 \left( \frac{C_1}{C_2} \right) RT_g^2. \quad (5)$$

The values of activation energies for PC and BEDO-TTF/PC films were found to be 813 kJ/mol and 785 kJ/mol, respectively. These values for PC are in the range of values of 480 and 835 kJ/mol as reported in the literature [45, 55, 72].

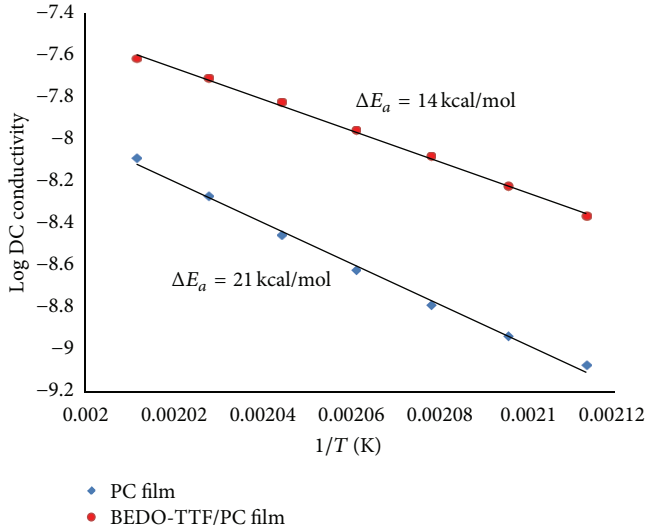


FIGURE 12: Log  $\sigma_{DC}$  versus inverse temperature plots of PC (red) and BEDO-TTF/PC film (blue).

WLF behavior for PC had been previously reported by others [39, 73–78].

Work herein demonstrates that BEDO-TTF plasticizes the PC matrix and reduces the glass transition temperature. Main chain motion occurs at lower temperatures in the BEDO-TTF plasticized film.

(3) *Ionic Conductivity Relaxation.* The high temperature region of the relaxation spectra was analyzed to confirm that the relaxation behavior was due to conductivity and not obstructed by any viscoelastic effects. Three proofs for this statement were undertaken, and these are described in the “the appendix” [28, 35]. This part of the research demonstrated that conductivity was enhanced in the PC containing BEDO-TTF, and this is likely a result of plasticization of the matrix.

#### 4. Conclusion

This study first summarizes some of the excellent background work done by researchers in this field. The initial work reported herein reveals that films processed via the reticulate doped polymer method can be reduced by cyclic voltammetry to yield conductive, colorless, transparent films. These features make it possible to design optimum sensors. DSC studies of PC and BEDO-TTF/PC films reveal that the dye is soluble in and plasticized the PC matrix. Dielectric measurements carried out on PC and BEDO-TTF/PC confirm multiple transitions within the temperature range of  $-120$  to  $225^\circ\text{C}$  for the frequency range  $1$ – $100$  kHz. Different parameters such as relaxation broadening, activation energy, and conductivity (AC or DC) were found to be composition dependent. The AC conductivity becomes higher with the addition of BEDO-TTF. This is most likely due to enhanced mobility due to the plasticizing effect of the dye.

#### Appendix

*Proof (Argand plot).* The dielectric permittivity and loss factor for a relaxation with a single relaxation can be described by (A.1)

$$\epsilon' = \epsilon_U + \frac{(\epsilon_R - \epsilon_U)}{1 + \omega^2 \tau_E^2}, \quad (\text{A.1})$$

$$\epsilon'' = (\epsilon_R - \epsilon_U) \frac{\omega \tau_E}{1 + \omega^2 \tau_E^2},$$

where  $\tau_E$  is the dielectric relaxation time and  $\omega$  is the angular frequency.  $\epsilon_U$  represents the high frequency, unrelaxed state, while  $\epsilon_R$  represents the low frequency, relaxed state. By arranging (A.1), (A.2) is derived as

$$\left\{ \epsilon' - \frac{(\epsilon_R - \epsilon_U)}{2} \right\}^2 + (\epsilon'')^2 = \left( \frac{\epsilon_R - \epsilon_U}{2} \right)^2. \quad (\text{A.2})$$

Cole-Cole proposed that by plotting dielectric loss ( $\epsilon''$ ) against permittivity ( $\epsilon'$ ) at a particular temperature, and a semicircle of radius  $((\epsilon_R - \epsilon_U)/2)$  is obtained [38]. In Cole-Cole plots the high frequency region is on left side, while the low frequency exists on the right side of the plot. The Argand plots identify viscoelastic and conductivity effects [38, 79–81]. Argand plots were plotted between imaginary part ( $M''$ ) of the complex modulus against real part ( $M'$ ) of the complex modulus as functions of the frequency at fixed temperatures. In an Argand plot, low frequency measurements exist on the left side of the semicircle, while the high frequency is on the right side. Argand plots can be obtained from

$$\left( M' - \left\{ \frac{M_U - M_R}{2} \right\} \right)^2 + (M'')^2 = \left( \frac{M_U - M_R}{2} \right)^2. \quad (\text{A.3})$$

Semicircular behavior is characteristic of Debye behavior for small rigid molecules and molecular liquids. This indicates a single relaxation time due to ionic conduction in the absence of any viscoelastic relaxation behavior [43]. By using the electric modulus, the space charge effects are reduced, and ionic conductivity peaks appear [82, 83]. Figure 9 shows semicircular behavior at  $224^\circ\text{C}$ .  $\square$

*Proof (log  $M''$ ,  $M'$  versus frequency).* Ambrus et al. derived the electric modulus in terms of time, frequency, and modulus (see (A.4) and (A.5)) [84]. Starkweather et al. show that plots of  $\log M''$  and  $\log M'$  versus  $\log$  frequency at low frequencies will yield slopes of 1 and 2, respectively, when the electric modulus arises purely from ion conduction without contributions from viscoelastic relaxations [44]. Above  $T_g$ , the conduction is pure due to the diffusion of ions and independent of viscoelastic relaxation [14, 42, 81] as follows:

$$\begin{aligned} M &= M_s \left( \frac{i\omega\tau_\sigma}{1 + i\omega\tau_\sigma} \right) \\ &= M_s \left[ \frac{(\omega\tau_\sigma)^2}{1 + (\omega\tau_\sigma)^2} \right] + iM_s \left[ \frac{\omega\tau_\sigma}{1 + (\omega\tau_\sigma)^2} \right], \end{aligned} \quad (\text{A.4})$$

where

$$M_s = \frac{1}{\varepsilon_s}. \quad (\text{A.5})$$

Figure 10 shows that above  $T_g$ , PC, and BEDO-TTF/PC films samples approach ideal value of 2 or 1, respectively, confirming ionic conductivity.  $\square$

*Proof* (AC and DC conductivities). When viscoelastic effects are negligible, the loss factor is described by (A.6). Upon rearrangement, AC conductivity can be obtained by (A.7)

$$\varepsilon'' = \frac{\sigma_{AC}}{\omega\varepsilon_0}, \quad (\text{A.6})$$

where  $\sigma$  is the ionic conductivity,  $\omega$  is the angular frequency ( $2\pi f$ ), and  $\varepsilon_0$  is the absolute permittivity of free space ( $8.854 \times 10^{-14}$ ) as follows:

$$\sigma_{AC} = \varepsilon'' \omega \varepsilon_0. \quad (\text{A.7})$$

As shown in Figures 11(a) and 11(b), the loss factor increases in the conductivity region at high temperatures and low frequencies.

Figure 11 shows frequency dependency of  $\sigma_{ac}$  at temperatures where conductivity effects dominate viscoelastic behavior. As temperature increases,  $\sigma_{ac}$  conductivity develops a plateau (ca. 184°C) from 1 Hz to  $10^2$  Hz, signifying the beginning of the conductivity relaxation region. The  $\sigma_{ac}$  plateau then expands to higher frequencies  $10^4$  Hz as the temperature is increased, thus showing a frequency independent conductivity relaxation region. The absence of a frequency dependent region signifies negligible viscoelastic effects. This study reveals that the conductivity relaxation region exists between 180 and 224°C. At a lower temperature, where dielectric relaxation is dominant, the apparent conductivities (AC and DC) are strongly dependent on frequency. As temperature increases, conductivity becomes almost independent of the frequency. The BEDO-TTF/PC film has higher  $\sigma_{ac}$  values than that of the PC. The addition of BEDO-TTF presumably increases the amorphous content of the polymer. It speeds up segmental motion by increasing available free volume, thereby facilitating easy ion migration.

The DC conductivity values ( $\sigma_{DC}$ ) have been obtained through the AC conductivity measurement [85–87] as shown by

$$\sigma_{AC}(\omega) = \omega\varepsilon_0\varepsilon''(\omega) = \sigma_{DC} + A\omega^s, \quad (\text{A.8})$$

where  $\omega$  is the angular frequency,  $\varepsilon_0$  is the vacuum permittivity,  $\varepsilon''$  is the imaginary part of the complex permittivity,  $A$  is the temperature dependent parameter, and  $s$  is the frequency dependent exponent of the “universal” power law. The exponent  $s$  lies between  $0 \leq s \leq 1$  [81, 83]. Frequency independent AC conductivity has been observed at higher temperatures, which signifies the long-range movement of mobile charge carriers. At higher temperatures, the graph is seen as linear on a logarithmic scale. The plateau values give DC conductivity. The Arrhenius relationship is expressed by

$$\log \sigma_{DC} = \log \sigma_0 \exp\left(\frac{-E_A}{kT}\right), \quad (\text{A.9})$$

where  $E_A$  is the apparent activation energy,  $\sigma_{DC}$  is the DC conductivity,  $\sigma_0$  is the preexponential factor (conductivity at infinite temperature), and  $k$  is the Boltzmann constant.

Plots of  $\ln$  DC conductivity versus  $1/\text{temperature}$  yield ionic conductivity and activation energies from the slopes. At higher temperatures, this plot exhibits a linear response. Figure 12 shows higher activation energy for PC (21 kcal/mole) due to lack of plasticization as compared to the plasticized BEDO-TTF/PC film which has activation energy of 14 kcal/mole.  $\square$

## Conflict of Interests

None of the authors have conflict of interests with any of the aspects of this paper.

## Acknowledgment

The authors would like to thank National Science Foundation for providing funding under Grant CBET 0808053 to support research.

## References

- [1] D. D. L. Chung, “Polymer-matrix composites for microelectronics,” *Polymers and Polymer Composites*, vol. 8, no. 4, pp. 219–229, 2000.
- [2] M. Gerard, A. Chaubey, and B. D. Malhotra, “Application of conducting polymers to biosensors,” *Biosensors and Bioelectronics*, vol. 17, no. 5, pp. 345–359, 2002.
- [3] B. W. Rowe, B. D. Freeman, and D. R. Paul, “Physical aging of ultrathin glassy polymer films tracked by gas permeability,” *Polymer*, vol. 50, no. 23, pp. 5565–5575, 2009.
- [4] C. M. Stafford, B. D. Vogt, C. Harrison, D. Julthongpiput, and R. Huang, “Elastic moduli of ultrathin amorphous polymer films,” *Macromolecules*, vol. 39, no. 15, pp. 5095–5099, 2006.
- [5] D. C. Wedge, A. Das, R. Dost et al., “Real-time vapour sensing using an OFET-based electronic nose and genetic programming,” *Sensors and Actuators*, vol. 143, no. 1, pp. 365–372, 2009.
- [6] C. Vree and S. G. Mayr, “Structure and surface morphology of vapor deposited polycarbonate thin films,” *Journal of Applied Physics*, vol. 104, no. 8, Article ID 083517, 2008.
- [7] J. K. Jeszka, A. Tracz, J. Ulanski, and M. Kryszewski, “Surface-conductive polymer films by reticulate doping with organic metals,” *Journal of Physics D*, vol. 18, no. 10, pp. L167–L170, 1985.
- [8] D. Jerome, A. Mazaud, M. Ribault, and K. Bechgaard, “Superconductivity in a synthetic organic conductor (TMTSF)2PF6,” *Journal de Physique Lettres*, vol. 41, no. 4, pp. 95–98, 1980.
- [9] T. Ishiguro, K. Yamaji, and G. Saito, *Organic Superconductors*, 2nd edition, 1998.
- [10] R. P. Shibaeva, S. S. Khasanov, L. V. Zorina, and S. V. Simonov, “Structural features of low-dimensional molecular conductors: representatives of new hybrid polyfunctional materials: review,” *Crystallography Reports*, vol. 51, no. 6, pp. 949–967, 2006.
- [11] R. P. Shibaeva and E. B. Yagubskii, “Molecular conductors and superconductors based on trihalides of BEDT-TTF and some of its analogues,” *Chemical Reviews*, vol. 104, no. 11, pp. 5347–5378, 2004.

- [12] H. Kobayashi, A. Kobayashi, Y. Sasaki, G. Saito, and H. Inokuchi, "The crystal and molecular structures of bis(ethylenedithio)tetrathiafulvalene," *Bulletin of the Chemical Society of Japan*, vol. 59, no. 1, pp. 301–302, 1986.
- [13] T. Suzuki, H. Yamochi, G. Srdanov, K. Hinkelmann, and F. Wudl, "Bis(ethylenedioxy)tetrathiafulvalene: the first oxygen-substituted tetrathiafulvalene," *Journal of the American Chemical Society*, vol. 111, no. 8, pp. 3108–3109, 1989.
- [14] D. L. Lichtenberger, R. L. Johnston, K. Hinkelmann, T. Suzuki, and F. Wudl, "Relative electron donor strengths of tetrathiafulvene derivatives: effects of chemical substitutions and the molecular environment from a combined photoelectron and electrochemical study," *Journal of the American Chemical Society*, vol. 112, no. 9, pp. 3302–3307, 1990.
- [15] M. A. Beno, H. H. Wang, A. M. Kini et al., "The first ambient pressure organic superconductor containing oxygen in the donor molecule,  $\beta$ m-(BEDO-TTF) $_3$ Cu $_2$ (NCS) $_3$ ,  $T_c = 1.06$  K," *Inorganic Chemistry*, vol. 29, no. 9, pp. 1599–1601, 1990.
- [16] N. Driehko, R. Vlasova, V. Semkin et al., "Optical properties of a new organic metal (BEDO-TTF) $_5$ [CsHg(SCN) $_4$ ] $_2$ ," *Synthetic Metals*, vol. 109, no. 1, pp. 123–127, 2000.
- [17] S. Horiuchi, H. Yamochi, G. Saito, K.-I. Sakaguchi, and M. Kusunoki, "Nature and origin of stable metallic state in organic charge-transfer complexes of bis(ethylenedioxy)tetrathiafulvalene," *Journal of the American Chemical Society*, vol. 118, no. 36, pp. 8604–8622, 1996.
- [18] H. Yamochi, T. Haneda, A. Tracz, and G. Saito, "Humidity dependent properties of a transparent conducting film doped with BEDO-TTF complex," *Physica Status Solidi*, vol. 249, no. 5, pp. 1012–1016, 2012.
- [19] H. Yamochi, T. Nakamura, G. Saito et al., "The cation radical salts of the oxygen-substituted donor, BEDO-TTF," *Synthetic Metals*, vol. 42, no. 1-2, pp. 1741–1744, 1991.
- [20] A. Graja, A. Brau, and J.-P. Farges, "Study of new conducting organic composites based on BEDO-TTF molecule," *Synthetic Metals*, vol. 122, no. 2, pp. 233–235, 2001.
- [21] S. Horiuchi, H. Yamochi, G. Saito, and K. Matsumoto, "Structural and physical properties of molecular metals based on BEDO-TTF," *Synthetic Metals*, vol. 86, no. 1, pp. 1809–1810, 1997.
- [22] H. Mochizuki, T. Mizokuro, N. Tanigaki, T. Hiraga, and I. Ueno, "Crystallization of bisphenol-A polycarbonate by a vacuum process," *Polymers for Advanced Technologies*, vol. 16, no. 1, pp. 67–69, 2005.
- [23] H. Ohnuki, Y. Ishizaki, M. Suzuki et al., "Metallic Langmuir and Langmuir: blodgett films based on TTF derivatives and fatty acid," *Materials Science and Engineering C*, vol. 22, no. 2, pp. 227–232, 2002.
- [24] S. C. Tjong and Y. Z. Meng, "Mechanical and thermal properties of polycarbonate composites reinforced with potassium titanate whiskers," *Journal of Applied Polymer Science*, vol. 72, no. 4, pp. 501–508, 1999.
- [25] M. E. L. Wouters, D. P. Wolfs, M. C. van der Linde, J. H. P. Hovens, and A. H. A. Tinnemans, "Transparent UV curable antistatic hybrid coatings on polycarbonate prepared by the sol-gel method," *Progress in Organic Coatings*, vol. 51, no. 4, pp. 312–320, 2004.
- [26] J. K. Jeszka, A. Tracz, A. Sroczynska et al., "Metallic polymer composites with bis(ethylenedioxy)-tetrathiafulvalene salts. Preparation-properties relationship," *Synthetic Metals*, vol. 106, no. 2, pp. 75–83, 1999.
- [27] N. A. Alcantar and J. Harmon, "Transparent conducting composites (TCCS) for creating chemically active surfaces," US Patent 8034302 B1, 2011.
- [28] A. Tracz, J. K. Jeszka, A. Sroczynska et al., "New transparent, colorless, metallically conductive polymer films and their electrochemical transformations," *Synthetic Metals*, vol. 86, no. 1, pp. 2173–2174, 1997.
- [29] A. Maroto, P. Kissingou, A. Diascorn et al., "Direct laser photo-induced fluorescence determination of bisphenol A," *Analytical and Bioanalytical Chemistry*, vol. 401, no. 9, pp. 3011–3017, 2011.
- [30] P. H. Qi and J. B. Hiskey, "Electrochemical behavior of gold in iodide solutions," *Hydrometallurgy*, vol. 32, no. 2, pp. 161–179, 1993.
- [31] Y. A. Yariyev, "Oxidation of iodide ions by means of cyclic voltammetry," *Electrochimica Acta*, vol. 29, no. 9, pp. 1213–1214, 1984.
- [32] J.-P. Griffiths, R. J. Brown, P. Day, C. J. Matthews, B. Vital, and J. D. Wallis, "Synthesis of bis(ethylenedithio)tetrathiafulvalene derivatives with metal ion ligating centres," *Tetrahedron Letters*, vol. 44, no. 15, pp. 3127–3131, 2003.
- [33] S. Horiuchi, H. Yamochi, G. Saito, and K. Matsumoto, "Highly-oxidized states of organic donor bis(ethylenedioxy)tetrathiafulvalene (BEDO-TTF)," *Molecular Crystals and Liquid Crystals Science and Technology*, vol. 284, pp. 357–365, 1996.
- [34] M. D. Shelby and G. L. Wilkes, "Thermodynamic characterization of the oriented state of bisphenol A polycarbonate as it pertains to enhanced physical aging," *Journal of Polymer Science B*, vol. 36, no. 12, pp. 2111–2128, 1998.
- [35] M. C. Delpech, F. M. B. Coutinho, and M. E. S. Habibe, "Bisphenol A-based polycarbonates: characterization of commercial samples," *Polymer Testing*, vol. 21, no. 2, pp. 155–161, 2002.
- [36] J. Wang and Z. Xin, "Flame retardancy, thermal, rheological, and mechanical properties of polycarbonate/polysilsesquioxane system," *Journal of Applied Polymer Science*, vol. 115, no. 1, pp. 330–337, 2010.
- [37] TA Instruments, DEA, 2790 dielectric analyzer, A - 057, TA instruments applications application library, <http://www.tainst.com>.
- [38] N. G. McCrum, B. E. Read, and G. Williams, *Anelastic and Dielectric Effects in Polymeric Solids*, John Wiley and Sons, London, UK, 1967.
- [39] J. P. Runt and J. J. Fitzgerald, *Dielectric Spectroscopy of Polymeric Materials: Fundamentals and Applications*, 1997.
- [40] J. C. Maxwell, *Electricity and Magnetism*, vol. 1, Clarendon, Oxford, UK, 1892.
- [41] K. W. Wagner, "Erklärung der dielectrischen nachwirkungsworgänge auf grund maxwellscher vorstellungen," *Archiv Für Elektrotechnik*, vol. 2, pp. 371–387, 1914.
- [42] R. W. Sillars, "The properties of a dielectric containing semiconducting particles of various shapes," *Journal of the Institution of Electrical Engineers*, vol. 80, no. 484, pp. 378–394, 1937.
- [43] G. M. Tsangaris, G. C. Psarras, and N. Kouloumbi, "Electric modulus and interfacial polarization in composite polymeric systems," *Journal of Materials Science*, vol. 33, no. 8, pp. 2027–2037, 1998.
- [44] H. W. Starkweather Jr. and P. Avakian, "Conductivity and the electric modulus in polymers," *Journal of Polymer Science B*, vol. 30, no. 6, pp. 637–641, 1992.
- [45] S. Matsuoka and Y. Ishida, "Multiple transitions in polycarbonates," *Journal of Polymer Science, Polymer Symposia*, vol. 14, pp. 247–259, 1966.

- [46] L. J. Garfield, "Molecular motions in some polycarbonates," *Journal of Polymer Science*, no. 30, pp. 551–559, 1970.
- [47] D. Stefan and H. L. Williams, "Molecular motions in bisphenol A polycarbonates as measured by pulsed NMR techniques. I. Homopolymers and copolymers," *Journal of Applied Polymer Science*, vol. 18, no. 5, pp. 1279–1293, 1974.
- [48] M. Wehrle, G. P. Hellmann, and H. W. Spiess, "Phenylene motion in polycarbonate and polycarbonate/additive mixtures," *Colloid & Polymer Science*, vol. 265, no. 9, pp. 815–822, 1987.
- [49] S. Arrese-Igor, A. Arbe, A. Alegría, J. Colmenero, and B. Frick, "Secondary relaxation in two engineering thermoplastics by neutron scattering and dielectric spectroscopy," *Applied Physics A*, vol. 74, no. 1, pp. S454–S456, 2002.
- [50] J. H. Shih and C. L. Chen, "Molecular dynamics simulation of bisphenol A polycarbonate," *Macromolecules*, vol. 28, no. 13, pp. 4509–4515, 1995.
- [51] F. P. Reding, J. A. Faucher, and R. D. Whitman, "Mechanical behavior of polycarbonates," *Journal of Polymer Science*, vol. 54, pp. S56–S58, 1961.
- [52] C. I. Chung and J. A. Sauer, "Low-temperature mechanical relaxations in polymers containing aromatic groups," *Journal of Polymer Science*, vol. 9, no. 6, pp. 1097–1115, 1971.
- [53] K. Varadarajan and R. F. Boyer, "Effects of thermal history, crystallinity, and solvent on the transitions, and relaxations in poly(bisphenol-A carbonate)," *Journal of Polymer Science*, vol. 20, no. 1, pp. 141–154, 1982.
- [54] J. Y. Jho and A. F. Yee, "Secondary relaxation motion in bisphenol a polycarbonate," *Macromolecules*, vol. 24, no. 8, pp. 1905–1913, 1991.
- [55] F. H. Muller and K. Huff, "Changes in the dielectric relaxation spectrum of high polymers on pulling and pretreatment," *Kolloid-Zeitschrift*, vol. 164, pp. 34–37, 1959.
- [56] E. Sacher, "The contribution of the linear viscoelastic region to the impact properties of thin polymer films," *The American Chemical Society, Division of Organic Coatings and Plastics Chemistry*, vol. 34, no. 2, pp. 257–260, 1974.
- [57] B. Erman, D. Wu, P. A. Irvine, D. C. Marvin, and P. J. Flory, "Optical anisotropy of the polycarbonate of diphenylolpropane," *Macromolecules*, vol. 15, no. 2, pp. 670–673, 1982.
- [58] M. Dettenmaier and H. H. Kausch, "Light scattering of bisphenol-A polycarbonate in the amorphous state and at the beginning of thermal crystallization," *Colloid and Polymer Science*, vol. 259, no. 2, pp. 209–214, 1981.
- [59] G. Floudas, A. Lappas, G. Fytas, and G. Meier, "Optical anisotropy and orientational dynamics of polycarbonate dilute solutions," *Macromolecules*, vol. 23, no. 6, pp. 1747–1753, 1990.
- [60] Y. Aoki and J. O. Brittain, "Isothermal and nonisothermal dielectric relaxation studies on polycarbonate," *Journal of Polymer Science*, vol. 14, no. 7, pp. 1297–1304, 1976.
- [61] H.-E. Carius, A. Schönhals, D. Guigner, T. Sterzynski, and W. Brostow, "Dielectric and mechanical relaxation in the blends of a polymer liquid crystal with polycarbonate," *Macromolecules*, vol. 29, no. 14, pp. 5017–5025, 1996.
- [62] G. Locati and A. V. Tobolsky, *Studies of the Toughness of Polycarbonate of Bisphenol A in Light of Its secondary transition*, Princeton University, Princeton, NJ, USA, 1969.
- [63] L. Delbreilh, E. Dargent, J. Grenet, J.-M. Saiter, A. Bernès, and C. Lacabanne, "Study of poly(bisphenol A carbonate) relaxation kinetics at the glass transition temperature," *European Polymer Journal*, vol. 43, no. 1, pp. 249–254, 2007.
- [64] O. Mitxelena, J. Colmenero, and A. Alegría, "Effect of cold-drawing on the secondary dielectric relaxation of bisphenol-A polycarbonate," *Journal of Non-Crystalline Solids*, vol. 351, no. 33–36, pp. 2652–2656, 2005.
- [65] A. Alegría, S. Arrese-Igor, O. Mitxelena, and J. Colmenero, "Dielectric secondary relaxation and phenylene ring dynamics in bisphenol-A polycarbonate," *Journal of Non-Crystalline Solids*, vol. 353, no. 47–51, pp. 4262–4266, 2007.
- [66] S. A. Madbouly and J. U. Otaigbe, "Broadband dielectric spectroscopy of nanostructured maleated polypropylene/polycarbonate blends prepared by in situ polymerization and compatibilization," *Polymer*, vol. 48, no. 14, pp. 4097–4107, 2007.
- [67] G. J. Pratt and M. J. A. Smith, "Dielectric response of commercial polycarbonate," *British Polymer Journal*, vol. 18, no. 2, pp. 105–111, 1985.
- [68] H. W. Spiess, "Molecular dynamics of solid polymers as revealed by deuterium NMR," *Colloid & Polymer Science*, vol. 261, no. 3, pp. 193–209, 1983.
- [69] M. L. Williams, R. F. Landel, and J. D. Ferry, "The temperature dependence of relaxation mechanisms in amorphous polymers and other glass-forming liquids," *Journal of the American Chemical Society*, vol. 77, no. 14, pp. 3701–3707, 1955.
- [70] U. W. Gedde, *Polymer Physics*, Springer, 1995.
- [71] E. Catsiff and A. V. Tobolsky, "Stress-relaxation of polyisobutylene in the transition region," *Journal of Colloid Science*, vol. 10, no. 4, pp. 375–392, 1955.
- [72] J. M. Pochan, H. W. Gibson, M. F. Froix, and D. F. Hinman, "Dielectric relaxation studies of bisphenol A-diphenyl carbonate/lexan polycarbonate solid solutions," *Macromolecules*, vol. 11, no. 1, pp. 165–171, 1978.
- [73] J. A. Campbell, A. A. Goodwin, and G. P. Simon, "Dielectric relaxation studies of miscible polycarbonate/polyester blends," *Polymer*, vol. 42, no. 10, pp. 4731–4741, 2001.
- [74] B. J. Factor, F. I. Mopsik, and C. C. Han, "Dielectric behavior of a polycarbonate/polyester mixture upon transesterification," *Macromolecules*, vol. 29, no. 6, pp. 2318–2320, 1996.
- [75] G. Katana, F. Kremer, E. W. Fischer, and R. Plaetschke, "Broadband dielectric study on binary blends of bisphenol-A and tetramethylbisphenol-A polycarbonate," *Macromolecules*, vol. 26, no. 12, pp. 3075–3080, 1993.
- [76] C. Liu, C. Li, P. Chen, J. He, and Q. Fan, "Influence of long-chain branching on linear viscoelastic flow properties and dielectric relaxation of polycarbonates," *Polymer*, vol. 45, no. 8, pp. 2803–2812, 2004.
- [77] A. S. Merenga, C. M. Papadakis, F. Kremer, J. Liu, and A. F. Yee, "Comparative broad-band dielectric study on poly(ester carbonate)s with 1,4-cyclohexylene linkages," *Macromolecules*, vol. 34, no. 1, pp. 76–81, 2001.
- [78] E. El Shafee, G. R. Saad, and M. Zaki, "Calorimetric and dielectric study on poly(trimethylene terephthalate)/ polycarbonate blends," *Journal of Polymer Research*, vol. 15, no. 1, pp. 47–58, 2008.
- [79] K. Mohomed, T. G. Gerasimov, F. Moussy, and J. P. Harmon, "A broad spectrum analysis of the dielectric properties of poly(2-hydroxyethyl methacrylate)," *Polymer*, vol. 46, no. 11, pp. 3847–3855, 2005.
- [80] S. J. Havriliak and S. Havriliak Jr., *Dielectric and Mechanical Relaxation in Materials*, 1996.
- [81] S. K. Emran, Y. Liu, G. R. Newkome, and J. P. Harmon, "Viscoelastic properties and phase behavior of 12-tert-butyl

- ester dendrimer/poly(methyl methacrylate) blends," *Journal of Polymer Science B*, vol. 39, no. 12, pp. 1381–1393, 2001.
- [82] P. Pissis and A. Kyritsis, "Electrical conductivity studies in hydrogels," *Solid State Ionics*, vol. 97, no. 1–4, pp. 105–113, 1997.
- [83] M. G. Parthun and G. P. Johari, "Analyses for a dipolar relaxation in the featureless dielectric spectrum, and a comparison between the permittivity, modulus and impedance representations," *Journal of the Chemical Society, Faraday Transactions*, vol. 91, no. 2, pp. 329–335, 1995.
- [84] J. H. Ambrus, C. T. Moynihan, and P. B. Macedo, "Conductivity relaxation in a concentrated aqueous electrolyte solution," *Journal of Physical Chemistry*, vol. 76, no. 22, pp. 3287–3295, 1972.
- [85] A. K. Jonscher, "Dielectric relaxation in solids," *Journal of Physics D*, vol. 32, no. 14, pp. R57–R70, 1999.
- [86] A. K. Jonscher, *Dielectric Relaxation in Solids*, 1983.
- [87] R. A. Kalgaonkar and J. P. Jog, "Molecular dynamics of copolyester/clay nanocomposites as investigated by viscoelastic and dielectric analysis," *Journal of Polymer Science B*, vol. 46, no. 23, pp. 2539–2555, 2008.

## Research Article

# Nylon/Graphene Oxide Electrospun Composite Coating

Carmina Menchaca-Campos,<sup>1</sup> César García-Pérez,<sup>1</sup> Iván Castañeda,<sup>1</sup>  
Miguel A. García-Sánchez,<sup>2</sup> René Guardián,<sup>1</sup> and Jorge Uruchurtu<sup>1</sup>

<sup>1</sup> UAEM Centro de Investigación en Ingeniería y Ciencias Aplicadas, Avenida Universidad 1001,  
Col Chamilpa, 62209 Cuernavaca, MOR, Mexico

<sup>2</sup> Departamento de Química, UAM-Iztapalapa, Avenida San Rafael Atlixco 186, Vicentina, 09340 México, DF, Mexico

Correspondence should be addressed to Jorge Uruchurtu; [juch25@uaem.mx](mailto:juch25@uaem.mx)

Received 23 March 2013; Revised 2 July 2013; Accepted 3 July 2013

Academic Editor: Osman Gencel

Copyright © 2013 Carmina Menchaca-Campos et al. This is an open access article distributed under the Creative Commons Attribution License, which permits unrestricted use, distribution, and reproduction in any medium, provided the original work is properly cited.

Graphite oxide is obtained by treating graphite with strong oxidizers. The bulk material disperses in basic solutions yielding graphene oxide. Starting from exfoliated graphite, different treatments were tested to obtain the best graphene oxide conditions, including calcination for two hours at 700 °C and ultrasonic agitation in acidic, basic, or peroxide solutions. Bulk particles floating in the solution were filtered, rinsed, and dried. The graphene oxide obtained was characterized under SEM and FTIR techniques. On the other hand, nylon 6-6 has excellent mechanical resistance due to the mutual attraction of its long chains. To take advantage of the properties of both materials, they were combined as a hybrid material. Electrochemical cells were prepared using porous silica as supporting electrode of the electrospun nylon/graphene oxide films for electrochemical testing. Polarization curves were performed to determine the oxidation/reduction potentials under different acidic, alkaline, and peroxide solutions. The oxidation condition was obtained in KOH and the reduction in H<sub>2</sub>SO<sub>4</sub> solutions. Potentiostatic oxidation and reduction curves were applied to further oxidize carbon species and then reduced them, forming the nylon 6-6/functionalized graphene oxide composite coating. Electrochemical impedance measurements were performed to evaluate the coating electrochemical resistance and compared to the silica or nylon samples.

## 1. Introduction

Graphite oxide is a compound of carbon, oxygen, and hydrogen in variable ratios, commonly obtained by treating graphite with strong oxidizers. Strictly speaking “oxide” is an incorrect but historically established name, since graphite is not a metal. The bulk material disperses in basic solutions yielding monomolecular sheets, known as graphene oxide by analogy to graphene, the single-layer form of graphite [1]. Graphene oxide (GO) sheets have recently attracted substantial interest as a possible intermediate for the manufacture of graphene. It typically preserves the layer structure of the parent graphite, but the layers are buckled and the interlayer spacing is about two times larger (~0.7 nm) than that of graphite. Graphene oxide layers are about 1.1 ± 0.2 nm thick [2–6]. The edges of each layer are terminated with carboxyl

and carbonyl groups. The detailed structure is still not understood due to the strong disorder and irregular packing of the layers [1].

One of the methods used to separate the layers of graphite consists in an aggressive oxidative processes which functionalize the periphery and some places of the graphene surface, principally in those places in which defects exist. As consequence oxygenated organic functions can be attached in those places inducing attractions with polar species and solvents and repulsion with the hydrophobic regions of the grapheme layer. The existence of organic functions attached in the surface and periphery of the grapheme layers made possible its covalent union with other chemical or biochemical species, susceptible of being used in diverse technological areas. This modification induces that layers losses their planarity and promote their separation.

Since nylon discovery, a great interest has been developed due to its technological importance, its commercial characteristic, and its complexity related to the morphological changes associated to its crystallinity, not only in solid state but also in solution and under melting point conditions. In general, nylon 6-6 (Ny) has excellent mechanical resistance due to the mutual attraction of their long chains due to hydrogen bonds and their cross-linking [7].

Electrospinning is a recognized technique to create polymer fibers with diameter ranging from 40 to 2000 nanometers. Fibers can be electrospun direct from solution or from the fused material state, controlling the diameter size through adjustment of the surface tension, solution concentration, conductivity, and so forth [5–7]. Electrospinning occurs when the electric force of the solution surface overcomes the surface tension and triggers an electric spark provoking the solution to be expelled from the containing device (syringe), and the jet flow impacts, deposits, and is collected in a metal screen. When the expelled material dries out or solidifies, it forms an electric charged fiber, and this could be directed or speeded up by electric forces. In other words, a polymer solution in a syringe is charged to a high electrical potential. As the jet stretches and dries, radial electrical forces cause it to splash repeatedly. The dried, solidified fibers are collected on an electrically conducting screen (Figure 1).

This work proposes a possible application for commercial nylon 6-6 electrospun fibers and functionalized graphene oxide (Ny/FGO) producing a corrosion protection composite coating, through electrochemical procedures. It was characterized throughout spectroscopic analysis and the coating electrochemical performance was evaluated.

## 2. Experimental

**2.1. Coating Preparation.** Two types of coatings were prepared, from electrospinning commercial nylon 6-6 over porous silica, at ambient temperature. The system consists of a controlled power source (Glassman High Voltage, Inc.) providing a high voltage to create a high electrostatic field, an injector or perfusion pump (SryngePump.com, Model NE300, 11 VDC Volts/Hertz, 0.75 Amperes) generating pressure to a connected syringe, expelling the fluid. When the effects of polarization and electric charge, as a consequence of the electric field are present, a jet solution is triggered over the porous silica collector placed over a conducting screen or plate electrically down earthed (in this case commercial aluminum sheet). During the jet formation, the solvent gradually evaporates and the fluid discharges are induced through the separation distance of the electrodes (syringe tip and collector) breaking up the surface tension across the electric field forming a tangential ( $\tau_t$ ) and a normal ( $\tau_n$ ) components, forming Taylor's cone (see Figure 1).

**2.1.1. Graphene Oxide.** Starting from mechanically exfoliated graphite (MEG), different treatments were tested in order to obtain the best graphene oxide (GO) conditions. These included calcinations in a muffle for two hours at 700°C, in order to remove contaminants and undesirable functional groups that maintain the graphite oxide layers bonded. After

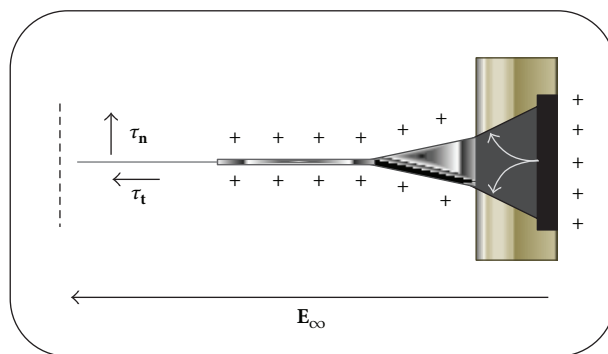


FIGURE 1: Taylor's cone in the electrospinning system.

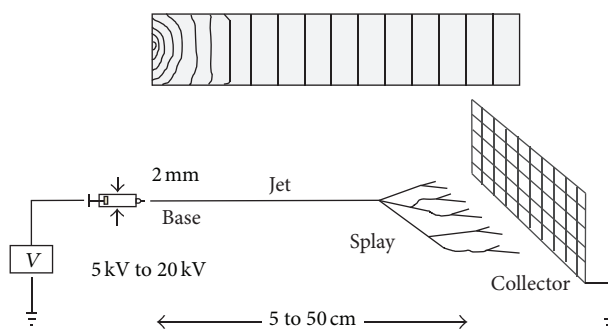


FIGURE 2: Electrospinning system.

that, ultrasonic agitation for three hours: in formic acid, KOH-NaOH basic or peroxide solution was performed. Afterwards, floating particles were collected, filtered, rinsed, and dried at ambient temperature to obtain the GO.

**2.1.2. Nylon 6-6 Electrospun Film.** Two types of coating samples were prepared; one was electrospinning Nylon (Ny) fibers under environmental room temperature (25°C) with 1.20 g nylon 6-6 dissolved in 7 ml of formic acid. This mixture was left under gentle agitation for approximately 12 h. The other coating was prepared adding graphene oxide (GO) to the nylon solution. Electrospinning was carried out using a power source and a dosage syringe, at 12 kV voltage and a tip-collector distance of 12 cm and a flow rate of 0.2 mL/h (Figure 2). An electrospun nylon 6-6 film was formed after a few hours and collected over a porous silica (because it is a conductive material) plate used as screen.

### 2.2. Electrodes Preparation

**2.2.1. Ny/FGO Electrochemical Coating Preparation.** Two different electrospun Ny/GO coatings were prepared from a polymeric solution, consisting of 90% of formic acid, 0.36% or 2% by wt. of GO, and the rest of Ny. To functionalize the GO to form the composite coating the system was electrochemically treated, preparing electrochemical cells using porous silica covered with electrospun Ny/GO films as electrodes. Further oxidation and reduction by electrochemical procedures to obtain Ny/FGO composite were carried

out. Polarization curves were performed to determine the best oxidation/reduction potentials under different acidic ( $\text{H}_2\text{SO}_4$ ), alkaline (KOH), and peroxide ( $\text{H}_2\text{O}_2$ ) solutions.

After obtaining the best electrochemical conditions, the procedure adopted was to oxidize in alkaline and reduce in acid solutions, adding up a few drops of hydrazine to suppress the oxygen reduction reaction improving the efficiency of the reduction process to obtain the nylon-graphene oxide composite bonding taking place during this process.

**2.2.2. Ny/GO Coating Prepared by Deposit.** Another sample of coating was prepared in order to compare the efficiency of the electrospun coating. In this case, a nylon 6-6 electrospun film was collected over a porous silica substrate, and then a GO layer was placed over it, followed by the oxidation/reduction process from the electrolytic solution, obtaining the Ny/FGO composite coating at the end.

**2.3. Characterization.** Functionalized graphene oxide samples were characterized using SEM and FTIR techniques. Nylon fiber samples were characterized, and the results were presented by the authors previously [8].

**2.3.1. Scanning Electron Microscopy.** To determine their size or form, GO flakes samples, used as part of the composite electrode coating for electrochemical measurements, were prepared for SEM (Model LEO operating at 6 kV, at 1, 2, and 10 kX resolution) analysis. Flakes were vacuum sputtered and covered with Au-Pd to provide conductivity.

Energy dispersive X-Ray spectroscopy (EDX), a semianalytical technique attached to SEM, was performed to determine the elemental analysis of GO in order to corroborate the presence of oxygenated functional groups.

**2.3.2. Infrared Spectroscopy (FT-IR).** FT-IR spectra were registered, in the frequency range  $500\text{--}4000\text{ cm}^{-1}$ , resolution  $4\text{ cm}^{-1}$ , in a spectrophotometer Model Bruker Vector 22, equipped with ATR accessory and the OPUS 5.5 software.

**2.3.3. UV-Visible.** UV-visible absorption spectra were recorded on a Cary 5000 UV-Vis-NIR scanning spectrophotometer and using nylon fiber as the reference sample (blank).

**2.4. Electrochemical Measurements.** Electrochemical measurements, namely, polarization curves and electrochemical impedance (EIS), were performed using a Gill ACM electrochemical instrument. Polarization curves were performed to determine the best oxidation/reduction potentials under different acidic, alkaline, and peroxide solutions. Polarization curves were performed from  $-1500$  to  $1500$  mV at a rate of  $100\text{ mV/min}$ . Potentiostatic oxidation and reduction curves were performed at  $1000$  and  $-1000$  mV, respectively, versus a  $\text{Ag/AgCl}_2$  electrode, to further oxidize carbon species and then to reduce them in both types of Ny/GO films. The Ny/FGO composite coatings were formed.

Electrochemical impedance measurements were performed to evaluate the coating and compared to the silica or nylon “only” samples. EIS measurements were done at

the open circuit potential, in the frequency interval  $10000$  to  $0.05\text{ Hz}$  with  $\pm 20\text{ mV}$  amplitude using an SCE and a graphite auxiliary electrode. Fifty points were obtained, and 7 decades of frequency were covered during measurements [9–11].

### 3. Results

**3.1. SEM Graphene Oxide Characterization.** Figure 3 presents the SEM micrographs characterizing the MEG and treated graphite with temperature and different solutions in ultrasound (Figures 3(a) to 3(d)). Apparently the acid or basic treatments render solids consisting of aggregates of smaller, disordered, and slightly folded layers of graphene oxide. In the thermally treated sample a porous structure was observed, probably due to impurities present in the original graphite and eliminated during the thermal treatment at  $700^\circ\text{C}$  (Figure 3(a)). After the thermal treatment, to facilitate the separation of the graphite plates from the porous structure, a subsequent chemical treatment in acid, basic, and peroxide solutions (formic acid,  $\text{KOH}:\text{NaOH}$  or  $\text{H}_2\text{O}_2$ ), and with ultrasonic vibrations was performed (Figures 3(b), 3(c), and 3(d), resp.). This procedure renders a solid with lower dimensions in the graphene oxide plates or sheets, especially in the case for the peroxide solution treatment, in which planar or slightly folded separated GO layers are clearly seen over the surface.

**3.2. EDX Graphene Oxide Characterization.** Folded particle samples thermally pretreated at  $700^\circ\text{C}$  followed by ultrasonic vibration in an  $\text{H}_2\text{O}_2$  solution are presented in Figures 4 and 5. A SEM general view ( $2000\times$ ) of the surface and a higher magnification ( $10000\times$ ) show the effect of this treatment that rendered folded sheets thinner and varied in size.

A folded particle sample was characterized using SEM and EDX as can be seen in Figure 5. The chemical composition of a GO thin sheet (Figure 5(a)) was determined through energy dispersive X-rays (EDX), as seen in Figure 5(b). Sheet characterization shows the presence of carbon and oxygen in its structure, confirming the presence of oxygen groups attached over a structure principally constituted by carbon (Figure 5(b)). The low oxygen percentage may be due to the weak peroxide oxidation process, compared to other chemical oxidation, such as the Hummer's process. The O/C ratio obtained in our procedure is  $0.048$  between the ratios for pristine graphite ( $0.014$ ) and GO ( $0.582$ ) [12, 13].

**3.3. FT-IR Characterization.** Taking into consideration the best conditions for the graphene oxide particles formed under peroxide solution, analysis with SEM, FT-IR, and UV was performed. This analysis was carried out to observe the material structural changes and compared to the MEG blank (Figure 6). The graph presents the spectrum obtained for MEG after chemical treatment in the peroxide solution showing characteristic bands related to the graphene oxide (GO), around  $1628\text{ cm}^{-1}$  corresponding to the stretching vibration of the C=C bond, assigned to the  $\pi$ -bonds that form the extended conjugated and aromatic layer of graphene.

Other bands around  $1050\text{ cm}^{-1}$  correspond to the characteristic vibration of C–O bonds, as well as the bands

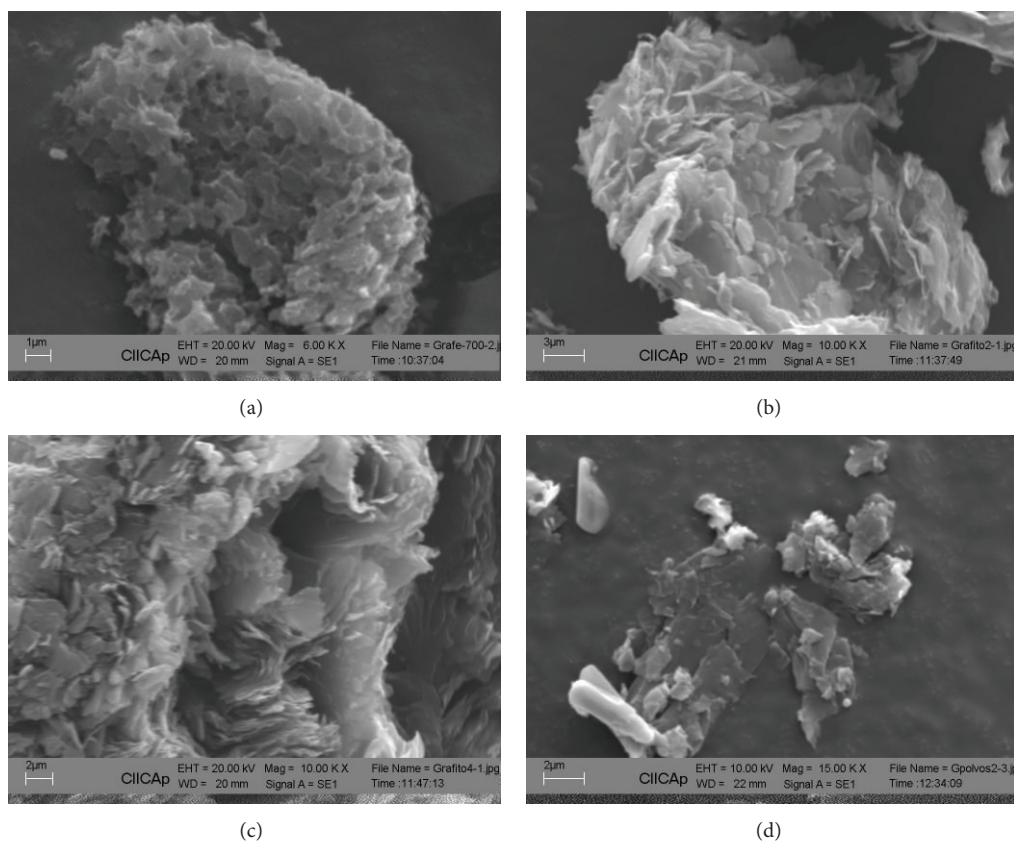


FIGURE 3: SEM images of MEG under thermal treatment at 700°C with temperature and in different solutions with ultrasound: (a) treated to 700°C, (b) treated to 700°C and formic acid, (c) treated to 700°C and KOH : NaOH 1 M (1 : 1), and (d) treated to 700°C and H<sub>2</sub>O<sub>2</sub>.

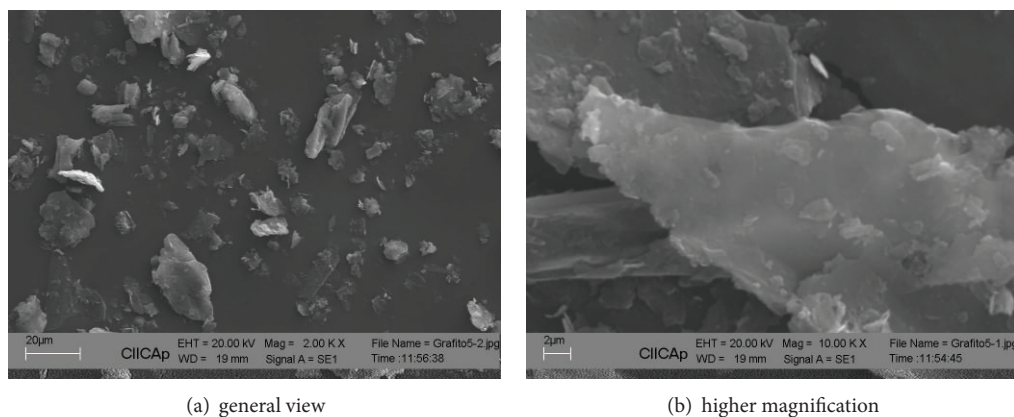
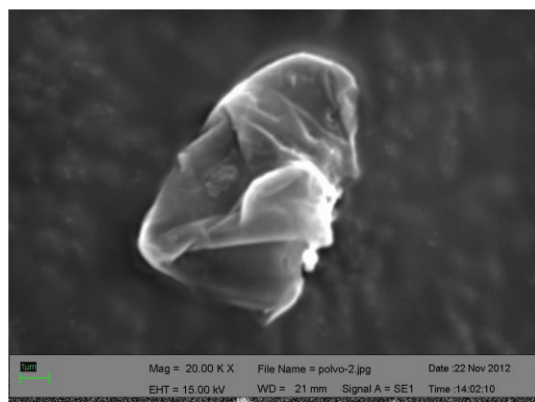


FIGURE 4: SEM images of the GO sample pretreated at 700°C and ultrasonic vibration in H<sub>2</sub>O<sub>2</sub> solution.

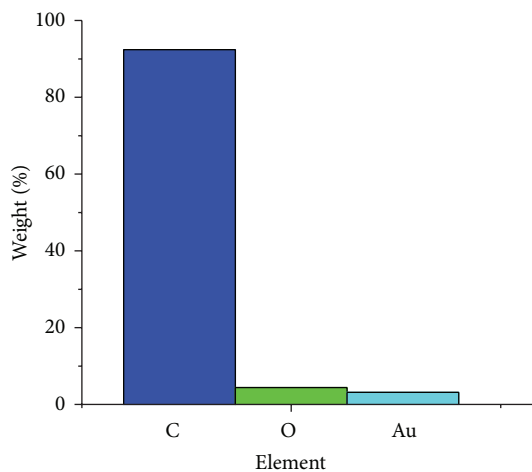
associated to the stretching and bending of the OH bond at 3000–3500 cm<sup>-1</sup> and 1419 cm<sup>-1</sup>, respectively. Also an 880 cm<sup>-1</sup> band was observed, attributed to vibrations of the epoxy group, although small bands near the region of the 1700 cm<sup>-1</sup> could be related to the presence of carbonyl (C=O) or carboxyl (-COO) groups formed at the edges of the graphite plate layers. These results confirm the best condition for graphene oxide plate formation. The presence of all the above oxygen in the GO layer is accompanied with loss of planarity

of the affected carbons which, combined with the more hydrophilic nature of these groups, induces the penetration of solvent molecules and makes possible the separation of some layers.

According to the literature [14], the most characteristic features in the FT-IR spectrum of GO are the adsorption bands corresponding to the C=O carbonyl stretching at 1733 cm<sup>-1</sup>, the O-H deformation vibration at 1412 cm<sup>-1</sup>, the C-OH stretching at 1226 cm<sup>-1</sup>, and the C-O stretching at



(a) GO layer



(b) EDX

FIGURE 5: SEM image of GO and the characterized area through EDX.

$1053\text{ cm}^{-1}$ . The O–H stretches appear at  $3400\text{ cm}^{-1}$  as a broad and intense signal; the resonances at  $1621\text{ cm}^{-1}$  are assigned to the vibrations of the adsorbed water molecules, overlapped with the C=C skeletal vibrations of unoxidized graphitic domains. This is compared to the bands obtained (Figure 6).

Once the best GO sheets formation conditions were established, they were used to form the composite electrospun Ny/GO coating. The nylon film thickness formed during three hours was established and determined through SEM analysis and presented in Figure 7. An average around  $9.5\text{ }\mu\text{m}$  film thickness of nylon fibers was obtained through the electrospinning deposition. In the film area the presence of large and well-defined nylon fibers can be observed in an intricate and compact mesh that covers the substrate. Because of its size, the presence of the GO layers cannot be clearly seen.

### 3.4. Electrochemical Coating Formation

**3.4.1. Polarization Curves.** To obtain the best electrochemical conditions for the Ny/FGO coating formation, polarization curves were determined under acid, neutral, and basic solutions to observe the best oxidation-reduction conditions. Figure 8 presents the polarization curves, where the higher oxidation and reduction current densities can easily be observed. The best oxidation condition was obtained in KOH and peroxide solutions, and the best reduction with hydrogen peroxide was obtained when  $\text{H}_2\text{SO}_4$  solution was used. These conditions were established according to the polarization curves obtained.

In view of the above-mentioned results, potentiostatic oxidation and reduction curves were applied to further oxidize carbon species and then to reduce them over the porous silica substrate containing either the electrospun Ny/GO composite film or the electrospun nylon film covered with a layer of GO, to form the Ny/FGO composite coating in both cases.

The potentiostatic oxidation/reduction polarization curves obtained, using KOH (0.5 M) or  $\text{H}_2\text{SO}_4$  ( $\text{pH} = 2$ )

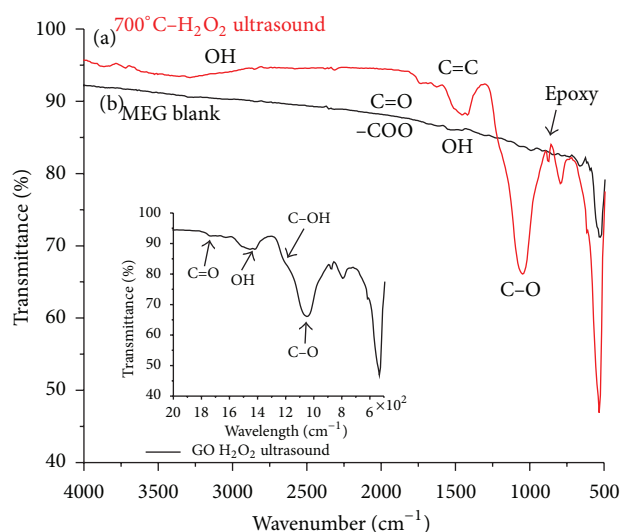


FIGURE 6: FT-IR spectra: (a) thermally pretreated graphene oxide plates in peroxide solution and ultrasonic vibration and (b) MEG blank.

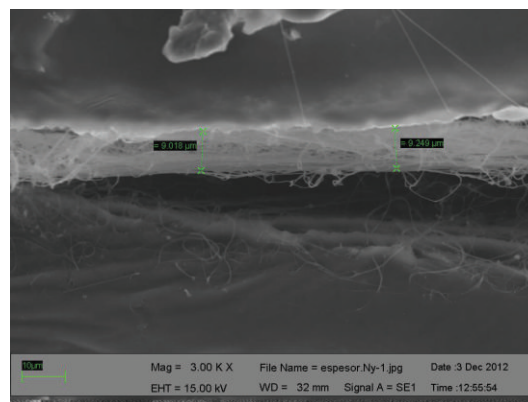


FIGURE 7: Ny/GO fibre film thickness formed after three hours of electrospinning.

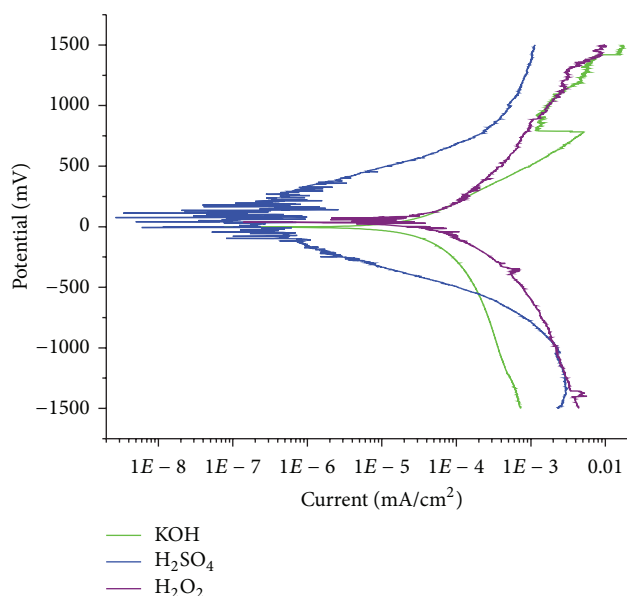


FIGURE 8: Polarization curve for electrospun Ny/FGO coating under acid, neutral, and basic solutions.

solutions, as a function of time, are presented in Figures 9(a) and 9(b). For comparison, potentiostatic polarization curve for a porous silica electrode was performed and included as a reference sample (blank). For the potentiostatic oxidation (Figure 9(a)) and reduction (Figure 9(b)) curves, the highest current density values were for the graphene oxide deposited over the electrospun nylon film electrode. The lower values registered were for the porous silica electrode (blank), as expected. A composite electrospun Ny/FGO film coating was obtained.

Furthermore, an electrospun Ny/FGO composite coating was obtained, which SEM micrographs show a general view and magnification of the coated system (Figure 10). In Figure 10(a) a complex network of Ny/FGO plates can be observed. It is possible to observe, in the micrograph of Figure 10(b), the presence of functionalized graphite oxide layers bonded and surrounded but not crossed by the nylon fibres. This peculiar pathway suggests that the presence of hydrophilic groups in the periphery of the GO layers makes possible its interaction with the amide groups ( $-\text{CO}-\text{NH}-$ ) of the nylon fibres. The nature of both species in the materials can be observed and confirmed through visible UV spectroscopy.

**3.4.2. UV-Vis Characterization.** In the visible UV absorption spectra of the Ny/GO 0.36% and 2% systems were observed. For the Ny/GO 2% system an absorption peak at 230 nm assigned to the  $\pi-\pi^*$  transition of the aromatic C=C bonds is observed (Figure 11). Also, an absorption peak at 300 nm for both compounds is present and representing the graphite oxide reduction [15]. As long as the absorption spectrum displacement is larger towards the visible region, the graphite oxide deoxygenation is higher according to some authors [16]. This especially occurs when the reduction does not reconstitute the double bonds C=C to the rest of the conjugated

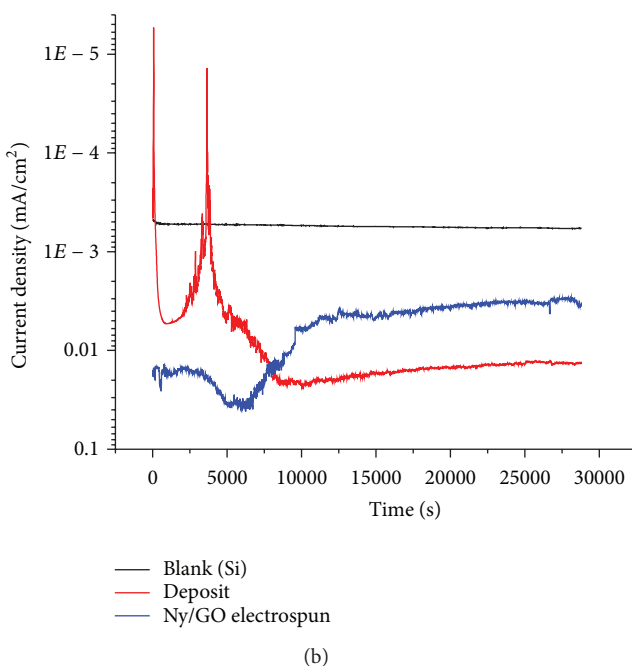
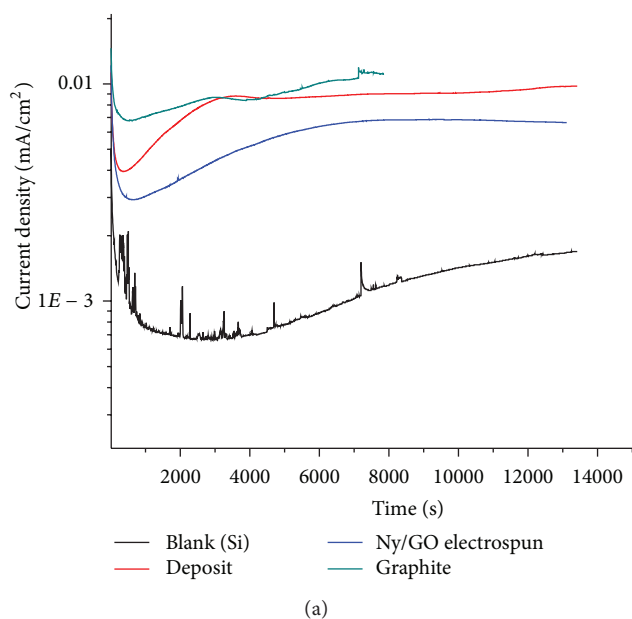


FIGURE 9: Potentiostatic curves, at 1000 mV for the (a) oxidation of the Ny/GO in basic KOH, 0.5 M solution during 3.5 hr and (b) reduction of the Ny/GO in  $\text{H}_2\text{SO}_4$ , pH 2 solution during 8 hr.

$\pi$ -electrons system of the graphite oxide layer. As was above-mentioned, the presence of more  $\text{sp}^3$  carbon hybridization, as consequence of the oxidation reaction, increases the nonplanarity of GO. Reduction of few oxide groups was reached.

Electrochemical impedance measurements were performed to evaluate the Ny/FGO at 2% electrospun composite coating under different  $\text{Na}_2\text{SO}_4$  concentration solutions. The Bode plots presented in Figure 12 show the total impedance values for the Ny/FGO sample for different solution concentration. In general, an inverse relation was obtained for the overall impedance as a function of solution concentration,

TABLE 1: Determined capacitance at low and high frequency of the Ny/FGO systems using different  $\text{Na}_2\text{SO}_4$  concentrations.

$\text{Na}_2\text{SO}_4$ concentration	Ny/FGO 0.36% electrospun Capacitance ( $\text{F}/\text{cm}^2$ ) $f = 0.8$	Ny/FGO 2% electrospun Capacitance ( $\text{F}/\text{cm}^2$ ) $f = 0.8$	Ny/FGO 2% deposited Capacitance ( $\text{F}/\text{cm}^2$ ) $f = 0.8$
0.001 M	$1.37803E - 05$	$8.90726E - 07$	$1.52E - 4$
0.01 M	$2.66143E - 05$	$1.06257E - 07$	$1.60E - 4$
0.1 M	$4.48955E - 05$	$8.58827E - 07$	$1.52E - 4$
1 M	$4.49426E - 05$	$7.47008E - 07$	$1.81E - 4$

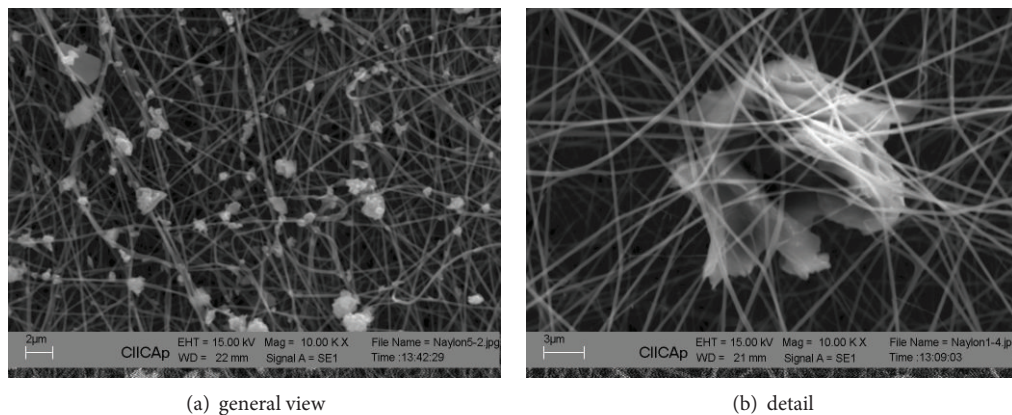


FIGURE 10: SEM of electrospun Ny/FGO composite at 10 k x magnification.

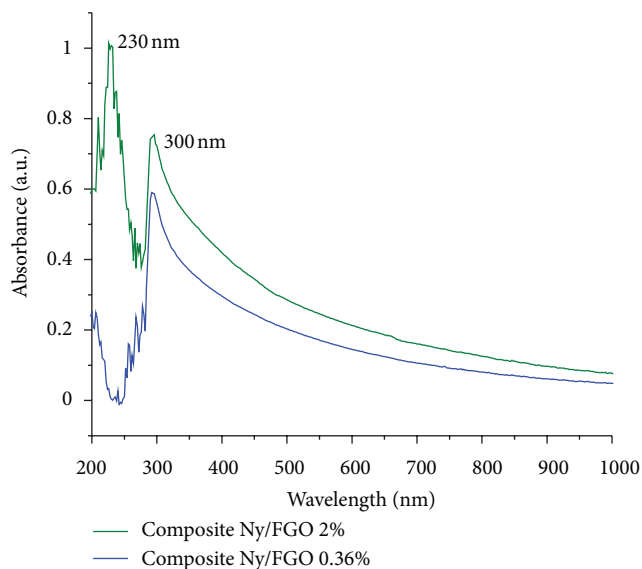
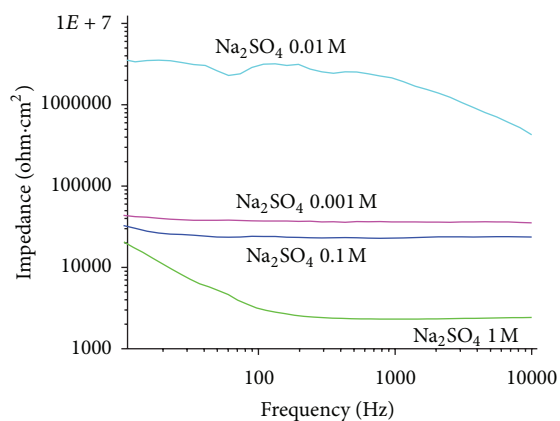


FIGURE 11: UV-Vis spectra of the systems: Ny/FGO with 2% and with 0.36%.

reflecting coating performance [17]. This is possibly due to the possible difficulty of aggressive species diffusing through the coating as well as modifying the electron discharge of the cathodic reaction, therefore diminishing the metal degradation [18, 19]. This also reflects the effects of the solution over the porous silica substrate [17].

FIGURE 12: Electrochemical evaluation of the system Ny/FGO at 2% GO with the impedance as a function of  $\text{Na}_2\text{SO}_4$  solution concentration.

Coating capacitance was obtained from (1). The values obtained from the impedance parameters for Ny/FGO at 0.36 and 2% for different  $\text{Na}_2\text{SO}_4$  solution concentrations are shown in Table 1:

$$C_{\text{coat}} = \frac{1}{2\pi f R_{\text{pore}}}, \quad (1)$$

where  $C_{\text{coat}}$  represents the coating capacitance and  $R_{\text{pore}}$  the coating resistance related to the porosity.

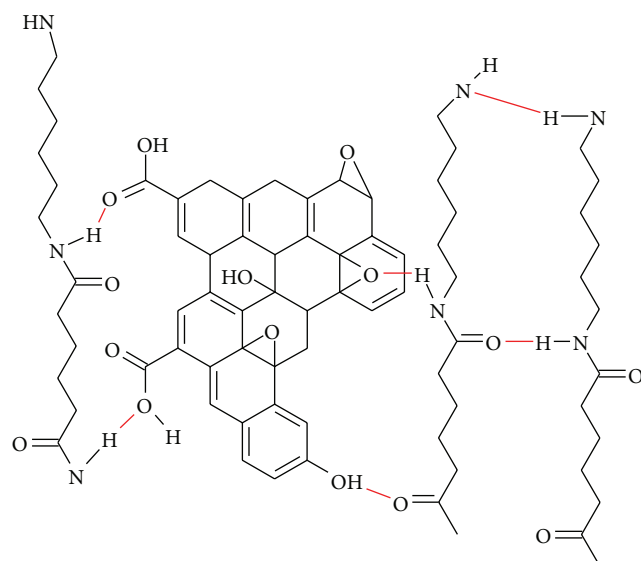


FIGURE 13: Possible coupling of nylon and FGO through hydrogen bonds and dipole-dipole interactions.

Capacitance values obtained for the Ny/FGO suggest a charge storage capacity for the coating condition. The capacitance obtained for the deposited GO sample presents higher values, therefore greater charge storage. A proposal is made of the functionalized graphene oxide, and polymeric fibres association occurs by means of the dipole-dipole and hydrogen bridge interactions, according to the proposed model in Figure 13. This union is formed between the hydrogen or oxygen from the amide group ( $-\text{CO}-\text{NH}-$ ) and one hydrogen or oxygen from the functional groups present in the graphite oxide, possibly carboxyl ( $-\text{COOH}$ ) or carbonyl ( $\text{C}=\text{O}$ ) groups [20].

#### 4. Conclusions

A composite coating consisting of electrospun Ny/FGO was produced through electrochemical procedures. The coupling of nylon and the graphite oxide layers can be explained mainly by the interactions of the amide groups of nylon and the hydrophilic groups present in the periphery of the GO. Their coating electrochemical performance was evaluated presenting good coating properties and capacitance values. The best coating capacitance was obtained for the Ny/FGO 2% sample by deposit. Good charge storage properties were obtained.

#### Conflict of Interests

The authors declare in this paper there is no conflict of interests.

#### Acknowledgments

The authors wish to thank the Ministry of Education (SEP-PROMEP) for the support provided both to the Academic Body “Desarrollo y Análisis de Materiales Avanzados” (UAEMOR-CA-43) and to the Academic Network “Diseño

Nanoscópico y Textural de Materiales Avanzados.” Finally, the authors thank CONACyT for the grants received during this work.

#### References

- [1] D. R. Dreyer, S. Park, C. W. Bielawski, and R. S. Ruoff, “The chemistry of graphene oxide,” *Chemical Society Reviews*, vol. 39, no. 1, pp. 228–240, 2010.
- [2] C. Gómez-Navarro, R. T. Weitz, A. M. Bittner et al., “Electronic transport properties of individual chemically reduced graphene oxide sheets,” *Nano Letters*, vol. 7, no. 11, pp. 3499–3503, 2007.
- [3] A. I. Altsybeeva and S. Z. Levin, *Metal Corrosion Inhibitors*, edited by L. I. Antropov, Khimiya, Leningrad, Russia, 1968.
- [4] R. Yuhnevich, V. Bogdanovich, E. Valashkovsky, and A. Vidukhovskiy, *Technika Przeciwkorozyjna*, Wydawnictwa Szkolne i Pedagogiczne, Warszawa, Poland, 1976.
- [5] A. L. Yarin, S. Koombhongse, and D. H. Reneker, “Taylor cone and jetting from liquid droplets in electrospinning of nanofibers,” *Journal of Applied Physics*, vol. 90, no. 9, pp. 4836–4846, 2001.
- [6] Y. M. Shin, M. M. Hohman, M. P. Brenner, and G. C. Rutledge, “Experimental characterization of electrospinning: the electrically forced jet and instabilities,” *Polymer*, vol. 42, no. 25, pp. 9955–9967, 2001.
- [7] C. Menchaca, B. Manoun, G. Martínez-Barrera, V. M. Castaño, and H. López-Valdivia, “In situ high-temperature Raman study of crystalline nylon 6,12 fibers gamma-irradiated in argon atmosphere,” *Journal of Physics and Chemistry of Solids*, vol. 67, no. 9-10, pp. 2111–2118, 2006.
- [8] C. Menchaca, I. Castañeda, A. Soto-Quintero et al., “Characterization of a “smart” hybrid varnish electrospun nylon benzotriazole copper corrosion protection coating,” *International Journal of Corrosion*, vol. 2012, Article ID 925958, 10 pages, 2012.
- [9] R. Cottis and S. Turgoose, *Electrochemical Impedance and Noise*, NACE Internacional, Houston, Tex, USA, 1999.
- [10] J. Botana and M. Marcos, *Ruido Electroquímico, Métodos de Análisis*, SEPTM, Oviedo, España, 2006.
- [11] M. A. González-Núñez and J. Uruchurtu-Chavarin, “R/S fractal analysis of electrochemical noise signals of three organic coating samples under corrosion conditions,” *Journal of Corrosion Science and Engineering*, vol. 6, supplement C117, 2003.
- [12] W. S. Hummers Jr. and R. E. Offeman, “Preparation of graphitic oxide,” *Journal of the American Chemical Society*, vol. 80, no. 6, p. 1339, 1958.
- [13] K. Haubner, J. Morawski, P. Olk et al., “The route to functional graphene oxide,” [http://tu-dresden.de/die\\_tu\\_dresden/fakultaeten/fakultaet\\_mathematik\\_und\\_naturwissenschaften/fachrichtung\\_chemie/mc/publikationen/download/Haubner10.pdf](http://tu-dresden.de/die_tu_dresden/fakultaeten/fakultaet_mathematik_und_naturwissenschaften/fachrichtung_chemie/mc/publikationen/download/Haubner10.pdf).
- [14] S. Stankovich, R. D. Piner, S. T. Nguyen, and R. S. Ruoff, “Synthesis and exfoliation of isocyanate-treated graphene oxide nanoplatelets,” *Carbon*, vol. 44, no. 15, pp. 3342–3347, 2006.
- [15] D. Li, M. B. Müller, S. Gilje, R. B. Kaner, J. Gordon, and G. Wallace, “Processable aqueous dispersions of graphene nanosheets,” *Nature Nanotechnology*, vol. 3, no. 2, pp. 101–105, 2008.
- [16] J. I. Paredes, S. Villar-Rodil, M. J. Fernández-Merino, L. Guardia, A. Martínez-Alonso, and J. M. D. Tascón, “Environmentally friendly approaches toward the mass production of processable graphene from graphite oxide,” *Journal of Materials Chemistry*, vol. 21, pp. 298–306, 2011.

- [17] J. Uruchurtu and J. L. Ramírez, *Método Experimental en la Corrosión: Impedancia Electroquímica*, Editorial Académica Española, Berlin, Germany, 2011.
- [18] A. S. Khanna, M. K. Totlani, and S. K. Singh, *Corrosion and Its Control*, vol. 2, Elsevier, Amsterdam, The Netherlands, 1998.
- [19] D. H. Reneker and I. Chun, "Nanometre diameter fibres of polymer, produced by electrospinning," *Nanotechnology*, vol. 7, no. 3, pp. 216–223, 1996.
- [20] A. Castro-Beltrán, S. Sepúlveda-Guzmán, W. J. de la Cruz-Hernández, and R. Cruz-Silva, "Obtención de grafeno mediante la reducción química del óxido de grafito," *Ingenierías*, vol. 7–9, no. 14, article 52, 2011.

## Research Article

# Synthesis and Characterization of Polyphosphazenes Modified with Hydroxyethyl Methacrylate and Lactic Acid

Evelyn Carolina Martínez Ceballos,<sup>1,2</sup> Ricardo Vera Graziano,<sup>2</sup>  
Gonzalo Martínez Barrera,<sup>3</sup> and Oscar Olea Mejía<sup>4</sup>

<sup>1</sup> Facultad de Química, Universidad Autónoma del Estado de México, Paseo Colón esq. Paseo Tollocan, 50120 Toluca, ME, Mexico

<sup>2</sup> Departamento de Polímeros, Instituto de Investigaciones en Materiales, Universidad Nacional Autónoma de México, 04510 Coyoacán, DF, Mexico

<sup>3</sup> Laboratorio de Investigación y Desarrollo de Materiales Avanzados (LIDMA), Facultad de Química, Universidad Autónoma del Estado de México, Km 12 de la carretera Toluca-Atlaconulco, 50200 San Cayetano, ME, Mexico

<sup>4</sup> Centro Conjunto de Investigación en Química Sustentable UAEM-UNAM, Facultad de Química, Universidad Autónoma del Estado de México, Carretera Toluca-Atlaconulco, Km 14.5, Unidad El Rosedal, 50200 San Cayetano, ME, Mexico

Correspondence should be addressed to Evelyn Carolina Martínez Ceballos; [evycam74@gmail.com](mailto:evycam74@gmail.com)

Received 14 March 2013; Revised 29 May 2013; Accepted 25 June 2013

Academic Editor: Carmina Menchaca-Campos

Copyright © 2013 Evelyn Carolina Martínez Ceballos et al. This is an open access article distributed under the Creative Commons Attribution License, which permits unrestricted use, distribution, and reproduction in any medium, provided the original work is properly cited.

Poly(dichlorophosphazene) was prepared by melt ring-opening polymerization of the hexachlorocyclotriphosphazene. Poly[bis(2-hydroxyethyl-methacrylate)-phosphazene] and poly[(2-hydroxyethyl-methacrylate)-graft-poly(lactic-acid)-phosphazene] were obtained by nucleophilic condensation reactions at different concentrations of the substituents. The properties of the synthesized copolymers were assessed by FTIR, <sup>1</sup>H-NMR and <sup>31</sup>P-NMR, thermal analysis (DSC-TGA), and electron microscopy (SEM). The copolymers have a block structure and show two  $T_g$ 's below room temperature. They are stable up to a temperature of 100°C. The type of the substituents attached to the PZ backbone determines the morphology of the polymers.

## 1. Introduction

Polyesters, polyorthoesters, polyanhydrides, poly(R-amino acids), and polyphosphazenes are degradable polymers that have been investigated for a variety of biomedical applications such as sutures, drug delivery systems, and scaffolds for tissue engineering [1]. Useful properties can be obtained by blending two different polymers. However, compatible polymer blends require strong molecular interactions between polymer chains [2]. Poly(organophosphazenes) offer an appealing platform for the design and synthesis of novel biodegradable polymers as well as critical advantages for the design of biologically functional macromolecules with a broad structural diversity [3], high functional density, and tailored biodegradability [4]. These polymers are of scientific and technological concern since the first work of synthesis reported by Allcock et al. [5, 6]. Polyphosphazenes (PZs) possess special

characteristics, including flame-retardant properties, high resistance to oil and solvents, and feasibility for tailored properties according to the choice of organic, inorganic, or organometallic side groups [7]. As biomaterials they have inherent advantages, due to their biocompatibility and fast degradation rate. In addition, degradation residues, phosphate, ammonia, and side groups are either nontoxic when they are present in small quantities or are easily metabolized by the human body [8, 9]. Polyphosphazenes are hybrid polymers with a flexible inorganic backbone of alternating phosphorus and nitrogen atoms and organic side groups. Their composition vary from 3 to 10,000 (–N=P–) repetitive units having two substituents (–R) attached to the phosphorus atom [7]. Polyphosphazenes are synthesized by reactions with alkoxides, aryloxides, or amines from a highly reactive macromolecular intermediate, poly(dichlorophosphazene), which is prepared by thermal ring opening polymerization

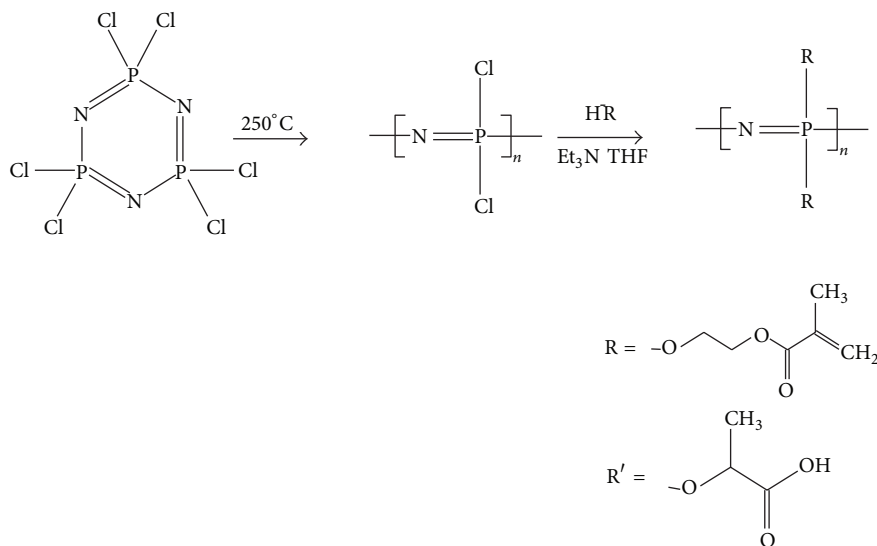


FIGURE 1: Synthesis by substitution of poly(organophosphazenes).

of hexachlorocyclotriphosphazene (HCCP) at 250°C. The chlorine atoms can be further replaced via nucleophilic substitution, using amino acid ester, imidazolyl, glyceryl, or glycosyl side groups that are also hydrolytically sensitive [5]. The flexible inorganic backbone of the poly(phosphazene) structure plays an important role in tissue regeneration. It can be modified with ester, anhydride, and unsaturated groups to improve chemical stability and mechanical properties. Cosubstituted poly(organophosphazenes) with unsaturated side groups are used to prepare interpenetrating polymer networks with acrylonitrile, styrene, acrylic acid, and methyl methacrylate, using sequential interpenetrating methods. Such polyphosphazenes can be readily crosslinked either by exposure to heat or to ultraviolet light [10]. In this work, poly[(2-hydroxyethyl methacrylate)-graft-poly(lactic acid)-phosphazene] and poly[bis(2-hydroxyethyl-methacrylate)-phosphazene] were synthesized by condensation polymerization reactions. The 2-hydroxyethyl methacrylate (HEMA) was selected to improve biocompatibility and bifunctionality. HEMA was firstly attached to the side chain along with glycine-ethyl ester to form a precursor with the unsaturated substituents. HEMA is used for prosthesis, teeth, and bones reconstructive materials, and it is frequently mixed with acrylic polymers, like bisphenol-A-glycidyl-dimethacrylate (Bis-GMA), in photopolymerizable dental resins. HEMA is intended to infiltrate the demineralised dentin and prevent collagen collapse [11]. HEMA melts at about -12°C. The lactic acid, LA, was selected because it is a biocompatible and biodegradable material with good mechanical properties and is neither nontoxic nor cancerogenous to the human body [5, 12]. The poly(lactic acid) (PLA) chemistry involves the processing and polymerization of lactic acid monomer. Lactic acid (HOCH<sub>2</sub>CHCOOH) is a simple chiral molecule which exists as two enantiomers, L- and D-lactic acid. The polymer is relatively hard, with a glass transition temperature between 60°C and 70°C and a melting point between 170 and 180°C.

## 2. Experimental

**2.1. Materials and Methods.** Hexane (MERK), n-heptane (Aldrich), tetrahydrofuran (THF-Aldrich), and triethylamine (TEA-Aldrich) were distilled from CaH<sub>2</sub> and drying with MgSO<sub>4</sub>. HEMA (Aldrich) and acid lactic (Purac H588) were distilled just before use. HCCP (Aldrich) was purified by two times sublimation (30°C/0.1 mmHg). The melting point of the purified HCCP was 113-114°C.

ATR infrared spectra were obtained in a Thermo Nicolet Avatar 360 FTIR Spectrometer (Thermo Scientific, USA). The <sup>1</sup>H (400 MHz) and <sup>31</sup>P (161.9 MHz) Nuclear Magnetic Resonance (NMR) spectra were recorded in the Fourier transform mode with CDCl<sub>3</sub> as solvent (Bruker Avance NMR 400, USA). Chemical shifts were relative to tetramethylsilane at δ = 0 ppm for protons and carbons. The phosphorus chemical shifts were relative to external 85% H<sub>3</sub>PO<sub>4</sub> at δ = 0 ppm. The glass transition temperatures (T<sub>g</sub>) were measured by differential scanning calorimetry (DSC) at a heating rate of 10°C/min from -100 to 150°C under dry nitrogen atmosphere (MDSC 2910 TA Instruments, USA). The thermogravimetric analysis (TGA) were measured in the range of 25-600°C at a heating rate of 10°C min<sup>-1</sup> using dry nitrogen as purge gas (SDT Q600 TA Instruments, USA). Finally, the morphology of the copolymers were characterized by Scanning Electron Microscopy at an acceleration voltage of 20 kV (JSM5900-LV SEM, JEOL, USA).

**2.2. Syntheses of Polymers.** The scheme of the poly(organophosphazenes) synthesis by nucleophilic substitution is shown in Figure 1. The single substituted and cosubstituted PZs were obtained from poly(dichlorophosphazene) as described below. The poly(dichlorophosphazene) (PZ) was obtained by melt ring-opening polymerization of hexachlorocyclotriphosphazene (HCCP) under vacuum at 250°C for 3 h. After this time, the polymer was dissolved at room

temperature in anhydrous THF, and it was separated by precipitation into n-heptane. Its characteristics were 98% yield; characteristic IR bands were 1215 and 748  $\text{cm}^{-1}$  (linear phosphazene);  $^{31}\text{P}$ -NMR peak at  $-16.1$  ( $\delta = \text{ppm}$  relative to 85% of  $\text{H}_3\text{PO}_4$  at 0 ppm).

The substitution of poly(dichlorophosphazene) (PZ) with HEMA was made at two molar relations: 1:3 and 1:6 mmol PZ-HEMA. Triethylamine (TEA) was added at 1:1 mmol relation HEMA:TEA as effective acceptor to trap hydrogen chloride. The PZ was dissolved in THF (10 mL) under stirring, after 10 min HEMA and TEA were added and the glass vial reactor was kept for two days at room temperature. The product was purified following the procedure described for PZ; the yield was 51%. The phosphazene backbone characteristic IR bands ( $\text{cm}^{-1}$ ) were 2947 ( $\text{CH}_2$ ), 1720 ( $\text{C}=\text{O}$ ), 1635 ( $\text{C}=\text{C}$ ), 1473 ( $\text{CO}-\text{O}$ ), 1033 ( $\text{P}-\text{O}-\text{C}$ ), 1168 (phosphazene backbone  $\text{C}-\text{O}$ ), and the  $^{31}\text{P}$ -NMR peaks: 1.5 ( $\delta = \text{ppm}$ );  $^1\text{H}$ -NMR<sub>HEMA</sub> [13] at 6.0 (1H), 5.4 (1H), 4.3 (2H), 2.0 (3H), and 1.7 (2H) ( $\delta = \text{ppm}$ ).

The substitution reactions of PZ with HEMA and LA were carried out in a similar way. The PZ:HEMA:LA molar relation was 1:3:3 mmol, and for HEMA-TEA the relation was 1:1 mmol. The product was purified following the procedure described for PZ; obtaining a 50% yield [14]. The typical IR bands ( $\text{cm}^{-1}$ ) were 3452 (polymeric  $-\text{OH}$ ), 2947 ( $\text{CH}_2$ ), 1745 and 1724 ( $\text{C}=\text{O}$ ), 1635 ( $\text{C}=\text{C}$ ), 1477 and 1150 ( $\text{CO}-\text{O}$ ), 1037 ( $\text{P}-\text{O}-\text{C}$ ), and 1172 (phosphazene backbone) and the  $^{31}\text{P}$ -NMR peaks 1.5 and 0.6 ( $\delta = \text{ppm}$ );  $^1\text{H}$ -NMR<sub>HEMA</sub>, 6.0 (1H), 5.4 (1H), 4.3 (3H), 2.0 (2H), and 1.7 (2H) ( $\delta = \text{ppm}$ ), as well as  $^1\text{H}$ -NMR<sub>LA</sub> peaks: 1.3 (3H), 3.5 (1H), and 11.5 (1H) ( $\delta = \text{ppm}$ ).

### 3. Results and Discussion

In the Figure 2(a) we show the IR spectra of PZ-HEMA-1:3; PZ-HEMA-1:6, PZ-HEMA-PLA and the Figure 2(b) present de comparative groups (zoom) between the blank and substituent copolymers. The band at 1170  $\text{cm}^{-1}$  corresponds to the phosphazene backbone. The substitution of the chlorine on PZ chain (Figure 2(b)) by the two components is observed by the elimination or reduction of peak in 748  $\text{cm}^{-1}$ , also by the presence of a band at 1035  $\text{cm}^{-1}$  corresponding to the interaction  $\text{P}-\text{O}-\text{C}$ .

With the formation of a new band at 1720  $\text{cm}^{-1}$  for PZ-HEMA and the evidence of two shifts of similar intensities at 1724 and 1745  $\text{cm}^{-1}$  for PZ-HEMA-LA, the carbonyl groups of the monomers could be confirmed within the copolymer due the substitution of the chlorines.

Additionally, the new bond  $\text{P}-\text{O}-\text{C}$  could be confirmed too with the absence of the band of the  $\text{OH}$  at 3516  $\text{cm}^{-1}$  and the presence of the double bonds bands in 1635  $\text{cm}^{-1}$  for the HEMA (Figure 2(a)). In the case of lactic acid, the  $\text{OH}$  band decreases for primary alcohol, but remain present for the polymeric  $\text{OH}$  in 3452  $\text{cm}^{-1}$ , an indication that we conserved the  $\text{OH}$  of lactic acid in the copolymer.

The stepwise substitution reactions of PZ were monitored by  $^{31}\text{P}$ -NMR spectroscopy (Figure 3). The PZ spectrum shows a peak at  $-16.1$  ppm corresponding to low molecular

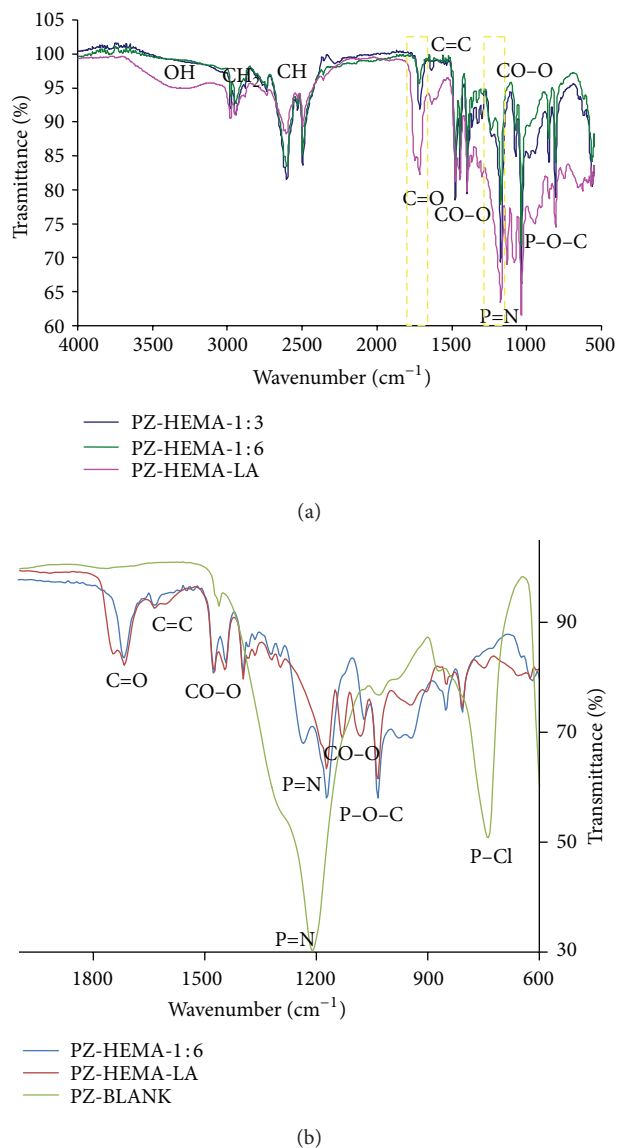


FIGURE 2: FTIR spectra of (a) PZ-HEMA-1:3, PZ-HEMA-1:6, and PZ-HEMA-LA and (b) PZ-BLANK, PZ-HEMA-1:6, and PZ-HEMA-LA.

weight  $[\text{P}(\text{Cl}_2)=\text{N}]_n$  [15], while the polymers PZ-HEMA-1:3, PZ-HEMA-1:6, and PZ-HEMA-PLA show a peak in positive values; it may be presumed that chlorine atoms were completely replaced by subsequent reaction. The peak at 1.5 ppm is assigned to modified phosphazene  $[\text{P}(\text{OR})_2=\text{N}]_n$ . In addition, the PZ-HEMA-1:3 shows a peak at 20 ppm which is assigned to  $[\text{R}-\text{P}=\text{O}]$ . When the HEMA ratio was increased to 6 mmol a complete chlorine substitution was obtained, the spectrum only presents one peak; in another hand, for PZ-HEMA-LA, another peak appears at 0.6 ppm assigned to the substitution of chlorine by LA.

The  $^1\text{H}$  NMR spectrum of PZ-HEMA-1:6 and PZ-HEMA-LA is shown in Figure 4. We observed the peaks corresponding to different hydrogens of the organic substituents. The presence of the signals at 6 and 5.58 ppm indicates that

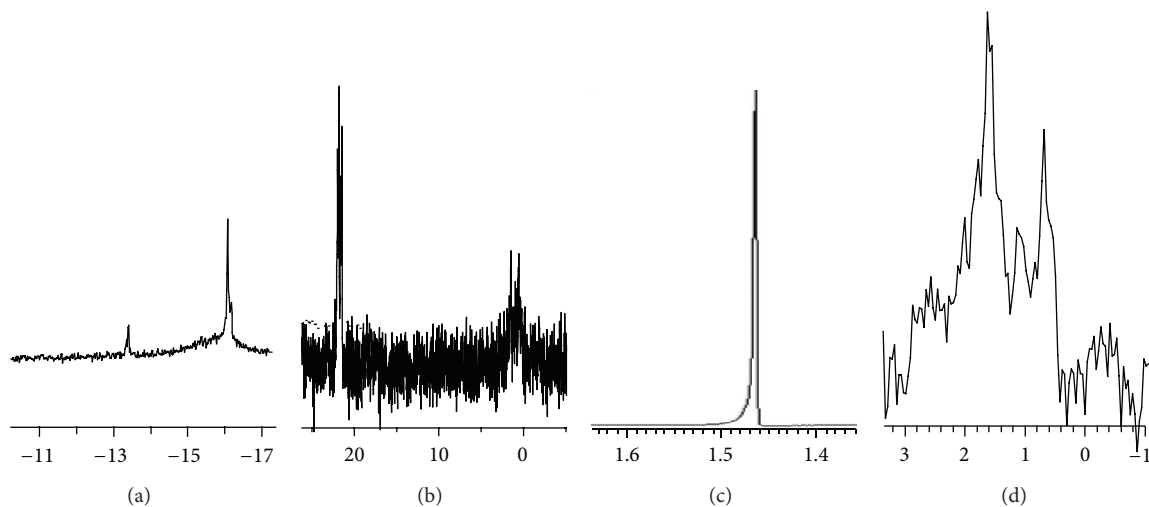


FIGURE 3:  $^{31}\text{P}$  NMR spectra of (a) PZ, (b) PZ-HEMA-1:3, (c) PZ-HEMA-1:6, and (d) PZ-HEMA-LA.

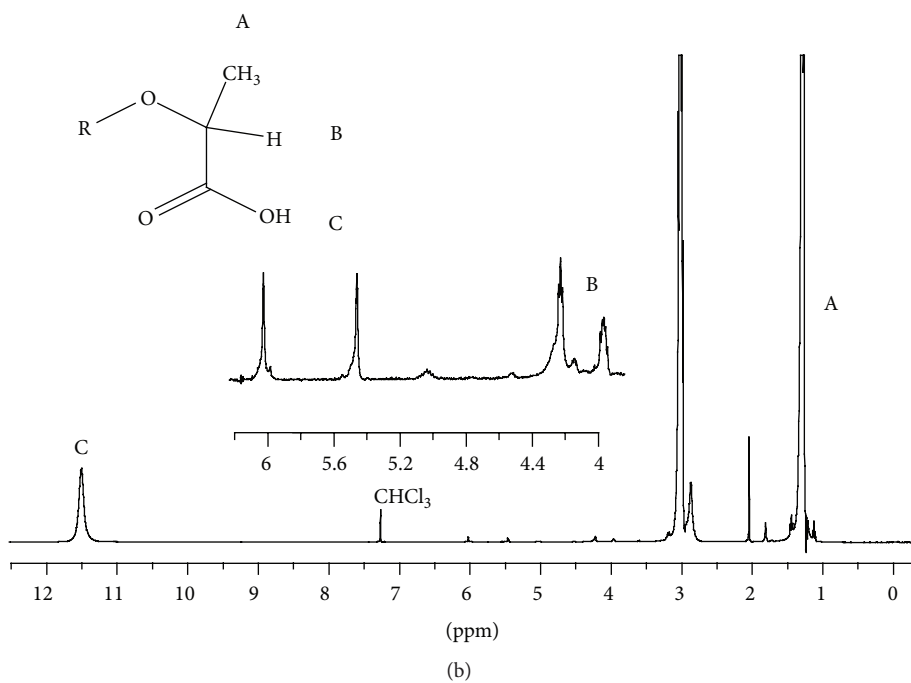
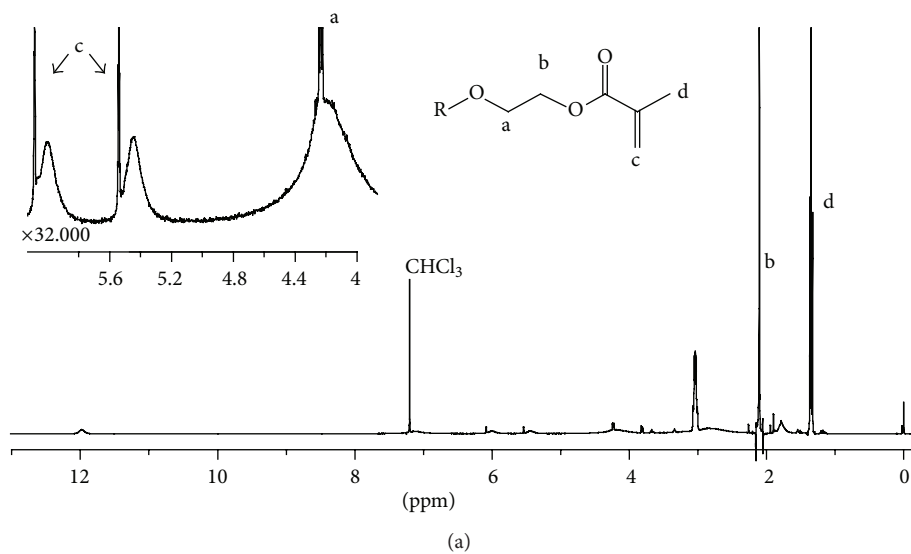


FIGURE 4:  $^1\text{H}$  NMR spectra of (a) PZ-HEMA-1:6 and (b) PZ-HEMA-LA.

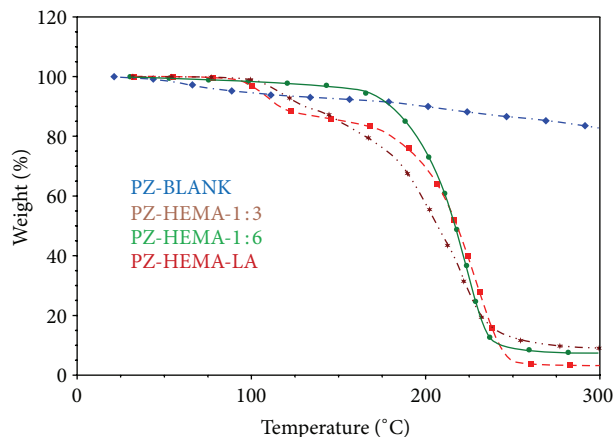


FIGURE 5: TGA thermograms of PZ BLANK, PZ-HEMA-1:3, PZ-HEMA-1:6, and PZ-HEMA-LA.

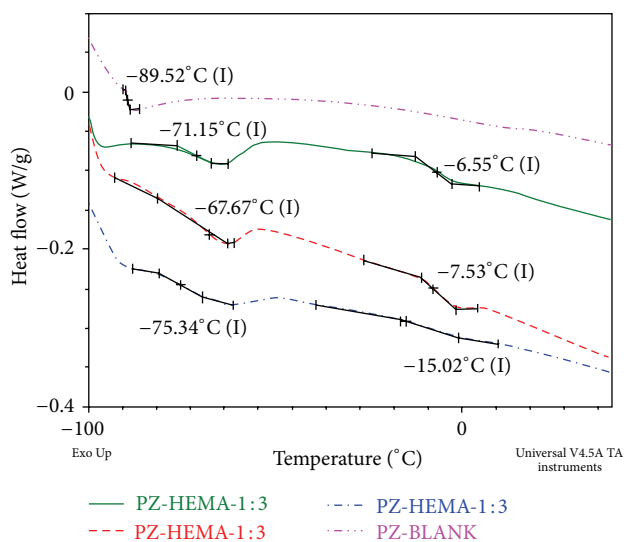


FIGURE 6: DSC Thermograms of PZ, PZ-HEMA-1:3, PZ-HEMA-1:6, and PZ-HEMA-LA.

the majority of the end double bonds are on the material. In addition, the peaks to OH in 4.9 ppm (HEMA) and 3.4 ppm (AL) are not present in the spectrum.

The thermal stability of the polymers was analyzed by TGA (Figure 5). PZ lost about 5% of weight between 50°C and 100°C due to residual monomer evaporation. Between 200°C and 300°C there is another 5% loss of weight, which is attributed to the elimination of chlorine. Nevertheless, the PZ is fairly stable up to 300°C.

In contrast, when the inorganic back bone is substituted for organic molecules the temperature of decomposition decreased at ~225°C; according to the literature, the pure poly(HEMA) began its decomposition at ~300°C. This means that HEMA was grafted in the inorganic chain and changed the thermal stability of PZ.

PZ-HEMA and PZ-HEMA-LA are quite stable up to 100°C, the stability of PZ-HEMA increases with the content of HEMA attached on PZ because of the good thermal stability of HEMA, the initial thermal decomposition of poly(HEMA) exhibited at 195°C [16]. In PZ-HEMA-LA the decomposition temperature of LA starts at 109°C, this value is much less than of the initial decomposition of the PLA at ~300°C [17]. Excluding monomer evaporation in PZ, its thermal stability is greater than that observed in the copolymers.

The thermal transitions of the polymers were determined by DSC (Figure 6). The obtained data indicate that all polymers are flexible above 0°C. PZ showed a single  $T_g$  at -90°C while both PZ-HEMA and PZ-HEMA-LA have two  $T_g$ 's: (a) for PZ-HEMA-1:3 -71°C and -6.6°C; (b) for PZ-HEMA-1:6 -67°C and -7.5°C; and (c) for PZ-HEMA-LA -75°C and -15°C. The lowest  $T_g$  value shown by each copolymer corresponds to the PZ backbone. The  $T_g$  of PZ-HEMA-LA at -15°C corresponds to the LA grafted on the PZ backbone. The  $T_g$  of PZ-HEMA at about -7°C is attributed to the HEMA chemically attached to the PZ backbone. The observed  $T_g$  temperatures are similar to those reported elsewhere [14, 18].

The properties of the poly(organophosphazenes) depend on the type of side groups linked to the polymer chain. If the side groups are small or are highly flexible organic units, like 2-butenoxy or trifluoroethoxy, the polymers will show low glass transition temperatures (-100 to -30°C) [16].

The surface of the polymers was examined by SEM (Figure 7). The PZ was an amorphous white solid and shows a semiuniform surface while the copolymers show distinctive characteristics. PZ-HEMA-1:3 and PZ-HEMA-1:6 show a rod like microstructure that is enhanced as the concentration of HEMA; it is possible that polyphosphazene had a crosslinking reaction between itself and conducive to a geometry structure. PZ-HEMA-PLA shows a rod structure with more plastic appearance. Thus, morphology depends on the type of the substituent attached to the PZ backbone [19].

After obtaining the copolymers, it is intended to add them to an acrylic resin to increase the mechanical properties and subsequently will be made of composite fibers by electrospinning technique to improve their lifetime.

## 4. Conclusions

Poly(dichlorophosphazene) was prepared directly by melt ring-opening polymerization of hexachlorocyclotriphosphazene. This polymer was useful for the design and synthesis of Poly [(2-hydroxyethyl-methacrylate)-graft-poly(lactic-acid)-phosphazene] and poly[bis(2-hydroxyethyl-methacrylate)-phosphazene] by ring-opening polymerization reactions, at different concentrations of the substituents. The incorporation of organic substituents HEMA and AL was proved by FTIR, NMR, and DSC. All polymers are flexible above 0°C and are thermally stable up to 100°C. The morphology of the polymers was considerably modified by the incorporation of substituents and will be of great importance when testing copolymers in dental resins. The PZ-HEMA-1:6 copolymer yields the best results and suggest that it could potentially be used in biomedical applications such as dental resins.

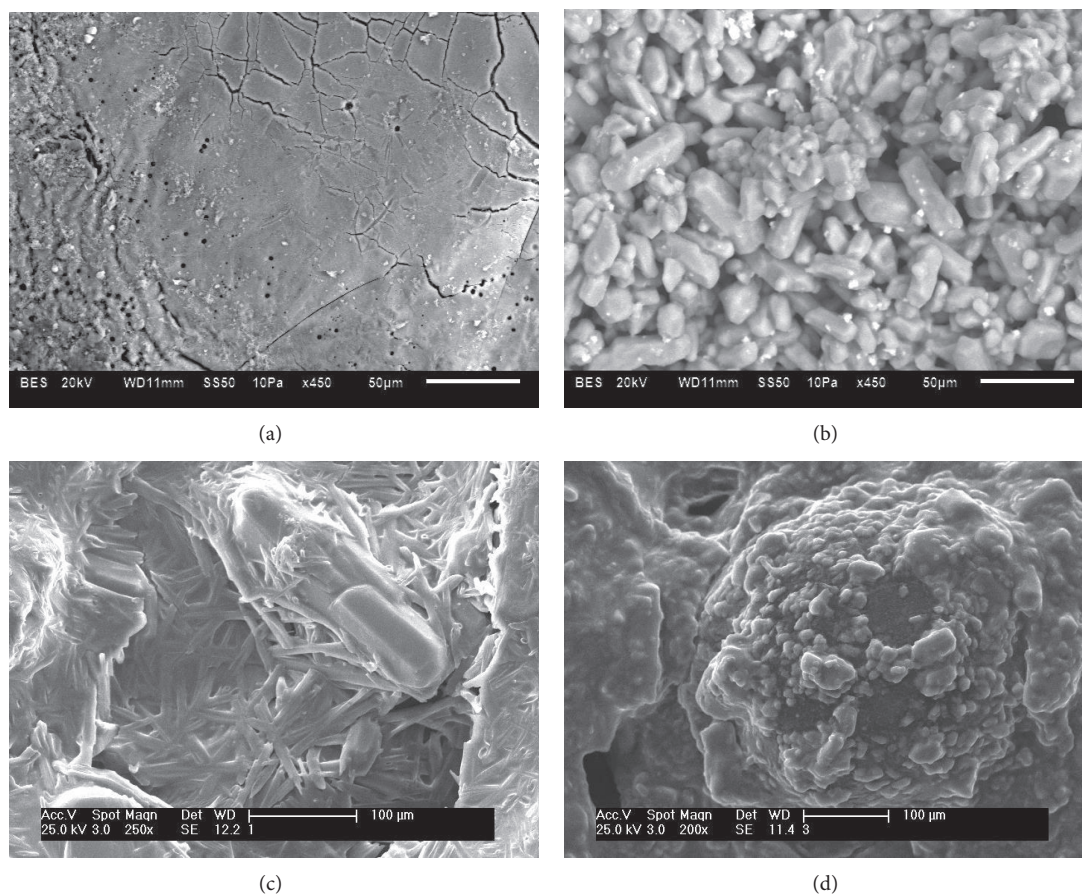


FIGURE 7: SEM images of (a) PZ, (b) PZ-HEMA-1:3, (c) PZ-HEMA-1:6, and (d) PZ-HEMA-LA.

## Conflict of Interests

The authors do not have a direct financial relation or conflict of interests with the commercial identities mentioned in this submitted paper, and the commercial trademarks such as Bruker Avance, Thermo Scientific, TA Instruments, and JEOL, only were reported to guarantee the reproducibility, in the same conditions, of the different tests.

## Acknowledgments

The authors acknowledge the technical support of Esteban Fregoso (TGA-DSC), Enrique Viguera-Santiago (FTIR), and Gerardo Cedillo (RMN). The authors also acknowledge the grants of UNAM, PAPIIT-IN116809/21, and Instituto de Ciencia y Tecnología del Distrito Federal, México. They also appreciate the scholarships granted by CONACYT.

## References

- [1] J. Jagur-Grodzinski, "Biomedical application of functional polymers," *Reactive and Functional Polymers*, vol. 39, no. 2, pp. 99–138, 1999.
- [2] N. R. Krogman, A. L. Weikel, N. Q. Nguyen et al., "Hydrogen bonding in blends of polyesters with dipeptide-containing polyphosphazenes," *Journal of Applied Polymer Science*, vol. 115, no. 1, pp. 431–437, 2010.
- [3] H. R. Allcock, "Recent developments in polyphosphazene materials science," *Current Opinion in Solid State and Materials Science*, vol. 10, no. 5-6, pp. 231–240, 2006.
- [4] A. Singh, N. R. Krogman, S. Sethuraman et al., "Effect of side group chemistry on the properties of biodegradable l-alanine cosubstituted polyphosphazenes," *Biomacromolecules*, vol. 7, no. 3, pp. 914–918, 2006.
- [5] H. R. Allcock and S. R. Pucher, "Polyphosphazenes with glucosyl and methylamino, trifluoroethoxy, phenoxy, or (methoxyethoxy)ethoxy side groups," *Macromolecules*, vol. 24, no. 1, pp. 23–34, 1991.
- [6] H. R. Allcock and K. B. Visscher, "Preparation and characterization of poly(organophosphazene) blends," *Chemistry of Materials*, vol. 4, no. 6, pp. 1182–1187, 1992.
- [7] M. Gleria and R. De Jaeger, "Aspects of Phosphazene Research," *Journal of Inorganic and Organometallic Polymers*, vol. 11, no. 1, pp. 1–45, 2001.
- [8] A. K. Andrianov, Y. Y. Svirkin, and M. P. LeGolvan, "Synthesis and biologically relevant properties of polyphosphazene polyacids," *Biomacromolecules*, vol. 5, no. 5, pp. 1999–2006, 2004.
- [9] D. Puppi, F. Chiellini, A. M. Piras, and E. Chiellini, "Polymeric materials for bone and cartilage repair," *Progress in Polymer Science*, vol. 35, no. 4, pp. 403–440, 2010.
- [10] Y. Cui, X. Zhao, X. Tang, and Y. Luo, "Novel micro-crosslinked poly(organophosphazenes) with improved mechanical properties and controllable degradation rate as potential biodegradable matrix," *Biomaterials*, vol. 25, no. 3, pp. 451–457, 2004.

- [11] P. Sharrock and G. Grégoire, "HEMA reactivity with demineralized dentin," *Journal of Dentistry*, vol. 38, no. 4, pp. 331–335, 2010.
- [12] B. Gupta, N. Revagade, and J. Hilborn, "Poly(lactic acid) fiber: an overview," *Progress in Polymer Science*, vol. 32, no. 4, pp. 455–482, 2007.
- [13] E. Martínez-Ceballos, *Síntesis y caracterización de biopolímeros modificados para usos biomédicos [M.S. thesis]*, Universidad Autónoma del Estado de México, 2011.
- [14] R. Vera-Graziano, J. Palacios-Aiquisiraa, A. Martínez-Richab, F. Barcelóc, T. Halachevd, and V. M. Castañod, "On the structure and physicochemical properties of acrylic compounds," *International Journal of Polymeric Materials and Polymeric Biomaterials*, vol. 52, no. 2, pp. 85–95, 2003.
- [15] G. Kister, G. Cassanas, and M. Vert, "Effects of morphology, conformation and configuration on the IR and Raman spectra of various poly(lactic acid)s," *Polymer*, vol. 39, no. 2, pp. 267–273, 1998.
- [16] Y. Zhou, D. Yang, X. Gao et al., "Semi-interpenetrating polymer network hydrogels based on water-soluble N-carboxylethyl chitosan and photopolymerized poly (2-hydroxyethyl methacrylate)," *Carbohydrate Polymers*, vol. 75, no. 2, pp. 293–298, 2009.
- [17] L.T. Lima, R. Auras, and M. Rubino, "Processing technologies for poly(lactic acid)," *Progress in Polymer Science*, vol. 33, no. 8, pp. 820–852, 2008.
- [18] H. R. Allcock, K. B. Visscher, and Y.-B. Kim, "New polyphosphazenes with unsaturated side groups: Use as reaction intermediates, cross-linkable polymers, and components of interpenetrating polymer networks," *Macromolecules*, vol. 29, no. 8, pp. 2721–2728, 1996.
- [19] N. R. Krogman, A. L. Weikel, N. Q. Nguyen, L. S. Nair, C. T. Laurencin, and H. R. Allcock, "Synthesis and characterization of new biomedical polymers: serine-and threonine-containing polyphosphazenes and poly(L-lactic acid) grafted copolymers," *Macromolecules*, vol. 41, no. 21, pp. 7824–7828, 2008.

## Research Article

# Effects of Crumb Rubber Size and Concentration on Performance of Porous Asphalt Mixtures

**Altan Cetin**

*Civil Engineering Department, Engineering Faculty, Anadolu University, 26555 Eskisehir, Turkey*

Correspondence should be addressed to Altan Cetin; [accetin74@gmail.com](mailto:accetin74@gmail.com)

Received 26 April 2013; Accepted 12 June 2013

Academic Editor: Osman Gencel

Copyright © 2013 Altan Cetin. This is an open access article distributed under the Creative Commons Attribution License, which permits unrestricted use, distribution, and reproduction in any medium, provided the original work is properly cited.

The purpose of this study is to investigate the effect of size distribution and concentration of crumb rubber on the performance characteristics of porous asphalt mixture. The recycling of scrap tires in asphalt pavements appears as an important alternative providing a large-scale market. The characteristics of bitumen are very important with regard to service life of porous asphalt pavement. The experimental study consists of two main steps. Firstly, the mixture design was performed to determine the optimum bitumen content. In the latter step, the mixtures were modified by dry process using crumb rubber in three different grain size distributions of #4~#20, #20~#200, and #4~#200 and rubber content of 10%, 15%, and 20% as weight of optimum bitumen. The permeability, Cantabro abrasion loss, indirect tensile strength, moisture susceptibility, and resilient modulus tests were carried out on the specimens. Test results show that #20~#200 sized rubber particles reduced air voids and coefficient of permeability, while they increased the Cantabro abrasion loss. In general, increasing the crumb rubber size and content decreased the performance characteristics of the porous asphalt mixtures.

## 1. Introduction

The worn-out tires from vehicles leave billions of waste tires every year becoming a significant source of waste materials. Scrap tires are still a serious environmental and financial issue for many countries in the world occupying landfill spaces and becoming a threat for health and safety hazards to the community. The scrap tires consist of rubber, carbon black, steel, and so forth potentially to be very useful in various applications which have been evaluated effectively as a valuable resource. There are some different recycling strategies developed for waste tires. The main markets in the assessment of waste tires include tire-derived fuel (TDF), civil engineering applications, and ground rubber. The recycling of waste tire has a good trend. However, it has still potential to consume more waste tires. In addition, TDF corresponds to 54% of the total scrap tires which may not represent an ideal application in the current recycling methods for waste tires from environmental conservation perspective [1]. More value-added alternatives are required to be discovered in order to motivate public and private agency to recycle them.

One of the approaches of recycling scrap tires is to use crumb rubber from the tires as a component in asphalt pavement mixtures. The crumb rubber is combined in asphalt mixtures to improve the performance of asphalt concrete pavements. The large-scale usage of crumb rubber from waste tyres in asphalt mixtures appears to be more feasible alternative in terms of engineering applications and environmental consideration. Asphalt-rubber pavements can minimize environmental impact and maximize the conservation of natural resources.

The ability of crumb rubber to improve the asphalt mixture performance depends on many factors such as the mixing methods, reaction time with bitumen, nature of the rubber, and size and concentration of the rubber particles. There are two different processes using crumb rubber in the asphalt mixtures, a dry process and a wet process. In the wet process, the finer crumb rubber is mixed with asphalt cement at high temperature. It reacts with the bitumen and creates modified bitumen. In the dry process, the crumb rubber is mixed together with the aggregates prior to the addition to the asphalt. During dry process in which the crumb rubber

is used as an aggregate, the chemical reaction between crumb rubber and bitumen is quite limited [2].

The advancement in hot-mix asphalt pavement technology resulted in the development of a different type of asphalt mixture. Porous asphalt is used widely as an application of pavement surface in Europe. Porous asphalt or open-graded asphalt concrete is an environmentally friendly road material which was developed by using advanced technology in hot-mix asphalt mixture design. It is used effectively in regions with the highest level of precipitation. The porous asphalt used as surface layer mostly has an air void content of 20% and can improve the ride quality for drivers during wet weather by reducing skidding. This pavement system prevents hydroplaning and spraying on the road surface and improves visibility by eliminating the light reflected from the road surface. The porous asphalt mixture is designed by using a relatively large proportion of coarse aggregates (more than 80%) with few fine aggregates to create a large space for water drainage. It also significantly reduces traffic induced noise emissions by means of the high porosity [3]. The selection of asphalt binder with high viscosity is an important issue on account of the specific structure of its high void content in the mixtures. To improve the durability of porous asphalt mixtures, polymer-modified bitumen was recommended to be used in moderate and hot climates with heavy traffic [4].

Modified bitumen with polymers and synthetic and natural rubber used in porous asphalt surfaces significantly reduce the level of noise from vehicles compared with the dense graded asphalt surfaces [5]. The use of polymer-modified or rubberized binders instead of unmodified binder in the 4.75 mm open-graded mixture reduced permeability but increased acoustic absorption. Mixtures containing rubberized bitumen show the most acoustic absorption improvement [6]. One advantage of using rubber modified asphalt is that it raises the viscosity of the bitumen and provides increase of the bitumen content in the mixture. Thus, massive asphalt film surrounding the aggregate enhances durability of the asphalt mixtures. The open-graded asphalt with asphalt-rubber binder had significantly reduced not only moisture sensitivity but also superior fatigue resistance and cracking as compared to traditional porous or semiporous asphalt mixtures [7, 8]. A previous study claim that Large Stone Porous Asphalt-Rubber Mixture has better performance than conventional large stone porous asphalt mixture using polymer-modified asphalt, and it could be used as stress absorbing layers of semirigid base asphalt pavement [9]. Moreover, the experimental results of repeated triaxial-loaded and wheel tracking permanent deformation tests confirmed that the asphalt-rubber porous mixtures have superior performance against rutting [10]. Several studies have shown that rubber content between 10% and 30% of the bitumen improves resistance to moisture damage, the susceptibility to temperature, and the tendency to flow [11, 12]. The particular facts of performance evaluation of test sites in Florida indicated that the wet process addition of asphalt-rubber blended into the bitumen improved the cracking resistance of the surface mixtures [13]. The characteristics of the crumb rubber can influence properties of asphalt rubber such as rubber quantity in the blend and particle size

TABLE 1: The physical properties of coarse aggregate.

Properties	Specification	Results	Specification	
			Min.	Max.
Los Angeles abrasion (%)	ASTM C131	13.5	—	30
Sodium sulfate soundness (%)	ASTM C88	0.64	—	12
Percent fractured faces (%)	ASTM D5821	100	100	—
Flakiness index (%)	BS 812	20	—	25
Polish value	ASTM C3319	53	50	—
Stripping resistance (%)	ASTM D1664	60–65	—	50

TABLE 2: Test results on aggregate specific gravity and absorption properties.

Properties	Course aggregate	Fine aggregate	Filler
Bulk specific gravity	2.586	2.639	—
Apparent specific gravity	2.735	2.763	2.782
Water absorption (%)	2.1	1.7	—

distribution. Additional factors include crumb rubber surface area, grinding process, crumb rubber chemical composition, and contaminants as water, fibre, and metal [14].

Considering the preceding information from the literature, this study was designed to examine the effects of the content and size of crumb rubber on the porous asphalt mixture performance.

## 2. Experimental Program

This section includes material characterization of basalt aggregate, bitumen and crumb rubber, and test methods such as permeability, Cantabro abrasion loss, indirect tensile strength, moisture susceptibility, and resilient modulus tests.

*2.1. Materials Characterization.* Crushed basalt aggregates and conventional bitumen of penetration grade 50/70 were used in this experimental study. Also, crumb rubber obtained from waste tires was used as a modifier in different sizes and concentrations. The characterization tests conducted in the laboratory were given in this section.

*2.1.1. Aggregate.* High-quality aggregates are required to provide the field performance of the large-void porous asphalt during the service life. In this study, one type of crushed basalt aggregate was used as coarse and fine aggregate. Also, stone dust which was obtained from the same basalt aggregate was used as the filler material. The basalt aggregate was provided from a quarry in Eskişehir, Turkey. The main physical properties of the coarse aggregate with the criteria are given in Table 1. The aggregate specific gravity and absorption test results were shown in Table 2.

The aggregate gradation for porous asphalt mixtures was selected between broad bands (boundary lines) according to Porous European Mix (PEM) Specification. The aggregate gradation is given in Figure 1.

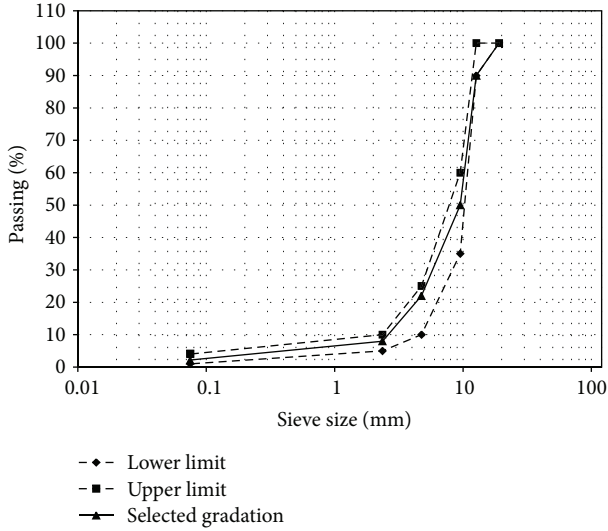


FIGURE 1: Aggregate gradation of porous asphalt mixture with specification limits of PEM.

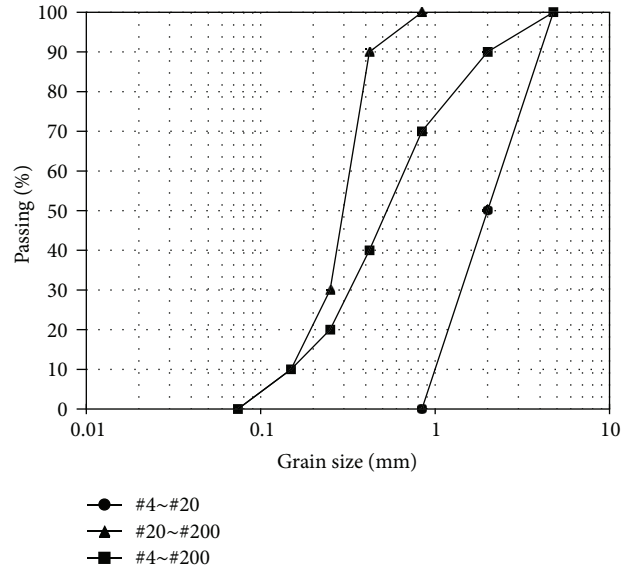


FIGURE 2: Grain size distributions of crumb rubber.

TABLE 3: Physical properties of conventional bitumen.

Properties	Specification	Results
Penetration at 25°C, 100 g, 5 s (0.1 mm)	ASTM D5	63
Softening point (°C)	ASTM D36	49
TFOT residue	ASTM D2872-04	
Mass loss (%)	ASTM D2872	0.096
Retained penetration (%)	ASTM D5	37
Softening point after hardening (°C)	ASTM D36	61
Flashing point (°C)	ASTM D92	240
Specific gravity at 25°C	ASTM D70	1.021

2.1.2. *Bitumen.* Bitumen from one source was used in this study. The penetration grade bitumen of 50/70 obtained from the Asphalt Production Refinery is widely used in Turkey. This type of asphalt binder was chosen instead of modified bitumen so that effect of the crumb rubber on porous asphalt mixtures could be clearly determined. Table 3 gives physical properties of the bitumen.

2.1.3. *Crumbed Rubber.* The crumb rubber was obtained from tire buffing process. It includes removing the worn tread by a special machine and applying a new tread. The different sizes of rubber were separated by sieves. The grain size distributions of crumb rubber were given in Figure 2. The grain size distribution group of #4~#20, #20~#200, and #4~#200 includes different sizes of rubber particles. Figure 3 represents a general appearance of each group. Even though Figure 3 gives some information about the form of #4~#20, the forms of small particles such as #100~#200 mesh size cannot be determined from it. Therefore, Scanning Electron Microscopy (SEM) images of the crumb rubber in Figure 4 were presented. The fiber-like shape of the pine needle rubber can contribute to reinforcing the porous pavement and decrease the bitumen drain down.

2.2. *Test Methods.* The test program in this study consisted of two steps. Step I covered the mix design of porous asphalt mixtures. Step II was to investigate the effect of crumb rubber concentration and size on design and performance characteristics of the porous asphalt mixtures.

The principle design of porous asphalt mixtures is to determine the bitumen content that will optimize its engineering properties in relation with the in-service behavior during pavement life. The Porous European Mix Specification including the tests of air void, permeability, particle loss resistance (Cantabrian), and indirect tensile were used to determine the optimum bitumen content. In addition, performance-related tests such as moisture susceptibility and resilient modulus tests were conducted on the porous asphalt mixtures with and without crumb rubber.

2.2.1. *Mixing and Production.* Each specimen was comprised of about 1200 g of aggregate batches and bitumen. Modified specimens were prepared by dry process in which crumb rubber was added in the aggregate batch and mixed for 2 minutes. The aggregates and asphalt binder were blended at their corresponding mixing temperatures. A compaction process was followed subsequently by applying 50 blows on each face of the specimen using the standard Marshall hammer.

2.2.2. *Air Voids Determination.* To provide sufficient permeability in the porous asphalt mixtures, an air void content ranging between 16% and 22% (or greater) is recommended [15, 16]. The air void percentages of the porous asphalt specimens were very difficult to determine due to the higher porosity. This test procedure determines the bulk specific gravity of specimens of compacted asphalt mixtures. In this method, compacted specimens were coated with paraffin

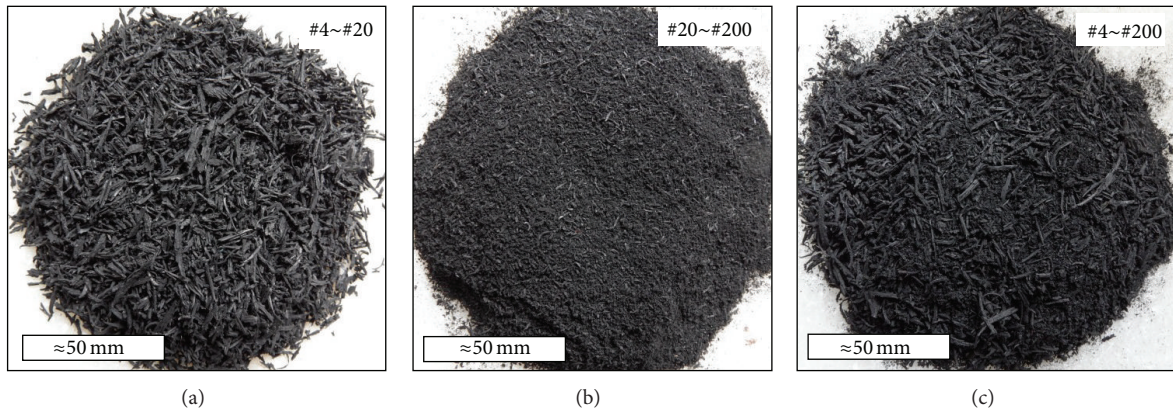


FIGURE 3: Appearance of crumb rubber particles: (a) #4~#20; (b) #20~#200; (c) #4~#200.

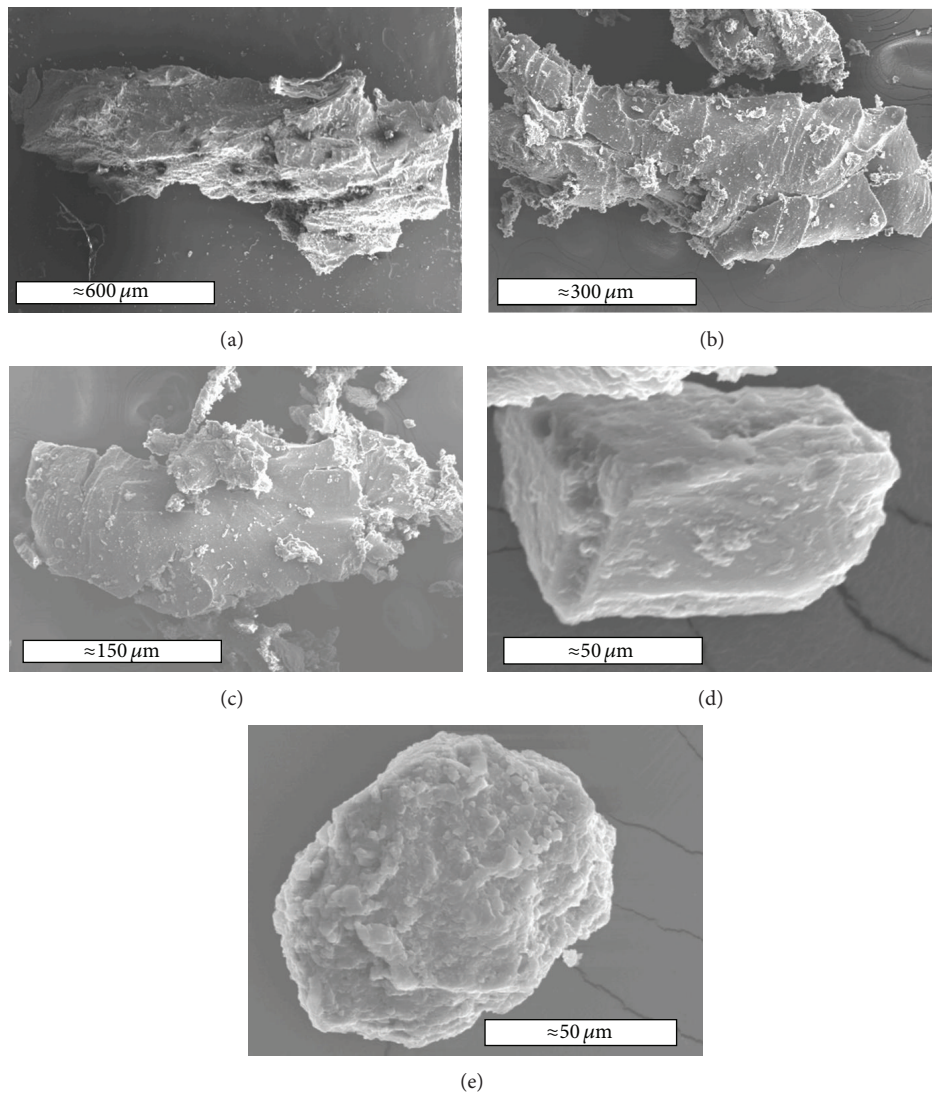


FIGURE 4: Scanning Electron Microscopy (SEM) pictures for different sizes of crumb rubber particles: (a) #4~#20; (b) #20~#200; (c) #4~#200; (d) #100~#200; (e) #100~#200.

film, and then the bulk specific gravity with regard to the procedure in AASHTO T275 [17] was determined.

**2.2.3. Hydraulic Conductivity Test.** Hydraulic conductivity is a significant characteristic of porous asphalt mixtures on account of designing a drainage layer in pavement structures. The hydraulic conductivity of the compacted specimens symbolized in terms of the coefficient of permeability ( $k$ ) was determined by using a falling-head water permeameter. The apparatus of falling-head permeability test consists of a metal cylinder and demountable metal plates at the top and bottom of the metal mold. The top plate has a hole with at least 31.75 mm inner diameter of graduated pipe for water inflow, and the bottom plate has an outlet hole of minimum inner diameter of 18 mm and valve so that water can flow out. The specimen in the mold was placed between the bottom plate and the top plate and compressed by using clamps for sealing the bottom and top plates. The graduated pipe is filled with distilled water, and the valve is opened to flow through a saturated specimen. The time period taken for level change of water between two fixed points on the perspex pipe was recorded. The coefficient of permeability is then determined based on Darcy's law. A minimum permeability coefficient of  $10^{-2}$  cm/s ( $\approx 100$  m/day) is commonly recommended for the pervious pavement structure [18, 19].

**2.2.4. Cantabro Abrasion Test (Particle Loss Resistance).** The Cantabro test was conducted to evaluate the resistance to particle loss of the mixtures according to ASTM D7064 [20]. The compacted specimens were individually put in the Los Angeles testing machine without steel balls. After Los Angeles drum had been rotated for 300 revolutions at a speed of 30–33 revolutions per minute, the loose material broken off from surface of the test specimen was discarded. The masses of the specimens before and after the test were recorded. The percentage loss by weight of original specimen was calculated as the Cantabro abrasion. The percentage of Cantabro abrasion must be less than 25% in the European Specification.

**2.2.5. Indirect Tensile Strength Test.** The indirect tensile (IDT) strength test has been widely used for hot-mix asphalt (HMA) mixture design. The splitting strength is determined in this test as an indicator of the tensile strength of the compacted specimen. The results of (IDT) strength are employed to obtain the comparative relative strength of asphalt mixtures and predict the potential for pavement distress. Since the performance of porous mixtures depends on tensile strength of bitumen film, the IDT strength is also an important characterization test for porous asphalt mixture. The test is performed by using Marshall stability test equipment at 50 mm/min deformation rate and 25°C temperature in accordance with ASTM D6931 procedure [21]. In the test, a cylindrical specimen is exposed to a compressive load. It acts along the vertical diameter plane by a curved loading strip. The developed tensile stress, perpendicular to the direction of the applied load, ultimately causes the specimen to fail by splitting along the vertical diameter. The ultimate load at

failure is recorded and used to calculate the IDT strength of the specimen.

**2.2.6. Moisture Susceptibility.** Moisture causes a loss of adhesion between the bitumen and the aggregate surface and accelerates the process of distresses such as rutting, cracking, and raveling in the asphalt mixture. Moisture susceptibility is extremely an important characteristic for the performance of the porous asphalt mixtures exposed to water damage. The test was performed according to Modified Lottman Test (AASHTO T283) that is one of the most largely used procedures for determining HMA water damage [22]. Six compacted specimens are required at 6%–8% air voids in the Modified Lottman Test. The specimens are separated into two groups. The first group of three is unconditioned specimens as the control group. The second group is conditioned specimens of vacuum-saturated saturation level between 55 percent and 80 percent. After conditioned specimens are placed in a freezer at  $-18^{\circ}\text{C}$  for 16 hours, they are moved to at  $60^{\circ}\text{C}$  water bath for 24 hours. All of the specimens are subjected to the IDT strength test conducted with a loading rate of 50 mm/min at  $25^{\circ}\text{C}$ . The tensile strength ratio (TSR) is calculated by the average IDT strength of conditioned subset divided by the average IDT strength of control subset. The allowable value of TSR must be more than 70% for this test method.

**2.2.7. Resilient Modulus (Stiffness Modulus) Test.** Resilient modulus of asphalt mixtures is the most popular form of stress-strain measurement used to evaluate elastic properties. The five-pulse indirect tensile modulus test used to determine the stiffness of material was performed in accordance with ASTM D4123 [23] using Universal Testing Machine (UTM-5P). In the test, the cylindrical specimen is subjected to a pulsed diametric loading force, and the resulting total recoverable diametric strain is then measured at axes  $90^{\circ}$  from the applied force. Because the strain in the same axes is not measured, a value of 0.4 for Poisson's ratio of asphalt mixtures is accepted as a constant. The specimens were placed in the indirect tensile test equipment, and test results were recorded in the computer by data logger system. The test load sequence consists of 150 conditioning pulses and five-pulse test periods. The conditioning stage provides that the loading plates are seated onto the specimen for consistent results. The stiffness module is calculated by five-pulse test period. In addition, the specimen's skin and core temperatures were measured by transducers inserted in a dummy specimen located near the test specimen in order to control the testing temperature. In this study, specimens prepared in the laboratory were tested under the waveform type of Haversine at load pulse period of 3000 ms, pulse width of 80 ms, and peak loading force of 1000 N.

### 3. Test Result and Discussion

The results of porous asphalt mixture design were given in this section. In addition, the effects of rubber size and concentration on performance characteristics were discussed.

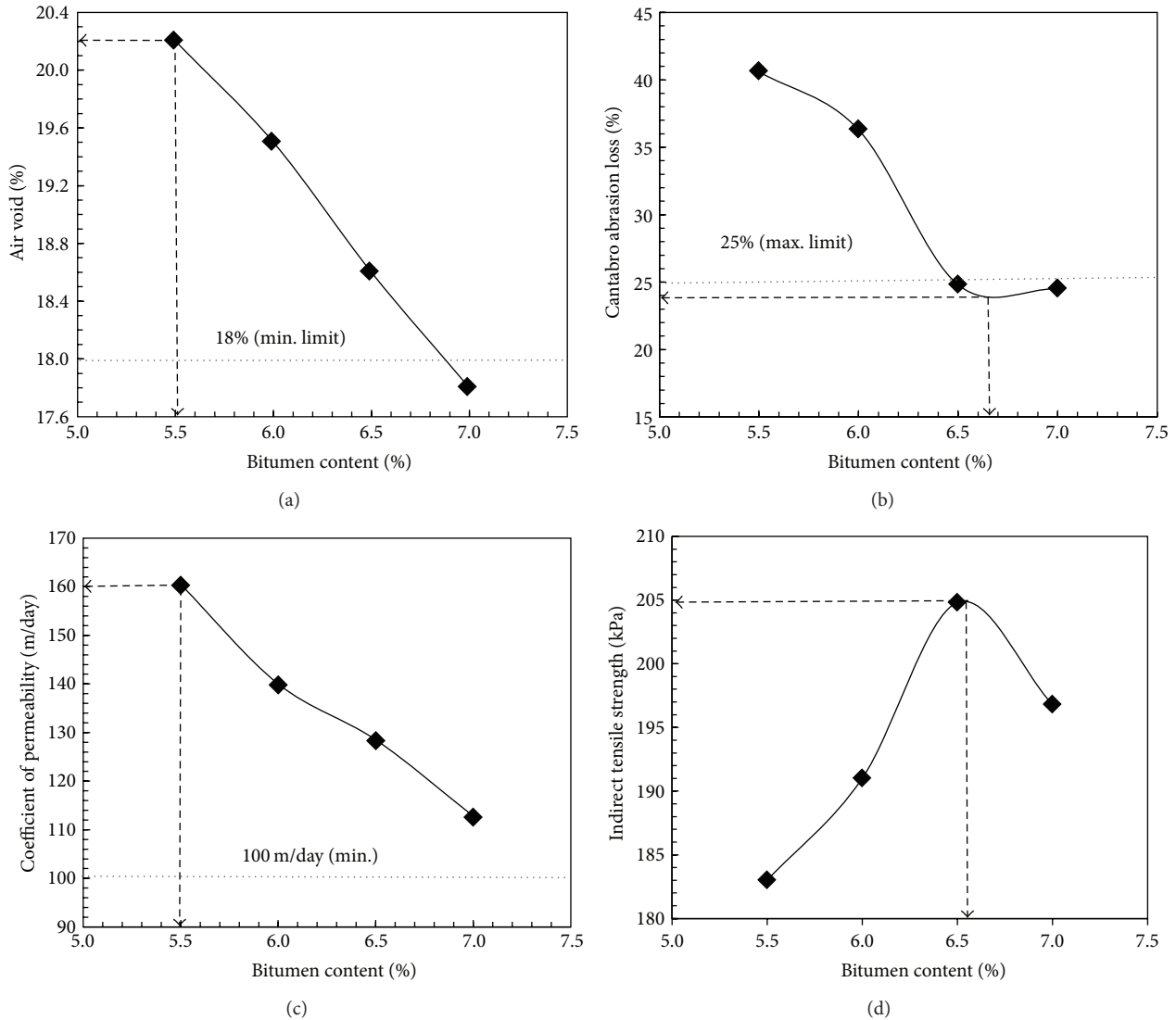


FIGURE 5: Graphics of mix design for porous asphalt mixtures: (a) air voids; (b) Cantabro abrasion loss; (c) coefficient of permeability; (d) indirect tensile strength.

**3.1. Mix Design.** European Porous Asphalt Mix Design Approach is generally based on determining the voids and the percentage of particle abrasion loss at various binder contents. The design bitumen content is optimized for air voids and abrasion. It is recommended that the modified bitumen is used to improve the resistance against particle loss. It achieved a longer durability by means of its higher cohesion and viscosity [4].

Porous asphalt design procedures used in Europe and America mostly include the air void ratio, permeability, Cantabro abrasion loss, and indirect tensile strength tests. In this study, the following design criteria widely accepted in these countries were selected. The minimum permeability coefficient depends on the target air voids (18–23%) and is 100 m/day. A maximum Cantabro particle loss of 25% is allowed at 25°C. The allowable asphalt content ranges 4–6

percent. The bitumen content ensuring these limit values was selected as a percentage of optimum bitumen. The graphics of the mix design were given in Figure 5.

The air void and permeability coefficients were decreased by increasing bitumen content (Figures 5(a) and 5(c)). The maximum values of these characteristics were obtained for bitumen content of 5.5%. The minimum Cantabro abrasion loss provided the bitumen content of 6.5%. However, test result at bitumen content of 7% is quite close to results at 6.5% as shown in Figure 5(b). The maximum value for indirect tensile strength was also obtained for bitumen content of 6.5% as shown in Figure 5(d). The optimum bitumen content of 6.5% was determined according to these results. All design values of porous asphalt mixture were given in Table 4. Although the mix design of porous asphalt mixture was achieved, design requirements with the penetration grade

TABLE 4: Result of the Porous Asphalt Mix Design.

Design characteristics	Results
Optimum bitumen, %	6.5
Air void, %	18.6
Cantabro abrasion loss, %	24.8
Coefficient of permeability, m/day	128.5
Indirect tensile strength, kPa	204.8

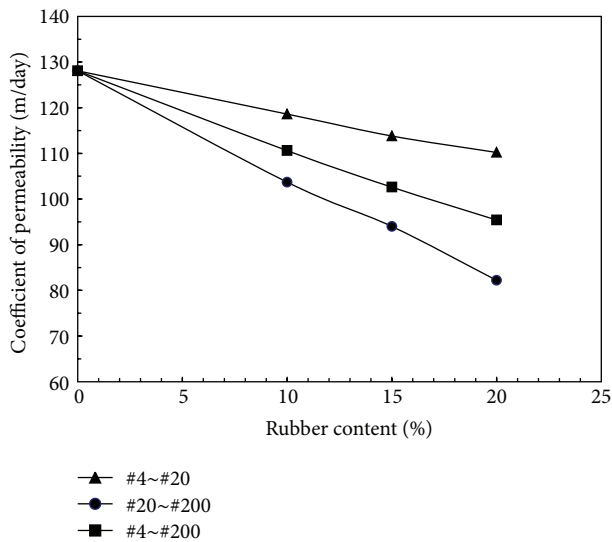


FIGURE 6: Effect of crumb rubber size and content on coefficient of permeability.

bitumen of 50/70, the low values in Cantabro abrasion loss, and IDT strength test were introduced due to the necessity of modified bitumen.

**3.2. Effect of Crumb Rubber on Performance Characteristics.** The effects of crumb rubber size and content on performance characteristics of porous asphalt mixtures were analyzed and discussed in this section.

**3.2.1. Hydraulic Conductivity.** Figure 6 illustrates the variations of permeability coefficient with rubber content for all three sizes (#4~#20, #20~#200, and #4~#200). Increasing the content of the crumb rubber significantly reduced the coefficient of permeability. Analyzing the crumb rubber in terms of particle size, it was indicated that #4~#20 rubber size had the maximum value of permeability coefficient. The addition of crumb rubber remained below limit value of permeability coefficient (100 m/day) except in the case of the 10% content of the #20~#200 crumb rubber. For #4~#200 crumb rubber, the addition of 20% crumb rubber similarly remained below limit value of 100 m/day. In all other cases, coefficient of permeability was provided over the limit value. These results show that the small size of rubber particle reduced air voids and the coefficient of permeability due to its surface area.

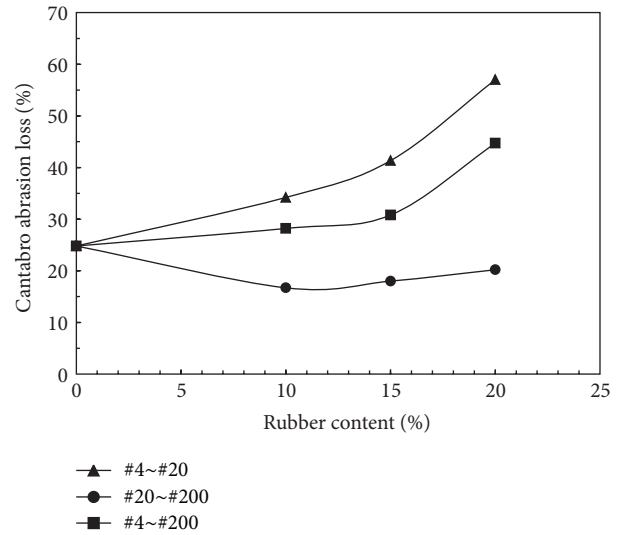


FIGURE 7: Effect of crumb rubber size and content on Cantabro abrasion loss.

**3.2.2. Cantabro Abrasion Loss.** The experimental results were analyzed as given in Figure 7. It can be clearly seen that Cantabro abrasion loss was achieved less than control specimens in the case of all contents of the #20~#200 crumb rubber. The addition of 10%, 15%, and 20% rubber content of #20~#200 showed an improvement of 19%, 27%, and 33%, respectively, compared to control. Particle loss of mixtures increased as the content of rubber increased for all rubber particle sizes. The optimum rubber concentration of 10% was determined. The degree of particle loss in the mixtures with #4~#20 and #4~#200 was observed to increase in comparison with control specimens. This increase of 130% reached at 20% content of #4~#20 rubber sizes in which the maximum particle loss occurred. #20~#200 mesh size include finer particles in comparison to the other mesh size (Figure 3). Finer rubber particles formed homogeny and rigid matrix (bitumen-fine aggregate, crumb rubber) due to the fact that they were uniformly mixed in the asphalt mixture. Because the coarse rubber particles in #4~#20 and #4~#200 mesh sizes caused increasing discontinuity in the bitumen film, it weakened the strength of the bitumen film. In addition, the #20~#200 mesh size increased the surface area which required surrounding particles by bitumen. Thus, decreasing bitumen film thicknesses tended to improve tensile strength of porous asphalt mixtures. As a result, Cantabro abrasion loss values decrease by using #20~#200 crumb rubber.

**3.2.3. Indirect Tensile Strength.** The indirect tensile (IDT) strength test is very useful in deciding the performance of porous asphalt mixtures which depend on the cohesion of bitumen film. The variations of indirect tensile strength with rubber content for all three sizes are given in Figure 8. IDT strength test results were in compliance with Cantabro abrasion test results. The addition of crumb rubber significantly reduced the IDT strength except in the case of the 10% content of the #20~#200 crumb rubber. The case was the only one

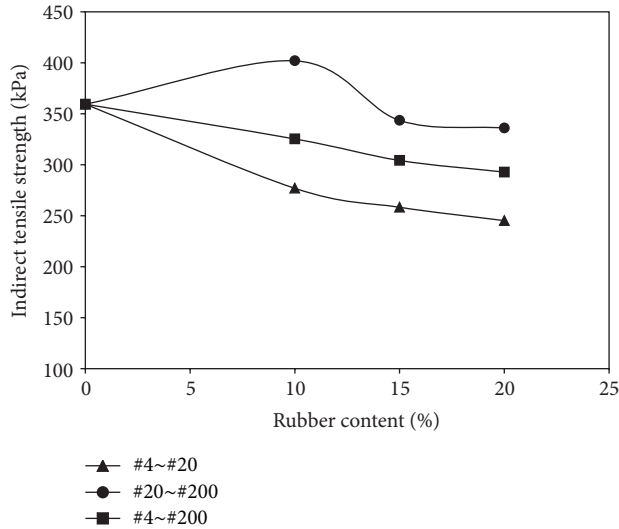


FIGURE 8: Effect of crumb rubber size and content on indirect tensile (IDT) strength.

combination which increased the indirect tensile strength by 12% compared to the control specimens. IDT strength values were less than the control specimens for all rubber contents of #4~#20 and #4~#200. The maximum reduction in IDT strength by 32% was obtained in the case of the 20% content of the #4~#20 crumb rubber. In general, increasing the crumb rubber size has decreased the IDT strength of the porous asphalt mixtures. These results can be explained by the fact that the strong matrix was formed by homogeneously mixing small rubber particles in the mixtures and maintained an adhesion between the bitumen and the aggregate. It can be concluded that the cohesion and IDT strength of the bitumen film were negatively affected by the form of rubber particle as shown in Figure 4. Although larger crumb rubber particle shaped like pine needle rubber improves indirect tensile strength of dense graded asphalt pavement [24], it affects the performance of porous asphalt mixtures negatively because the porous asphalt mixtures have less fine aggregate.

**3.2.4. Moisture Susceptibility.** The moisture damage in the asphalt concrete pavements is an important problem. The porous asphalt pavement is particularly subjected to moisture damage more than dense graded asphalt mixtures. The moisture damage counts on the loss of adhesion between bitumen and aggregate surface or cohesion of the bitumen. The modification of bitumen or mixture is the most commonly used method in the improvement of the resistance to the moisture damage.

The TSR value for the control specimens was determined to be 58%. This value remained below the limit value of 70% because unmodified bitumen was used to prepare the control specimens. The unmodified bitumen was preferred to be employed for a better understanding of the effect of crumb rubber on the porous asphalt mixtures. An examination of the graphical presentations in Figure 9; the addition of crumb rubber significantly reduced the TSR value except

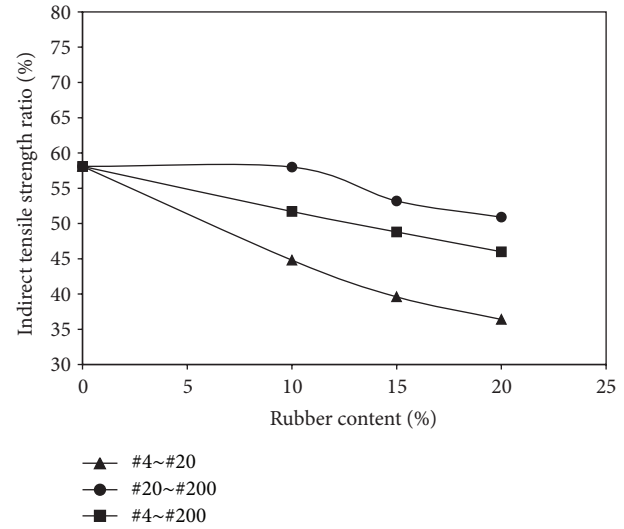


FIGURE 9: Effect of crumb rubber size and content on moisture susceptibility.

in the case of the 10% content of the #20~#200 crumb rubber. For #20~#200 crumb rubber, the addition of %10 crumb rubber has obtained a similar TSR value with control specimens. TSR values were less than the control specimens for all rubber contents of #4~#20 and #4~#200. Increasing the crumb rubber size has substantially decreased the TSR values. The maximum reduction in TSR by 63% was obtained from the addition of the 20% content for the #4~#20 crumb rubber. As explained above, while the mixtures with small rubber particles improved performance of porous asphalt, the big size rubber particle negatively affected cohesion of bitumen and IDT strength. This effect increased largely the IDT strength of conditioned specimens. Therefore, the TSR values are significantly reduced compared to the control specimens.

**3.2.5. Resilient Modulus.** The resilient modulus measured in the indirect tensile mode represents the elastic properties of asphalt mixtures under repeated load effectively. The resilient modulus was one of the most commonly used methods for measuring the stiffness modulus of hot-mix asphalt. The variations of resilient modulus with rubber content and rubber size were given in Figures 10 and 11, respectively. The addition of crumb rubber reduced the resilient modulus except in the case of the 10% and 15% contents of the #20~#200 crumb rubber. The maximum resilient modulus value was obtained in rubber content of 10% at #20~#200. In this case resilient modulus was increased by 22% compared to the control specimens. Increasing the crumb rubber size reduced the resilient modulus of the porous asphalt mixtures substantially. The maximum decrease in resilient modulus of 56% was determined in rubber content of 20% for #4~#200 crumb rubber. Resilient modulus values were decreased as crumb rubber content in the mixtures for all rubber particle sizes. The optimum content of crumb rubber was determined in 10%. This test results coincided with IDT

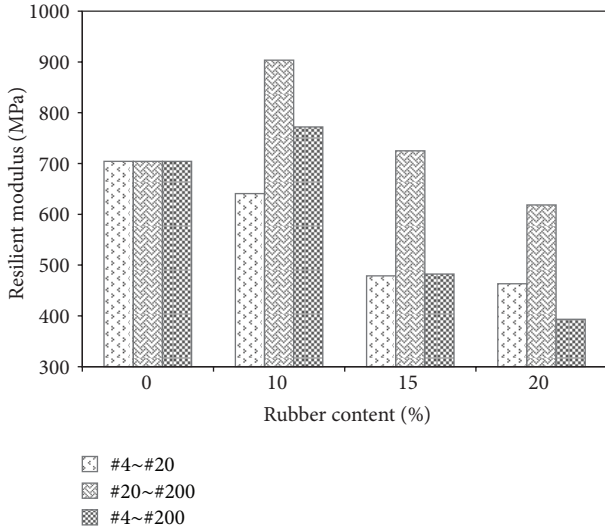


FIGURE 10: Effect of crumb rubber content on resilient modulus.

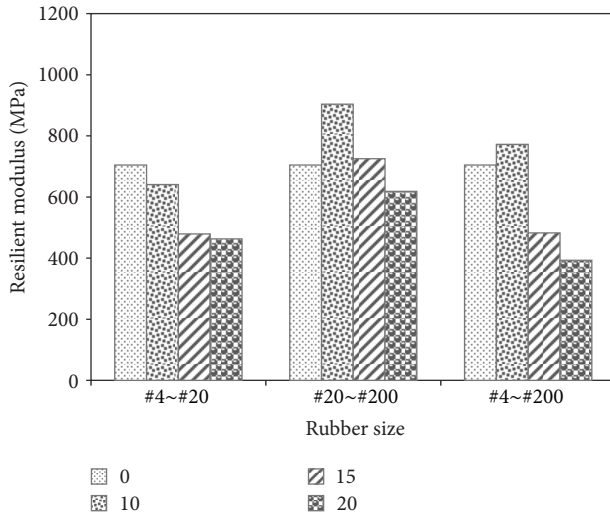


FIGURE 11: Effect of crumb rubber size on resilient modulus.

strength and Cantabro abrasion test results. Therefore, the impact of crumb rubber size and content on resilient modulus can be interpreted as noted above.

#### 4. Conclusion and Recommendation

This study presented an evaluation of recycled scrap tire obtained from tire recapping or tire buffing in the porous asphalt mixtures. The impacts of crumb rubber size and concentration on the performance characteristics of porous asphalt mixtures were investigated in this experimental study. Porous asphalt mixtures were modified by dry process using crumb rubber in three different grain size distributions (#4~#20, #20~#200, and #4~#200) and rubber contents of 10%, 15%, and 20% as weight of bitumen. The permeability, Cantabro abrasion, indirect tensile, moisture susceptibility (Modified Lottman), and resilient modulus tests were carried

out in this experimental program. Based on the analysis of the results obtained from this study, the following conclusion and recommendation can be drawn.

- (i) The optimum bitumen content in the design of porous asphalt was determined to be 6.5%. Although the mix design of porous asphalt mixture has achieved design requirements with penetration grade bitumen of 50/70, the low values in Cantabro abrasion loss and IDT strength tests have demonstrated the necessity of modified bitumen.
- (ii) Increasing the crumb rubber size and content significantly reduced the coefficient of permeability. The #20~#200 crumb rubber exhibited better performance than other grain size distributions, and the coefficient of permeability at the 10% rubber content remained over the limit value (100 m/day). The permeability test result showed that the small size of rubber particle reduced air voids and the coefficient of permeability due to its surface area.
- (iii) Cantabro abrasion loss of mixtures increased as the content of rubber increased for all rubber particle sizes. The optimum rubber concentration was determined to be 10%. All rubber contents of #20~#200 indicated an improvement of Cantabro abrasion loss compared with other rubber gradation. The maximum particle loss of 130% occurred at 20% content of #4~#20. The larger rubber particle size leads to an increase in the Cantabro abrasion loss on the account of the discontinuity in the bitumen matrix.
- (iv) While IDT strength of 12% only improved at 10% content of the #20~#200 crumb rubber, IDT values were significantly reduced for all rubber contents compared to the control specimens. In general, increasing the crumb rubber size decreased the IDT strength of the porous asphalt mixtures. The discontinuity in the matrix formed by large size rubber particle has a negative effect on the cohesion and IDT strength.
- (v) The addition of crumb rubber significantly reduced the TSR value except in the case of the 10% content of the #20~#200 crumb rubber. This value was similar to the TSR of control specimens of 58% which remained below limit value of TSR (70%) because of the fact that the control specimens were prepared with unmodified bitumen. Increasing the crumb rubber size has substantially decreased the TSR values. Modified Lottman Test results indicated that the addition of crumb rubber did not improve the moisture susceptibility performance.
- (vi) Resilient modulus test results corresponded to the IDT strength and Cantabro abrasion test results. Resilient modulus values were decreased with addition of crumb rubber to the mixtures for all rubber particle sizes. In addition, increasing the crumb rubber size decreased it substantially. The maximum resilient modulus value was obtained in rubber content of 10% at #20~#200. The optimum content of crumb rubber was determined in 10%.

- (vii) All test results show that #20~#200 mesh size which includes more spherically formed rubber particles than the other mesh sizes (Figure 4(d)) mixed uniformly in the mixtures and constituted a more rigid bituminous matrix. Therefore, it has partially improved the performance characteristics of porous asphalt mixtures. In contrast, larger rubber particle size leads to the discontinuity in the bitumen film. This larger size affected tensile strength of bitumen film negatively resulting in loss of performance. This effect largely increased the IDT strength of conditioned specimens due to loss of adhesion.
- (viii) The larger fiber-like shaped crumb rubber particles improve the indirect tensile strength of dense graded asphalt pavement, but it negatively affects the performance of porous asphalt mixtures depending on less finer aggregate in the porous asphalt mixtures.

It can be recommended that the case of 10% content of the #20~#200 crumb rubber should be used to improve the performance characteristics of porous asphalt mixtures. The rubber content higher than %10 and the size larger than #20~#200 decrease the performance of the mixture significantly. Although the rubber particles size and concentration which was determined in this study by using dry process crumb rubber modification has provided the performance improvement for porous asphalt mixtures, the future investigation can be carried out about fractions of #20~#200 rubber gradation and concentrations less than 10%. Moreover, the wet process which requires additional cost in application should be studied to improve the performance of porous asphalt mixture.

## References

- [1] Rubber Manufacturers Association, "Scrap tire markets in the United States," 9th Biennial Report, Washington, DC, USA, 2009.
- [2] Federal Highway Administration, "User guidelines for waste and by product materials in pavement construction," Tech. Rep. FHWA-RD-97-148, 1997.
- [3] A. A. A. Molenaar, A. J. J. Meerkerk, M. Miradi, and T. van der Steen, "Performance of porous asphalt concrete," in *Proceedings of the Annual Meeting and Technical Session (CD-ROM)*, Association of Asphalt Paving Technologists, Lino Lakes, Minn, USA, 2006.
- [4] A. Ruiz, R. Alberola, F. Perez, and B. Sanchez, "Porous asphalt mixtures in Spain," *Transportation Research Record*, vol. 1265, pp. 87-94, 1990.
- [5] P. M. Nelson and P. G. Abbott, "Acoustical performance of previous Macadam surfaces for high-speed roads," *Transportation Research Record*, no. 1265, pp. 25-33, 1990.
- [6] Q. Lu and J. Harvey, "Laboratory evaluation of open-graded asphalt mixes with small aggregates and various binders and additives," *Transportation Research Record*, no. 2209, pp. 61-69, 2011.
- [7] M. N. Partl, E. Pasquini, F. Canestrari, and A. Virgili, "Analysis of water and thermal sensitivity of open graded asphalt rubber mixtures," *Construction and Building Materials*, vol. 24, no. 3, pp. 283-291, 2010.
- [8] California Department of Transportation, *Open Graded Friction Course Usage Guide*, Sacramento, Calif, USA, 2006.
- [9] W. D. Cao, Z. Y. Yao, Q. S. Shang, Y. Y. Li, and Y. S. Yang, "Performance evaluation of large stone porous asphalt-rubber mixture," *Advanced Materials Research*, vol. 150-151, pp. 1184-1190, 2011.
- [10] T. Hsu, S. Chen, and K. Hung, "Performance evaluation of asphalt rubber in porous asphalt-concrete mixtures," *Journal of Materials in Civil Engineering*, vol. 23, no. 3, pp. 342-349, 2011.
- [11] R. C. Haas, E. Thompson, F. Meyer, and G. R. Tessier, "The role of additives in asphalt paving technology," *Proceeding of the Association of Asphalt Paving Technologists*, vol. 52, pp. 324-344, 1983.
- [12] J. W. Oliver, "Optimising the improvements obtained by the digestion of comminuted scrap rubbers in paving asphalt," *Proceeding of the Association of Asphalt Paving Technologists*, vol. 51, pp. 169-188, 1982.
- [13] B. Choubane, G. A. Sholar, J. A. Musselman, and G. C. Page, "Ten-year performance evaluation of asphalt-rubber surface mixes," *Transportation Research Record*, no. 1681, pp. 10-18, 1999.
- [14] R. G. Hicks and J. A. Epps, *Quality Control for Asphalt Rubber Binders and Mixes*, Rubber Pavements Association, Tempe, Ariz, USA, 2000.
- [15] National Asphalt Pavement Association, *Porous Asphalt Pavement*, National Asphalt Pavement Association, Lanham, MD, USA, 2003.
- [16] M. Backstrom and A. Bergstrom, "Draining function of porous asphalt during snowmelt and temporary freezing," *Canadian Journal of Civil Engineering*, vol. 27, no. 3, pp. 594-598, 2000.
- [17] AASHTO T275-91, *Standard Method of Test for Bulk Specific Gravity of Compacted Bituminous Mixtures Using Paraffin-Coated Specimens*, American Association of State and Highway Transportation Officials, Washington, DC, USA, 2005.
- [18] R. B. Mallick, P. S. Kandhal, L. A. Cooley Jr., and D. E. Watson, "Design, construction, and performance of new generation open-graded friction courses," NCAT Report 2000-01, National Center for Asphalt Technology, Auburn University, 2000.
- [19] Florida Department of Transportation, "Florida method of test for measurement of water permeability of compacted asphalt paving mixtures," Designation FM 5-565, 2012.
- [20] "ASTM D7064-08, standard practice for open-graded friction course (OGFC) mix design," in *Annual Book of ASTM Standards, Road and Paving Materials*, vol. 04.03, ASTM International, West Conshohocken, Pa, USA, 2008.
- [21] "ASTM D6931-07, standard test method for indirect tensile (IDT) strength of bituminous mixtures," in *Annual Book of ASTM Standards, Road and Paving Materials*, vol. 04.03, ASTM International, West Conshohocken, Pa, USA, 2007.
- [22] "Standard method of test for resistance of compacted asphalt mixtures to moisture-induced damage," AASHTO T283-03, American Association of State and Highway Transportation Officials, Washington, DC, USA, 2007.
- [23] "ASTM D4123-82, standard test method for indirect tension test for resilient modulus of bituminous mixtures," in *Annual Book of ASTM Standards, Road and Paving Materials*, vol. 04.03, ASTM International, West Conshohocken, Pa, USA, 1995.
- [24] M. Tuncan, A. Tuncan, and A. Cetin, "The use of waste materials in asphalt concrete mixtures," *Waste Management and Research*, vol. 21, no. 2, pp. 83-92, 2003.

## Research Article

# Synthesis, Electrical Conductivity, and Dielectric Behavior of Polyaniline/ $V_2O_5$ Composites

Shama Islam,<sup>1</sup> G. B. V. S. Lakshmi,<sup>2</sup> Azher M. Siddiqui,<sup>1</sup> M. Husain,<sup>1</sup> and M. Zulfequar<sup>1</sup>

<sup>1</sup> Department of Physics, Jamia Millia Islamia, New Delhi 110025, India

<sup>2</sup> Material Science Group, Inter University Accelerator Centre, New Delhi 110025, India

Correspondence should be addressed to M. Zulfequar; [mzulfe@rediffmail.com](mailto:mzulfe@rediffmail.com)

Received 31 March 2013; Accepted 12 June 2013

Academic Editor: Enrique Viguera-Santiago

Copyright © 2013 Shama Islam et al. This is an open access article distributed under the Creative Commons Attribution License, which permits unrestricted use, distribution, and reproduction in any medium, provided the original work is properly cited.

Conducting polymer composites of polyaniline/vanadium pentoxide PANI/ $V_2O_5$  (with different initial weight percentage of  $V_2O_5$ ) has been synthesized by *in situ* polymerization method. DC conductivity of compressed pellets has been analyzed in the temperature range 300–550 K and was found to increase with  $V_2O_5$  doping. This increase in conductivity is mainly due to band conduction. It has also been observed that the dielectric constant and dielectric loss increase with the level of doping of  $V_2O_5$  but remain independent of the frequency (50 KHz–1 MHz). X-ray diffraction pattern shows some order of crystallinity of composites due to interaction of polyaniline with  $V_2O_5$ . UV-visible spectroscopy shows an increase in the optical band gap with doping.

## 1. Introduction

The conducting polymers have emerged as a new class of materials because of their unique electrical, optical, and chemical properties. By proper doping the conductivity of these materials can be varied from semiconducting to metallic regime, which offers new concept of charge transport mechanism. Among different conducting polymers, conductive polyaniline (PANI) has been studied extensively because of its ease of synthesis in aqueous media, its environmental stability, special electrical, and other properties. PANI and its derivatives have received much attention because of their various technological applications, reversible proton doping, high electrical conductivity, and ease of bulk synthesis. PANI is also a suitable candidate for a variety of technological applications such as solar cells, electromagnetic shielding, electrodes for rechargeable batteries, and sensors [1–11].

Many authors have studied the progress of chemical polymerization and doping of aniline and its derivatives. The effort was to correlate mechanisms of oxidation of anilines and properties of PANI such as electrical conductivity, molecular weight, and crystallinity. However, when they were taken in the composite form, their electrical as well as dielectric properties alter from those of basic materials. A number of

groups had reported on the electrical conductivity and dielectric properties of composites of a variety of conducting polymers [12–15]. Recently heterogeneous conducting polymer composites, especially organic-inorganic composites, became the subject of extensive study. Among the base materials used, polyaniline (PANI) is one of the most extensively studied conducting polymer. Ever since its discovery in a pioneering work by Mc Diarmid et al. [16–21]. The DC conductivity of a conjugated polymer depends on the doping level, and for a given dopant in a particular polymer, the conductivity increases up to a certain level and then saturates.

The vanadium oxygen system ( $V_2O_5$  and  $VO_2$ ) has been widely studied because the system shows metal semiconductor transitions, which imply an abrupt change in their optical and electrical properties. For example,  $VO_2$  exhibits a change in electrical resistivity in the order of  $10^5 \Omega \text{ cm}$  over a temperature change of 0.1 at 68°C in a single crystal. This oxide is therefore used in thermal sensing and switching. Similarly,  $V_2O_5$  has been a subject of several theoretical and applied studies, due to its industrial importance for many technological applications, such as heterogeneous catalyst.  $V_2O_5$  also plays the role of active electrode in a rechargeable lithium battery. High electrochemical activity, high stability, and ease of thin film formation by numerous deposition

techniques led to its use as a highly promising intercalation material in solid state microbattery applications. It is the most stable oxide in the V–O system with an energy gap of  $\sim 2.2$  eV and shows a semiconductor-metal transition at about  $250^\circ\text{C}$  [22–26].

In the present study, composites of PANI/ $\text{V}_2\text{O}_5$  have been synthesized by *in situ* polymerization of aniline using ammonium persulphate ( $(\text{NH}_4)_2\text{S}_2\text{O}_8$ ) as oxidizing agent, in the presence of  $\text{V}_2\text{O}_5$ . The  $\text{V}_2\text{O}_5$  concentrations were varied from 0 to 40% weight. The composites obtained have different concentrations of  $\text{V}_2\text{O}_5$ .

In present work electrical conductivity by two-probe method and dielectric behavior by LCR methods of these synthesized composites have been studied. X-ray diffraction (XRD) and UV-visible absorption spectroscopy have been carried out to characterize these samples.

## 2. Experimental

All chemicals used were of analytical reagent (AR) grade. The monomer aniline was doubly distilled prior to use. Ammonium persulphate ( $(\text{NH}_4)_2\text{S}_2\text{O}_8$ ), hydrochloric acid (HCl), and vanadium pentoxide  $\text{V}_2\text{O}_5$  were used as received in the present study.

Polyaniline has been synthesized by *in situ* oxidative polymerization of aniline, hydrochloric acid (HCl), and ammonium persulphate ( $(\text{NH}_4)_2\text{S}_2\text{O}_8$ ) as oxidant. The oxidant monomer ratio is 1:1.25. Aniline (1.25 M) has been dissolved in 10 mL of HCl (1 M) taken in 200 mL round bottom flask and stirred well. Further finely ground  $\text{V}_2\text{O}_5$  powder taken in different (20, 30, and 40) wt% with respect to aniline concentration has been added to the previous mixture under vigorous stirring in order to keep  $\text{V}_2\text{O}_5$  powder suspended in solution. The reaction mixture has been cooled up to  $5^\circ\text{C}$ , and the precooled solution of ammonium persulfate (1 M) has been slowly added drop by drop over a period of 30 min. The reaction has been allowed to proceed for 6–8 h. The mixture was further cooled down to  $4^\circ\text{C}$  for 24–36 hours. It was then filtered and washed with ammonia until filtrate was colorless. The dark colored polymer powder so obtained was dried thoroughly in an oven at  $100^\circ\text{C}$  until constant weight was attained, then grinded and sieved. PANI has been synthesized in the same manner in the absence of  $\text{V}_2\text{O}_5$ .

The DC conductivity of pure PANI and PANI/ $\text{V}_2\text{O}_5$  composites was measured by using two-probe method in the temperature range 300–550 K. The powder was made into pellets of 1 cm diameter and different thickness for PANI/ $\text{V}_2\text{O}_5$  composites. The bulk DC conductivity was measured by mounting between two steel electrodes inside a specially designed metallic sample holder [22]. The temperature was measured with a calibrated copper-constantan thermocouple mounted near the electrodes. The samples were annealed at a temperature of  $100^\circ\text{C}$  to avoid any effect of moisture absorption. These measurements were made at a pressure of about  $10^{-3}$  Torr. A stabilized voltage of 1.5 V was applied across the sample, and the resultant current was measured with a picoammeter.

In order to get information about the crystallinity, X-ray diffraction patterns of all samples are recorded at room temperature by using a Panalytical (PW 3710) X-ray powder diffractometer with  $\text{Cu K}\alpha$  radiation. All the samples were scanned in angular range of  $0$ – $90^\circ$  with scan speed of  $0.01^\circ/\text{s}$  under the similar conditions. UV-visible spectroscopy has been carried out using Camspec M550 double beam UV-visible spectrophotometer [22–26].

## 3. Results and Discussion

**3.1. Temperature DC Conductivity Studies.** The variation of DC conductivity with temperature for pure PANI and the PANI/ $\text{V}_2\text{O}_5$  composites (with different wt%) is shown in Figure 1. Arrhenius plot of DC conductivity shows straight line behavior. The DC conductivity of pure PANI increased exponentially with doping, exhibiting semiconductor characteristics. The conductivity as a function of temperature can be represented by the relation [27]

$$\sigma_{\text{DC}} = \sigma_0 \exp\left(-\frac{\Delta E}{kT}\right), \quad (1)$$

where  $(\Delta E)$  is the activation energy for the DC conduction mechanism, “ $k$ ” is the Boltzmann constant, and “ $\sigma_0$ ” is the preexponential factor. The activation energy  $(\Delta E)$  has been calculated from the slope of Figure 1 for pure PANI and the PANI/ $\text{V}_2\text{O}_5$ . The DC conductivity of undoped PANI is measured to be  $3.58 \times 10^{-9}$  S/cm. After doping with different weight % of  $\text{V}_2\text{O}_5$  the conductivity was found to change from  $10^{-7}$  to  $10^{-9}$  S/cm, attaining a maximum value at 30 weight % of  $\text{V}_2\text{O}_5$  and then reduced at 40 weight % of  $\text{V}_2\text{O}_5$ . The doping of conducting polymers implies charge transfer, the associated insertion of a counter ion, and the simultaneous control of Fermi level or chemical potential. Through doping, electronic and optical properties of conducting polymers can be controlled over a long range. The electrical conductivity of conducting polymers results from mobile charge carriers introduced into the  $\pi$ -electronic system through doping. At low doping levels these charge carriers are self-localized and form nonlinear configurations. Because of large interchain transfer integrals, the transport of charge is believed to be principally along the conjugated chains, with interchain hopping as a necessary secondary condition [28–31]. When the polymer is heavily doped (40 weight %), the wave functions are delocalized over many lattice constants along the polymer chain. In PANI, since there are nearly degenerate ground states, the dominating charge carriers are polarons and bipolarons [32]. When PANI is doped with  $\text{V}_2\text{O}_5$  hydrochloric acid, the charge carriers form nonlinear configurations, and as a result the conductivity does not change substantially. The nonlinear formation may be more in the case of heavy doping of 40 weight % of  $\text{V}_2\text{O}_5$ , due to which it exhibits lesser conductivity than 30 weight % doped polymer.

The activation energy  $\Delta E$ , DC conductivity  $\sigma_{\text{DC}}$ , and preexponential factor  $\sigma_0$  of pure PANI and PANI/ $\text{V}_2\text{O}_5$  composites have been measured and tabulated in Table 1.

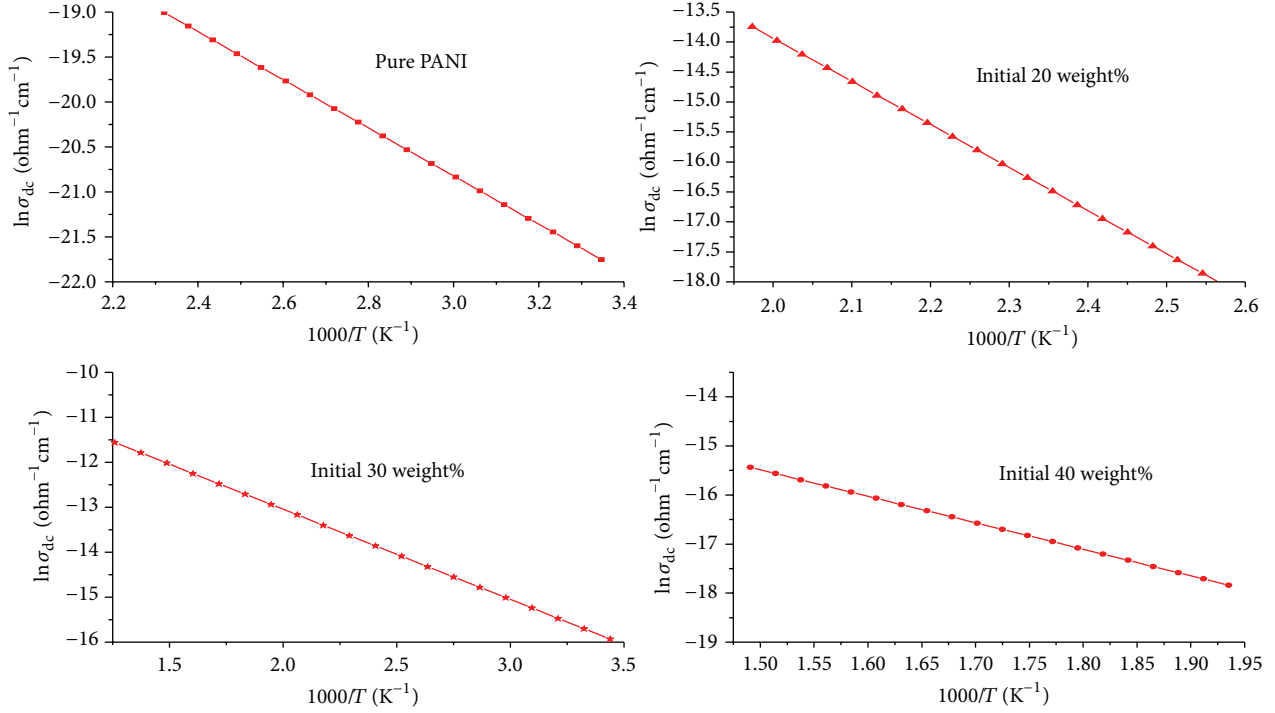


FIGURE 1: Temperature dependence of DC conductivity in the temperature range (300–550 K) for pure PANI and PANI/V<sub>2</sub>O<sub>5</sub> composites (different weight %).

TABLE 1: Electrical and dielectric parameters of pure PANI and PANI/V<sub>2</sub>O<sub>5</sub> composite (different weight %).

Sample	$\sigma_{dc}$ ( $\Omega^{-1} \text{ cm}^{-1}$ )	$\Delta E$ (eV)	$\sigma_0$ ( $\Omega^{-1} \text{ cm}^{-1}$ )	$T = 302 \text{ K}$ and $f = 850 \text{ KHz}$	
				$\epsilon'$	$\epsilon''$
PANI	$3.58 \times 10^{-9}$	0.22	$2.99 \times 10^{-6}$	7.59	173.43
PANI/V <sub>2</sub> O <sub>5</sub> 20 wt%	$6.20 \times 10^{-8}$	0.61	$2.00 \times 10^{-1}$	8.35	3158.35
PANI/V <sub>2</sub> O <sub>5</sub> 30 wt%	$2.48 \times 10^{-6}$	0.17	$1.10 \times 10^{-4}$	235.68	3193.48
PANI/V <sub>2</sub> O <sub>5</sub> 40 wt%	$6.16 \times 10^{-8}$	0.46	$8.6 \times 10^{-4}$	242.34	85682.81

3.2. Dielectric Parameters as a Function of Frequency and Temperature. Dielectric parameters as a function of frequency and temperature are calculated using the values of the equivalent parallel capacitance,  $C_p$ , dissipation factor,  $D$ , and parallel equivalent resistance,  $R_p$ , recorded by the LCR meter (Model Wayne Kerr) at selected frequencies range. Temperature dependence of the dielectric constant ( $\epsilon'$ ) and dielectric loss ( $\epsilon''$ ) is studied for PANI and PANI/V<sub>2</sub>O<sub>5</sub> composites in the different range of temperature (300–320 K) and frequency range from 50 kHz to 1 MHz. Dielectric parameters have been calculated using the following equations:

$$\epsilon' = \frac{C_p}{C_0}, \quad (2)$$

$$\epsilon'' = \frac{\epsilon'}{\omega C_p R_p} = \epsilon' D,$$

where  $C_0 = (0.08854A/t)$  pf is the geometrical capacitance of vacuum of the same dimensions as that of the sample,  $A$  and  $t$  are the area and thickness of the sample, respectively,  $C_p$  is the

capacitance measured in pf,  $\omega = 2\pi f$ , and  $D = \tan \delta$ , with  $\delta$  being the phase angle. The  $\epsilon'$  and  $\epsilon''$  are, respectively, the real and imaginary parts of the complex dielectric constant  $\epsilon(f)$ , which are represented by the relation

$$\epsilon(f) = \epsilon'(f) - i\epsilon''(f). \quad (3)$$

The dielectric constant of a material consists of ionic, electronic, and dipolar polarizations. Temperature dependence of the dielectric constant ( $\epsilon'$ ) and dielectric loss ( $\epsilon''$ ) is shown in Figures 2 and 3. It is clear that dielectric constant ( $\epsilon'$ ) and dielectric loss ( $\epsilon''$ ) remain constant with temperature for pure PANI and 20 weight % of PANI/V<sub>2</sub>O<sub>5</sub>, whereas a slightly increase is observed in ( $\epsilon'$ ) for 30% and 40% doped samples, and ( $\epsilon''$ ) slightly increases for 40 weight %. Figures 4 and 5 show variation of dielectric constant and dielectric loss as a function of frequency for pure polyaniline and V<sub>2</sub>O<sub>5</sub> composite (different wt%). The results show constant behavior with frequency; their value increases with doping of V<sub>2</sub>O<sub>5</sub> (different wt%). At 850 KHz, the dielectric constant for the composite samples with 40 weight % of oxide is about

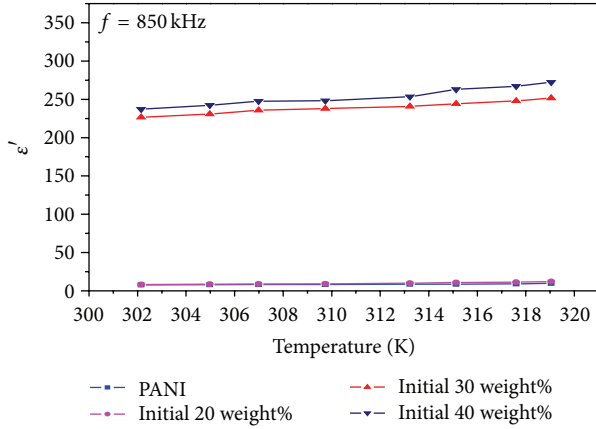


FIGURE 2: Dielectric constant ( $\epsilon'$ ) versus temperature at fixed frequency for pure polyaniline and PANI/ $V_2O_5$  composites (different weight %).

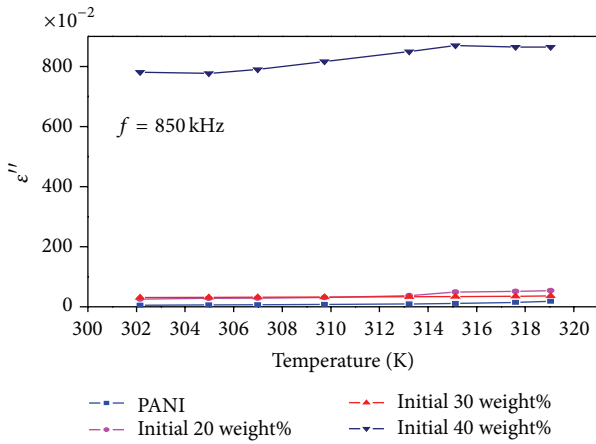


FIGURE 3: Dielectric loss ( $\epsilon''$ ) versus temperature at fixed frequency for pure polyaniline and PANI/ $V_2O_5$  composites (different weight %).

242.34. This value decreases to about 8.35 for the composite samples having 20 weight % of oxide. On the other hand, the value of the dielectric constant for pure PANI at this frequency is about 7.59. The corresponding dielectric loss for the composite samples with 40 weight % of oxide is about 85682.81 at 850 KHz frequency. The value decreases to about 3158.35 for the composite with 20 weight % of oxide. Similarly, the value of dielectric loss for pure PANI is about 173.43 at same frequency. Similar trend in the dielectric behaviour of PPY/ $Fe_3O_4$  composites has been reported [33, 34]. Higher dielectric constant and dielectric loss observed with high doping of oxide.

The dielectric loss consists of two contributions, one from the dielectric polarization processes and the other from DC conduction. To study the origin of the dielectric loss in the operating temperature range, the DC conduction loss was calculated using the relation

$$\epsilon''_{DC} = \frac{\sigma_{DC}}{\epsilon_0 \omega} \quad (4)$$

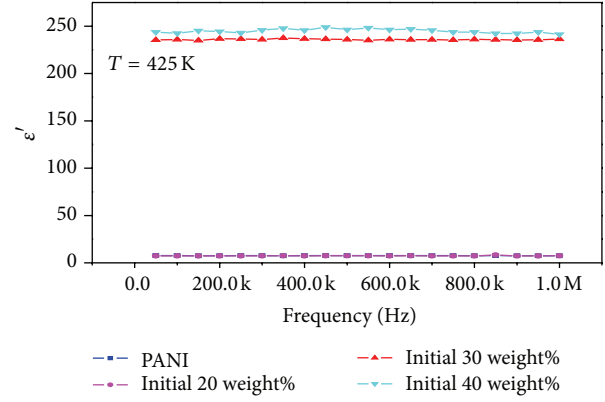


FIGURE 4: Dielectric constant ( $\epsilon'$ ) versus frequency at fixed temperature (302 K) for pure polyaniline and PANI/ $V_2O_5$  composites (different weight %).

The DC conduction loss is small compared to the observed dielectric loss ( $\epsilon''$ ). It can also be noted that the DC conduction loss increases with increasing dopant's concentration due to the increase of polarons and bipolarons. Various other workers have also observed such type of behavior [35, 36]. Polaron formation depends upon the viscosity of the medium. The theories based on charged defect centers serve as basis for understanding the dielectric response and conduction mechanisms of such materials. In the correlated barrier hopping model of Elliott (CBH) [37, 38], two electrons are assumed to transfer between charged defect sites ( $D^+$  and  $D^-$ ) by hopping over a potential barrier separating them. The maximum value of the potential barrier separating the charged defect sites ( $W_m$ ) can be approximately equated to the band gap of the material. Based on the same model of Elliott [38], the slope obtained from Figure 6 can be written as

$$(m) = \frac{-4kT}{W_m}, \quad (5)$$

where  $m$  is defined here as  $s - 1$  and  $m$  is in line with  $T$ . As an outcome of CBH model, the value of  $s$  decreases from unity with increasing temperature, and  $s$  is a band gap-dependent property [39, 40]. The values of  $m$  are calculated from the slopes of these straight lines in Figure 6. The values of  $m$  are negative, and the magnitude of  $m$  decreases linearly with increasing weight % of  $V_2O_5$ . Thus, these results indicate that the observed dielectric dispersion is recognized mainly to dipolar type dispersion in the present study. The DC conduction loss and numerical value of power ( $m$ ) are given in Table 2.

**3.3. Powder X-Ray Diffraction Analysis.** XRD patterns of all the four samples, pure PANI, PANI/ $V_2O_5$  composites (with different weight %), show similar structure of amorphous nature in Figure 7. In undoped powder, an intense hump near  $19^\circ$ – $24^\circ$  is found, which is shifted towards lower angle side at  $14$ – $18^\circ$  in doped samples. There are other three small peaks appearing in 20 weight %  $V_2O_5$  doped samples near  $15^\circ$  (200),  $20^\circ$  (001), and at  $26^\circ$  (110), which conform the concentration

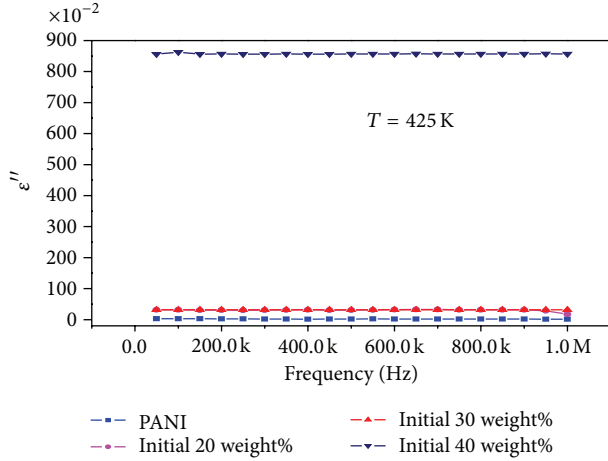


FIGURE 5: Dielectric loss ( $\epsilon''$ ) versus frequency at fixed temperature (302 K) for pure PANI and PANI/ $V_2O_5$  composites (different weight %).

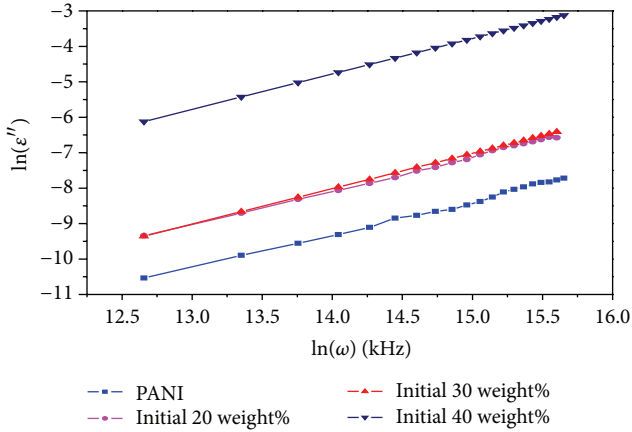


FIGURE 6:  $\ln(\epsilon'')$  versus  $\ln(\omega)$  at fixed temperature for pure PANI and PANI/ $V_2O_5$  (different wt%).

TABLE 2: Temperature dependence of slope ( $m$ ) and DC conduction loss of pure PANI and PANI/ $V_2O_5$  composites (different weight %).

Sample	$\epsilon''_{dc}$	( $m$ )	Indirect band gap $E_g$ (eV)
PANI	$2.9 \times 10^{-3}$	-0.2	3.22
PANI/ $V_2O_5$ 20 wt%	$1.5 \times 10^{-3}$	-0.03	3.27
PANI/ $V_2O_5$ 30 wt%	1.28	-0.009	3.31
PANI/ $V_2O_5$ 40 wt%	$4.8 \times 10^{-3}$	-0.0034	3.32

of  $V_2O_5$  in the composites. These peaks continued to be up to 40 weight % doped samples. Thus  $V_2O_5$  dopant is interacting well with PANI; this explains the continuous increase in the conductivity as well as crystallinity of composites. Sharpness of the peaks also shows increase in the crystallinity of composites [41, 42].

**3.4. Optical Properties.** The optical parameters of the pure PANI and PANI/ $V_2O_5$  composites have been calculated by

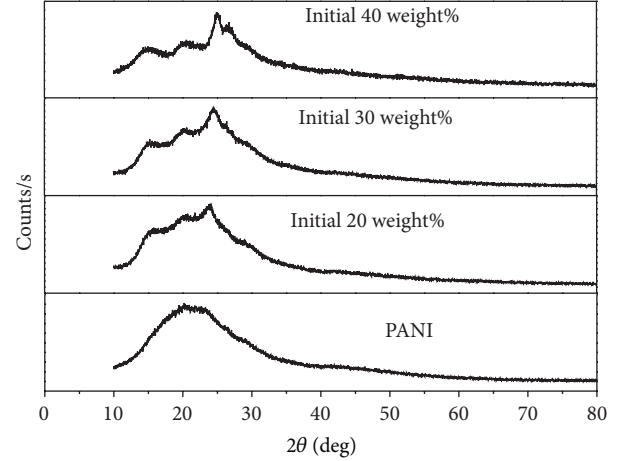


FIGURE 7: XRD of pure PANI and PANI/ $V_2O_5$  composites (different weight %).

using the UV-spectrophotometer (190–1100 nm). In amorphous materials, the optical band gap between the valence band and the conduction band [43] is given by

$$\alpha h\nu = B(h\nu - E_g)^m, \quad (6)$$

where " $E_g$ " is the optical band gap and " $B$ " is band tailing parameter related constant. At the fundamental edge of amorphous materials, two types of optical transitions can take place. In both types of optical transitions, the photon interacts with the electron in the valence band and raises it to the conduction band. There is no interaction with lattice in the direct transition, and the photon interacts with lattice in indirect transition. In the given equation " $m$ " decides the transition; for  $m = 1/2$  the transition is direct allowed,  $m = 2$  for indirect allowed transition,  $m = 3$  for indirect forbidden, and  $m = 3/2$  for direct forbidden band gap. After applying all values of  $m$ , the composites  $m = 2$  (indirect transition) is found most suitable to calculate band gap. Extinction coefficient ( $K$ ) is calculated by using the relation [44]

$$K = \frac{\alpha\lambda}{4\pi}, \quad (7)$$

where " $\alpha$ " is the absorption coefficient and " $\lambda$ " is the wavelength of photon. The extinction coefficient is a measure of fractional loss due to absorption and scattering per unit distance of the medium participating [45–47]. Figure 8 gives the  $(\alpha h\nu)^{1/2}$  dependence on energy for composites. The intercept of slope on  $x$ -axis gives the value of optical band gap. The optical band gap measured for pure PANI and PANI/ $V_2O_5$  is given in Table 2 which is found to increase with the increase of the concentration of  $V_2O_5$ . Due to the increase in the band gap with  $V_2O_5$  concentration the disorderliness reduces, and defect state density decreases. With the addition of  $V_2O_5$ , the unsaturated defects decrease in composites, and a number of saturated bonds are produced. The density of localized states decreases with the reduction in the number of unsaturated defects. According to the Davis and Mott

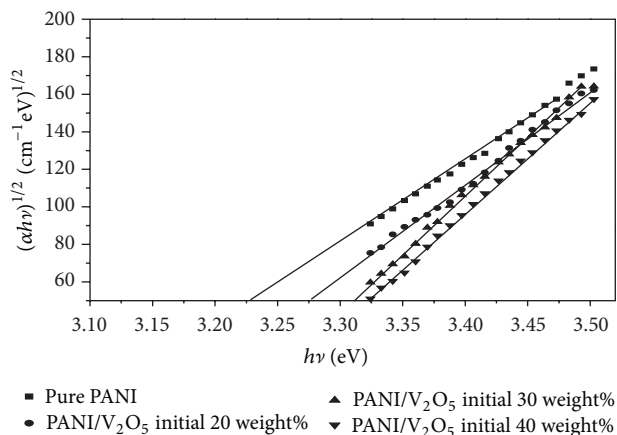


FIGURE 8:  $(\alpha h\nu)^{1/2}$  versus photon energy of pure PANI and PANI/ $V_2O_5$  composites (different weight %).

model [48] of density of states, the width of the localized states near the mobility edge depends on defects and degree of disorder present in amorphous structure. It is known that, with saturated bonds, some unsaturated bonds are produced as a result of some insufficient numbers of atoms deposited in the amorphous materials. The high concentration of these localized states is responsible for the low value of optical band gap. The addition of  $V_2O_5$  in the PANI decreases the unsaturated defects producing a number of saturated bonds. This reduction in the unsaturated bonds or defects decreases the density of localized states in band structure increasing the optical band gap.

#### 4. Conclusion

A series of PANI/ $V_2O_5$  composites have been prepared by *in situ* polymerization with different weight percentage of  $V_2O_5$ . XRD study reveals the encapsulation of oxide particles by polymer and some degree of crystallinity. The DC conductivity of polyaniline and PANI/ $V_2O_5$  composites together with the dielectric constant and dielectric loss measurements have been determined from the measured values of capacitance in the frequency range from 50 KHz to 1 MHz and in the temperature range of 300–550 K. The conductivity measured is in the range  $10^{-7}$ – $10^{-9}$  S/cm at a temperature 302 K. The conductivity increased with doping, as well as the crystallinity increased when compared to undoped sample. This increase in conductivity of composites at dielectric constant and dielectric loss results indicates that the observed dielectric dispersion is recognized mainly to dipolar type dispersion in the present study and shows independent behavior of frequency. Indirect transition ( $m = 2$ ) is found most suitable to calculate band gap. The optical band gap ( $E_g$ ) increases as the concentration of  $V_2O_5$  increases; it shows that the disorderliness reduces and defect state density decreases. Dielectric behavior is possible for application in conductive paints, rechargeable batteries, sensors, MOS devices, and so forth.

#### References

- [1] J. Aguilar-Hernández and K. Potje-Kamloth, "Evaluation of the electrical conductivity of polypyrrole polymer composites," *Journal of Physics D: Applied Physics*, vol. 34, no. 11, pp. 1700–1711, 2001.
- [2] A. Dey, A. De, and S. K. De, "Electrical transport and dielectric relaxation in  $Fe_3O_4$ -polypyrrole hybrid nanocomposites," *Journal of Physics Condensed Matter*, vol. 17, no. 37, pp. 5895–5910, 2005.
- [3] C. J. Mathai, S. Saravanan, M. R. Anantharaman, S. Venkitchalam, and S. Jayalekshmi, "Characterization of low dielectric constant polyaniline thin film synthesized by ac plasma polymerization technique," *Journal of Physics D: Applied Physics*, vol. 35, no. 3, pp. 240–245, 2002.
- [4] T. K. Vishnuvardhan, V. R. Kulkarni, C. Basavaraja, and S. C. Raghavendra, "Synthesis, characterization and a.c. conductivity of polypyrrole/ $Y_2O_3$  composites," *Bulletin of Materials Science*, vol. 29, no. 1, pp. 77–83, 2006.
- [5] W. Chen, L. Xingwei, X. Gi, W. Zhaoquang, and Z. Wenqing, "Magnetic and conducting particles: preparation of polypyrrole layer on  $Fe_3O_4$  nanospheres," *Applied Surface Science*, vol. 218, no. 1–4, pp. 216–222, 2003.
- [6] S. D. Patil, S. C. Raghavendra, M. Revansiddappa, P. Narsimha, and M. V. N. A. Prasad, "Synthesis, transport and dielectric properties of polyaniline/ $Co_3O_4$  composites," *Bulletin of Materials Science*, vol. 30, no. 2, pp. 89–92, 2007.
- [7] C. Li and G. Shi, "Synthesis and electrochemical applications of the composites of conducting polymers and chemically converted graphene," *Electrochimica Acta*, vol. 56, no. 28, pp. 10737–10747, 2011.
- [8] Y. Chen, C. Xu, and Y. Wang, "Viscoelasticity behaviors of lightly cured natural rubber/zinc dimethacrylate composites," *Polymer Composites*, vol. 33, pp. 1206–1214, 2012.
- [9] T. Matsunaga, H. Daifuku, T. Nakajima, and T. Gawa-goe, "Development of polyaniline-lithium secondary battery," *Polymers for Advanced Technologies*, vol. 1, no. 1, pp. 33–39, 1990.
- [10] G. Gustafsson, Y. Cao, G. M. Treacy, F. Klavetter, N. Colaneri, and A. J. Heeger, "Flexible light-emitting diodes made from soluble conducting polymers," *Nature*, vol. 357, no. 6378, pp. 477–479, 1992.
- [11] A. Olcani, M. Abe, M. Ezoe, T. Doi, T. Miyata, and A. Miyake, "Synthesis and properties of high-molecular-weight soluble polyaniline and its application to the 4MB-capacity barium ferrite floppy disk's antistatic coating," *Synthetic Metals*, vol. 57, p. 3969, 1993.
- [12] J. Yang, J. Hou, W. Zhu, M. Xu, and M. Wan, "Substituted polyaniline-polypropylene film composites: preparation and properties," *Synthetic Metals*, vol. 80, no. 3, pp. 283–289, 1996.
- [13] C. O. Yoon, M. Reghu, D. Moses, Y. Cao, and A. J. Heeger, "Transports in blends of conducting polymers," *Synthetic Metals*, vol. 69, no. 1-3, pp. 255–258, 1995.
- [14] R. Murugesan and E. Subramanian, "Charge dynamics in conducting polyaniline-metal oxalate composites," *Bulletin of Materials Science*, vol. 26, no. 6, pp. 529–535, 2003.
- [15] C. Brosseau, P. Queffelec, and P. Talbot, "Microwave characterization of filled polymers," *Journal of Applied Physics*, vol. 89, no. 8, article 4532, 2001.
- [16] A. G. Mac Diarmid, J. C. Chiang, M. Halpern et al., "Polyaniline": interconversion of metallic and insulating forms," *Molecular Crystals and Liquid Crystals*, vol. 121, no. 1–4, pp. 173–180, 1985.

- [17] S. P. Armes and J. F. Miller, "Optimum reaction conditions for the polymerization of aniline in aqueous solution by ammonium persulphate," *Synthetic Metals*, vol. 22, no. 4, pp. 385–393, 1988.
- [18] M. L. Gautu and P. J. G. Romero, "Synthesis and characterization of intercalate phases in the organic-inorganic polyaniline/ $V_2O_5$  system," *Journal of Solid State Chemistry*, vol. 147, no. 2, pp. 601–608, 1999.
- [19] W. Jia, E. Segal, D. Kornemandel, Y. Lamhot, M. Narkis, and A. Siegmann, "Polyaniline-DBSA/organophilic clay nanocomposites: synthesis and characterization," *Synthetic Metals*, vol. 128, no. 1, pp. 115–120, 2002.
- [20] S. J. Su and N. Kuramoto, "Processable polyaniline-titanium dioxide nanocomposites: effect of titanium dioxide on the conductivity," *Synthetic Metals*, vol. 114, no. 2, pp. 147–153, 2000.
- [21] S. Wang, Z. Tan, Y. Li, L. Sun, and T. Zhang, "Synthesis, characterization and thermal analysis of polyaniline/ $ZrO_2$  composites," *Thermochimica Acta*, vol. 441, no. 2, pp. 191–194, 2006.
- [22] M. A. M. Khan, M. Zulfequar, A. Kumar, and M. Husain, "Conduction mechanism in amorphous  $Se_{75}In_{25-x}Pb_x$  films," *Materials Chemistry and Physics*, vol. 87, no. 1, pp. 179–183, 2004.
- [23] G. T. Kim, J. Muster, V. Krstic et al., "Field-effect transistor made of individual  $V_2O_5$  nanofibers," *Applied Physics Letters*, vol. 76, no. 14, pp. 1875–1877, 2000.
- [24] Q. H. Wu, A. Thissen, W. Jaegermann, and M. Liu, "Photoelectron spectroscopy study of oxygen vacancy on vanadium oxides surface," *Applied Surface Science*, vol. 236, no. 1–4, pp. 473–478, 2004.
- [25] C. V. Ramana, R. J. Smith, O. M. Hussain, C. C. Chusuei, and C. M. Julien, "Correlation between growth conditions, microstructure, and optical properties in pulsed-laser-deposited  $V_2O_5$  thin films," *Chemistry of Materials*, vol. 17, no. 5, pp. 1213–1219, 2005.
- [26] G. B. V. S. Lakshmi, V. Ali, A. M. Siddiqui, P. K. Kulriya, and M. Zulfequar, "Optical studies of SHI Irradiated poly(o-toluidine)-PVC blends," *The European Physical Journal—Applied Physics*, vol. 39, no. 3, pp. 251–255, 2007.
- [27] Z. H. Khani, M. M. Malik, M. Zulfequar, and M. Husain, "Electrical conduction mechanism in a- $Se_{80-x}Te_xGa_{20}$  films ( $0 < x < 20$ )," *Journal of Physics: Condensed Matter*, vol. 7, no. 47, pp. 8979–8991, 1995.
- [28] P. M. Grant and I. P. Batra, "Band structure of polyacetylene,  $(CH)_x$ ," *Solid State Communications*, vol. 29, no. 3, pp. 225–229, 1979.
- [29] J. Fink and G. Leising, "Momentum-dependent dielectric functions of oriented trans-polyacetylene," *Physical Review B*, vol. 34, no. 8, pp. 5320–5328, 1986.
- [30] P. Dutta, S. Biswas, M. Ghosh, S. K. De, and S. Chatterjee, "The dc and ac conductivity of polyaniline-polyvinyl alcohol blends," *Synthetic Metals*, vol. 122, no. 2, pp. 455–461, 2001.
- [31] S. De, A. Dey, and S. K. De, "Charge transport mechanism of vanadium pentoxide xerogel-polyaniline nanocomposite," *The European Physical Journal*, vol. 46, pp. 355–361, 2005.
- [32] A. J. Heeger, S. Kivelson, J. R. Schrieffer, and W.-P. Su, "Solitons in conducting polymers," *Reviews of Modern Physics*, vol. 60, no. 3, pp. 781–850, 1988.
- [33] A. Dey, A. De, and S. K. De, "Electrical transport and dielectric relaxation in  $Fe_3O_4$ -polypyrrole hybrid nanocomposites," *Journal of Physics Condensed Matter*, vol. 17, no. 37, pp. 5895–5910, 2005.
- [34] N. N. Mallikarjuna, S. K. Manohar, P. V. Kulkarni, A. Venkataraman, and T. M. Aminabhavi, "Novel high dielectric constant nanocomposites of polyaniline dispersed with  $\gamma$ - $Fe_2O_3$  nanoparticles," *Journal of Applied Polymer Science*, vol. 97, no. 5, pp. 1868–1874, 2005.
- [35] R. Singh, R. P. Tandon, V. S. Panwar, and S. Chandra, "Low-frequency ac conduction in lightly doped polypyrrole films," *Journal of Applied Physics*, vol. 69, no. 4, pp. 2504–2511, 1991.
- [36] N. Musahwar, M. A. Majeed Khan, M. Husain, and M. Zulfequar, "Dielectric and electrical properties of Se-S glassy alloys," *Physica B: Condensed Matter*, vol. 396, no. 1–2, pp. 81–86, 2007.
- [37] S. R. Elliott, "A theory of a.c. conduction in chalcogenide glasses," *Philosophical Magazine*, vol. 36, no. 6, pp. 1291–1304, 1977.
- [38] S. R. Elliott, "Temperature dependence of a.c. conductivity of chalcogenide glasses," *Philosophical Magazine B*, vol. 37, pp. 553–560, 1978.
- [39] J. C. Giuntini, J. V. Zanchetta, D. Jullien, R. Eholie, and P. Houenou, "Temperature dependence of dielectric losses in chalcogenide glasses," *Journal of Non-Crystalline Solids*, vol. 45, no. 1, pp. 57–62, 1981.
- [40] W. K. Lee, J. F. Liu, and A. S. Nowick, "Limiting behavior of ac conductivity in ionically conducting crystals and glasses: a new universality," *Physical Review Letters*, vol. 67, no. 12, pp. 1559–1561, 1991.
- [41] H. K. Chaudhari and D. S. Kekler, "X-ray diffraction study of doped polyaniline," *Journal of Applied Polymer Science*, vol. 62, no. 1, pp. 15–18, 1996.
- [42] B. P. Barbero and L. E. Cadus, " $V_2O_5$ - $SmVO_4$  mechanical mixture: oxidative dehydrogenation of propane," *Applied Catalysis A: General*, vol. 237, no. 1–2, pp. 263–273, 2002.
- [43] J. I. Pankove, *Optical processes in Semiconductors*, Prentice-Hall, Englewood Cliffs, NJ, USA, 1971.
- [44] A. Abdel-Aal, "Dielectric relaxation in  $Cd_xInSe_{9-x}$  chalcogenide thin films," *Egyptian Journal of Solids*, vol. 29, p. 293, 2006.
- [45] G. D. Cody, C. R. Wronski, B. Abeles, R. B. Stephens, and B. Brooks, "Optical characterization of amorphous silicon hydride films," *Solar Cells*, vol. 2, no. 3, pp. 227–243, 1980.
- [46] J. Tauc, *Amorphous and Liquid Semiconductors*, Plenum Press, New York, NY, USA, 1974.
- [47] E. Marquez, J. Ramirez-Malo, P. Villares, R. Jimenez-Garay, P. J. S. Ewen, and A. E. Owen, "Calculation of the thickness and optical constants of amorphous arsenic sulphide films from their transmission spectra," *Journal of Physics D: Applied Physics*, vol. 25, no. 3, pp. 535–541, 1992.
- [48] N. F. Mott and E. A. Davis, *Electronics Processes in Non-Crystalline Materials*, Clarendon, Oxford, UK, 1979.

## Research Article

# Effect of Gamma-Irradiated Recycled Low-Density Polyethylene on the High- and Low-Temperature Properties of Bitumen

Perviz Ahmedzade,<sup>1</sup> Alexander Fainleib,<sup>2</sup> Taylan Günay,<sup>3</sup>  
Olga Starostenko,<sup>2</sup> and Tetyana Kovalinska<sup>4</sup>

<sup>1</sup> Transportation Division, Department of Civil Engineering, Faculty of Engineering, Ege University, Izmir, Turkey

<sup>2</sup> Institute of Macromolecular Chemistry of the National Academy of Sciences of Ukraine (NASU), Kyiv, Ukraine

<sup>3</sup> Department of Civil Engineering, Ege University, Izmir, Turkey

<sup>4</sup> Institute of Nuclear Research of the NASU, Kyiv, Ukraine

Correspondence should be addressed to Perviz Ahmedzade; [perviz.ahmedzade@ege.edu.tr](mailto:perviz.ahmedzade@ege.edu.tr)

Received 29 March 2013; Accepted 3 June 2013

Academic Editor: Gonzalo Martínez-Barrera

Copyright © 2013 Perviz Ahmedzade et al. This is an open access article distributed under the Creative Commons Attribution License, which permits unrestricted use, distribution, and reproduction in any medium, provided the original work is properly cited.

This paper describes polymer modification of bitumen with gamma-irradiated recycled ( $\gamma$ -LDPE<sub>R</sub>) low-density polyethylene. The recycled low-density polyethylene (LDPE<sub>R</sub>) was obtained from greenhouse films exposed to sunlight at least one year. The surface of the LDPE<sub>R</sub> was treated by gamma beam irradiation that provided formation of free radicals and some functional groups that may contribute to the creation of strong chemical bonds between polymer modifier and bitumen. Five different samples of bitumen/ $\gamma$ -LDPE<sub>R</sub> compositions with the modifier content, wt. %: 1, 3, 5, 7 and 9, were prepared. The effects of the  $\gamma$ -LDPE<sub>R</sub> on original and aged bitumen were investigated by means of morphological, chemical, and physical testing program, including FTIR spectroscopy, conventional tests, rotational viscosity (RV), dynamic shear rheometer (DSR), and bending beam rheometer (BBR) tests. Superior performing asphalt pavements (Superpave) specifications were used to analyze mechanical test results as well as to determine the performance grades (PG) of the binders. Optimum usage of the  $\gamma$ -LDPE<sub>R</sub> as modifier in bitumen were suggested after testing program. The results reveal the stiffening effect of the  $\gamma$ -LDPE<sub>R</sub> on bitumen that provide enhanced temperature susceptibility and also promise better performance grades (PG) with  $\gamma$ -LDPE<sub>R</sub> polymer modification.

## 1. Introduction

The modification of bitumen by means of polymers is the most widespread method in flexible pavement applications. The polymers such as Styrene Butadiene Styrene (SBS), Ethylene vinyl acetate (EVA) are satisfactorily used to enhance temperature susceptibility by increasing stiffness at high temperature and decreasing stiffness at low temperature [1–4]. In addition to SBS, various polymers are utilized in bituminous materials. Polyolefins such as low-density polyethylene (LDPE), high density polyethylene (HDPE), and polypropylene (PP) have been used as modifier, for generally to enhance mechanical properties of bitumen [5–8].

On the other hand, using recycled polymers contributes to reducing amount of waste materials; it has many benefits, such as environmental protection, lower energy

consumption, and their affordable cost. Therefore, it is fundamental to find an application area for recycled polymers, in order to increase their commercial use [9–11].

The aim of this work is to study the effect of recycled LDPE (LDPE<sub>R</sub>) as modifier on bitumen by means of morphologic, chemical, and mechanical test methods. However, there is no chemical reaction between LDPE<sub>R</sub> and bitumen which results in a two-phase mixture after the preparation of modified bitumen. In order to provide strong polymer/bitumen bonding, surface of the recycled LDPE was activated by using gamma beam irradiation. The surface activation helps to create double bonds ( $>C=C<$ ) that can interact with bitumen.

The study contains a comprehensive laboratory evaluation of the  $\gamma$ -irradiated recycled LDPE ( $\gamma$ -LDPE<sub>R</sub>) modified bitumen ( $\gamma$ -LDPE<sub>R</sub>/B) in terms of morphology and physical-chemical properties. Fluorescence microscopy has been used

TABLE 1: Physical properties of the base bitumen.

Properties	Standard	160/220
Penetration (25°C; 0.1 mm)	ASTM D5	195.5
Softening point (°C)	ASTM D36	38.7
Ductility (25°C; cm)	ASTM D113	103
Penetration index (PI)	—	-0.73
Specific gravity (25°C; gr/cm <sup>3</sup> )	ASTM D70	1.03

to observe morphological changes, while rheological testing have been undertaken by means of dynamic shear rheometer (DSR) and bending beam rheometer (BBR). To understand the influence of  $\gamma$ -irradiation on structure and efficiency of the LDPE<sub>R</sub> recycled LDPE, Fourier transform infrared (FTIR) spectroscopy has been performed as well.

## 2. Experimental

**2.1. Materials.** The binders were prepared with the type of bitumen having 160/220 penetration grade. Physical properties of the bitumen are given in Table 1. The LDPE<sub>R</sub> used as modifier in bitumen was supplied from Sicily, Italy. The LDPE<sub>R</sub> was obtained from greenhouse films exposed to sunlight, as well as to other external environmental factors for one year. The waste films were washed, dried, cut into the pieces of dimensions 12 × 12 mm, and finally extruded. The chemical composition of the LDPE<sub>R</sub> used was LDPE 65–70%, LLDPE 12–17%, EVA copolymer 12–15%,  $T_m = 109^\circ\text{C}$ ,  $E = 180\text{ MPa}$ ,  $TS = 16\text{ MPa}$ ,  $EB = 500\%$ ,  $MFI_{190/2.16} = 0.29\text{ g/10 min}$ , and  $MFI_{230/2.16} = 0.95\text{ g/10 min}$ .

**2.2. Gamma Irradiation Activation Method.** In order to provide a chemical bonding between bitumen and polymer modifier, gamma irradiation method was applied to the LDPE<sub>R</sub> [12]. Gamma irradiation method is used in several applications such as food processing, cancer treatments, and some sterilization systems. Gamma irradiation is electromagnetic of high frequency and rays are ionizing radiation. It provides a reformed chemical composition of the materials exposed to decay that might contribute to creating strong bonds between polymer modifier and bitumen. The irradiation source was an electron accelerator—complex electric device, where the transition from regimes of treatment with charged particles (electrons) to regimes of treatment with stream of gamma quanta of a wide range of energies is possible. The LDPE<sub>R</sub> granules were  $\gamma$  irradiated with a dose of 20 kGy.

**2.3. Preparation of Samples.**  $\gamma$ -LDPE<sub>R</sub> granules were obtained as pellet shaped. In order to work with smaller pieces, they were milled by using grinder and the particles were sieved with No 50. The amount of additives was selected as %: 1, 3, 5, 7, and 9 by total weight of the binder which is enough to examine the effect of the polymer modified bitumen. High shear mixer was employed for preparing sample. 160/220 penetration grade bitumen was heated for 90 minutes at 163°C and then poured into the mixer flask adjusted to 500 rpm. Subsequently, the  $\gamma$ -LDPE<sub>R</sub> was added

to bitumen by portions in 15 minutes at certain intervals and then the mixing rate was increased to 1300 rpm and mixing was continued for 150 minutes. After the end of the mixing process, the samples were removed from the flask, divided into small containers, covered with aluminum foil, and stored for various testing.

The different binders were coded as follows:

- (i) base bitumen–“B;”
- (ii) base bitumen + 1%  $\gamma$ -LDPE<sub>R</sub>–“B-1- $\gamma$ -LDPE<sub>R</sub>;”
- (iii) base bitumen + 3%  $\gamma$ -LDPE<sub>R</sub>–“B-3- $\gamma$ -LDPE<sub>R</sub>;”
- (iv) base bitumen + 5%  $\gamma$ -LDPE<sub>R</sub>–“B-5- $\gamma$ -LDPE<sub>R</sub>;”
- (v) base bitumen + 7%  $\gamma$ -LDPE<sub>R</sub>–“B-7- $\gamma$ -LDPE<sub>R</sub>;”
- (vi) base bitumen + 9%  $\gamma$ -LDPE<sub>R</sub>–“B-9- $\gamma$ -LDPE<sub>R</sub>;”

### 2.4. Testing Program

**2.4.1. Fourier Transform Infrared Spectroscopy.** Fourier transform infrared (FTIR) spectroscopy was used to characterize various functional groups in asphalt and polymer modifier. FTIR spectra were recorded with a Bruker Tensor 27 DTGS spectrometer between 4000 and 450  $\text{cm}^{-1}$  using the attenuated total reflection (ATR) mode. For each spectrum, 32 consecutive scans with a resolution of 4  $\text{cm}^{-1}$  were averaged.

**2.4.2. Morphology.** In order to determine the grade of the dispersion of the modifier within the bitumen, fluorescent microscopy was used. Florescent microscopy allows researchers to study the morphology of bitumen by using a principle in which polymers become swollen after absorbing some of the constituents of the original bitumen [13].

The method of sample preparation for fluorescent microscopy followed the regular procedure that is consisted of heating, homogenizing, and cooling process. The samples were examined under a Carl Zeiss Primo Star generated from a 40 W halogen lamp and magnify up to 1000X.

**2.4.3. Conventional Bitumen Tests.** The samples of the base and modified bitumen were subjected to conventional tests that are, namely, penetration (ASTM D5), softening point (ASTM D36), and ductility (ASTM D 113). By using penetration and softening point values, penetration index was calculated for each sample of bitumen to investigate the temperature susceptibility of bitumen. A classical approach related to PI calculation has been given in the Shell Bitumen Handbook [14] as shown in the following equation:

$$PI = \frac{1952 - 500 \times \log(\text{Pen}_{25}) - 20 \times SP}{50 \times \log(\text{Pen}_{25}) - SP - 120}, \quad (1)$$

where  $\text{Pen}_{25}$  is the penetration at 25°C and SP is the softening point temperature of the unmodified and modified bitumen.

**2.4.4. Rotational Viscosity Test.** The rotational viscometer determines the bitumen viscosity by measuring the torque necessary to maintain a constant rotational speed of a cylindrical spindle submerged in a bitumen specimen held

at a constant temperature, described in AASHTO TP48. Unlike the capillary viscometers used with the viscosity-graded method, the rotational viscometer can evaluate modified bitumen binders. Viscosity of bitumen binders can be measured within the range from 0.01 Pa·s (0.1 poise) to 200 Pa·s (2000 poise) [15]. Though this test, which is one of the Superpave Performance Grade (PG) asphalt binder specification, can be conducted at various temperatures for different purposes, the test performed for Superpave PG asphalt binder specification is always conducted at 275°F (135°C). In order to observe the changes in viscosity at various temperatures, a second viscosity reading is taken generally at 165°C. A Brookfield viscometer (DVRV-II Pro Extra) was used in this study for the viscosity tests of the base and the modified bitumens. Viscosity values were measured at 135°C and 165°C, respectively.

**2.4.5. Dynamic Shear Rheometer Test.** The most commonly used methods for the fundamental rheological characterization of bitumen are dynamic mechanical methods using oscillatory type testing, generally conducted within the region of linear viscoelastic response by using a dynamic shear rheometer (DSR). In order to characterize the viscoelastic behavior of bitumen binders at intermediate and high service temperatures, DSR is used in Superpave specification providing an indication of the rutting resistance of bitumen immediately following the construction. It is also possible to evaluate the resistance to rutting at high service temperatures in the early stages of pavement life and fatigue cracking at intermediate service temperatures in the later stages of service life by DSR [16].

The principal viscoelastic parameters obtained from DSR are the complex shear modulus ( $G^*$ ) and the phase angle ( $\delta$ ).  $G^*$  is defined as the ratio of maximum (shear) stress to maximum strain, a measure of the total resistance to deformation when the bitumen is subjected to shear loading. The phase difference between stress and strain in an oscillatory test is named as  $\delta$ , a measure of the viscoelastic balance of the material behavior [17].

In this study, the principal viscoelastic parameters such as  $G^*$ ,  $\delta$ , rutting parameter ( $G^*/\sin\delta$ ), and high-temperature performance grades of the base and modified bitumens were determined by DSR test.

**2.4.6. Bending Beam Rheometer Test.** The bitumen binder plays a critical role in the thermal cracking potential of hot mix asphalt (HMA) pavement. HMA pavements with a high stiffness modulus at low temperatures are susceptible to thermal cracking. Bitumen binders become harder, or stiffer, as the ambient temperature decreases. Given that the stiffness of an HMA pavement is directly proportional to the stiffness of bitumen binder, high stiffness at low temperatures increases the potential of thermal cracking. The bending beam rheometer (BBR) was developed to determine the stiffness of bitumen binders at low service temperatures and to evaluate the potential of the binder for thermal cracking [16].

Creep tests were conducted at -6, -12, and -18°C which are equivalent to -16, -22, and -28°C, respectively, in low

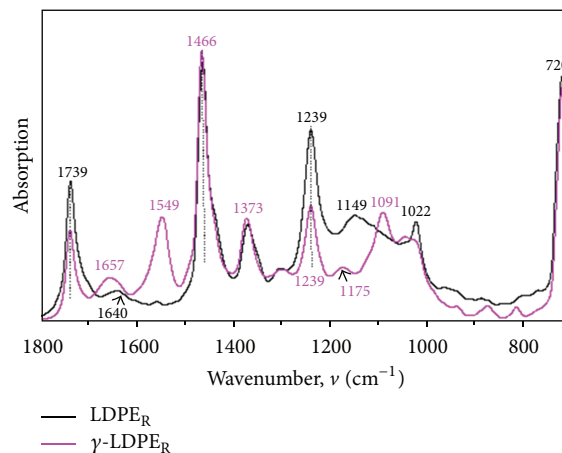


FIGURE 1: The normalized FTIR spectra of the LDPE<sub>R</sub> and  $\gamma$ -LDPE<sub>R</sub>.

temperature performance grade, using a BBR according to ASTM D6648-01. The bitumen beam (125 mm long, 12.5 mm wide, and 6.25 mm thick) was submerged in a constant-temperature bath and kept at the test temperature for 60 min. After preloading procedure, a constant load of 100 g (980 mN) was then applied to the rectangular beam supported at both ends by stainless steel half-rounds (102 mm apart), and the deflection of center point was measured continuously. Creep stiffness ( $S$ ) and creep rate ( $m$ -value) of the binders were determined at several durations of loading ranging from 8 to 240 s [18]. The creep stiffness is an indicator of the specimen's ability to resist the constant creep load and the creep rate is the rate at which the creep stiffness changes with loading time [16]. For an adequate low-temperature cracking resistance, the creep stiffness must be less than 300 MPa and the  $m$ -value must be greater than 0.3 to be in compliance with Superpave specification [19].

### 3. Results and Discussions

**3.1. FTIR Spectroscopy.** In Figure 1, the normalized FTIR spectra (the band at  $\nu \approx 720 \text{ cm}^{-1}$  has been used as internal standard) of the virgin LDPE<sub>R</sub> and  $\gamma$ -LDPE<sub>R</sub> are shown. As can be seen from Figure 1, there is no significant difference in position and intensity of the main absorption bands at  $\nu \approx 720, 1022, 1373,$  and  $1466 \text{ cm}^{-1}$ , which are the characteristics for vibrations of C-C and C-H bonds of hydrocarbon chain of virgin LDPE and  $\gamma$ -LDPE<sub>R</sub>. However, the new peaks are additionally observed at  $\nu \approx 1091, 1175, 1549,$  and  $1657 \text{ cm}^{-1}$  in the spectrum of  $\gamma$ -LDPE<sub>R</sub> accompanied by decreasing intensity of the peaks at  $1239 \text{ cm}^{-1}$  and  $1739 \text{ cm}^{-1}$ . These new peaks evidence formation of unsaturated bonds in macromolecular chains of gamma-irradiated LDPE (the peak with maximum at  $\nu \approx 1657 \text{ cm}^{-1}$  corresponds to the non-conjugated C=C bond) that is occurred as a result of high-energy action of the gamma-rays on LDPE. At irradiation treatment free radicals appear at breakage of polymer chains, which can then transform to different groups and bonds including formation of double bonds ( $>C=C<$ ). Certainly,

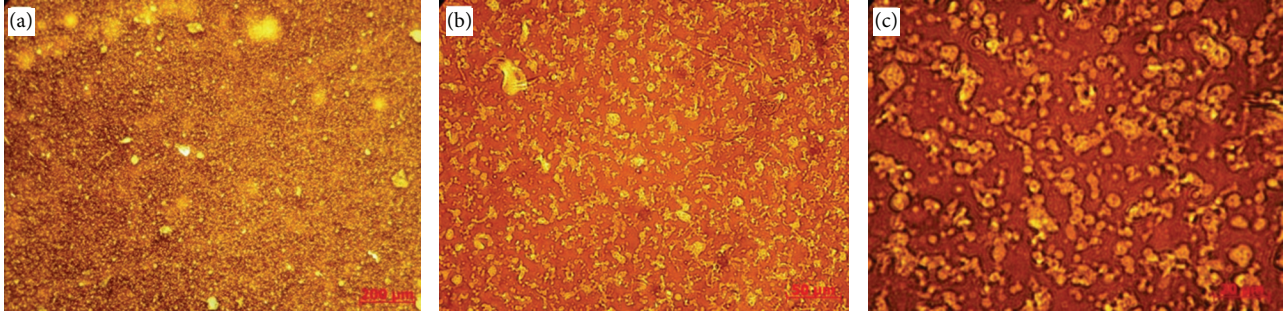


FIGURE 2: (a) 50X magnification, (b) 200X magnification, and (c) 500X magnification.

TABLE 2: Characteristic properties of base and  $\gamma$ -LDPE<sub>R</sub> modified bitumens before and after short-term ageing.

Properties	Binder types					
	Base	1- $\gamma$ -LDPE <sub>R</sub>	3- $\gamma$ -LDPE <sub>R</sub>	5- $\gamma$ -LDPE <sub>R</sub>	7- $\gamma$ -LDPE <sub>R</sub>	9- $\gamma$ -LDPE <sub>R</sub>
Penetration (25°C; 0.1 mm)	195.5	168.8	135	102	83.1	57.2
Softening point (°C)	38.7	42.5	48.4	64.2	60.3	70.5
Ductility (cm) at 25°C	103	92	84	77	69	63
Penetration index (PI)	-0.73	0.23	1.31	1.85	2.54	3.28
	After ageing					
Change of mass (%)	0.76	0.68	0.65	0.40	0.37	0.35
Penetration (25°C; 0.1 mm)	102	85.6	125	93.8	76.5	52.5
Retained penetration (%)	52	50.7	92.5	91.9	92	92
Softening point (°C)	42.7	45.3	49.5	65.1	61.1	66.5
Change in softening point (°C)	4	2.8	1.1	0.9	0.8	-4

the unsaturated bonds formed in  $\gamma$ -LDPE<sub>R</sub> are reactive towards the unsaturated bonds of bitumen components that provides effective reactive compatibilization of the blends of modifier with bitumen through the chemical reactions of the surface functional groups of the activated polyethylene and the double bonds of the bitumen components. In air, the free radicals formed can react with oxygen forming some oxygen-containing functional groups in polymer structure (e.g., C(O)O- group of organic acids or esters with a maximum around  $\nu \approx 1549 \text{ cm}^{-1}$  and -C-O-C- bond in ethers with an absorption bands around  $\nu \approx 1091, 1175$ ). These groups can also contribute to physical-chemical compatibilization of  $\gamma$ -LDPE<sub>R</sub> with bitumen.

**3.2. Morphology.** The morphology of  $\gamma$ -LDPE<sub>R</sub> modified bitumen was observed with a fluorescent microscope. The images given in Figure 2 belong to B-9- $\gamma$ -LDPE<sub>R</sub>, the highest polymer content among the all binders. The surface images were taken with using different magnification (i.e. 50X, 200X and 500X). Figure 2(a) shows the texture of the modified bitumen in general, whereas Figure 2(c) shows a detailed image on texture and allows observing the phase structure of the modified bitumen. Two major phases that can be clearly seen (Figures 2(a), 2(b), and 2(c)) are a continuous bitumen-rich phase (brown) and a dispersed polymer phase (yellow). Excluding a few greater particles, the main amount of  $\gamma$ -LDPE<sub>R</sub> is mostly ranging from 3 to 10  $\mu\text{m}$  in diameter and

is quite well dispersed in bitumen. While modifier particles with a size greater than 30  $\mu\text{m}$  were not seen generally in the modified bitumen samples, it can be said that polymer particles have been swollen by absorbing an amount of the bitumen content. A third phase (mixed phase) can be observed in the image taken at the 500X magnification (Figure 2(c)) formed in interface region obviously due to chemical bonding between bitumen and gamma-irradiated polymer particles.

**3.3. Conventional Bitumen Test.** In order to understand the effect of  $\gamma$ -LDPE<sub>R</sub> additives on physical properties of the bitumen, conventional tests were conducted. The results, including both before and after short-term ageing, are given in Table 2. As can be seen, penetration decreases continuously with increasing amount of  $\gamma$ -LDPE<sub>R</sub> polymer content.

Hence, B-9- $\gamma$ -LDPE<sub>R</sub> binder has the lowest penetration value with 57.2. Softening point test results support penetration results, as it increases with increasing  $\gamma$ -LDPE<sub>R</sub> polymer content. These physical tests results point out a significant increase in stiffness of the bitumen with increasing amount of the polymer modifier. There is no specification limits for ductility, it is generally expected to be higher than 100 cm. Consequently, decreasing ductility means, binders become more brittle with increasing amount of  $\gamma$ -LDPE<sub>R</sub> modifier.

The PI values increase progressively from -0.73 to 3.28, as modifier content increases that signifies  $\gamma$ -LDPE<sub>R</sub> polymer

TABLE 3: Viscosity values of the of base and  $\gamma$ -LDPE<sub>R</sub> modified bitumens.

Binder types	Rotational viscosity (cP)		$\eta_{\text{modified}}/\eta_{\text{pure}}$		Temperature range (°C)	
	135°C	165°C	135°C	165°C	Mixing	Compaction
B	202.5	65.5	1	1	135–142	122–128
B-1- $\gamma$ -LDPE <sub>R</sub>	250	80	1.23	1.22	142–148	129–135
B-3- $\gamma$ -LDPE <sub>R</sub>	380	122.5	1.88	1.87	152–159	139–145
B-5- $\gamma$ -LDPE <sub>R</sub>	702.5	208	3.47	3.18	165–171	154–159
B-7- $\gamma$ -LDPE <sub>R</sub>	798	330	3.94	5.04	187–195	170–177
B-9- $\gamma$ -LDPE <sub>R</sub>	1286	435	6.35	6.64	189–195	175–181

modified bitumen can be used in a wider temperature range than base bitumen.

The tests performed on aged samples reveal that  $\gamma$ -LDPE<sub>R</sub> additives have a positive effect on ageing properties of bitumen, as mass loss of the bitumen diminishes. Furthermore, the results of all the samples are within the limitation of change of mass (i.e., 1%). After short-term ageing, the retained penetration tends to increase as  $\gamma$ -LDPE<sub>R</sub> content increases which shows that increasing polymer content helps to diminish the effects of ageing on bitumen binders.

**3.4. Rotational Viscosity Results.** Rotational viscosities performed at 135 and 165°C for base and  $\gamma$ -LDPE<sub>R</sub> modified bitumens are shown in Table 3. For all the samples, mixing and compaction temperatures were determined from the viscosity versus temperature graph given in Figure 3. The results reveal a gradual increase in viscosity with modification. As in the penetration and softening point test, this increasing in viscosity gives a clear indication of the stiffening effect of  $\gamma$ -LDPE<sub>R</sub> modification. Modification indices, which can be calculated as the viscosity of modified bitumen divided by the viscosity of base bitumen, especially have greater values for B-5- $\gamma$ -LDPE<sub>R</sub>, B-7- $\gamma$ -LDPE<sub>R</sub>, and B-9- $\gamma$ -LDPE<sub>R</sub> binders. Calculated mixing and compaction temperatures for the base and modified binders tend to increase continuously. Although there are no viscosity values exceeding the Superpave specifications (i.e., 3000 cP) for both base and modified bitumen, this increase in mixing and compaction temperatures means that the workability of bitumen considerably decreases. Besides, mixing temperature of B-7- $\gamma$ -LDPE<sub>R</sub> and B-9- $\gamma$ -LDPE<sub>R</sub> binders reaches 195°C, which can be considered as unfavorable result, because it means that the energy consumption will increase to high levels in applications.

**3.5. Dynamic Shear Rheometer Test.** In this study, high-temperature performances grades of base and modified bitumens were investigated by means of DSR tests. The fundamental rheological parameters for bitumen such as  $G^*$ ,  $\delta$ , and  $G^*/\sin \delta$  were also determined for original and aged samples in this DSR testing program, and the results are given in Table 4 and Figure 4. Table 4 also contains the high-temperature performance grades (PG) calculated with minimum rutting parameter ( $G^*/\sin \delta$ ) criteria of 1 kPa for original samples and 2.2 kPa for aged samples recommended in Superpave binder specifications. As can be seen, the

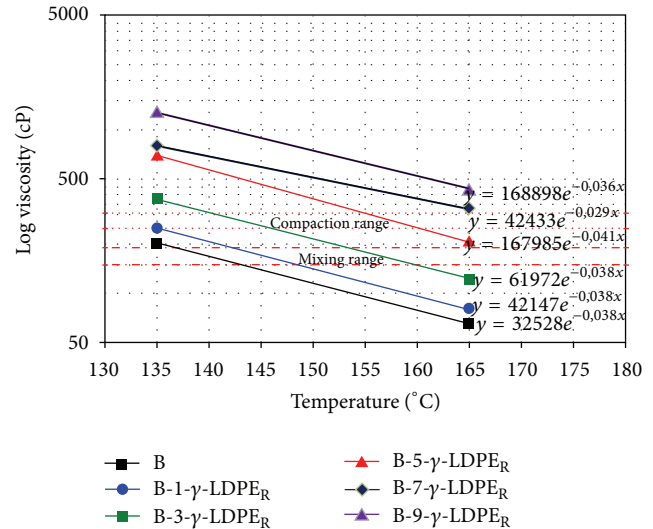


FIGURE 3: The mixing-compaction temperatures for the base and  $\gamma$ -LDPE<sub>R</sub> modified bitumens.

values of  $G^*$ , the measure of the total resistance of bitumen against the deformation subjected to the shear stress, increase significantly for both original and aged samples with increasing  $\gamma$ -LDPE<sub>R</sub> modifier content. This result determines that binders become hardened after  $\gamma$ -LDPE<sub>R</sub> modification. Therefore, it can be said that the  $\gamma$ -LDPE<sub>R</sub> modified binders are more durable than original binders against shear stress deformations.

The phase angle ( $\delta$ ) is generally considered to be more sensitive to the chemical structure than the complex modulus,  $\delta$  generally tends to decrease as the amount of modifier increases, and, therefore, predominantly viscous behavior with increasing temperatures,  $\gamma$ -LDPE<sub>R</sub> modifier improves the elastic response of the modified binders.

The effect of  $\gamma$ -LDPE<sub>R</sub> modification on the rheological parameters ( $G^*$  and  $\delta$ ) leads to an increased rutting parameter ( $G^*/\sin \delta$ ) of binders that promises an improvement of the rutting deformation. As values of  $G^*/\sin \delta$  within the limitations, DSR test is maintained to the next test temperatures.

The increased  $G^*/\sin \delta$  parameters also affect the PG of the binders. There is a significant increase in PG with increase of  $\gamma$ -LDPE<sub>R</sub> modifier, especially content of 5, 7, and 9%. For instance, high-temperature performance grades step up to

TABLE 4: DSR test results of the original and aged of base and  $\gamma$ -LDPE<sub>R</sub> modified bitumens.

Binders	Temperature (°C)	G* (KPa)	$\delta$ (°)	G*/sin $\delta$ (KPa)	Specification limits (Pa)	Performance grading	
B	Original	52	4.64	86.6	4.65	≥1000	PG 52-Y
		58	1.85	87.4	1.85		
		64	0.766	88.2	0.767		
	Aged	52	3.06	87.1	3.07	≥2200	
		58	1.39	87.2	1.39		
		64	1.88	84.9	1.89		
B-1- $\gamma$ -LDPE <sub>R</sub>	Original	52	2.75	80.7	2.78	≥1000	PG 58-Y
		58	1.31	77.3	1.35		
		64	0.702	72.7	0.735		
	Aged	52	9.47	82.3	9.56	≥2200	
		58	4.07	84	4.10		
		64	1.88	84.9	1.89		
B-3- $\gamma$ -LDPE <sub>R</sub>	Original	52	3.60	85.8	3.61	≥1000	PG 58-Y
		58	1.66	85.5	1.66		
		64	0.843	84.3	0.84		
	Aged	52	10.6	78.7	10.6	≥2200	
		58	4.66	77.9	4.76		
		64	2.42	74.7	2.42		
B-5- $\gamma$ -LDPE <sub>R</sub>	Original	52	5.36	81.6	5.42	≥1000	PG 64-Y
		58	2.47	79.9	2.51		
		64	1.27	77.1	1.30		
	Aged	70	0.72	73.4	0.75	≥2200	
		52	16.8	80	17.1		
		58	7.07	82.4	7.13		
B-7- $\gamma$ -LDPE <sub>R</sub>	Original	64	3.14	83.7	3.16	≥2200	PG 64-Y
		64	3.14	83.7	3.16		
		70	1.52	84.3	1.53		
	Aged	52	7.69	84.5	7.72	≥1000	
		58	3.34	85.4	3.35		
		64	1.62	85.4	1.63		
B-9- $\gamma$ -LDPE <sub>R</sub>	Original	70	0.863	84.1	0.868	≥1000	PG 76-Y
		70	0.863	84.1	0.868		
		52	20.7	77.7	21.2		
	Aged	58	9.04	80.2	9.18	≥2200	
		64	4.26	81.7	4.30		
		70	2.13	82.3	2.15		
B-9- $\gamma$ -LDPE <sub>R</sub>	Original	52	10.3	71.9	10.8	≥1000	PG 76-Y
		58	5.37	68.4	5.78		
		64	3.13	64.6	3.47		
	Aged	70	1.99	60.7	2.28	≥2200	
		76	1.33	57	1.59		
		82	0.881	53.4	1.10		
B-9- $\gamma$ -LDPE <sub>R</sub>	Original	52	51.4	69.1	55	≥1000	PG 76-Y
		58	25	70.9	26.4		
		64	13	71.7	13.7		
	Aged	70	5	70.3	5.31	≥2200	
		76	2.89	68.2	3.11		
		82	1.78	65.2	1.96		

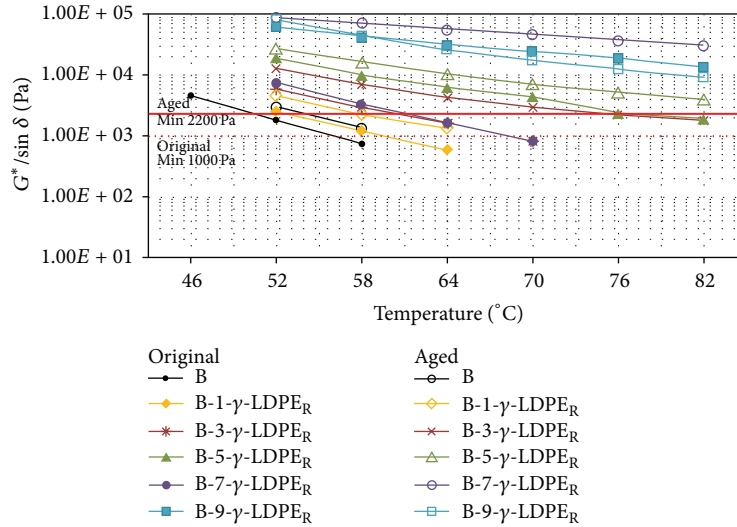


FIGURE 4: Rutting parameter of binders.

TABLE 5: Creep stiffness and  $m$ -value of the binders at a loading time of 60 s and different temperatures.

Binder types	Creep stiffness (MPa)			$m$ -value			Performance grading (PG)
	$-16^{\circ}\text{C}$	$-22^{\circ}\text{C}$	$-28^{\circ}\text{C}$	$-16^{\circ}\text{C}$	$-22^{\circ}\text{C}$	$-28^{\circ}\text{C}$	
B	42.13	99.50	199.05	0.479	0.432	0.309	PG Y-28
B-1- $\gamma$ -LDPE <sub>R</sub>	40.71	139.69	219.12	0.381	0.343	0.281	PG Y-22
B-3- $\gamma$ -LDPE <sub>R</sub>	67.61	146.12	228.33	0.325	0.318	0.274	PG Y-22
B-5- $\gamma$ -LDPE <sub>R</sub>	66.93	156.68	248.98	0.324	0.301	0.285	PG Y-22
B-7- $\gamma$ -LDPE <sub>R</sub>	78.77	176.58	—	0.311	0.267	—	PG Y-16
B-9- $\gamma$ -LDPE <sub>R</sub>	79.39	143.8	—	0.310	0.263	—	PG Y-16

64-Y and 76-Y from 52-Y, when content of the modifier is 5 and 9%, respectively.

**3.6. Bending Beam Rheometer Test.** In order to study the influence of polymer additives on the low-temperature creep responses of bitumen, the bending beam rheometer test was employed at different loading times of 8, 15, 30, 60, 120, and 240 s and temperatures of  $-16^{\circ}\text{C}$ ,  $-22^{\circ}\text{C}$ , and  $-28^{\circ}\text{C}$ . Table 5 contains of compares creep stiffness and  $m$ -values obtained at three temperatures and at a loading time of 60 s. The creep stiffness values and  $m$ -values of the base and  $\gamma$ -LDPE<sub>R</sub> modified bitumens are also graphed in Figures 5 and 6. As can be seen, creep stiffness of binders increases with increasing polymer modifier content. It can be said that this result was expected, as conventional and rotational viscosity test results indicate the effect stiffening of  $\gamma$ -LDPE<sub>R</sub> modification. Although it is known that binders with higher creep stiffness are not convenient for cold regions, as we can see from the results, the creep stiffness values of binders obtained do not exceed Superpave specifications (i.e., 300 MPa) at any test temperatures. As to  $m$ -value, there is a trend to exceed limitations with increasing polymer modifier content. Consequently, binders of B-7- $\gamma$ -LDPE<sub>R</sub> and B-9- $\gamma$ -LDPE<sub>R</sub> are failed at  $-22^{\circ}\text{C}$  to remain within specifications (i.e., 0.3) whereas the rest of the binders step up to next testing

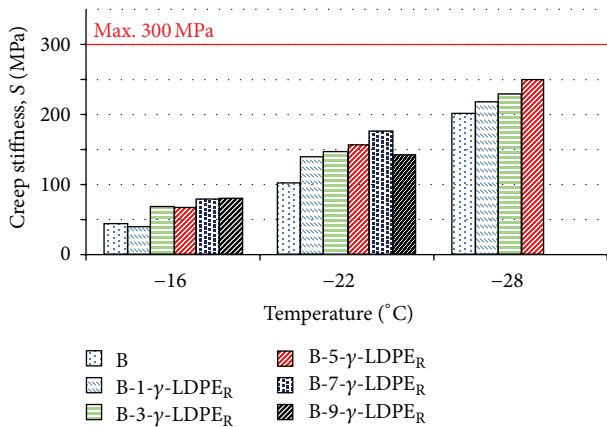
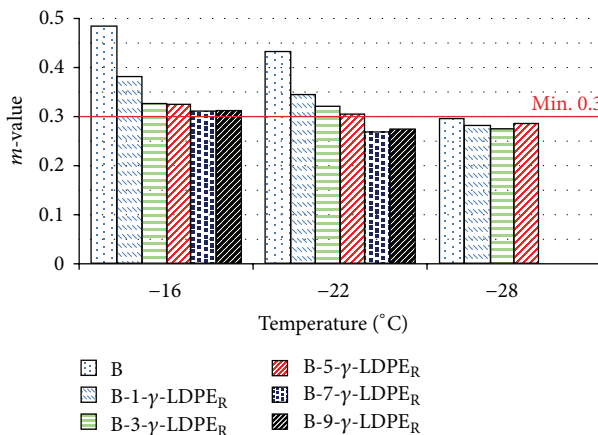
temperature. However, any of the binders were not able to provide  $m$ -value specification at  $-28^{\circ}\text{C}$  excepting base bitumen. Since creep stiffness is within the limitations,  $m$ -values determine the low-temperature performance grade of binders. Hence, there is a slightly decreasing trend in low-temperature performance grades as polymer modifier content increases. As can be seen from Table 5, it steps down to  $-22$  and  $-16$  from  $-28^{\circ}\text{C}$ , as polymer modified content is increased to 1% and 7%, respectively.

**3.7. The Effect of  $\gamma$ -LDPE<sub>R</sub> on Performance of Modified Bitumen.** As it was discussed above,  $\gamma$ -LDPE<sub>R</sub> has positive the effect on high temperature performance grades, while it decreases slightly low temperature performance grades. Thus, in order to clarify the total effects of  $\gamma$ -LDPE<sub>R</sub> on the performance and to recommend for optimum usage of  $\gamma$ -LDPE<sub>R</sub> in bitumen, Table 6 was prepared to show dependence of the modifier content on failure temperatures of binders for DSR and BBR test. Table 6 also contains the PG of the binders.

The results indicate that, the improvement at high temperatures can be seen clearly at even low polymer modification. For instance, B-1- $\gamma$ -LDPE<sub>R</sub>, which is able to be used in regions with a wider temperature range, as improvement of the binder, is  $4.53^{\circ}\text{C}$ . As content of polymer modifier increases, the improvement also continues to increase.

TABLE 6: The effect of  $\gamma$ -LDPE<sub>R</sub> on high and low service temperatures and on performance grade (PG).

Binder types	Fails at HT (°C)	Fails at LT (°C)	HT (°C) improvement	LT (°C) decrement	Improvement/decrement	Performance grading (PG)
B	54.3	-28.78	—	—	—	PG 52-28
B-1- $\gamma$ -LDPE <sub>R</sub>	61	-26.61	6.7	2.17	4.53	PG 58-22
B-3- $\gamma$ -LDPE <sub>R</sub>	63.5	-24.45	9.2	4.33	4.87	PG 58-22
B-5- $\gamma$ -LDPE <sub>R</sub>	66.9	-22	12.6	6.78	5.82	PG 64-22
B-7- $\gamma$ -LDPE <sub>R</sub>	68.6	-20.5	14.3	8.28	6.02	PG 64-16
B-9- $\gamma$ -LDPE <sub>R</sub>	80.5	-17.95	26.2	10.83	15.37	PG 76-16

FIGURE 5: Creep stiffness values of the base and  $\gamma$ -LDPE<sub>R</sub> modified bitumens.FIGURE 6:  $m$ -values of the base and  $\gamma$ -LDPE<sub>R</sub> modified bitumens.

Thereby, temperature improvement of B-3- $\gamma$ -LDPE<sub>R</sub> and B-5- $\gamma$ -LDPE<sub>R</sub> binders rises up to 4.87 and 5.82°C, respectively. B-9- $\gamma$ -LDPE<sub>R</sub> has the largest improvement with 15.37°C. However, although failure temperatures are more precise than PG classifications, it is necessary that analyzing the effect of the polymer modifier by using both the failure temperatures and PG.

The PG of the base bitumen was found as PG 52–28, whereas B-1- $\gamma$ -LDPE<sub>R</sub> was a binder of PG 58–22. It can

be understood that there is no improvement since high-temperature performance grade steps up to one level (52 to 58) while the decreasing in the low-temperature PG is the same (–28 to –22). However, in fact, as can be seen above there is an improvement in terms of failure temperatures.

B-3- $\gamma$ -LDPE<sub>R</sub> has the same PG (58–22) with B-1- $\gamma$ -LDPE<sub>R</sub>, whereas B-5- $\gamma$ -LDPE<sub>R</sub> has PG 64–22, which indicates there is an improvement in terms of both failure temperatures and PG. As for B-7- $\gamma$ -LDPE<sub>R</sub>, low-temperature performance grading steps down to two level compared with base bitumen (–16), thereby B-7- $\gamma$ -LDPE<sub>R</sub> has a poorer PG than B-5- $\gamma$ -LDPE<sub>R</sub>. The B-9- $\gamma$ -LDPE<sub>R</sub> has the biggest PG (76–16) along all the binders due to vast high-temperature improvement. It might be interpret as a benefit; however, this stiffening effect causes some problems in application while binder is being mixed and compacted. Nevertheless, it is undesirable due to high energy consumptions, as discussed in RV results.

Consequently, in spite of gradual increasing in temperature improvement as polymer content increases, as can be seen B-7- $\gamma$ -LDPE<sub>R</sub> and B-9- $\gamma$ -LDPE<sub>R</sub> have a lower temperature grade of –16 that also indicates that there must be a limitation to the usage of  $\gamma$ -LDPE<sub>R</sub>. According to the rheological test (DSR and BBR), and considering RV results it can be suggested that the usage of  $\gamma$ -LDPE<sub>R</sub> polymers as modifier in bitumen with content of 5% as B-5- $\gamma$ -LDPE<sub>R</sub> has the most stable results due to the previously mentioned reasons.

#### 4. Conclusion

$\gamma$ -LDPE<sub>R</sub> modified bitumen has been investigated by means of conventional, chemical, and mechanical tests. It was found that the rheological properties of bitumen are enhanced with  $\gamma$ -LDPE<sub>R</sub> polymer modification as identified by testing program. The surface images of the binders obtained with fluorescence microscopy revealed formation of multiphase system with bitumen continuous phase,  $\gamma$ -LDPE<sub>R</sub> dispersed phase, and mixed phase (interfacial layer), which is a sign of the presence of chemical bonding between bitumen and gamma-irradiated polymer particles.

FTIR spectroscopy confirmed the appearance of reactive (>C=C<) bonds in  $\gamma$ -LDPE<sub>R</sub> macromolecules after gamma irradiation of the LDPE<sub>R</sub>. Conventional tests, such as penetration and softening point, indicate a significant increase in stiffness of the bitumen with increasing amount of the  $\gamma$ -LDPE<sub>R</sub> modifier.

After short-term ageing by means of RTFOT, all the modified binders are within the Superpave limitations. Furthermore,  $\gamma$ -LDPE<sub>R</sub> polymer has a positive effect on bitumen ageing. In addition to the observed stiffening effect of  $\gamma$ -LDPE<sub>R</sub> on bitumen, RV test results also suggest that using  $\gamma$ -LDPE<sub>R</sub> as modifier more than 5% in bitumen can cause some mixing and compacting problems in applications.

The results obtained from the DSR tests show that  $\gamma$ -LDPE<sub>R</sub> modifier provides an increased complex shear modulus ( $G^*$ ) values and rutting parameters ( $G^*/\sin \delta$ ) and decreased phase angle ( $\delta$ ) values which means the  $\gamma$ -LDPE<sub>R</sub> modified binders are more resistant against rutting compared to the base bitumen. This improvement also affects the PG of the binders that increases gradually with increasing modifier content. However, there must be a limitation for the usage of the  $\gamma$ -LDPE<sub>R</sub> polymer due to BBR results that indicate an increasing creep stiffness and decreasing  $m$ -value as polymer content increases.

Consequently, in this paper, with taking into account the rheological tests and RV results, it was suggested that the optimum usage of  $\gamma$ -LDPE<sub>R</sub> is 5% by weight of bitumen.

## Acknowledgments

This work was carried out in the framework of the joint international Project no 110M400 of Ege University (Izmir, Turkey) and Institute of Macromolecular Chemistry of the National Academy of Sciences of Ukraine (NASU, Kyiv, Ukraine) under the agreement between TUBITAK (Turkey) and NASU (Ukraine).

## References

- [1] D. R. Gershkoff, J. Carswell, and J. C. Nicholls, *Rheological Properties of Polymer-Modified Binders for Use in Rolled Asphalt Wearing Course*, Transport Research Laboratory, Crowthorne, UK, 1997.
- [2] U. Isacson, "Laboratory investigation of polymer modified bitumens," *Journal of the Association of Asphalt Paving Technology*, vol. 68, pp. 35–63, 1999.
- [3] G. D. Airey, "Rheological evaluation of ethylene vinyl acetate polymer modified bitumens," *Construction and Building Materials*, vol. 16, no. 8, pp. 473–487, 2002.
- [4] A. Pérez-Lepe, F. J. Martínez-Boza, C. Gallegos, O. González, M. E. Muñoz, and A. Santamaría, "Influence of the processing conditions on the rheological behaviour of polymer-modified bitumen," *Fuel*, vol. 82, no. 11, pp. 1339–1348, 2003.
- [5] M. García-Morales, P. Partal, F. J. Navarro, F. Martínez-Boza, M. R. Mackley, and C. Gallegos, "The rheology of recycled EVA/LDPE modified bitumen," *Rheologica Acta*, vol. 43, no. 5, pp. 482–490, 2004.
- [6] G. Polacco, S. Berlincioni, D. Biondi, J. Stastna, and L. Zanzotto, "Asphalt modification with different polyethylene-based polymers," *European Polymer Journal*, vol. 41, no. 12, pp. 2831–2844, 2005.
- [7] N. Z. Habib, I. Kamaruddin, M. Napiyah, and I. M. Tan, "Rheological properties of polyethylene and polypropylene modified bitumen," *International Journal Civil and Environmental Engineering*, vol. 3, pp. 96–100, 2011.
- [8] C. F. Ouyang, Q. Gao, Y. T. Shi, and X. Q. Shan, "Compatibilizer in waste tire powder and low-density polyethylene blends and the blends modified asphalt," *Journal of Applied Polymer Science*, vol. 123, no. 1, pp. 485–492, 2012.
- [9] M. García-Morales, P. Partal, F. J. Navarro, and C. Gallegos, "Effect of waste polymer addition on the rheology of modified bitumen," *Fuel*, vol. 85, no. 7–8, pp. 936–943, 2006.
- [10] Z. Z. Ismail and E. A. AL-Hashmi, "Use of waste plastic in concrete mixture as aggregate replacement," *Waste Management*, vol. 28, no. 11, pp. 2041–2047, 2008.
- [11] F. J. Navarro, P. Partal, M. García-Morales et al., "Bitumen modification with reactive and non-reactive (virgin and recycled) polymers: a comparative analysis," *Journal of Industrial and Engineering Chemistry*, vol. 15, no. 4, pp. 458–464, 2009.
- [12] Y. H. Gad, M. M. Magida, and H. H. El-Nahas, "Effect of ionizing irradiation on the thermal blend of waste low density polyethylene/ethylene vinyl acetate/bitumen for some industrial applications," *Journal of Industrial and Engineering Chemistry*, vol. 16, no. 6, pp. 1019–1024, 2010.
- [13] V. Wegan, *Sampling for Microscopy-Test Procedure*, Danish Road Institute, 1996.
- [14] J. Read and D. Whiteoak, *The Shell Bitumen Handbook*, Shell Bitumen, Thomas Telford, London, UK, 5th edition, 2003.
- [15] H. U. Bahia and D. A. Anderson, "Strategic highway research program binder rheological parameters: background and comparison with conventional properties," *Transportation Research Record*, no. 1488, pp. 32–39, 1995.
- [16] J. P. Zaniewski and M. E. Pumphrey, *Evaluation of Performance Graded Asphalt Binder Equipment and Testing Protocol*, West Virginia University, 2004.
- [17] G. D. Airey, "Rheological properties of styrene butadiene styrene polymer modified road bitumens," *Fuel*, vol. 82, no. 14, pp. 1709–1719, 2003.
- [18] S. Liu, W. Cao, J. Fang, and S. Shang, "Variance analysis and performance evaluation of different crumb rubber modified (CRM) asphalt," *Construction and Building Materials*, vol. 23, no. 7, pp. 2701–2708, 2009.
- [19] H. I. A. Wahhab, I. A. Al-Dubabe, I. M. Asi, and M. F. Ali, "Performance-based characterization of Arab asphalt," *Building and Environment*, vol. 33, no. 6, pp. 375–383, 1998.

## Research Article

# Silica Aerogel Improves the Biocompatibility in a Poly- $\epsilon$ -Caprolactone Composite Used as a Tissue Engineering Scaffold

Jianhua Ge,<sup>1,2</sup> Musen Li,<sup>1</sup> Qingguo Zhang,<sup>2</sup> Christopher Z. Yang,<sup>2</sup>  
Paul H. Wooley,<sup>2,3</sup> Xiaofeng Chen,<sup>4</sup> and Shang-You Yang<sup>2,3</sup>

<sup>1</sup> College of Material Science & Engineering, Shandong University, Jinan 250061, China

<sup>2</sup> Department of Biological Sciences, Wichita State University, 1845 N Fairmount Street, Wichita, KS 67260, USA

<sup>3</sup> Orthopaedic Research Institute, Via Christi Health, Wichita, KS 67214, USA

<sup>4</sup> School of Material Science & Engineering, South China University of Technology, Guangzhou 510641, China

Correspondence should be addressed to Shang-You Yang; [shang-you.yang@via-christi.org](mailto:shang-you.yang@via-christi.org)

Received 28 March 2013; Revised 17 June 2013; Accepted 18 June 2013

Academic Editor: Gonzalo Martínez-Barrera

Copyright © 2013 Jianhua Ge et al. This is an open access article distributed under the Creative Commons Attribution License, which permits unrestricted use, distribution, and reproduction in any medium, provided the original work is properly cited.

Poly- $\epsilon$ -caprolactone (PCL) is a biodegradable polyester that has received great attentions in clinical and biomedical applications as sutures, drug delivery tool, and implantable scaffold material. Silica aerogel is a material composed of SiO<sub>2</sub> that has excellent physical properties for use in drug release formulations and biomaterials for tissue engineering. The current study addresses a composite of silica aerogel with PCL as a potential bone scaffold material for bone tissue engineering. The biocompatibility evaluation of this composite indicates that the presence of silica aerogel effectively prevented any cytotoxic effects of the PCL membrane during extended tissue culture periods and improved the survival, attachment, and growth of 3T3 cells and primary mouse osteoblastic cells. The beneficial effect of silica aerogel may be due to neutralization of the acidic condition that develops during PCL degradation. Specifically, it appears that silica aerogel to PCL wt/wt ratio at 0.5 : 1 maintains a constant pH environment for up to 4 weeks and provides a better environment for cell growth.

## 1. Introduction

Poly- $\epsilon$ -caprolactone (PCL) is one of the polyester polymers that possess several advantages including benign biocompatibility, low cost, biodegradability, and easy fabrication. Previous studies have suggested that PCL was a good candidate biomaterial for cartilage tissue engineering in terms of cell attachment, proliferation, and matrix production [1–4]. Positive effects of PCL composites on osteoblasts when using as bone graft substitute have also been demonstrated [3, 5–7]. In addition, PCL has been investigated for reconstruction of many other tissues such as skin, nerve, and retina [8]. The major drawback to the use of PCL as tissue scaffold is the production of an acidic environment during the PCL degradation process, which may influence the local microenvironment and cell viability.

Aerogels are materials with extremely high porosity and a high surface area [9]. They are usually produced by supercritical extraction of a stable gel using sol-gel technology [10, 11]. Aerogels have useful properties such as high heat insulation [12, 13], low refractive index [14, 15], and dielectric constant close to gas properties [16, 17]. For the past decade, aerogels have gained increased attention in the biomedical field as a potential tool for targeted drug delivery systems [18–20]. Silica aerogel is a material composed of SiO<sub>2</sub> with physical properties that include (1) amorphous properties with extremely low bulk density (0.003–0.35 g/cm<sup>3</sup>), (2) optical transparency that facilitates the identification of captured material(s) within the aerogel, (3) high thermal insulation, and (4) light weight. Silica aerogel exhibits a high surface area with a structure comprised of three-dimensional beaded connections of silica particles with several nanometers in diameter, forming

uniform pore sizes of tens of nanometers in diameter [21]. Silica-based bioglass has been successfully used for bone-filling material in orthopedic surgery and dental care [22–24]. Hench et al. [25] first reported the development of 45S5 Bioglass in 1971, which contained the following compositions: 45 wt.% SiO<sub>2</sub>, 24.5 wt.% Na<sub>2</sub>O, 24.5 wt.% CaO, and 6 wt.% P<sub>2</sub>O<sub>5</sub> (46.1 SiO<sub>2</sub>, 24.4 Na<sub>2</sub>O, 26.9 CaO, and 2.6 P<sub>2</sub>O<sub>5</sub> mol%). Subsequently, various systems of silica bioglasses have been described for wide applications in regenerative medicine including bone graft substitutes [26–31]. Using a rat model, Sabri et al. tested the biocompatibility properties of a polyurea cross-linked silica aerogels implant as a potential biomaterial for biomedical applications [32].

Our long-term goal is to develop a biocompatible bone graft substitute with seeding cells. The current study will test our hypothesis that the addition of the basic silica aerogel in the composite scaffold can neutralize the acidic environment and promote cell survival and growth. Specifically, silica aerogel + PCL membranes were fabricated with various contents of silica aerogel, and *in vitro* tests were performed to evaluate their degradability, cell biocompatibility, and cytotoxicity.

## 2. Materials and Methods

**2.1. Silica Aerogel/PCL Membranes Preparation.** Silica aerogel was prepared as described previously [11]. In brief, 1 mL of silica sols (pH = 10, Shanghai Hengxin Chemical Reagent Co., China) was mixed with 2 mL of ethanol. The mixture was stirred and heated at 50 °C for 5 hours followed by addition of another 2 mL of ethanol to the mixture. The mixture was then heated at 60 °C for 24 h. After adding 0.4 mL of tetraethyl orthosilicate (TEOS) and 2 mL of ethanol, the mixture was further heated at 70 °C for 48 hours. The pulverized silica aerogel was obtained at the end of the heating process.

The silica aerogel/PCL composite membranes were fabricated at silica aerogel to PCL (Mn 80000, Sigma-Aldrich Chemicals, St. Louis, MO) wt/wt ratios of 0 : 1 (sample A), 0.125 : 1 (sample B), 0.25 : 1 (sample C), or 0.5 : 1 (sample D). Briefly, 1 g of PCL was dissolved in 10 mL of tetrahydrofuran (Sigma-Aldrich) followed by mixing silica aerogel powders. The mixture was then cast into petri dishes at room temperature. After evaporation of the solvent overnight at room temperature, the silica aerogel/PCL membranes were placed under vacuum for 5 h at room temperature to remove tetrahydrofuran residue.

**2.2. Determination of pH Changes in Solutions Soaking Silica Aerogel/PCL Membranes.** The composite membrane pieces (10 mm × 5 mm × 0.04 mm) with various silica aerogel, PCL, ratios were immersed, respectively, in 5 mL of distilled water for up to 4 weeks. pH values of the immersion water from different samples were tested every 7 days using a pH meter (model AB15, Fisher Scientific).

**2.3. Cell Cultures.** The 3T3 cells (ATCC, Manassas, VA) were cultured in Dulbecco's modified eagle's medium (DMEM) supplemented with 5% fetal bovine serum (FBS) (Invitrogen, Grand Island, NY), 2 mM glutamine (Invitrogen), 100 U/mL

penicillin (Invitrogen), and 100 µg/mL streptomycin (Invitrogen) at 37 °C with 5% CO<sub>2</sub> atmosphere.

Primary osteogenic cells were induced from mouse bone marrow mononuclear cells isolated by density centrifugation over Histopaque-1083 (Sigma-Aldrich, USA), as detailed previously [33, 34]. The cells were cultured in complete media consisting of DMEM supplemented with 10% FBS, 10 mM β-glycerol phosphate (Sigma-Aldrich), 10<sup>-4</sup> M L-ascorbic acid (Sigma-Aldrich), 10 nM dexamethasone (Sigma-Aldrich), 2 mM glutamine, 100 U/mL penicillin (Invitrogen), and 100 µg/mL streptomycin. Cells were subcultured when confluence and the 3rd passages of the cells were used for the biocompatibility studies. Over 90% of the induced osteoblastic cells were able to express alkaline phosphatase (ALP) and osteocalcin (established techniques in the lab, data not shown) [34, 35].

**2.4. Biocompatibility Evaluations on Cells with the Silica Aerogel/PCL Membranes.** At 90% confluence, 3T3 cells or the primary osteoblastic cells were subcultured in each well of a 24-well plate at 10<sup>4</sup> cells/well with the testing materials (in 16 mm diameter disc) for up to 7 days. Cells cultured without testing composite material were kept as nontreated controls. At day 4 or day 7, a cell proliferation assay (MTT assay) was performed as described previously [36]. Briefly, 100 µL MTT (3-(4,5-dimethylthiazol-2-yl)-2,5-diphenyltetrazolium bromide, Aldrich-Sigma) at 5 mg/mL in PBS was added into each well for 6 hour incubation, followed by 10% sodium dodecyl sulfate (SDS) treatment at 37 °C overnight. 200 µL of supernatant from each well was transferred to a 96-well plate the next day to read at 590 nm wavelength on a SpectraMax Plus 384 microplate spectrophotometer (Molecular Devices, Sunnyvale, CA). For cell viability estimation, the lactate dehydrogenase (LDH) assay was performed, using a CytoTox 96 Non-Radioactive Cytotoxicity Assay kit (Cat no. GI780, Promega, Madison, WI). LDH activity in the culture media and the lysed cells was, respectively, assayed by colorimetric reaction with the substrate provided in the kit. The optical density (OD) values were recorded spectrophotometrically at 490 nm; the cell viability and cytotoxicity were calculated by relative medium LDH level over the cell lysis LDH as stated in the vendor's protocol.

**2.5. Cytotoxicity Potential of the Eluted Solutions from the Silica Aerogel/PCL Membranes.** Testing membranes (10 mm × 10 mm) were immersed in 333 µL culture medium in a sterile test tube at 37 °C. The culture medium was collected 24 hours later (as day 1 release medium), and the same amount (333 µL) of fresh medium was added to the tube. The same procedure was repeated everyday to obtain day 2 to day 8 release media.

3T3 cells were seeded in a 96-well plate at 10<sup>4</sup>/100 µL medium/well for 24 h in an incubator (37 °C, 5% CO<sub>2</sub> in air) before introduction of the membrane release media (100 µL/well). Fresh culture medium without release medium was used as a control. Cells were then incubated at 37 °C, 5% CO<sub>2</sub> for 72 h, followed by adding 20 µL MTT (5 mg/mL) in each well. The MTT was replaced after 6 h incubation by 200 µL of 10% SDS, and the cells were incubated overnight

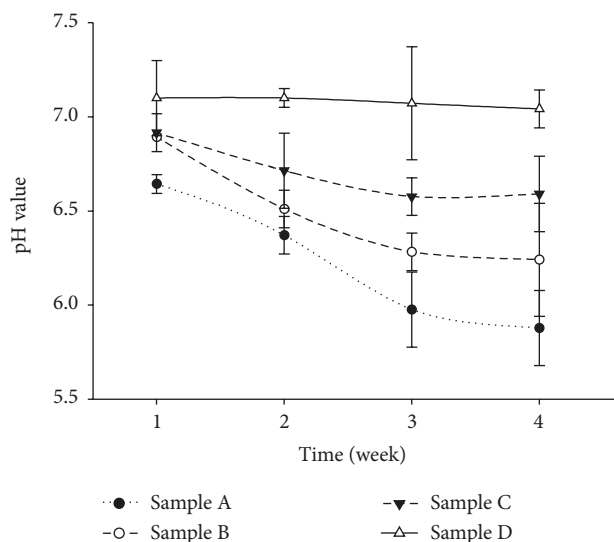


FIGURE 1: The pH values of the distilled water over the time (in weeks) with sample A (silica aerogel to PCL wt/wt ratio 0 : 1), sample B (silica aerogel to PCL 0.125 : 1), sample C (silica aerogel to PCL 0.25 : 1), and sample D (silica aerogel to PCL 0.5 : 1). \*  $P < 0.05$ .

at 37°C, 5% CO<sub>2</sub>. The next day, these 96-well plates were read at a 590 nm wavelength on a microplate photospectrometer (Molecular Devices). The OD values were recorded for cytotoxicity index determination. Cytotoxicity index of the samples was calculated by normalizing the MTT assay values with the proliferation data of the nontreated cells:

$$\text{Cytotoxicity Index} = 100 - \left( \frac{\text{sample's OD value}}{\text{mean OD value of controls}} \times 100 \right), \quad (1)$$

while the cytotoxicity index would be 0 if the sample OD value/controls mean OD value was larger than 0.7, suggesting no cytotoxic influence.

**2.6. Scanning Electron Microscope (SEM) Assessment.** Primary osteoblastic cells at 10<sup>5</sup>/mL were cultured on the testing materials in a 24-well plate at 37°C, 5% CO<sub>2</sub> for 4 days. The samples were then fixed in 1.5% glutaraldehyde (Fisher Scientific, USA) and 2% osmium tetroxide (Sigma-Aldrich, USA), followed by dehydration in series of ethanol. The samples were left air dry for 4 hours under a laminar flow hood before sputter coating with gold and observed using a S-2400 Hitachi scanning electron microscope at 15 kV.

**2.7. Statistical Analysis.** The results were expressed as arithmetic mean and standard deviation of six separate samples for each test and control group, with total of three independent experiments. Statistical analysis between groups was performed by single factor analysis of variance (ANOVA) test, with the LSD formula for *post hoc* multiple comparisons

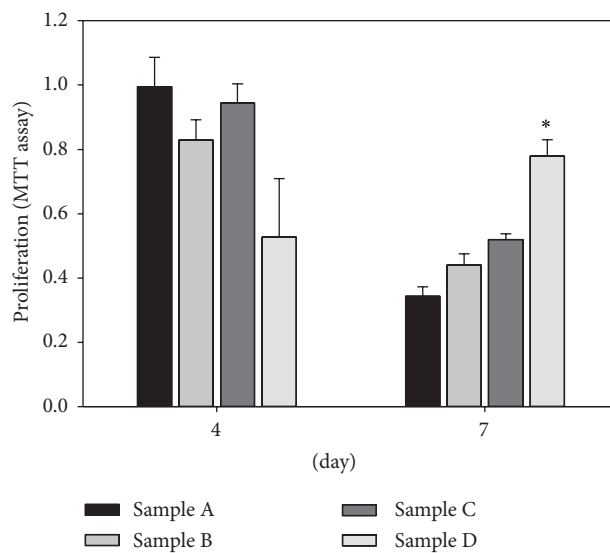


FIGURE 2: MTT assay was performed to assess the survival and proliferation of 3T3 cells when exposed to the testing materials (samples A–D). Significantly cell growth was observed in sample D (silica aerogel to PCL wt/wt ratio 0.5 : 1) at day 7 in comparison with other groups (\*  $P < 0.05$ ).

(SPSS v16, Chicago, IL). A  $P$  value of less than 0.05 was considered as significant difference.

### 3. Results

**3.1. pH Changes following Silica Aerogel/PCL Membranes Immersion in Distilled Water.** Figure 1 summarizes the pH changes during the immersion test over a period of 4 weeks. The results clearly showed that an increase in the silica aerogel ratio in the composite correlated with the elevation of pH. While the pH values of the distilled water immersed with samples A, B, and C progressively declined over the extended time period, the SiO<sub>2</sub>-PCL composite at 0.5 : 1 ratio (sample D) sustained in the water for up to 4 weeks without significant pH changes, and the data were statistically significant at 2, 3, and 4 weeks when compared to samples A and B ( $P < 0.05$ ).

**3.2. Biocompatibility of Silica Aerogel/PCL Membranes.** The MTT assay indicated a level of cell growth inhibition during the early days of culture with the high silica aerogel composite (sample D), in comparison with other testing materials (Figure 2). However, it appeared that increasing the SiO<sub>2</sub> ratios (samples B–D) positively correlated with the cell survival at the 7-day cultures ( $P < 0.05$ , Figure 2). LDH assay on the primary osteoblastic cell cultures clearly showed improved cell survival when exposed to the membranes with higher silica aerogel ratios ( $P < 0.05$ , Figure 3). The SEM observations correlated with the results of the proliferation and cell survival assays in that significantly more primary osteoblastic cells were attached on the surface of sample D compared to those on samples A and B after 4-day culture ( $P < 0.05$ , Figure 4).

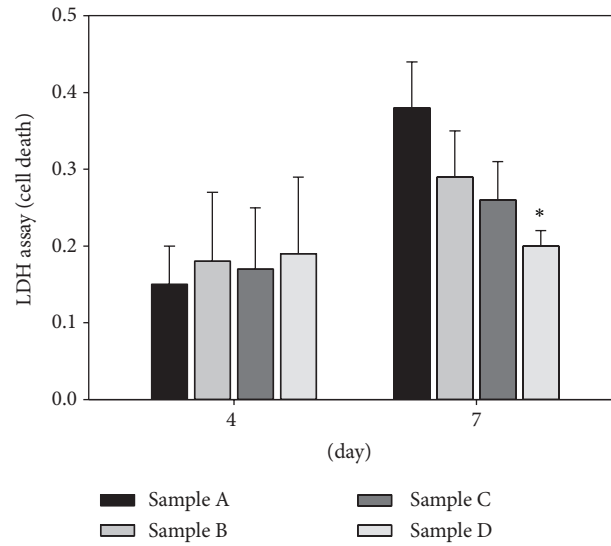


FIGURE 3: LDH assay was performed to evaluate the viability of the primary osteoblastic cells when exposed to the testing materials (samples A–D). While the cell death rate was low on all the groups at early days, elevated cell death was observed on samples A to C after 7-day culture except in the sample D group (\* $P < 0.05$ ).

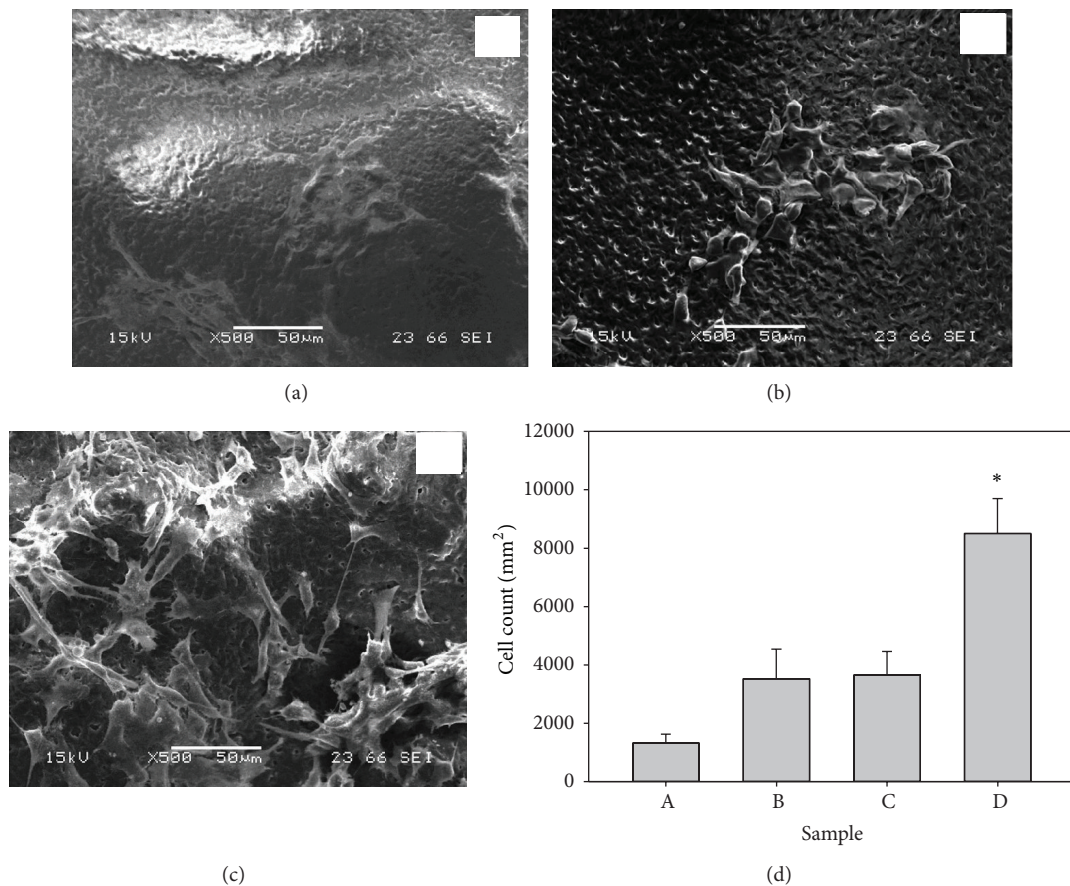


FIGURE 4: Representative SEM images of the primary osteoblastic cells cultured on the testing materials for 4 days: panel (a): sample A, panel (b): sample C, and panel (c): sample D. Panel (d) summarizes the cell numbers per mm<sup>2</sup> membrane on each group, using a computerized image analysis system (\* $P < 0.05$ ).

3.3. *Cytotoxicity Effects of the Elution Products from the Silica Aerogel/PCL Membranes.* MMT-based cytotoxicity assays were performed to assess the influence of the release media from the composite materials on the viability and growth of 3T3 cells. While there were no cytotoxic effects of the testing materials at the first 4 days elution, media from samples A, B, and C started to inhibit the cell growth after the 5-day immersion (Figure 5). However, the media from sample D (high SiO<sub>2</sub> to PCL ratio membrane) immersion remained nontoxic for at least 8 days ( $P < 0.05$ , Figure 5).

#### 4. Discussion

When developing a biomaterial scaffold for tissue engineering, it is desirable that the local microenvironment be maintained at pH 7.2–7.4. Since the acidic degradation product of PCL restrains the growth of cells or tissues, we hypothesize that addition of silica aerogel to PCL to form a PCL-silica aerogel composite material may neutralize the acidic condition that results from degradation of PCL and thus optimize the tissue repair microenvironment to allow cell growth and tissue regeneration. The data in this experiment is consistent with our hypothesis, showing that an increase in the ratio of SiO<sub>2</sub> resulted in an elevation and stabilization of the environmental pH, particularly for a silica aerogel to PCL wt/wt ratio of 0.5 : 1.

*In vitro* assays were performed in this study to evaluate the biocompatibility of the silica aerogel-PCL membranes. NIH3T3 cells are standard fibroblastic cells which represent the most common cells in various connective tissues and have been broadly used for *in vitro* determination of general biocompatibility of potential biomaterials, including in bone scaffold research [31, 37]. Primary osteoblastic cells were also used as a targeted cell type for bone graft substitutes. It is noteworthy that the presence of silica aerogel decreased the proliferation of the cells on the membranes during the early culture period, but the division rate of cells on the membranes recovered quickly and improved with the increase of silica aerogel amounts in the composite membranes. PCL, as one of the most popular synthetic polymers in tissue engineering and regenerative medicine, appears to be biocompatible yet not very intrinsic osteoinductive by itself [34, 38, 39]. In the current study, significant cell cytotoxicity was found in cultures on PCL alone and the lower ratios of SiO<sub>2</sub> composite starting around day 5, suggesting that a suboptimal environment such as lower pH for cell survival was developed at this stage. However, cell viability and proliferation on the sample with a high ratio of SiO<sub>2</sub> were maintained without overt cytotoxicity. It is apparent that the acidic degradation products of PCL were responsible for the inhibition of the cell growth, since the cell viability of PCL alone was approximately half of the values compared to the nonmaterial controls (Figure 2). The presence of silica aerogel neutralized the acidic condition and maintained the appropriate growth of cells. SEM revealed a significantly larger number of cells growing on the surface of sample D (Figure 4(c)). Cell quantification indicated that the cell attachment correlated with the increase of SiO<sub>2</sub> ratios in the composite membranes.

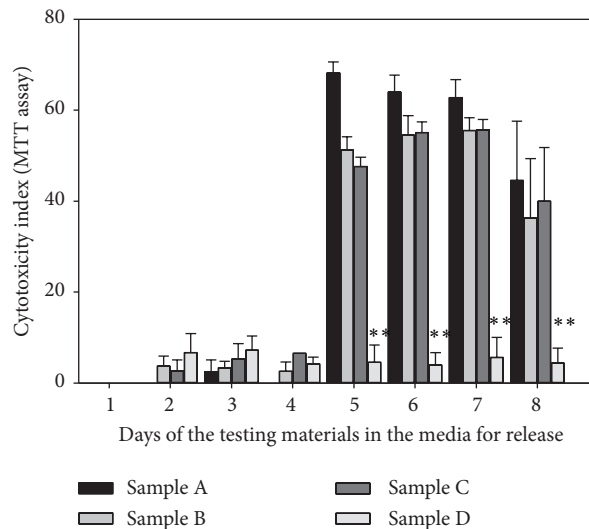


FIGURE 5: Cytotoxicity index was calculated based on MTT assay values to assess the cytotoxic influence of the release product from the testing materials (see Section 2 for calculation formula). Delayed cytotoxic effects were obvious on the testing samples except sample D (\*\* $P < 0.01$ ).

#### 5. Conclusions

The data suggest that the presence of silica aerogel in the silica aerogel/PCL composite may inhibit the cell growth to a minor extent during the initial culture period, but neutralization of the acidic condition at the extended culture period is beneficial in maintaining and stimulating the ultimate cell survival and growth. The study provides intriguing information of the silica aerogel/PCL composite, and further investigation is underway to characterize its properties in animal models for bone and cartilage tissue repair/engineering, as well as the cellular and molecular mechanisms that may be involved in the regulation of the cell survival and proliferation under the presence of the biomaterial components.

#### Conflict of Interests

None of the authors has conflict of interests to disclose on this work. Dr. Paul H. Wooley is a consultant to the legal representatives of DePuy, Inc., who received no financial benefit for this service.

#### Acknowledgments

The work was partially supported by grants from the National Science Funds of China (51072055, 50830101, and CB606204), the Science Funds of Shandong Province (BS2010YY020, ZR2009FM023), and funds from the Orthopaedic Research Institute, Via Christi Wichita Hospitals, Inc. Authors wish to thank Ms. Zheng Song and Dr. Steve Miller for their excellent technical assistance and guidance.

## References

- [1] R. Izquierdo, N. Garcia-Giralt, M. T. Rodriguez et al., "Biodegradable PCL scaffolds with an interconnected spherical pore network for tissue engineering," *Journal of Biomedical Materials Research A*, vol. 85, no. 1, pp. 25–35, 2008.
- [2] J. M. Kemppainen and S. J. Hollister, "Differential effects of designed scaffold permeability on chondrogenesis by chondrocytes and bone marrow stromal cells," *Biomaterials*, vol. 31, no. 2, pp. 279–287, 2010.
- [3] H. W. Kim, J. C. Knowles, and H. E. Kim, "Hydroxyapatite/poly( $\epsilon$ -caprolactone) composite coatings on hydroxyapatite porous bone scaffold for drug delivery," *Biomaterials*, vol. 25, no. 7-8, pp. 1279–1287, 2004.
- [4] W. J. Li, R. Tuli, C. Okafor et al., "A three-dimensional nanofibrous scaffold for cartilage tissue engineering using human mesenchymal stem cells," *Biomaterials*, vol. 26, no. 6, pp. 599–609, 2005.
- [5] L. Calandrelli, B. Immirzi, M. Malinconico et al., "Natural and synthetic hydroxyapatite filled PCL: mechanical properties and biocompatibility analysis," *Journal of Bioactive and Compatible Polymers*, vol. 19, no. 4, pp. 301–313, 2004.
- [6] S. C. Rizzi, D. J. Heath, A. G. A. Coombes, N. Bock, M. Textor, and S. Downes, "Biodegradable polymer/hydroxyapatite composites: surface analysis and initial attachment of human osteoblasts," *Journal of Biomedical Materials Research*, vol. 55, no. 4, pp. 475–486, 2001.
- [7] H. Yu, P. J. VandeVord, L. Mao, H. W. Matthew, P. H. Wooley, and S. Y. Yang, "Improved tissue-engineered bone regeneration by endothelial cell mediated vascularization," *Biomaterials*, vol. 30, no. 4, pp. 508–517, 2009.
- [8] L. Ghasemi-Mobarakeh, M. P. Prabhakaran, M. Morshed, M. H. Nasr-Esfahani, and S. Ramakrishna, "Bio-functionalized PCL nanofibrous scaffolds for nerve tissue engineering," *Materials Science and Engineering C*, vol. 30, no. 8, pp. 1129–1136, 2010.
- [9] H. Ren and L. Zhang, "In situ growth approach for preparation of Au nanoparticle-doped silica aerogel," *Colloids and Surfaces A*, vol. 372, no. 1–3, pp. 98–101, 2010.
- [10] M. Alnaief and I. Smirnova, "In situ production of spherical aerogel microparticles," *Journal of Supercritical Fluids*, vol. 55, no. 3, pp. 1118–1123, 2011.
- [11] J. Ge, Y. Z. Zhang, M. Li, and L. Song, "Research of bioactive PLGA tissue engineering materials processed by sol-gel method," *Polymeric Materials Science and Engineering*, vol. 27, no. 10, pp. 169–172, 2011.
- [12] W. C. Ackerman, M. Vlachos, S. Rouanet, and J. Fruendt, "Use of surface treated aerogels derived from various silica precursors in translucent insulation panels," *Journal of Non-Crystalline Solids*, vol. 285, no. 1–3, pp. 264–271, 2001.
- [13] A. Abu Obaid, S. Andersen, J. W. Gillespie Jr., R. Vaidyanathan, and A. Studley, "Investigation of thermal and acoustic performance of aerogel-based glass fiber composites," in *Proceedings of the International SAMPE Symposium and Exhibition*, pp. 2279–2290, May 2005.
- [14] N. D. Hegde and A. V. Rao, "Effect of processing temperature on gelation and physical properties of low density TEOS based silica aerogels," *Journal of Sol-Gel Science and Technology*, vol. 38, no. 1, pp. 55–61, 2006.
- [15] E. J. Lerner, "Less is more with aerogels," *Industrial Physicist*, vol. 10, no. 5, pp. 26–30, 2004.
- [16] H. Fan, H. R. Bentley, K. R. Kathan, P. Clem, Y. Lu, and C. J. Brinker, "Self-assembled aerogel-like low dielectric constant films," *Journal of Non-Crystalline Solids*, vol. 285, no. 1-3, pp. 79–83, 2001.
- [17] G. S. Kim and S. H. Hyun, "Synthesis and characterization of silica aerogel films for inter-metal dielectrics via ambient drying," *Thin Solid Films*, vol. 460, no. 1-2, pp. 190–200, 2004.
- [18] M. Alnaief and I. Smirnova, "Effect of surface functionalization of silica aerogel on their adsorptive and release properties," *Journal of Non-Crystalline Solids*, vol. 356, no. 33-34, pp. 1644–1649, 2010.
- [19] I. Smirnova, S. Suttiruengwong, and W. Arlt, "Feasibility study of hydrophilic and hydrophobic silica aerogels as drug delivery systems," *Journal of Non-Crystalline Solids*, vol. 350, pp. 54–60, 2004.
- [20] I. Smirnova, J. Mamic, and W. Arlt, "Adsorption of drugs on silica aerogels," *Langmuir*, vol. 19, no. 20, pp. 8521–8525, 2003.
- [21] S. Sakka, "Application of sol-gel technology," in *Handbook of Sol-Gel Science and Technology*, pp. 1–138, Kluwer Academic, New York, NY, USA, 2005.
- [22] Z. Jia, J. Zhang, C. Jia, J. Nie, and K. Chu, "Preparation and characterization of mechanical properties of carbon nanotube/45S5Bioglass composites for biologic applications," *Materials Science and Engineering A*, vol. 528, no. 3, pp. 1553–1557, 2011.
- [23] H. R. Stanley, M. B. Hall, A. E. Clark, C. J. King III, L. L. Hench, and J. J. Berte, "Using 45S5 bioglass cones as endosseous ridge maintenance implants to prevent alveolar ridge resorption: a 5-year evaluation," *International Journal of Oral and Maxillofacial Implants*, vol. 12, no. 1, pp. 95–105, 1997.
- [24] I. D. Xynos, M. V. J. Hukkanen, J. J. Batten, L. D. Buttery, L. L. Hench, and J. M. Polak, "Bioglass 45S5 stimulates osteoblast turnover and enhances bone formation in vitro: implications and applications for bone tissue engineering," *Calcified Tissue International*, vol. 67, no. 4, pp. 321–329, 2000.
- [25] L. L. Hench, R. J. Splinter, W. C. Allen, and T. K. Greenlee, "Bonding mechanisms at the interface of ceramic prosthetic materials," *Journal of Biomedical Materials Research*, vol. 5, no. 6, pp. 117–141, 1972.
- [26] A. L. Andrade, D. M. Souza, W. A. Vasconcellos, R. V. Ferreira, and R. Z. Domingues, "Tetracycline and/or hydrocortisone incorporation and release by bioactive glasses compounds," *Journal of Non-Crystalline Solids*, vol. 355, no. 13, pp. 811–816, 2009.
- [27] M. Corno and A. Pedone, "Vibrational features of phosphosilicate glasses: periodic B3LYP simulations," *Chemical Physics Letters*, vol. 476, no. 4–6, pp. 218–222, 2009.
- [28] G. Jiang, M. E. Evans, I. A. Jones, C. D. Rudd, C. A. Scotchford, and G. S. Walker, "Preparation of poly( $\epsilon$ -caprolactone)/continuous bioglass fibre composite using monomer transfer moulding for bone implant," *Biomaterials*, vol. 26, no. 15, pp. 2281–2288, 2005.
- [29] P. P. Lopes, B. J. M. L. Ferreira, N. A. F. Almeida, M. C. Fredel, M. H. V. Fernandes, and R. N. Correia, "Preparation and study of in vitro bioactivity of PMMA-co-EHA composites filled with a  $\text{Ca}_3(\text{PO}_4)_2$ - $\text{SiO}_2$ - $\text{MgO}$  glass," *Materials Science and Engineering C*, vol. 28, no. 4, pp. 572–577, 2008.
- [30] S. N. Salama, H. Darwish, and H. A. Abo-Mosallam, "HA forming ability of some glass-ceramics of the  $\text{CaMgSi}_2\text{O}_6$ - $\text{Ca}_3(\text{PO}_4)_2$ - $\text{F}$ - $\text{CaAl}_2\text{SiO}_6$  system," *Ceramics International*, vol. 32, no. 4, pp. 357–364, 2006.
- [31] Y. Zhou, H. Li, K. Lin, W. Gu, and J. Chang, "Effect of heat treatment on the properties of  $\text{SiO}_2$ - $\text{CaO}$ - $\text{MgO}$ - $\text{P}_2\text{O}_5$  bioactive glasses," *Journal of Materials Science Materials in Medicine*, vol. 23, no. 9, pp. 2101–2108, 2012.

- [32] F. Sabri, J. D. Boughter Jr., D. Gerth et al., "Histological evaluation of the biocompatibility of polyurea crosslinked silica aerogel implants in a rat model: a pilot study," *PLoS ONE*, vol. 7, no. 12, Article ID e50686, 2012.
- [33] Y. Jiang, T. Jia, W. Gong, P. H. Wooley, and S. Y. Yang, "Titanium particle-challenged osteoblasts promote osteoclastogenesis and osteolysis in a murine model of periprosthetic osteolysis," *Acta Biomaterialia*, vol. 9, no. 7, pp. 7564–7572, 2013.
- [34] H. Yu, P. H. Wooley, and S. Yang, "Biocompatibility of poly-caprolactone-hydroxyapatite composite on mouse bone marrow-derived osteoblasts and endothelial cells," *Journal of Orthopaedic Surgery and Research*, vol. 4, no. 1, article 5, 2009.
- [35] Y. Jiang, T. Jia, W. Gong, P. H. Wooley, and S.-Y. Yang, "Effects of Ti, PMMA, UHMWPE, and Co–Cr wear particles on differentiation and functions of bone marrow stromal cells," *Journal of Biomedical Materials Research A*, 2013.
- [36] H. L. Wamocha, H. E. Misak, Z. Song et al., "Cytotoxicity of release products from magnetic nanocomposites in targeted drug delivery," *Journal of Biomaterials Applications*, vol. 27, no. 6, pp. 661–667, 2013.
- [37] K. T. Shalumon, K. H. Anulekha, K. P. Chennazhi, H. Tamura, S. V. Nair, and R. Jayakumar, "Fabrication of chitosan/poly(caprolactone) nanofibrous scaffold for bone and skin tissue engineering," *International Journal of Biological Macromolecules*, vol. 48, no. 4, pp. 571–576, 2011.
- [38] N. S. Binulal, M. Deepthy, N. Selvamurugan et al., "Role of nanofibrous poly(caprolactone) scaffolds in human mesenchymal stem cell attachment and spreading for in vitro bone tissue engineering-response to osteogenic regulators," *Tissue Engineering A*, vol. 16, no. 2, pp. 393–404, 2010.
- [39] A. Polini, D. Pisignano, M. Parodi, R. Quarto, and S. Scaglione, "Osteoinduction of human mesenchymal stem cells by bioactive composite scaffolds without supplemental osteogenic growth factors," *PLoS ONE*, vol. 6, no. 10, Article ID e26211, 2011.

## Research Article

# Effects on Mechanical Properties of Recycled PET in Cement-Based Composites

Liliana Ávila Córdoba,<sup>1</sup> Gonzalo Martínez-Barrera,<sup>2</sup> Carlos Barrera Díaz,<sup>3</sup>  
Fernando Ureña Nuñez,<sup>4</sup> and Alejandro Loza Yañez<sup>5</sup>

<sup>1</sup> Facultad de Química, Universidad Autónoma del Estado de México, Paseo Colon Esquina Paseo Tollocan S/N, 50180 Toluca, MEX, Mexico

<sup>2</sup> Laboratorio de Investigación y Desarrollo de Materiales Avanzados (LIDMA), Facultad de Química, Universidad Autónoma del Estado de México, Km. 12 de la Carretera Toluca-Atacomulco, 50200 San Cayetano, MEX, Mexico

<sup>3</sup> Centro Conjunto de Investigación en Química Sustentable UAEM-UNAM, Universidad Autónoma del Estado de México Campus El Rosedal, Autopista Ixtlahuaca-Atacomulco, Km 14.5, 50200 San Cayetano, MEX, Mexico

<sup>4</sup> Instituto Nacional de Investigaciones Nucleares, Carretera México-Toluca S/N, 52750 La Marquesa Ocoyoacac, MEX, Mexico

<sup>5</sup> Facultad de Ingeniería, Universidad Autónoma del Estado de México, Avenida Universidad S/N, Cerro de Coatepec, Ciudad Universitaria, 50110 Toluca, MEX, Mexico

Correspondence should be addressed to Gonzalo Martínez-Barrera; gonzomartinez02@yahoo.com.mx

Received 29 March 2013; Accepted 22 May 2013

Academic Editor: Osman Gencel

Copyright © 2013 Liliana Ávila Córdoba et al. This is an open access article distributed under the Creative Commons Attribution License, which permits unrestricted use, distribution, and reproduction in any medium, provided the original work is properly cited.

Concretes consisting of portland cement (OPC), silica sand, gravel, water, and recycled PET particles were developed. Specimens without PET particles were prepared for comparison. Curing times, PET particle sizes, and aggregate concentrations were varied. The compressive strength, compressive strain at yield point, and Young modulus were determined. Morphological and chemical compositions of recycled PET particles were seen in a scanning electron microscopy. Results show that smaller PET particle sizes in lower concentrations generate improvements on compressive strength and strain, and Young's modulus decreases when the size of PET particles used was increased.

## 1. Introduction

Polyethylene terephthalate (PET) is one of the most used materials in the packaging of several kinds of products. The packages made with PET are light, transparent, and with high resistance to impact, they do not interact chemically with the contents, and they are not toxic. All these characteristics have made them gain presence in the polymer market and earn a major presence in the global industry. The growth demand in Mexico has been estimated 13% annually since 2000 [1]. Mexico has become the first per capita market of water packaged in PET bottles around the world. The annual average consumption per person is 234 liters; it means 13% of water sold in the whole world via PET bottles takes place in Mexico.

During 2009, the massive PET disposal in Mexico has reached more than 7800 million of nonreturnable bottles, because the nonbiodegradability nature of this material and the solid handle materials in all state jurisdictions have experienced an important impact. Approximately, 21.3 million bottles will be used every day by consumers; it is estimated that only 20% of these bottles will eventually reach the facilities for recycling solid, and the rest will be accumulated in rubbish dumps [2].

PET recycling consists in the transformation of bottles through two different kinds of processes: (1) mechanical process is the most employed physical process to recycle PET. It has three stages that include separation, washing, and grinding of containers. With this process, PET flakes produced can be directly employed without the need of being reprocessed as

pellets in the creation of products by injection or extrusion; (2) chemical process consists of the separation of the basic components or monomers. The methanolysis, glycolysis, and hydrolysis are the elemental processes to achieve this transformation.

One transcendental alternative to recycling PET materials consists of using them as substitute of concrete aggregates. Due to demands of technological development in the construction area, the possibility for generating alternative materials that can be applied with increasing functionality, low costs, and better physical, chemical, and mechanical properties than conventional materials is being explored [3–5].

Fiber-reinforced concrete represents the current tendency to apply more efficient crack-resistant concrete. For instance, PET has been widely used to produce fibers, particles, or flakes to obtain cement-based products with improved properties [6, 7]. Several studies using reinforced concrete with polymer fibers like polypropylene, polystyrene, polyethylene terephthalate, and polyethylene have evidenced variation of concrete properties according to the nature and size of the aggregate [8, 9].

Referring to environmental aspects, Rebeiz concludes that the inclusion of recycled PET can help diminish the production costs of concrete allowing long term disposal of plastics [10].

The effects of light aggregates of recycled PET in reinforced concrete were analyzed by compression, tension resistance, elasticity module, and density. Choi et al. concluded that 28-day compression index using a PET concentration of 75% diminishes approximately by 33% compared to plain concrete; however workability improves by 123% [11].

Another research showed that replacement of sand with less than 50% by volume with 5 mm granulated PET affects neither compression nor flexion strength [12]. Ochi et al. describe a method that can be used to produce concrete-reinforcing PET fiber from used PET bottles. By using this method, concrete and PET fibers are easily mixed with fiber contents as high as 3% [13].

Fibers with lengths of 10, 15, and 20 mm and volume fractions of 0.05, 0.18, and 0.30% related to the volume of the concrete were used. Physical and mechanical characterizations of concrete were performed, including determination of compressive strength, flexural strength, Young's modulus, and fracture toughness, as well as pore analysis using mercury intrusion and scanning electron microscopy. Flexure and impact tests were performed after 28 and 150 days. No significant effects on compressive strength and modulus of elasticity were observed with the addition of fibers [6]. Moreover, Young's modulus decreased as fiber volume increased. At 28 days, concrete flexural toughness and impact resistance increased with the presence of PET fibers, except for the sample with 0.05% by volume [6].

Other authors have made preliminary analysis of concrete reinforced and waste polyethylene terephthalate as an aggregate [14–16].

In the present paper, compressive strength and Young's modulus of cement-based materials with recycled PET were evaluated. Particle sizes and concentrations of recycled PET were obtained from waste bottles.

TABLE 1: Sieve analysis of silica sand (Fineness modulus = 1.59).

Sieve size (number)	Retained (g)	% Retained (individual)	% Retained (cumulative)
16	0	0	0
30	79.0	29	29
50	74.9	27	56
100	52.4	19	75
200	36.9	13	88
Bottom tray	33.7	12	100

TABLE 2: Sieve analysis of gravel.

Sieve size (in)	Retained (g)	% Retained (individual)	% Retained (cumulative)
3/4	0	0	0
3/8	20.3	2	2
4	902.8	91	93
8	57.8	6	99
Bottom tray	7	1	100

## 2. Materials and Methods

**2.1. Specimen Preparation.** Before preparing concrete specimens, one set of PET flakes was obtained from recycled PET bottles, in three different sizes: 0.5, 1.5, and 3 mm, and was used in concentrations of 1.0, 2.5, and 5.0% by volume; these values were intentionally selected higher than those reported in previous investigations in order to avoid problems concerning homogeneity and workability, even with the use of plasticizer additives [17].

To obtain PET flakes for being added to concrete, in first stage, PET bottles were collected and cut. In order to achieve homogeneous size and make the cutting easy, only the body was used, excluding the neck and the bottom of them. First cut provided 50 mm long and 5 mm width (in average) PET flakes, and with a second cut, one-fifth of the original size was obtained. Finally, these flakes were submitted to a grinding process for one hour, in an SG Granulator model SG-2324E, and screened for 45 minutes through different sieves (nos. 6, 10, 14, 18, and 35), corresponding to 3.3, 2.0, 1.4, 1.0, and 0.5 mm, respectively.

Different mixes were elaborated with portland cement (OPC); silica sand (1.4 mm size); gravel (9.5 mm maximum size), and water. Proportions of components in the mixes were 1/2.75 for cement/aggregates, with water/cement ratio of 0.485. All materials were mixed according to practice ASTM C-305 [18]. Sand and gravel aggregates were obtained from Calimaya county and Tula Hidalgo, Mexico, respectively.

Sieve analysis of silica sand and gravel aggregates is shown in Tables 1 and 2.

Three different sizes of PET flakes, 0.5, 1.5, and 3.0 mm, were considered for the study, and for each size, three different concentrations of recycled PET particles were considered, 1.0, 2.5, and 5.0% by volume as shown in Table 3.

TABLE 3: Components of concrete with recycled PET.

PET (vol %)	PET (g)	Portland cement (g)	Silica sand (g)	Gravel (g)	Water (g)	Total volume* (cm <sup>3</sup> )
1.0	3.26	420	914.7	1152	413	1338.9
2.5	8.17	420	909.8	1152	413	1339.9
5.0	16.33	420	901.6	1152	413	1342.8

\*Total volume was calculated considering specific gravity (g/cm<sup>3</sup>) of each material, as follows: PET (1.45), cement (3.15), silica sand (2.55), gravel (2.67), and water (1.00).

TABLE 4: Physical and mechanical properties of PET.

Mechanical properties	Units	Value
Density	lbs/in <sup>3</sup>	0.0499
Water absorption, 24 h	%	0.10
Specific gravity	g/cm <sup>3</sup>	1.38
Tensile strength at break, 73°F	psi	11,500
Tensile modulus, 73°F	psi	4 × 10 <sup>5</sup>
Elongation at break, 73°F	%	70
Flexural strength, 73°F	psi	15,000
Flexural modulus, 73°F	psi	4 × 10 <sup>5</sup>

2.2. *Physical and Mechanical Properties of PET.* For reference, some physical and mechanical properties of PET are presented in Table 4.

After mixing, concrete cylindrical specimens (2.0'' diameter and 4.0'' long) were molded. After 24 hours, they were placed in a controlled temperature room (at 23.0 ± 2.0°C and 95% of relative humidity according to ASTM C/192 M-00) [19], with the surface exposed to moisture. The moist room conditions were the same as above, according to ASTM C-511 [20]. It is important to remark that PET flakes replaced silica sand.

2.3. *Mechanical Tests.* Compressive strength evaluation of all concrete cylindrical specimens was carried out in an universal testing machine model 70-S17C2 (Controls, Cernusco, Italy), according to ASTM C-39M-01 [21], located at Laboratory of Research and Development of Advanced Materials (LIDMA) of the Autonomous University of the State of Mexico (UAEM). Specimens were tested after 7 and 28 days of moist curing. Testing tolerance allowed for the specimens was 7 days ± 6 hours and 28 days ± 12 hours.

2.4. *Morphological Characterization.* Before mechanical testing, some PET flakes were dried in a rotovapor for 24 hours; then their surfaces, particle size distribution, and chemical composition were analyzed by a scanning electron microscopy (SEM) in a JEOL model JSM-5200 machine, in the secondary-electron mode.

### 3. Results and Discussion

The composition and morphological surface of recycled PET particles were evaluated by a scanning electron microscopy

TABLE 5: Compressive strength values of plain concrete.

Curing time (days)	Compressive strength (MPa)
7	19.36
28	26.76

with EDS. The composition shows 72.55% of carbon and 27.45% of oxygen.

Recycled PET particles varying from 134 μm to 1 mm were obtained following a first cutting process of PET bottles (Figure 1(a)). Applying a continuous cutting process, PET particle sizes diminish as seen in Figure 1(b), with sizes less than 100 μm. In the present work, we decided to use PET particles ranging from 0.5 to 3.0 mm.

3.1. *Compressive Strength.* Compressive strength values of plain concrete are reported in Table 5.

Compressive strength values of concretes made with PET are shown in Figure 2. Analysis in terms of (a) PET particle size, (b) PET particle concentration, and (c) curing time was realized. Values of concrete strength range from 10.0 to 21.3 MPa, with a maximum improvement of 40% when 1.5 mm PET particles is added. Concretes without PET particles show moderate values, but when adding different sizes and volume percentages of PET particles, compressive strength increases. Moreover, the compressive strength values increase progressively for curing times ranging from 7 to 28 days given the condition that PET particle sizes do not exceed 1.5 mm as found in this investigation. Such behavior can be related to the presence of non degradable material (PET), which in principle can reduce the cement hydration. This is based on results, due to the fact that compressive strength at 7 days is less than the one obtained at 28 days.

According to PET particle size, the values are higher for concrete with 1.5 mm PET particles and lower for those with 3.0 mm PET particles. Moreover, the highest values are obtained for 2.5% by volume of PET particles. As it is known, the strength of materials can be improved by blending, insertion of fibers, using fillers, and/or combinations of these techniques. Smaller particles usually provide more reinforcement.

3.2. *Compressive Strain at Yield Point.* Results for compressive strain at the yield point are presented in Figure 3. The values for concretes with PET particles vary from 0.0032 to 0.009 mm/mm, higher than standard values for portland cement (OPC) concrete (0.003 mm/mm).

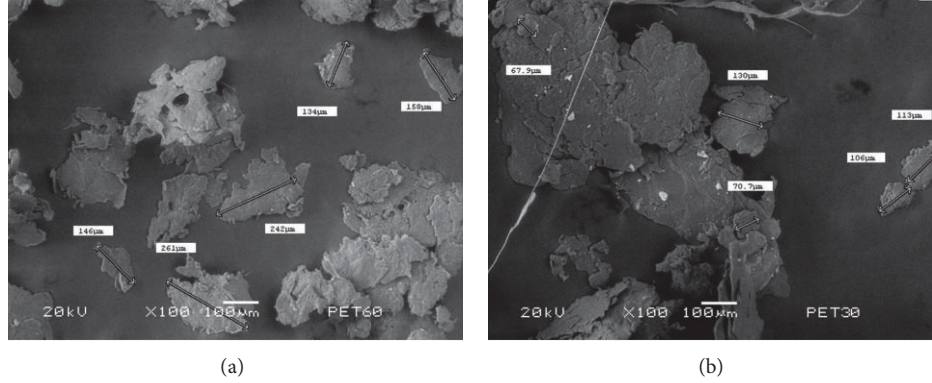


FIGURE 1: SEM images of (a) cut PET and (b) grinded PET.

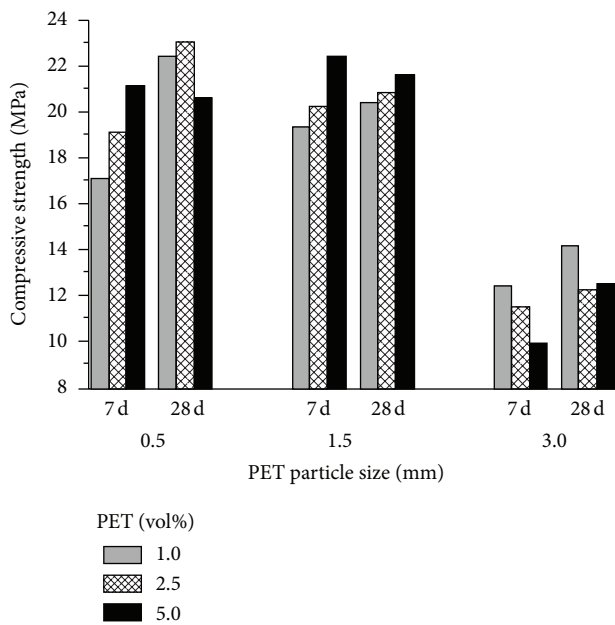


FIGURE 2: Compressive strength of concrete with recycled PET particles.

Different behaviours for concretes are seen. For concrete with PET particles of 0.5 mm and 1.5 mm of size, a continuous increase of compressive strain as a function of time can be observed. The highest compressive strain values are for concrete with 1.5 mm PET particles, followed by concrete with 0.5 mm PET particles. Nevertheless, bigger PET particle sizes (3.0 mm) generate lower compressive strain values.

In terms of time dependence, at 28 days of curing time, a minimum and maximum can be seen when using 0.5 mm or 1.5 mm, respectively. The PET particle concentration constitutes a minority component but plays a role in enhancing the compressive strain values with respect to concrete made with 3.0 mm PET particle size. The values decrease for higher concentration of PET particles and higher sizes, comparing results of concrete tested with PET. Thus, higher sizes mean detrimental values for strain. This can be noticed in Figure 2 where compressive strength shows roughly 40% higher values

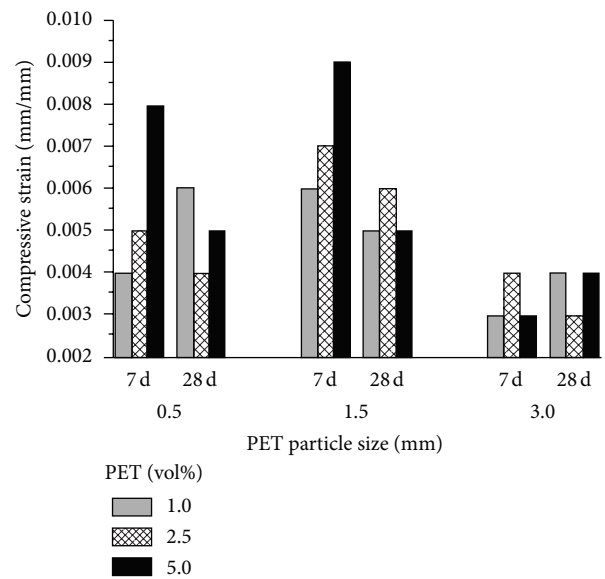


FIGURE 3: Compressive strain of concrete with recycled PET particles.

for 0.5 and 1.5 mm PET particle sizes than values obtained for 3.0 mm PET particle size. From Figure 2 and results shown in Table 5, it can be seen that compressive strength of plain concrete increased by 12% compared to concrete made with 1.5 mm PET particle size (which was the best result with PET), and the lowest strength was obtained in concrete made with 3 mm PET particle size (46% compared to plain concrete).

**3.3. Modulus of Elasticity under Compression.** Figure 4 shows modulus of elasticity of concretes under compression; the values range from 1.1 to 5.2 GPa, which means a maximum improvement of 153% with respect to plain concrete when PET particles are added. The highest values are for concrete with 1.5 mm PET particles at a concentration of 2.5% by volume and 28 days of curing time. On the other hand, the lowest value was obtained with 3.0 mm PET particle size, at a concentration of 5.0% by volume and 28 days of curing

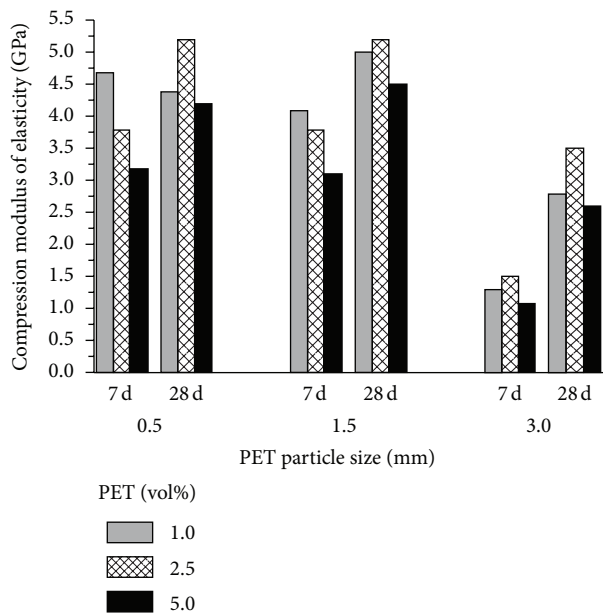


FIGURE 4: Modulus of elasticity under compression of concrete with recycled PET particles.

time. In general, the time dependence of concretes with PET particles shows maximum values at 28 days.

When analyzing elasticity results depending on PET particle size, the values are increasing from 0.5 mm to 1.5 mm, but for 3.0 mm the values decrease.

Finally, the highest Young's modulus was obtained with 0.5 mm PET particles and 2.5% by volume of PET in the concrete mix. For 1.5 mm PET particles, Young's modulus is quite the same for every dose of PET used (1.0, 2.5, and 5.0% by volume).

#### 4. Conclusions

As expected, mechanical properties of the concrete depend on the PET particle size and its concentration. Lower sizes and concentrations of PET particle create less space in the concrete, and in consequence the compressive strength and the compression strain increase and Young's modulus decreases when the size of PET particles used was increased. Whenever less PET size is used in the concrete mix, deformations tend to be lower but maximum stresses are increased in magnitude.

The highest compressive strength was obtained for PET particle sizes of 0.5 mm and 2.5% volume and cured for 28 days, while the highest strain values were detected for 1.5 mm and 5.0% volume and cured for 7 days.

On the other hand, in absolute terms, the highest Young's modulus was obtained using 0.5 mm PET at a 2.5% dose in the concrete mix. We can also conclude that PET size has an inverse relationship to the Young's modulus obtained, which means as less PET size is used, Young's Modulus increases.

#### Acknowledgments

The authors thank the National Council of Science and Technology of México (CONACYT) for the scholarship support and for the achievement of this research and Environmental Sciences Graduate Program of Universidad Autónoma del Estado de México (UAEM). They thank also Eng. Carlos Uriel de la Rosa Serrano, Professor José Saturnino Pérez Fajardo (chief of Materials Laboratory of Faculty of Engineering of Universidad Autónoma del Estado de México), and Mr. Arcadio Estrada Nava for the technical support.

#### References

- [1] J. Treviño, "Asociación para Promover el Reciclado del PET," A.C. APREPET. México, 2001, <http://www.aprepet.org.mx/>.
- [2] "Beverage Marketing Corporation Report," Tech. Rep., The Global Bottled Water Market, 2010, <http://www.beveragemarketing.com/>.
- [3] J. P. Schaffer, "Materiales compuestos," in *Ciencia y Diseño de Ingeniería de Los Materiales*, pp. 552–581, Compañía Editorial Continental, México city, México, 2000.
- [4] K. Gurudatt, P. De, A. K. Rakshit, and M. K. Bardhan, "Dope-dyed polyester fibers from recycled PET wastes for use in molded automotive carpets," *Journal of Industrial Textiles*, vol. 34, no. 3, pp. 167–179, 2005.
- [5] W. F. Smith and J. Hashemi, *Fundamentos de La Ciencia e Ingeniería de Materiales*, McGraw Hill, New York, NY, USA, 2006.
- [6] F. Pelisser, M. O. Klegues, P. J. Gleize, and R. H. Ramos, "Mechanical properties of recycled PET fibers in concrete," *Materials Research*, vol. 15, no. 4, pp. 1–8, 2012.
- [7] J. T. San-José, I. Vegas, and A. Ferreira, "Reinforced polymer concrete: physical properties of the matrix and static/dynamic bond behaviour," *Cement and Concrete Composites*, vol. 27, no. 9–10, pp. 934–944, 2005.
- [8] M. E. Tawfik and S. B. Eskander, "Polymer concrete from marble wastes and recycled poly(ethylene terephthalate)," *Journal of Elastomers and Plastics*, vol. 38, no. 1, pp. 65–79, 2006.
- [9] B. Israngkura and Y. Ungkoon, "Bond performance of fiber reinforced polymer (FRP) bars in Autoclaved Aerated Concrete," *Journal of Civil Engineering and Architecture*, vol. 4, pp. 41–44, 2010.
- [10] K. S. Rebeiz, "Time-temperature properties of polymer concrete using recycled PET," *Cement and Concrete Composites*, vol. 17, no. 2, pp. 119–124, 1995.
- [11] Y.-W. Choi, D.-J. Moon, J.-S. Chung, and S.-K. Cho, "Effects of waste PET bottles aggregate on the properties of concrete," *Cement and Concrete Research*, vol. 35, no. 4, pp. 776–781, 2005.
- [12] O. Y. Marzouk, R. M. Dheilily, and M. Queneudec, "Valorization of post-consumer waste plastic in cementitious concrete composites," *Waste Management*, vol. 27, no. 2, pp. 310–318, 2007.
- [13] T. Ochi, S. Okubo, and K. Fukui, "Development of recycled PET fiber and its application as concrete-reinforcing fiber," *Cement and Concrete Composites*, vol. 29, no. 6, pp. 448–455, 2007.
- [14] J. M. L. Reis and E. P. Carneiro, "Evaluation of PET waste aggregates in polymer mortars," *Construction and Building Materials*, vol. 27, no. 1, pp. 107–111, 2012.
- [15] D. Foti, "Preliminary analysis of concrete reinforced with waste bottles PET fibers," *Construction and Building Materials*, vol. 25, no. 4, pp. 1906–1915, 2011.

- [16] N. Saikia and J. de Brito, "Waste polyethylene terephthalate as an aggregate in concrete," *Materials Research*, vol. 16, no. 2, pp. 341–350, 2013.
- [17] American Concrete Institute-ACI Committee, *ACI 544. IR-96: State of the Art Report on Fiber Reinforced Concrete*, chapter 4, ACI Committee, Detroit, Mich, USA, 1996.
- [18] American Society for Testing Materials (ASTM), *Standard Practice For Mechanical Mixing of Hydraulic Cement Pastes and Mortars of Plastic Consistency*, 1999.
- [19] American Society for Testing Materials (ASTM), *Standard Practice For Making and Curing Concrete Test Specimens in the Laboratory*, 2000.
- [20] American Society for Testing Materials (ASTM), *Standard Specification For Mixing Rooms, Moist Cabinets, Moist Rooms, and Water Storage Tanks Used in the Testing of Hydraulic Cements and Concrets*, 1998.
- [21] American Society for Testing Materials (ASTM), *Standard Test Method For Compressive Strength of Cylindrical Concrete Specimens*, 2001.

## Research Article

# The Effect of Polymer-Cement Stabilization on the Unconfined Compressive Strength of Liquefiable Soils

Ali Ateş

*Geotechnical Division, Department of Civil Engineering, Technology Faculty, Düzce University, 81620 Düzce, Turkey*

Correspondence should be addressed to Ali Ateş; [aliateş@duzce.edu.tr](mailto:aliateş@duzce.edu.tr)

Received 29 March 2013; Accepted 14 May 2013

Academic Editor: Osman Gencil

Copyright © 2013 Ali Ateş. This is an open access article distributed under the Creative Commons Attribution License, which permits unrestricted use, distribution, and reproduction in any medium, provided the original work is properly cited.

Soil stabilization has been widely used as an alternative to substitute the lack of suitable material on site. The use of nontraditional chemical stabilizers in soil improvement is growing daily. In this study a laboratory experiment was conducted to evaluate the effects of waterborne polymer on unconfined compression strength and to study the effect of cement grout on pre-venting of liquefiable sandy soils. The laboratory tests were performed including grain size of sandy soil, unit weight, ultrasonic pulse velocity, and unconfined compressive strength test. The sand and various amounts of polymer (1%, 2%, 3%, and 4%) and cement (10%, 20%, 30%, and 40%) were mixed with all of them into dough using mechanical kneader in laboratory conditions. Grouting experiment is performed with a cylindrical mould of 150 × 300 mm. The samples were subjected to unconfined compression tests to determine their strength after 7 and 14 days of curing. The results of the tests indicated that the waterborne polymer significantly improved the unconfined compression strength of sandy soils which have susceptibility of liquefaction.

## 1. Introduction

Soil stabilization refers to produce in which a special soil, a cementing material, or other chemical materials are added to the liquefiable sandy soils to improve one or more of their properties. There are two methods to enhance the properties of sandy soils, one of them is the mechanical stabilization which is mixed the natural soil and stabilizing material together for obtaining a homogeneous mixture and the second one is adding stabilizing material into undisturbed soils to obtain interaction by letting it permeate through soil voids [1, 2]. Chemical stabilization is the modification of properties of a locally available soil to improve its engineering performance. The two most commonly used chemical stabilization methods are lime stabilization and cement stabilization. Additives such as fly ash and phosphogypsum can be added to the lime soil and cement soil mixtures to enhance the properties of the stabilized soil. The use of polymeric materials in setting soil improvement is growing daily. Unfortunately, little research has been completed to distinguish between products that deliver enhanced performance and those that do not. The nature of soil stabilization dictates that products may provide

soil-specific properties and/or provide compatibility with environment. In other words, some products may work well in specific soil types in a given environment but perform poorly when applied to dissimilar materials in a different environment. Application of stabilizing agent on soils has a long history [3]. Cement was first used as stabilizing agent at the beginning of the 20th century to mix with the soils and form road material in the United States. Since then many other materials such as lime [4, 5], organic polymers [6], and their mixtures [7] have been used as stabilizing agents. Also several researchers [8–10] have discussed aqueous polymer applications while others [11–13] have provided useful data on polymer-soil interactions that determine the effectiveness of polymer solution in various applications. The objective of this research is to evaluate the effect of waterborne polymer and cement on unconfined compressive strength of liquefiable sandy soils.

## 2. Materials

*2.1. The Properties of Cement.* The cement used for the study is Portland cement labelled CEMI 42.5 R and the properties of which are given in Table 1.

TABLE 1: Properties of the cement.

Properties	Values
Grade	42.5 R
Specific gravity	3.17
Fitness (%)	3750
Consistency (%)	1.3
Initial and final setting time (min)	200–260

TABLE 2: Important physicochemical properties of as-received emulsion.

Name	Vinyl Acrylic-Copolymer watered solution
Physical state	Liquid-white colour
Solvability in water	Solution
Boiling point	100°
Viscosity	280
Sparkling point	Over 600
Non-self-burning	Nonexplosive
Temperature	Over 3200
Density (g/cm <sup>3</sup> )	1.11 (20°)
PH	4–7.5

2.2. *Epoxy Resin.* A commercial product of epoxy resin was used, which is an emulsion synthetic elastic chemical substance that increases the bound with the substrate as additive in optimum moisture, as well as the cohesion and the strength. A multi component resin grout usually provides very high-tensile compression and bond strengths. Some important properties were given in Table 2.

2.3. *The Properties of Soil Sample.* Locally available sandy soil was utilized for this study and was obtained from source of sand in Duzce City in Turkey. It is necessary for the samples to be stabilized to lie in the interval of upper and lower borders on the sieve analysis graph determined by Union of Japanese Civil Engineers. For this purpose, the gradation of samples was prepared on the upper and lower borders of sieve analysis graph to be applied the emulsion according to the Union of Japanese Civil Engineers. The samples were sieved by the number of the 8 mm, 4.76 mm, 2 mm, 1 mm, and 0.425 mm and the gradation was supplied mixing the grains remained on those sieves [14, 15].

The grain-size distribution of the soils was presented in Figure 1. The properties of the tested soils in term of particle size and sandy soil parameters were given in Table 3.

2.4. *Laboratory Studies.* This experimental work has been conducted to investigate the influence of curing time and percentage of waterborne polymer on the unconfined compression strength of sandy soils in Department of Civil Engineering, Faculty of Technology in Duzce University. Use of unconfined compressive strength for soil stabilizers is a quick and simple test and provides a convenient basis for comparison between stabilizer types.

TABLE 3: Engineering properties of sandy soils.

Property	Sample
Specific gravity	2.73
Grain size	
Gravel (>20 mm) (%)	0
Sand (75–20 mm) (%)	100
Max. void ratio ( $e_{max}$ )	0.77
Min. void ratio ( $e_{min}$ )	0.45
Relative density, $D_r$ (%)	45
Void ratio, $e$ (%)	1.024
Optimum moisture content (%)	13
Maximum dry unit weight (g/cm <sup>3</sup> )	1.92
Soil classification (USCS)	S

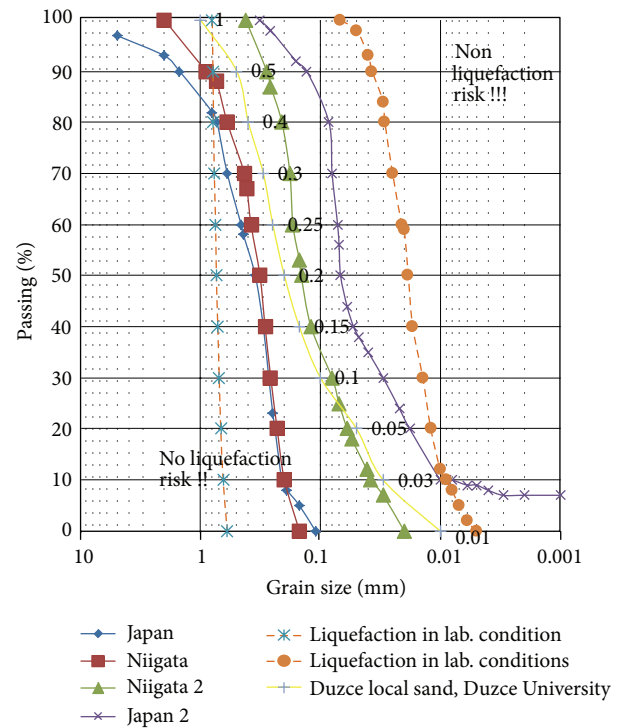


FIGURE 1: Grain size distribution of sandy soils.

Sandy soils with a different rate of cement mixing were used and various percentages of waterborne polymers were added to soils to investigate the ultrasonic pulse velocity, unit weight, and compressive strength of stabilized samples. The soils were dried before using in the mixtures. First, the required amounts of polymer as a percentage of dry weight of sample and cement were blended and then added to dry soils. The amount of aqueous polymer was chosen as 1, 2, 3, and 4% by total weight of dry sample and the amount of cement was chosen as 10, 20, 30, 40% by weight of dry sample, respectively. The mixing sample was placed into the mould. After 24 hours later, the specimens were taken out of the moulds and specimens were stored in the curing room at the temperature ranging from 21 to 25 centigrade and then tested at 7 and 14 days.



FIGURE 2: View of preparing the specimens in laboratory.

**2.4.1. Preparation of the Samples.** The preparation of the soil sample is of great importance for laboratory research. Because of using polymer which was insoluble in water, in all experiments, sands were oven dried for 24 hrs to eliminate sand's moisture and then specified amount of polymer added to the dry cement-sand. After completing this treatment, the specimens were prepared by mixing the polymer with sand in the loose dry density of  $19 \text{ kN/m}^3$ . The polymer mixture was developed in to dough using mechanical kneader. The uniformly mixed dough was subsequently placed into a steel mold measuring 150 mm in height and 300 mm in diameter (Figure 2). Finally, the molded specimens were left to cure at room's temperature. Specimens containing 1, 2, 3, and 4 wt.% (% by dry weight) polymer and 10, 20, 30, and 40 wt.% (% by dry weight) cement were prepared using this method. Other sets of samples were prepared using the same method and submerged in water to be cured for 7 and 14 days. In the following stage, the moisture content of the sandy soil was determined.

**2.5. Curing Time.** Curing times of 7 and 14 days were used in this research. Three samples for each curing time were prepared in order to provide an indication of reproducibility as well as to provide sufficient data for accurate interpolation of the results.

**2.6. Submerge of Specimens in Water.** In this study, each specimen was arranged vertically in a steel mould and submerged in a water tank after the specimen in each steel mould was allowed to be cured under room temperature. The specimens submerged in water for 7 and 14 days and then taken out from the water and tested within 24 hrs of removal from the soaking reservoir, and their unconfined compressive strength was recorded. Thus, the effect of curing period on compressive strength, unit weight, and ultrasonic pulse velocity of stabilized samples was evaluated.

**2.7. Unconfined Compressive Strength Testing.** Unconfined compressive strength testing was performed on all extracted specimens with a constant stress rate by manually controlled test machine (Figure 3). A data acquisition system was used to record the applied load. Each specimen was loaded until peak load was obtained.

**2.8. Ultrasonic Pulse Velocity Testing.** The ultrasonic pulse velocity (UPV) measuring devices can be applied for the

complex investigation of the soil properties (density, porosity, and strength, as well as its integrity). However, in many investigations up to now, there have been frequent references on the effect of soil stabilization close to the tested product soil cement mixing as it increases the UPV in soil. To investigate this issue more comprehensively, the specimens were made, where soil and cement with polymer of same diameter and length were assigned. The acoustic velocity wave speed of a given soil-concrete (that mixing soil is strengthened like concrete) specimen can easily be obtained with the travel time of a stress wave and the length of the specimen. The pulse is sent from the sending transducer to the receiving transducer through the soil concrete specimen as seen in Figure 4. The relationship of a specimen's acoustic velocity is simply calculated from a time and a length measurement. It should be noted that cracks, flaws, voids, and other anomalies within a material specimen could increase time of travel therefore decreasing the materials acoustic velocity. However, assuming the specimen in Figure 4 is free of anomalies, its acoustic velocity can be calculated simply by sending the pulse. The length of the specimen is 300 mm. Figure 4 shows typical ultrasonic pulse velocity test procedure.

### 3. Test Results

For this research, it was desired to evaluate the effectiveness of the soils mixed with stabilizer at dry and wet conditions being cured after 7 and 14 days. Low to high dosage rates were used for soils at dry and wet conditions. The stabilizer dosage rates used for this study were 1, 2, 3, and 4% as polymers and 10, 20, 30, and 40% as cement.

**3.1. Effect of Curing Time on Strength.** The results of curing times on unconfined compression strength results were shown in Figures 5 and 6. The unconfined compression strength of stabilized samples increases with curing time. Both specimens containing polymer content of 1–4% by wt.% and cement content of 10–40 wt.% were cured in air and water during 7 and 14 days. So, by increasing the polymer contents, cross-linking between polymer network increased and the strength of soil increased. The strength of the specimens containing 3% polymer and 30% cement content at 7 days of curing time achieved 90% of the 14 days compressive strength. It is clear from Figures 5 and 6 that compressive strength of the stabilized soils was increased while increasing



FIGURE 3: Arrangement of specimen for compressive test in lab.



FIGURE 4: Ultrasonic pulse velocity measurement.

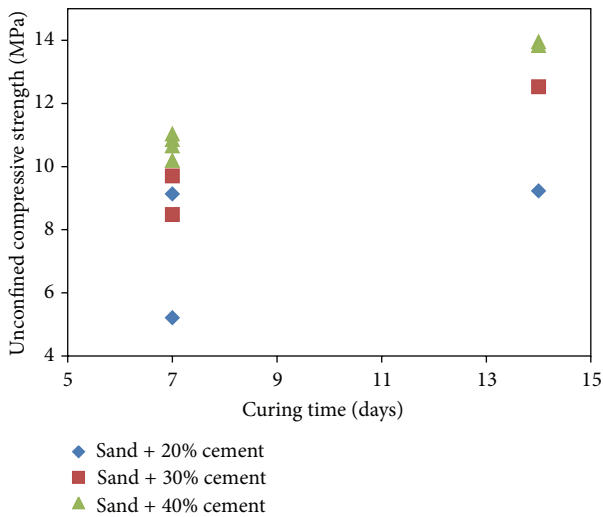


FIGURE 5: The unconfined compressive strength for specimens in water.

the curing time in both water and air curing conditions. As it is expected the effect of water curing on strength is more effective than air curing.

**3.2. Effect of Curing Condition on Strength.** Effects of wet conditions on unconfined compression strength stabilized soils containing polymer and cement were presented in Figure 5.

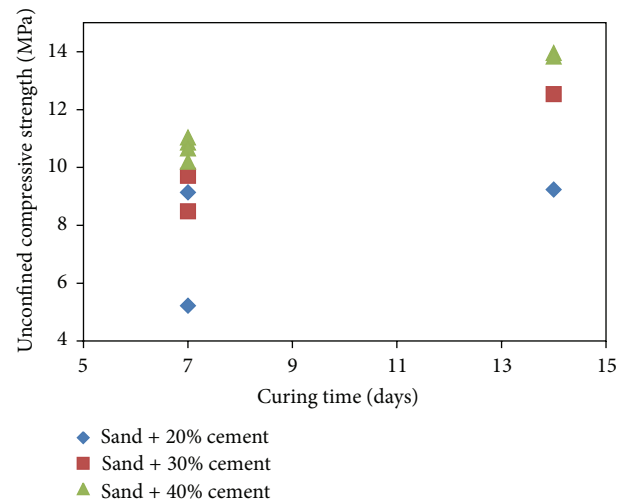


FIGURE 6: The unconfined compressive strength for specimens in air.

As discussed earlier in this paper, the treated samples were tested using dry and wet curing conditions to provide an indication of the material's moisture content. After 7-day curing period, placing the specimens in water tank provided an excellent indicator of the material's strength under wet conditions. Strength properties of the specimens that consist of 20–40 wt.% cement and 2–4% polymer content increased after submerging in water relatively. The reason of increasing the unconfined compressive strength of specimens is based on the role of water as catalyst.

**3.3. Effect of Cement and Polymer Content on Strength.** The results of unconfined compressive strength on stabilized soils with 10–40 wt.% cement and 1–4 wt.% polymer were presented in Figure 7. Stabilized soils with the 1% polymer have lower strength than 2, 3, and 4% polymer and could not record the value of unconfined compressive strength in this study. For each specimen, the unconfined compression strength increases with increment cement and polymer content. This means that the sandy soil becomes hardened with an increase in the cement content. This phenomenon

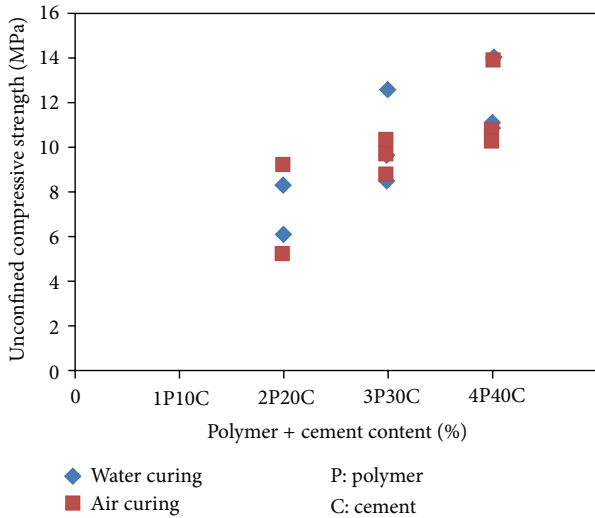


FIGURE 7: Unconfined compressive strength of soils modified with cement and polymer.

is explained by the fact that the fine grains of cement are positioned around and among the sand grains; the polymer covered all of sample's area.

The unconfined compressive strength increased linearly with a polymer concentration up to 4 wt.% for all of the sandy soil used. Comparing the performance of the emulsion in improving the unconfined compressive strength, it could be seen that the unconfined compression strength increases with increment polymer content. This phenomenon is explained by the fact that an increment in polymer content resulted in enhancing bond mechanisms of the sand-emulsion interface. It could be seen that specimens consist of 4 wt.% polymer gave the highest value for all specimens and specimens consist of 1 wt.% polymer gave the lowest values that furthermore the values could not be recorded for polymer at a rate of 1% successively. The unconfined compressive strength value of sand at 2 and 4 wt.% polymer content was 5.21 and 13.83 MPa, respectively, which are more than 100% increased.

The results obtained in the simple compression tests at 7 days have shown an increase in the strength of the stabilized material against the natural material whose strength was 10.65 MPa. The increases in strength obtained were proportional to the amount of polymer added, except for combination of 1% which reached 5.12 MPa, only achieved by the combination of the effect of the polymer matrix, not modified by low addition of polymer (at a rate of polymer 1%), and, on the other hand, the binding effect of the polymer. For content of 2% and upwards may modify the cement matrix. Therefore the increased strength was due only to the polymer. The results after 14 days showed values between 10.19 and 10.25 MPa in all combinations except that of 1%, which approximately reached 0.35 MPa. Even more, it was so weak that the result could not be recorded. The value of 10.65 Mpa was obtained in the combination of 3% and 4% polymer and the highest was obtained in the whole experiment. The values after 14 days, the results were very similar at those of 7 days,

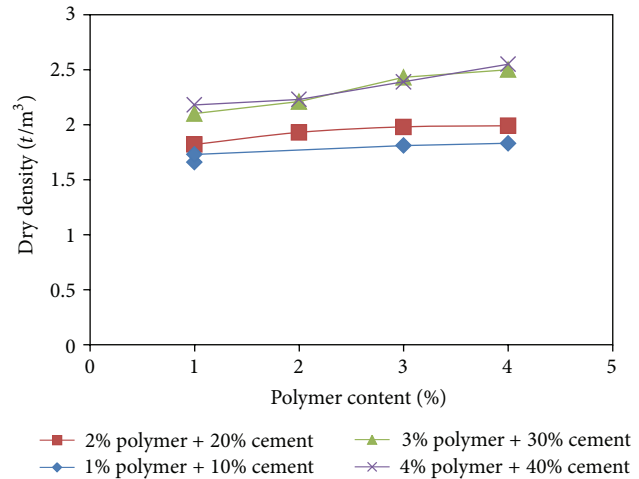


FIGURE 8: Effect of polymer content on maximum dry density of soil in dry conditions for 7 days.

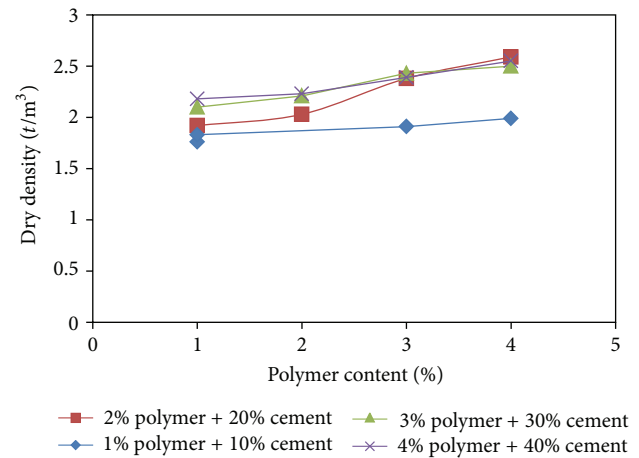


FIGURE 9: Effect of polymer content on maximum dry density of soil in wet conditions for 7 days.

reaching between 5.21–6.12 MPa except for the combination of 1%. For this curing time the greatest strength was obtained for the combination of 4%, with 10.65 MPa, a value very close to those obtained with combination of 3%, with 9.74 MPa. The analysis of test results of unconfined compression shows that the addition of 1% of polymer is insufficient since, while it changes the polymer nature of the soil, it is not enough for the formation of chemical reactions over the curing time. On the other hand, the combination of 4% clearly shows the excess values of polymer in the soil. The combination which improved optimal point from the standpoint of improving the resistant properties of soil tested against the addition of polymer was 4% and a compressive strength of 10.65 MPa.

3.4. Effect of Polymer Content on Maximum Dry Density. The effect of polymer content on maximum dry and specific density was presented in Figures 8, 9, 10, and 11. For any particular amount of polymer, an increase in polymer content

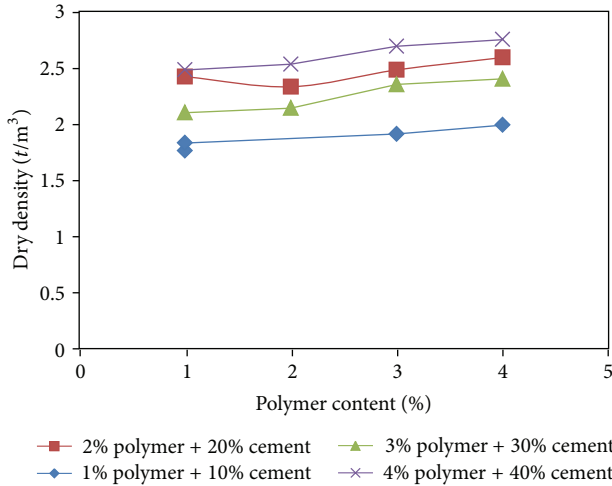


FIGURE 10: Effect of polymer content on maximum dry density of soil in dry conditions for 15 days.

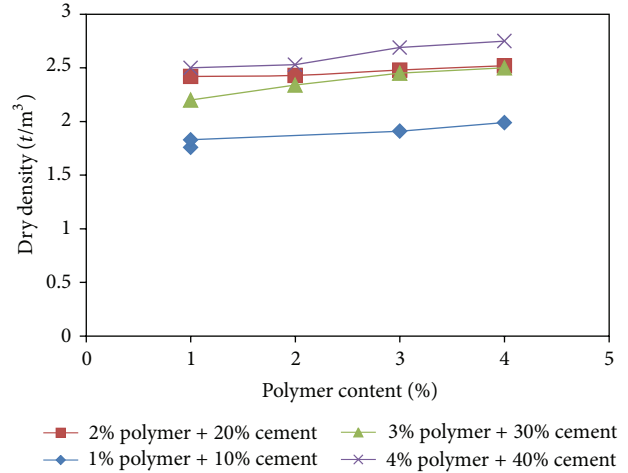


FIGURE 11: Effect of polymer content on maximum dry density of soil in wet conditions for 15 days.

causes an increment in dry density. As already explained, this is due to increment of average unit weight of solids in the sandy soil polymer mixture. It is observed from the Figures 8, 9, 10, and 11 that the plot of variation of dry density with respect to polymer content is more or less proportional in shape.

**3.5. Effect of Polymer Content on Optimum Moisture Content.** Optimum moisture content (OMC) is increased with increase in polymer content. The maximum OMC is recorded 13.8% for 4% polymer content, and as low as 5.4 for soil with 1% of polymer content. The initial inclusion of content of 1% caused a more sudden hike in the OMC than that of the ordinary sandy soil, and a further increase in polymer content increased the OMC. But in all cases, the OMC is greater than that of raw sandy soil. The effect of polymer content on OMC was presented in Figures 12, 13, 14, and 15.

**3.6. Ultrasonic Pulse Velocity Test Results.** The velocity versus density that results in pulse passing through in soil cement with polymer mixing was presented in Figures 16, 17, 18, and 19.

An increase in polymer content causes increment in velocity of soundings. This is due to increment of average unit weight of solids in the soil cement polymer mixture. It was observed from Figures 16, 17, 18, and 19 that the plot of variation of velocity versus density with respect to polymer content is more or less proportional.

**4. Conclusions**

This study was undertaken to investigate the influence of polymer percentage, curing time, and dry and wet conditions on the unconfined compressive strength of stabilized cement with sandy liquefiable soils. The results of the study were presented in following conclusions.

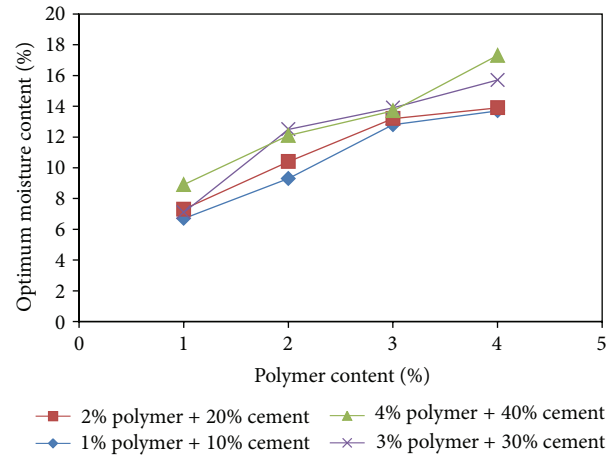


FIGURE 12: Effect of polymer content on OMC in dry conditions for 7 days.

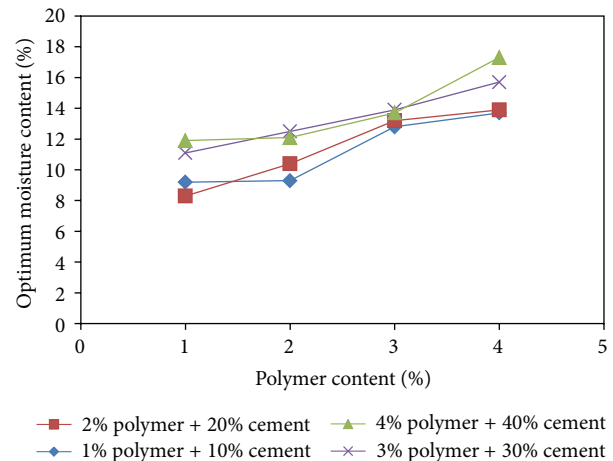


FIGURE 13: Effect of polymer content on OMC in wet conditions for 7 days.

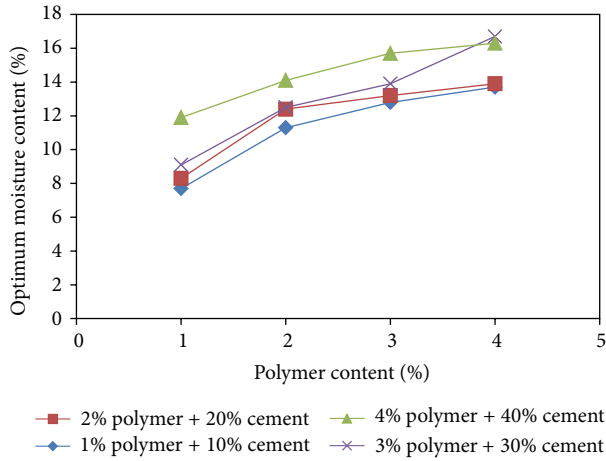


FIGURE 14: Effect of polymer content on OMC in dry conditions for 15 days.

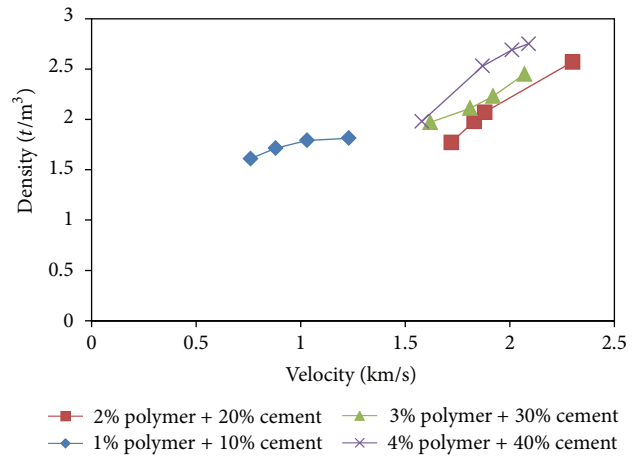


FIGURE 17: Ultrasonic pulse velocity test procedure in wet conditions for 7 days.

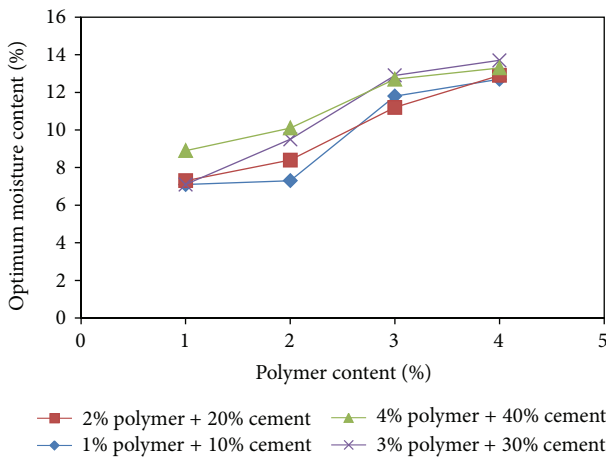


FIGURE 15: Effect of polymer content on OMC in wet conditions for 15 days.

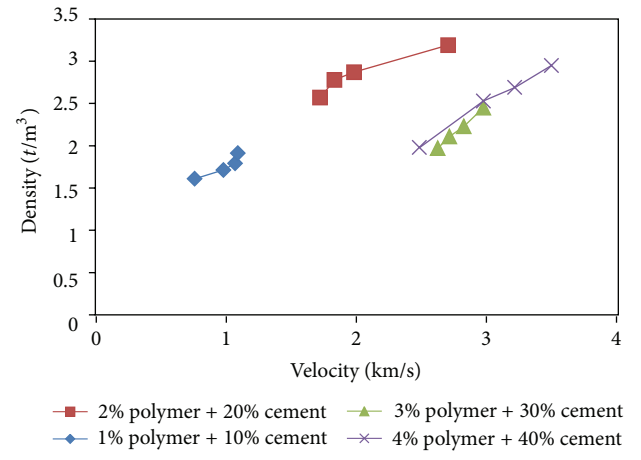


FIGURE 18: Ultrasonic pulse velocity test procedure in dry conditions for 14 days.

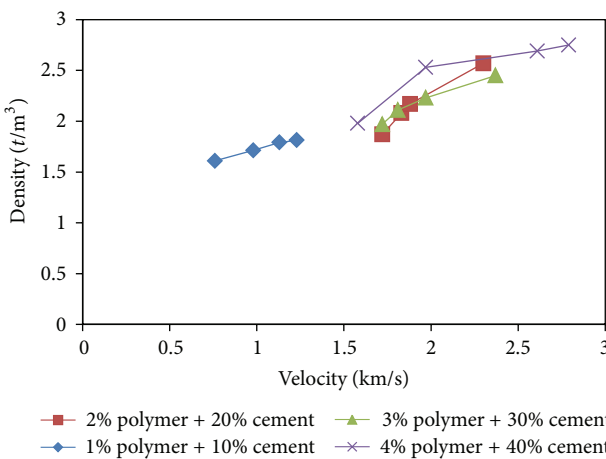


FIGURE 16: Ultrasonic pulse velocity test procedure in dry conditions for 7 days.

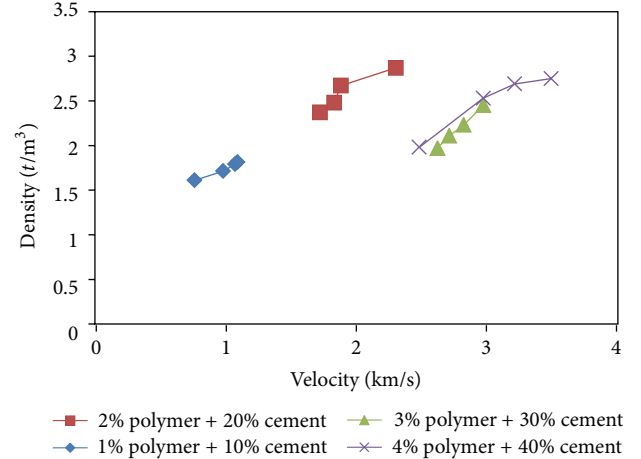


FIGURE 19: Ultrasonic pulse velocity test procedure in wet conditions for 14 days.

- (i) When the soil has stabilized with polymer, it increases the dry density of the soil due to specific gravity and unit weight of polymer. The variation is linear for both cases. Initial introduction of polymer content in to the soil causes an increase in OMC, so further increase in polymer content may cause to enhance in OMC.
- (ii) The addition of polymer to the natural soil produced an improvement in its mechanical capacities that were determined by unconfined compression tests, from the first period of curing examination. From the strength aspect of liquefiable sandy soils, the optimum polymer content estimated polymer at 3%, since in all tests it yielded the best result with the rate of 3% dosage of polymer.
- (iii) The strength of sandy soil mixtures has increased with increment of cement contents up to about 30% and above 30% cement content; the strength of the soil almost becomes constant. This phenomenon is explained by the fact that the fine grains of cement were covered and positioned around and among the sand grains.
- (iv) The unconfined compressive strength of specimens has increased with increment of polymer contents; this phenomenon is explained by the fact that increment of polymer and the polymer cover all of sample's area and increases cross-links.
- (v) For specimens submerging in water, there are two types of results. First one is about specimens that consist of 30 and 40 wt.% cement content at 4% polymer and 20 and 30 wt.% cement content at 3% polymer; the strength properties of these specimens were reduced after submerging in water. Second is about the rest of specimens. After 7 days of submerging, the unconfined compressive strength of the specimens increased while it was less than the dry condition. The reason of increasing the unconfined compressive strength of specimens is the role of water as catalyst. When specimens submerged in water, the  $H^+$  ions of water react with three-member epoxies' rings and the epoxies' ring was opened, then the hardener easily can react with resin. So, the strength of specimens increased.
- (vi) The unconfined compressive strength significantly increased with curing time. The unconfined compressive strength of the mixtures rapidly increased at 7 days.
- (vii) The maximum unconfined compressive strength values have increased with increase of the polymer content. Sandy soils stabilized with 3, 4% polymer at 30, 40% cement content have higher values on unconfined compressive strength than other percentages.

- [2] B. K. G. Theng, "Clay-polymer interactions: summary and perspectives," *Clay and Clay Minerals*, vol. 30, no. 1, pp. 1–10, 1982.
- [3] K. E. Clare and A. E. Cruchly, "Laboratory experiments in the stabilization of clays with hydrated lime," *Geotechnique*, vol. 7, pp. 97–110, 1957.
- [4] B. K. G. Theng, "Clay-polymer interactions: summary and perspectives," *Clay and Clay Minerals*, vol. 30, no. 1, pp. 1–10, 1982.
- [5] D. Dermatas and X. G. Meng, "Utilization of fly ash for stabilization/solidification of heavy metal contaminated soils," *Engineering Geology*, vol. 70, no. 3–4, pp. 377–394, 2003.
- [6] S. M. Lahalih and N. Ahmed, "Effect of new soil stabilizers on the compressive strength of dune sand," *Construction and Building Materials*, vol. 12, no. 6–7, pp. 321–328, 1998.
- [7] B. Indraratna, "Utilization of lime, slag and fly ash for improvement of a colluvial soil in New South Wales, Australia," *Geotechnical and Geological Engineering*, vol. 14, no. 3, pp. 169–191, 1996.
- [8] V. S. Green, D. E. Stott, L. D. Norton, and J. G. Graveel, "Polyacrylamide molecular weight and charge effects on infiltration under simulated rainfall," *Soil Science Society of America Journal*, vol. 64, no. 5, pp. 1786–1791, 2000.
- [9] A. B. Moustafa, A. R. Bazara, and A. R. Nour El Din, "Soil stabilization by polymeric materials," *Angewandte Makromolekular Chemie*, vol. 97, no. 1, pp. 1–12, 2003.
- [10] S. A. Naeini and A. Mahdavi, *Effect of polymer on shear strength of silty sand [M.S. thesis]*, Civil Engineering Department, Imam Khomeini International University, Qazvin, Iran, 2009.
- [11] J. L. Daniels, H. I. Inyang, and I. K. Iskandar, "Durability of Boston Blue Clay in waste containment applications," *Journal of Materials in Civil Engineering*, vol. 15, no. 2, pp. 144–152, 2003.
- [12] J. L. Daniels and H. I. Inyang, "Contaminant barrier material textural response to interaction with aqueous polymers," *Journal of Materials in Civil Engineering*, vol. 16, no. 3, pp. 265–275, 2004.
- [13] S. A. Naeini and M. Ghorbanalizadeh, "Effect of wet and dry conditions on strength of silty sand soils stabilized with epoxy resin polymer," *Journal of Applied Sciences*, vol. 10, no. 22, pp. 2839–2846, 2010.
- [14] ASTM, "Standard practice for classification of soils for engineering purposes (Unified Soil Classification System)," ASTM D2487, ASTM, West Conshohocken, Pa, USA, 2000, <http://www.astm.org/Standards/D2487.htm>.
- [15] H. Tsuchida, "Prediction and countermeasure against liquefaction in sand deposits," in *Proceedings of the Seminar of the Port and Harbour Research Institute*, vol. 3, pp. 1–3, Ministry of Transport, Yokosuka, Japan, 1970.

## References

- [1] W. H. Perloff, *Soil Mechanics, Principal and Applications*, John Wiley & Sons, New York, NY, USA, 1976.

## Research Article

# Facile Solventless Synthesis of a Nylon-6,6/Silver Nanoparticles Composite and Its XPS Study

Raúl A. Morales-Luckie,<sup>1</sup> Víctor Sánchez-Mendieta,<sup>2</sup> Oscar Olea-Mejía,<sup>1</sup>  
Alfredo R. Vilchis-Nestor,<sup>1</sup> Gustavo López-Téllez,<sup>1</sup> Víctor Varela-Guerrero,<sup>1</sup>  
L. Huerta,<sup>3</sup> and Jesús Arenas-Alatorre<sup>4</sup>

<sup>1</sup> Centro Conjunto de Investigación en Química Sustentable UAEM-UNAM (CCIQS), Facultad de Química, Universidad Autónoma del Estado de México, Km. 14.5 de la carretera Toluca-Atlacomulco, 50200 San Cayetano, MEX, Mexico

<sup>2</sup> Facultad de Química, Universidad Autónoma del Estado de México, Paseo Colón y Paseo Tollocan, 50120 Toluca, MEX, Mexico

<sup>3</sup> Instituto de Investigaciones en Materiales, Universidad Nacional Autónoma de México, Apartado Postal 70-360, 04510 México, DF, Mexico

<sup>4</sup> Instituto de Física, Universidad Nacional Autónoma de México, Apartado Postal 20-364, 01000 México, DF, Mexico

Correspondence should be addressed to Víctor Sánchez-Mendieta; [vsanchezm@uaemex.mx](mailto:vsanchezm@uaemex.mx)

Received 14 February 2013; Revised 22 April 2013; Accepted 9 May 2013

Academic Editor: Carmina Menchaca-Campos

Copyright © 2013 Raúl A. Morales-Luckie et al. This is an open access article distributed under the Creative Commons Attribution License, which permits unrestricted use, distribution, and reproduction in any medium, provided the original work is properly cited.

Silver nanoparticles were synthesized and supported on thin nylon membranes by means of a simple method of impregnation and chemical reduction of Ag ions at ambient conditions. Particles of less than 10 nm were obtained using this methodology, in which the nylon fibers behave as constrained nanoreactors. Pores on nylon fibres along with oxygen and nitrogen from amide moieties in nylon provide effective sites for *in situ* reduction of silver ions and for the formation and stabilization of Ag nanoparticles. Transmission electron microscopy (TEM) analysis showed that silver nanoparticles are well dispersed throughout the nylon fibers. Furthermore, an interaction between nitrogen of amides moieties of nylon-6,6 and silver nanoparticles has been found by X-ray photoelectron spectroscopy (XPS).

## 1. Introduction

Research on the synthesis of mesoporous materials containing nanoparticles represents a fast-developing area of nanoscience and nanotechnology. This interest is stimulated by several possible application areas of these materials including catalytic [1], magnetic [2], and optoelectronic [3, 4]. Metal nanoparticles dispersed in polymeric matrixes have recently been the subject of intense study aiming to develop nanocomposite films [5–8]. General approaches for the synthesis and support of nanoparticles inside porous materials include impregnation [9] and deposition-precipitation [10]. A drawback of this nanocomposites is the difficulty to disperse nanoparticles in most systems [11]; hence one potential advantage of such metal/polymer systems is that the size and distribution of dispersed metal nanoparticles can be readily controlled based on the properties of the host polymer [12, 13].

Silver particles with a narrow size distribution have been produced upon reversible chemical transformation between metallic and oxide states in a titania matrix [14] and in a mesoporous silica which was grafted with hydrophobic  $-\text{Si}(\text{CH}_3)_3$  groups at the pore surface [15].

Nylon is an electron-rich and polar synthetic polymer (polyamide) usually made from the monomers adipoyl chloride and hexamethylene diamine to form a linear molecular chain (Figure 1). Synthetic nylon membranes have a porous structure [16] and are composed of microfibrils that are interconnected forming a three-dimensional network. Such morphological features provide a unique reaction vessel for synthesizing and supporting metal nanoparticles, allowing enhanced access of guest molecules to catalytic centres, compared with nonporous films.

In this work, a facile synthesis of silver nanoparticles of less than 10 nm in diameter with a narrow size distribution,



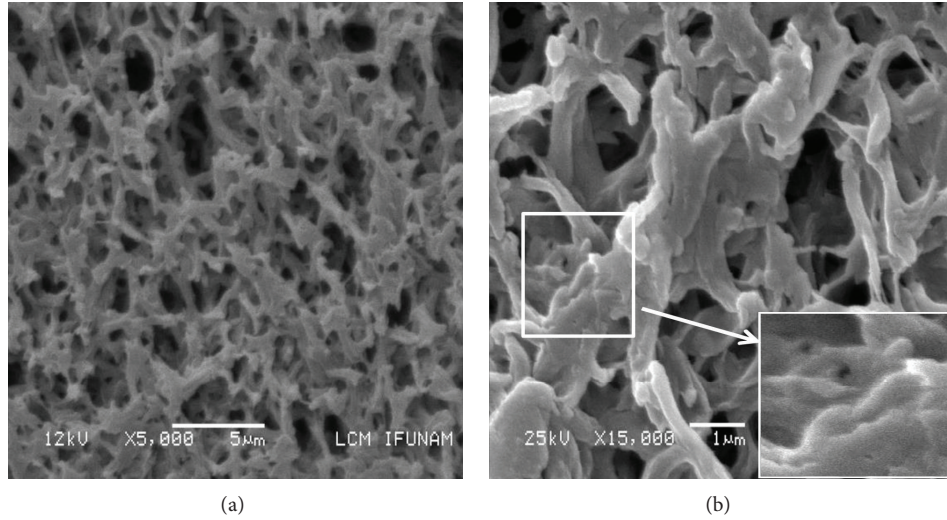


FIGURE 2: SEM image of the nylon-6,6 membrane.

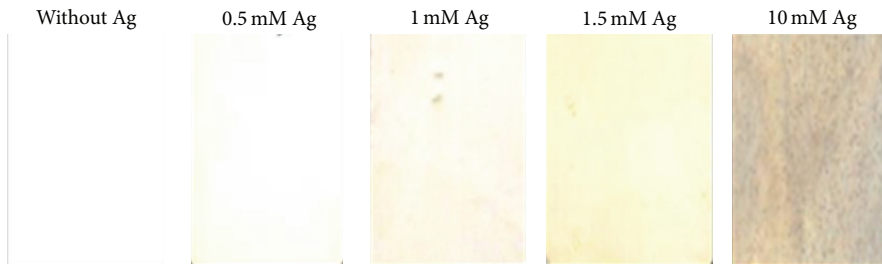


FIGURE 3: Nylon-6,6 without and with Ag nanoparticles formed at different AgNO<sub>3</sub> concentrations.

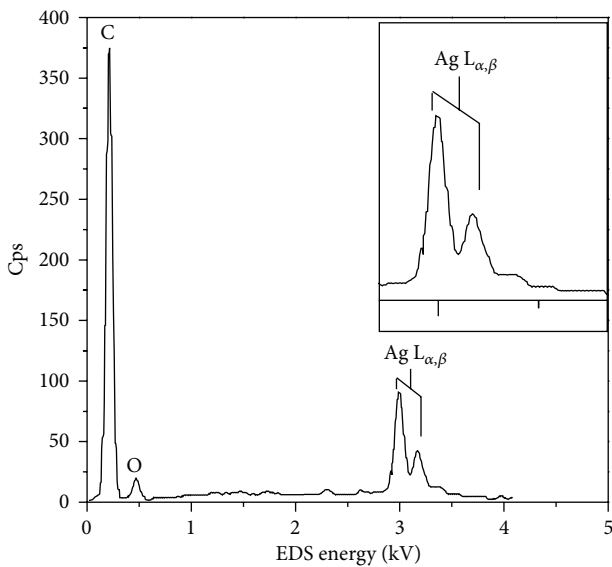


FIGURE 4: EDX spectrum of nylon-6,6 membrane coated with Ag nanoparticles.

located at 390 nm (Figure 5(a)); this is attributable to the surface plasmon resonance of silver nanoparticles in agreement with the observed yellow colour showed in Figure 3 [19]. No absorption was observed at wavelengths longer than 450 nm. These observations imply that Ag nanoparticles were formed. The surface plasmon peak underwent a shift to

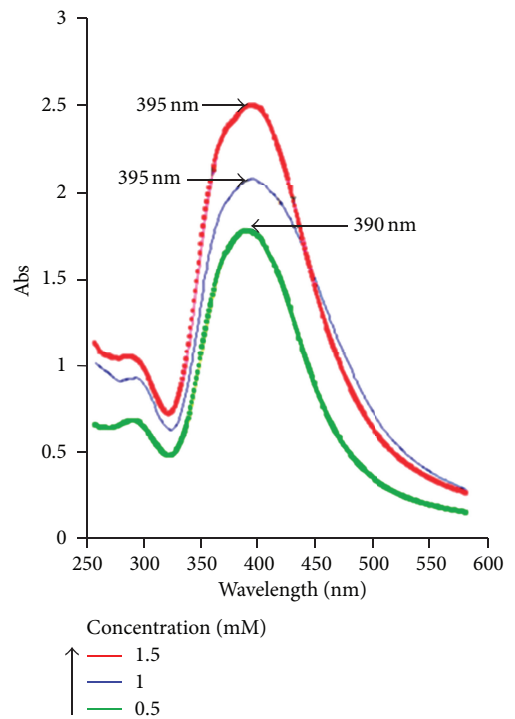


FIGURE 5: UV-Vis spectra of silver nanoparticles in nylon-6,6 membranes. Nanoparticles were prepared using aqueous AgNO<sub>3</sub> at 0.5 mM, 1.0 mM, and 1.5 mM, respectively.

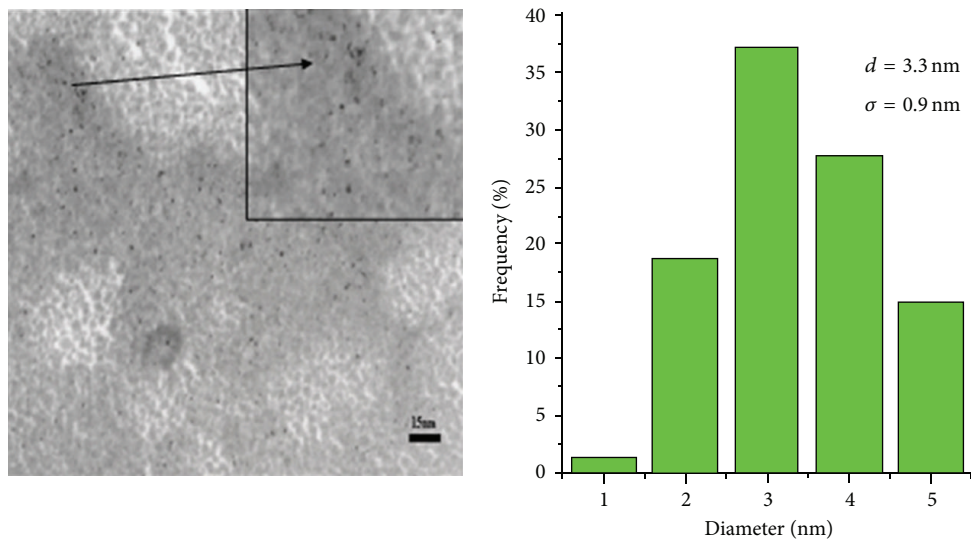


FIGURE 6: TEM micrograph and size distribution histogram of Ag nanoparticles in nylon-6,6 membranes ( $\text{AgNO}_3$  0.05 mM).

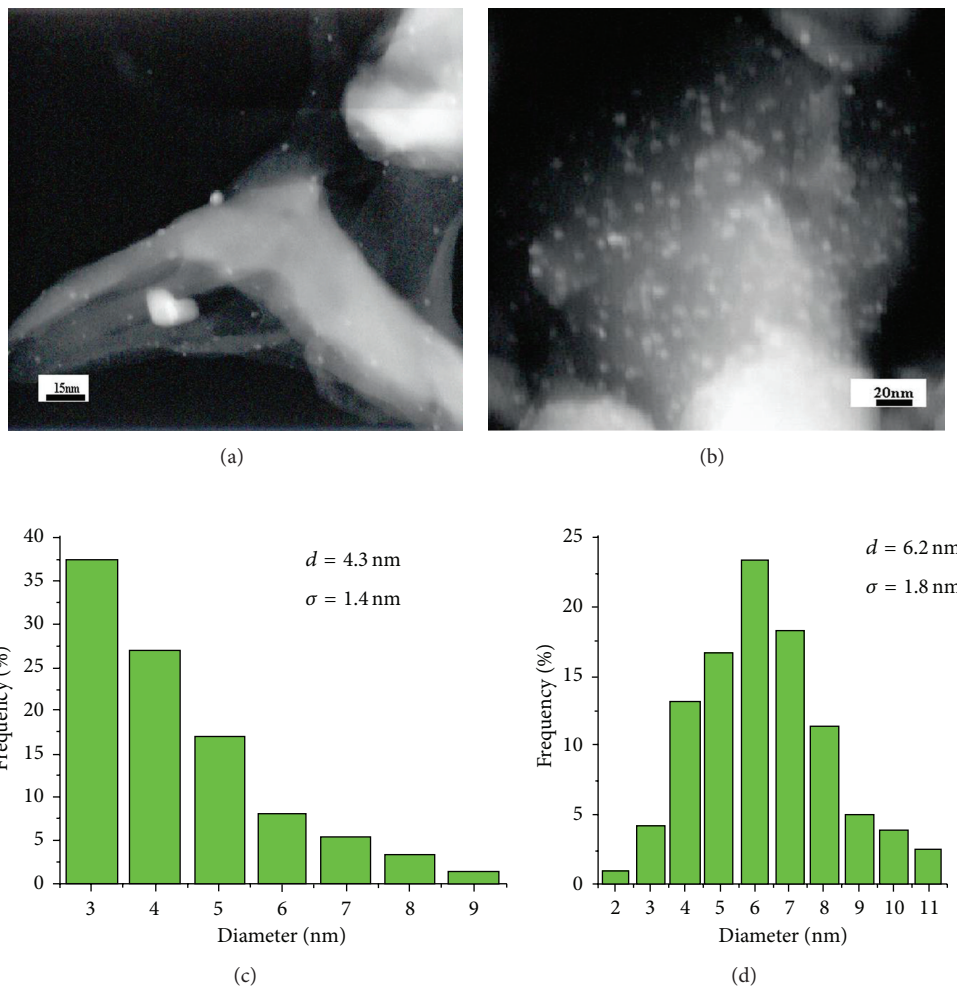


FIGURE 7: HAADF images and size distribution of Ag nanoparticles obtained from (a), (c)  $\text{AgNO}_3$  1.0 mM; (b), (d)  $\text{AgNO}_3$  1.5 mM.

395 nm and was slightly broadened when 1 mM  $\text{AgNO}_3$  was employed (Figure 5(b)). When 1.5 mM  $\text{AgNO}_3$  was used, the surface plasmon absorption becomes broader (Figure 5(c)). It is noted that the absorption intensity of the plasmon band increases as the concentration of aqueous  $\text{AgNO}_3$  augments, also in agreement with the membrane intensity changes in colour, which can be attributed to the increase in the Ag nanoparticles concentration.

These assumptions are confirmed by TEM observations. As shown in Figure 6 monodisperse Ag nanoparticles were obtained at  $\text{AgNO}_3$  0.5 mM. Their mean diameter ( $d$ ) was measured as 3.3 nm with a standard deviation ( $\sigma$ ) of 0.9 nm.

Figure 7 shows Z-contrast images of nylon fibres with Ag particles. Figures 7(a) and 7(c) correspond to a concentration of 1.0 mM of  $\text{AgNO}_3$  resulting in nanoparticles with an average size of 4.3 nm with a standard deviation of 1.4 nm. Using a solution of 1.5 mM  $\text{AgNO}_3$  (Figures 7(b) and 7(d)), the average particle size slightly increases to 6.2 nm with a standard deviation of 1.8 nm. Therefore, it is possible to control the size and size distribution by adjusting the concentration of metal ions in solution.

Because of the porous structure of nylon fibre and the strong interactions between  $\text{Ag}^+$  ions and the carbonyl and amide groups of nylon macromolecule,  $\text{Ag}^+$  ions were uniformly and tightly anchored to the nylon fibres [20]. Such interactions would lower the mobility of  $\text{Ag}^+$  ions, enhance the formation of silver nuclei, limit the formation of several morphologies, and prevent the growth of larger particles [21]. This is particularly true at low  $\text{Ag}^+$  ion concentrations and can explain the formation of monodisperse Ag nanoparticles (after  $\text{NaBH}_4$  reduction) under such conditions. At higher  $\text{AgNO}_3$  concentrations, larger amounts of  $\text{Ag}^+$  ions are embedded on nylon membranes, leading to large and widely distributed particles after reduction [22]. In these kinds of systems, it is expected that the carbonyl and amide groups may also play an important role in stabilization of metal nanoparticles in addition to the porous structure of nylon fibres.

The HRTEM image in Figure 8 shows Ag nanoparticles between 2 and 3 nm in diameter. This image possesses atomic resolution; therefore, several crystalline planes are distinguishable and the interplanar distances can be measured. The interplanar distances shown in the micrograph were measured from the Fourier transforms (FFT) of these nanoparticles (Figure 8, bottom), where the corresponding crystalline planes are specified. The interplanar distances and their corresponding crystalline planes match the ones of metallic Ag (FCC) phase. The measured interplanar distance is 2.36 Å and corresponds to the (111) plane [23].

In order to examine the chemical composition of the nylon-6,6/Ag nanoparticles fibre composite, as well as the possible interaction of silver metal with the nylon moieties, after formation of Ag nanoparticles, X-ray photoelectronic spectroscopy (XPS) was used. Figure 9 shows the XPS survey spectra obtained after  $\text{Ar}^+$  etching for 10 s.

Figure 9 shows the increase in the Ag 3d signal corresponding to the different concentrations of  $\text{AgNO}_3$  added in the solution reaction; a spectrum of nylon-6,6 is used as reference. Clearly an increase of the concentration of

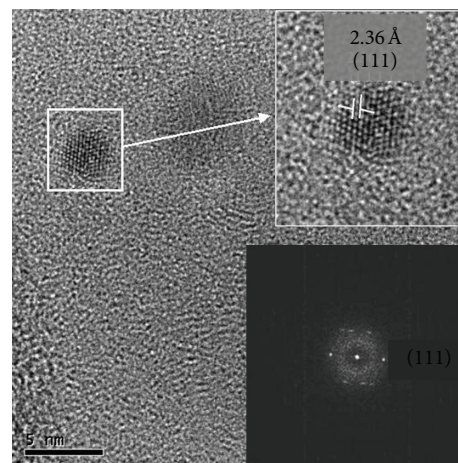


FIGURE 8: HRTEM image of Ag nanoparticles (top) and their corresponding Fourier transforms (FFT) (bottom) pattern.

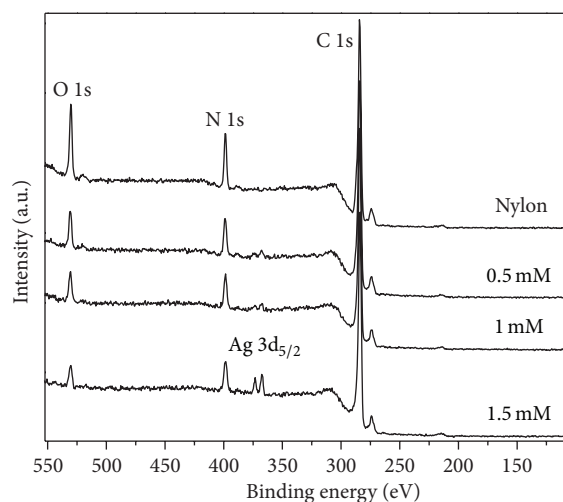


FIGURE 9: XPS spectra of nylon-6,6 and three different nylon-6,6/Ag composites.

the metal precursor salt favours the formation of the nylon/Ag composite.

In order to obtain more information about the chemical state of the Ag nanoparticles present in the composite a curve fit of the various signals was made and is shown in Figure 10.

Table 1 shows the binding energies of the XPS deconvolution of Ag 3d, C 1s, O 1s, and N 1s core levels samples with the Ag metallic, AgO, and nylon-6,6 as references. The peak energy position in the deconvolution and number of peaks were based in data reported by Beamson and Briggs [24] and Hoflund and Hazos [25] and calibrated with metallic Ag foil as reference.

From Table 1, a positive chemical shift in N 1s core level and negative chemical shift in Ag 3d<sub>5/2</sub> of Ag(0) of nanoparticles, with respect to N 1s and Ag 3d<sub>5/2</sub> of nylon and Ag metallic, are observed. From the data in Table 1 the general rule based on the electronegativity can explain both the positive chemical shift of the N 1s core level and the negative chemical shift of the Ag 3d<sub>5/2</sub> core level. This effect can be seen

TABLE I: The binding energy position by XPS of nylon-6,6- and Ag-containing samples core levels Ag 3d, C 1s, O 1s, and N 1s.

Sample	N 1s	O 1s		Ag 3d <sub>5/2</sub>		*C 1s			
		O=C	O-Ag	Ag	AgO (eV)	1	2	3	4
References*	398.69	530.33		368.21					
0.5 mM	398.91	530.33	531.30						
1.0 mM	398.80	530.33	531.30	368.20	367.31	283.84	284.14	285.00	286.81
1.5 mM	398.75	530.33	531.30						

\*References: nylon and metallic Ag.

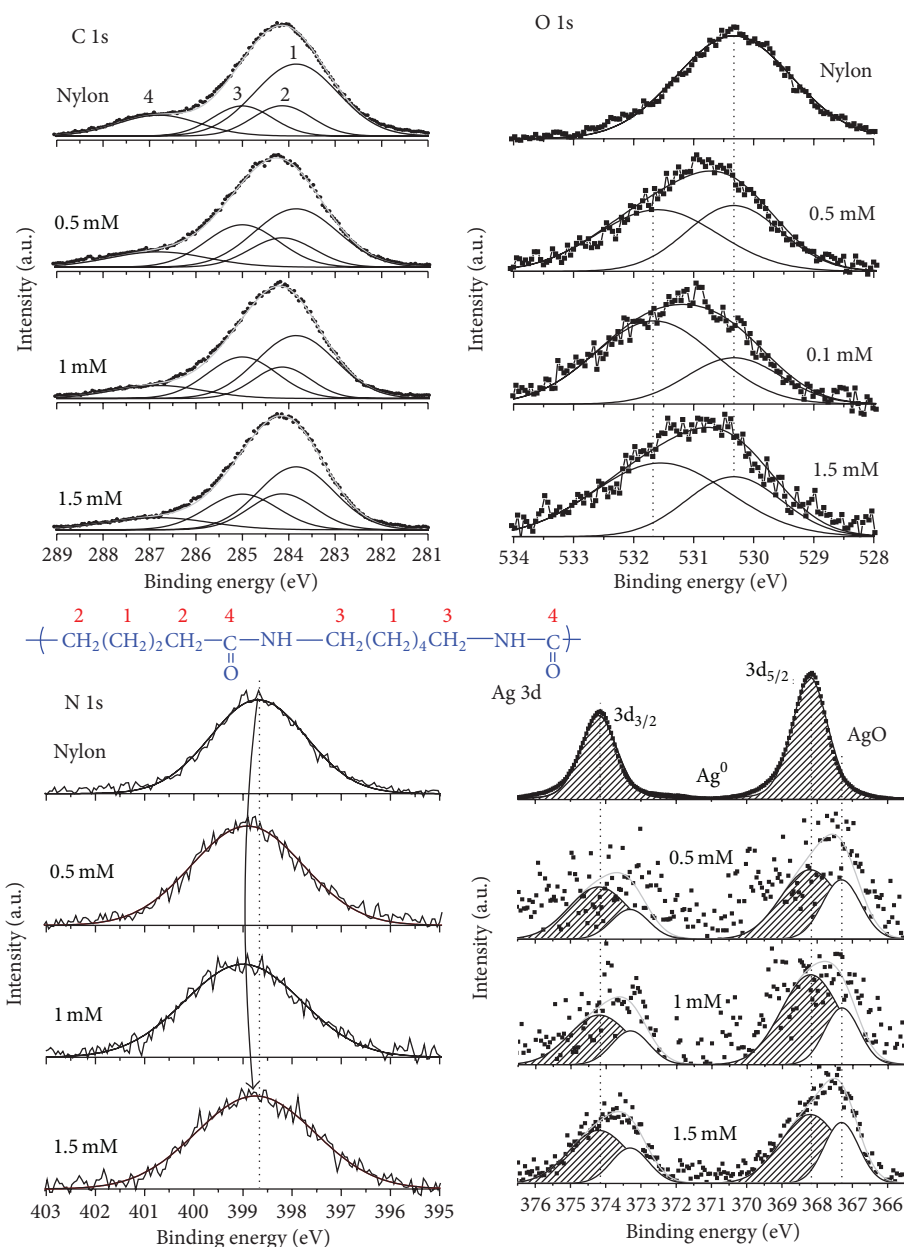


FIGURE 10: The XPS deconvolution for C 1s, O 1s, N 1s, and Ag 3d core levels.

in Figure 10 for N 1s. For the composite samples analysed, all C 1s, O 1s, and Ag 3d<sub>5/2</sub> of AgO core levels are in the same positions as exhibited in Table I and Figure 10. O 1s (530.33 eV) corresponds to O=C and Ag-O at 367.31 eV; C 1s corresponds to (1) C-CH<sub>2</sub> at 283.84 eV, (2) CH<sub>2</sub>-CH<sub>2</sub> at

284.14 eV, (3) CH<sub>2</sub>-N at 285 eV, and (4) C=O at 286.81 eV. It can be also observed that for N 1s the maximum shifting ( $\Delta$ ) occurs for the 0.5 mM simple with  $\Delta = 0.22$  eV; however, for 0.1 mM sample,  $\Delta = 0.11$ , it contains the largest amount of Ag nanoparticles, taking in account the amount

of AgO. For the 1.5 mM sample, Ag 3d peaks can be deconvoluted satisfactorily obtaining thus all oxidation states even in the samples with less Ag concentration. In addition, in Figure 10, the data obtained from the curve fitting show that there is no change in the binding energy of the orbitals of C 1s despite the use of different AgNO<sub>3</sub> concentrations. There is, however, a 0.31 eV shift in the N 1s peak corresponding to the sample with 1.5 mM AgNO<sub>3</sub>. This small shift in binding energy suggests there is an interaction of the nitrogen atoms in nylon during the stabilization of the silver nanoparticles. A similar chemical shift for N 1s binding energy in XPS spectra has been observed for the interactions of PVP with Pt nanoparticles and nitrocellulose with Ru [26, 27]. Hence, pores of nylon fibers, where the nitrogen atoms from the amide groups are found, not only interact with the metal ions presumably through ion-dipole forces, but once the reduction reaction occurs, they also stabilize the Ag nanoparticles. Analysis of the O 1s and Ag 3d<sub>5/2</sub> peaks shows the presence of AgO, which was expected due to the high reactivity of the silver nanoparticles at the sizes obtained. Nevertheless, the fact that there is still a signal corresponding to Ag<sup>0</sup> suggests that the oxidation takes place only on the surface of the nanoparticles, while metallic silver remains at their core; again this is possible due to the stabilizing effect of the amide groups present in the nylon fibers. This nylon-6,6/Ag nanoparticles composite will be probed in dyes removal from aqueous solutions and in applications regarding its antibacterial properties.

#### 4. Conclusions

It was demonstrated that using an aqueous Ag ion impregnation of nylon fibres followed by a reduction with NaBH<sub>4</sub>, a composite of Ag nanoparticles attached to the polymer can be formed. The whole process is carried out at ambient conditions. SEM, HRTEM, and XPS studies confirmed the presence of such Ag nanoparticles in the fibres, with an average size of 3.3 nm. This very simple and versatile synthetic route could be applied to obtain other composites made of metal nanoparticles and natural or synthetic polymer fibres. Moreover, an interaction between nitrogen of amides moieties of nylon-6,6 and silver nanoparticles has been found by X-ray photoelectron spectroscopy.

#### Acknowledgments

Financial support of this work was provided by Universidad Autónoma del Estado de México (UAEM) (Project no. 3246/2012U). The authors are indebted to Fernando Ureña (ININ), Samuel Tehuacanero (IFUNAM) for their assistance in SEM and image digitalisation, respectively.

#### References

- [1] J. Y. Ying, C. P. Mehert, and M. S. Wong, "Synthesis and applications of supramolecular-templated mesoporous materials," *Angewandte Chemie*, vol. 38, no. 1-2, pp. 56-77, 1999.
- [2] M. S. Morey, J. D. Bryan, S. Schartz, and G. D. Stucky, "Pore surface functionalization of MCM-48 mesoporous silica with tungsten and molybdenum metal centers: perspectives on catalytic peroxide activation," *Chemistry of Materials*, vol. 12, no. 11, pp. 3435-3444, 2000.
- [3] J. Liu, X. Feng, G. E. Fryxell, L. Wang, A. Y. Kim, and M. Gong, "Hybrid mesoporous materials with functionalized monolayers," *Advanced Materials*, vol. 10, no. 2, pp. 161-165, 1998.
- [4] J. J. Schneider, N. Czap, J. Hagen et al., "Metallorganic routes to nanoscale iron and titanium oxide particles encapsulated in mesoporous alumina: formation, physical properties, and chemical reactivity," *Chemistry*, vol. 6, no. 23, pp. 4305-4321, 2000.
- [5] J. S. Jung, W. S. Chae, R. A. McIntyre, C. T. Selp, J. B. Wiley, and C. J. O'Connor, "Preparation and characterization of Ni nanoparticles in an MCM mesoporous material," *Materials Research Bulletin*, vol. 34, no. 9, pp. 1353-1360, 1999.
- [6] K. Moller and T. Bein, "Inclusion chemistry in periodic mesoporous hosts," *Chemistry of Materials*, vol. 10, no. 10, pp. 2950-2963, 1998.
- [7] H. Shi, L. Zhang, and W. Cal, "Composition modulation of optical absorption in Ag<sub>x</sub>Au<sub>1-x</sub> alloy nanocrystals *in situ* formed within pores of mesoporous silica," *Journal of Applied Physics*, vol. 87, no. 3, p. 1572, 2000.
- [8] K. W. Powers and L. L. Hench, "The effect of pore size on metal cluster formation in silica sol gel monoliths," *Ceramic Transactions*, vol. 101, p. 253, 2000.
- [9] Y. Plyuto, J. M. Berquer, C. Jaquiod, and C. Ricolleau, "Ag nanoparticles synthesised in template-structured mesoporous silica films on a glass substrate," *Chemical Communications*, no. 17, pp. 1653-1654, 1999.
- [10] W. H. Zhang, J. L. Shi, L. Z. Wang, and D. S. Yan, "Preparation and characterization of ZnO clusters inside mesoporous silica," *Chemistry of Materials*, vol. 12, no. 5, pp. 1408-1413, 2000.
- [11] B. Lebeau, C. E. Fowler, S. Mann, C. Farcet, B. Charleux, and C. Sanchez, "Synthesis of hierarchically ordered dye-functionalised mesoporous silica with macroporous architecture by dual templating," *Journal of Materials Chemistry*, vol. 10, no. 9, pp. 2105-2108, 2000.
- [12] L. Zhang, T. Sun, and J. Y. Ying, "Oxidation catalysis over functionalized metalloporphyrins fixated within ultralarge-pore transition metal-doped silicate supports," *Chemical Communications*, no. 12, pp. 1103-1104, 1999.
- [13] V. L. Colvin, M. C. Schlamp, and A. P. Alivisatos, "Light-emitting diodes made from cadmium selenide nanocrystals and a semiconducting polymer," *Nature*, vol. 370, no. 6488, pp. 354-357, 1994.
- [14] B. O. Dabbousi, M. G. Bawendi, O. Onitsuka, and M. F. Rubner, "Electroluminescence from CdSe quantum-dot/polymer composites," *Applied Physics Letters*, vol. 99, p. 13834, 1995.
- [15] R. Lamber, S. Wetjen, G. Schulz-Ekloff, and A. Baalmann, "Metal clusters in plasma polymer matrices: gold clusters," *Journal of Physical Chemistry*, vol. 99, no. 38, pp. 13834-13838, 1995.
- [16] L. L. Beecroft and C. K. Ober, "Nanocomposite materials for optical applications," *Chemistry of Materials*, vol. 9, no. 6, pp. 1302-1317, 1997.
- [17] K. Akamatsu, N. Tsuboi, Y. Hatakenaka, and S. Deki, "In situ spectroscopic and microscopic study on dispersion of Ag nanoparticles in polymer thin films," *Journal of Physical Chemistry B*, vol. 104, no. 44, pp. 10168-10173, 2000.
- [18] SDP v4. 1 (32 bit) Copyright 2004, XPS International, LLC, Compiled January 17, 2004.

- [19] J. He, I. Ichinose, T. Kunitake, and A. Nakao, "Reversible conversion of nanoparticles of metallic silver and silver oxide in ultrathin TiO<sub>2</sub> films: a chemical transformation in nano-space," *Chemical Communications*, no. 17, pp. 1910–1911, 2002.
- [20] S. Besson, T. Gacoin, C. Ricolleau, and J. Boilot, "Silver nanoparticle growth in 3D-hexagonal mesoporous silica films," *Chemical Communications*, vol. 9, no. 3, pp. 360–361, 2003.
- [21] T. M. Fahmy, P. M. Fong, A. Goyal, and W. M. Saltzman, "Targeted for drug delivery," *Nanotoday*, vol. 8, no. 8, pp. 18–26, 2005.
- [22] J. He, I. Ichinose, T. Kunitake, A. Nakao, Y. Shiraishi, and N. Toshima, "Facile fabrication of Ag-Pd bimetallic nanoparticles in ultrathin TiO<sub>2</sub>-gel films: nanoparticle morphology and catalytic activity," *Journal of the American Chemical Society*, vol. 125, no. 36, pp. 11034–11040, 2003.
- [23] W. J. de Ruijter, R. Sharma, M. R. McCartney, and D. J. Smith, "Measurement of lattice-fringe vectors from digital HREM images: experimental precision," *Ultramicroscopy*, vol. 57, no. 4, pp. 409–422, 1995.
- [24] G. Beamson and D. Briggs, *High Resolution XPS of Organic Polymers*, John Wiley & Sons, Chichester, UK, 1992.
- [25] G. B. Hoflund and Z. F. Hazos, "Surface characterization study of Ag, AgO, and Ag<sub>2</sub>O using x-ray photoelectron spectroscopy and electron energy-loss spectroscopy," *Physical Review B*, vol. 62, no. 16, pp. 11126–11133, 2000.
- [26] L. Qiu, F. Liu, L. Zhao, W. Yang, and J. Yao, "Evidence of a unique electron donor—acceptor property for platinum nanoparticles as studied by XPS," *Langmuir*, vol. 22, no. 10, pp. 4480–4482, 2006.
- [27] V. K. Kaushik, "XPS core level spectra and Auger parameters for some silver compounds," *Journal of Electron Spectroscopy and Related Phenomena*, vol. 56, no. 3, pp. 273–277, 1991.

## Research Article

# Comparison of Cement-Based and Polymer-Based Concrete Pipes for Analysis of Cost Assessment

Orhan Bozkurt<sup>1</sup> and Mehmet İslamoğlu<sup>2</sup>

<sup>1</sup> *Inegol Faculty of Business, Uludag University, 16400 Bursa, Turkey*

<sup>2</sup> *Economics Department, Bartın University, 74100 Bartın, Turkey*

Correspondence should be addressed to Orhan Bozkurt; obozkurt@uludag.edu.tr

Received 28 March 2013; Accepted 8 May 2013

Academic Editor: Osman Gencil

Copyright © 2013 O. Bozkurt and M. İslamoğlu. This is an open access article distributed under the Creative Commons Attribution License, which permits unrestricted use, distribution, and reproduction in any medium, provided the original work is properly cited.

As the variety of materials utilized in construction industry has expanded, new techniques have been used in order to optimize the quality and efficiency of output. Therefore, recent innovations taking place in the construction industry led researchers to increase the mechanical efficiency of the output more than the cost effectiveness of it. However, especially professionals experiencing in the industry look into the cost effectiveness of the work. In other words, they also want researchers to justify the innovative techniques economically. The aim of this study is to provide a comparative analysis of the cost efficiency of polymer concrete used to manufacture durable and long-lasting reinforced concrete structures.

## 1. Introduction

Concretes are the most widely used construction materials in the world; a large variety of concretes are based on a variety of cements [1]. Low costs, ease of application, and high compressive strength are the main factors to be considered for a given application. Inorganic (mineral) concrete based on the Portland cement has shortcomings: poor flexural strength, low tensile strength, high porosity, freeze thaw deterioration, destruction by corrosive chemicals, and so forth [2]. These shortcomings are viewed as more and more acute since we have become more and more concerned with conservation of energy and materials. One approach is based on a combination of technologies of concrete and that of polymers. Thus, polymer concrete (PC) materials have become a viable choice for the civil construction sector in developed countries, particularly in applications such as making reinforced slabs, overlays for highway pavements, bridge decks, retaining walls, water tanks, and pipe lines, PCs are also used in repairing deteriorated mineral concretes (Portland cement concrete) in situations when high strength, fast cure, and durability are required [3]. Polymer concretes are composites in which the aggregates are bound together in a polymer matrix. They do not contain Portland cement.

Underground pipe systems have presented to improve human beings' standard of living since the dawn of civilization. Concrete pipes are frequently used in sewerage and storm water systems, under and over ground irrigation facilities, water transmission lines, water tanks, water towers, pumping lines, pumping stations, and water structures, such as tunnels. These concrete pipes are exposed to various harmful effects during their service life. However, factors leading to deterioration in cement-based concrete pipes may originate from physical, chemical, mechanical, or biological effects. Impact, wear, and erosion are some damages that occur mechanically. Chemical effects might occur, due to harmful substances leaking into the concrete or materials used in concrete production, as well. Common chemical effects are alkali-silica reactions, sulfate attacks, carbonation, corrosion, acid, and salt. Physical causes of deterioration are freeze-thaw, solvent salts, high temperatures, and so on [4].

Studies have been carried out to make more durable concrete pipes and prevent the aforementioned harmful effects since concrete pipes have been widely utilized for managing storm water, sewage, and drainage for more than a century as mentioned before. Deterioration of concrete pipes constitutes a serious problem to society. It has been reported that annual maintenance and repair costs of deteriorated concrete pipes

in Canada in the early 1990s were approximately \$2.5 billion dollars [6].

There are many types of piping materials in the construction sector today, ranging from rigid concrete to flexible thermal plastic. Pipes must have adequate strength and/or stiffness to perform their intended function. They must also be durable enough to last for their lifetime. With the usage of polymers in concrete technology, the concrete nature has increased significantly. Many important changes have occurred regarding the utilization of polymer in concrete technology, and presently the researches about polymer composites still continue. Typically polymer concrete has a longer maintenance-free service life than Portland cement concrete and possesses also other advantages compared to Portland cement concrete such as increased bond strength (bonding to previously existing concrete); increased freeze-thaw resistance; high abrasion resistance; increased flexural, compressive and tensile strengths; fast setting times (curing within 1 or 2 h); good durability; improved chemical resistance in harsh environments. Moreover, they exhibit good creep resistance and are highly UV resistant due to the very low polymer content and inert fillers. On the other hand, they exhibit reduced elastic modulus. The loss of strength can be attributed to an increase of porosity in polymer concrete with increased capillary diffusion of solutions, which weakens the bond between the aggregate and the matrix [3]. As clearly understood here, to decrease repair cost and to increase service life of pipes, polymer composites present a perfect choice.

A study was conducted in order to predict the remaining lifetime of preset pipes. In the study, four different used polyethylene pipes for gas and water supply with an age of up to more than 30 years have been investigated with respect to molecular and morphological changes. The molecular analysis did not show any significant polymer degradation as an indication of ageing of the materials [7].

In this study, cost analyses of cement-based concrete pipes and polymer concrete pipes were evaluated.

## 2. Methods of Calculating Manufacturing Cost

Nowadays, the calculation of the manufacturing cost gained an increasing importance. Cost saving will have a significant positive impact on decrease of firm costs and increase profitability [8]. The knowledge related to the unit cost determines the level of the price quote. Being able to offer a good price quote depends on the knowledge about the cost structure of the products. Therefore, the costs should be calculated accurately and the accounting should be done correctly. In management, the costs are generally composed of direct labor (55%), raw materials (35%), and manufacturing overheads (10%) [9]. The manufacturing overheads in the construction businesses are usually at this level. Direct labour cost forms the largest part of the total costs. Labor costs affect the profitability of a company [10]. The use of good quality products in order to diminish these costs may be considered as a solution for decreasing the total cost. While the use of high-quality products does not increase the construction costs, it ensures the fall of the cost in general by reinforcing the construction resistance [11].

Due to maintenance and repair costs being in excess in the construction businesses, it becomes a requirement to use more resistant raw material and auxiliary material. To protect concrete structures from physical, chemical, or biological degradation and increase their durability, high performance protective surface coating materials can be used [12].

All the motives suggest the calculation and the accounting of the costs to be done in a more accurate way. Otherwise, these costs might cause financial capital loss by increasing over time [13]. While the cost accounting is used in the cost calculation of the produced goods and services; it creates some effects in the management decisions and makes contributions for offering price quotes. In Turkey, the uniform cost accounting implementers have been organized in 1989 by the Professional Law number 3568. The general communiqué on accounting system application of December 26, 1992, has come into effect legally in January the 1st, 1994. It is required through the communiqué to declare the accounts as 1–9 kinds of expenses and 10–99 kinds of revenues. Furthermore, in application of cost accounting, new approaches such as 7/A and 7/B options have been introduced [14].

The construction activities last usually longer than one year. The construction activities are varied and have different features. In the determination of loss and profit in the construction businesses, it is waited in order to have the job achieved or the loss or profit is calculated as estimation at the end of every period. In the construction sector, the full cost method based on orders is usually applied. In this method through which all of the production expenses within the period are ascribed to the production cost, the product cost is composed of all of the production expenses. Pursuant to this, the total of the direct raw materials and supplies expenses, direct labor expenses, variable production overheads and fixed production overheads, give the “full cost” [15].

In the construction activities, the start-up expenses are important elements of the cost. These expenses are present particularly during the foundation stage. The use of non-durable materials and the repair and maintenance expenses in a short time decrease the return on capital. Meanwhile, it extends the return time of the investments. Furthermore, the increase of labor and material expenses at every stage of repair and maintenance suggests the requirement for more resistant products to be used in the construction businesses. Exactly at this point, the use of polymer concrete technology in manufacturing process becomes a crucial part of the activity. This method while enabling the construction resistance on the one hand, decreases the repair, maintenance, and labor expenses on the other hand. In Figure 1, below the cost elements are shown in total.

According to the Tax Procedure Law number 315, taxpayers will declare their assets subject to amortization with respect to rates announced by Ministry of Finance of the Republic of Turkey. In determining the rates of economic assets to be declared, their estimated service lives are taken into account. In accordance with Tax Procedure Law number 315, Communiqués 333, 339, and 365 are published which are related to amortization periods or service life of tangible assets subject to amortization or depreciation [16]. Communiqué 333 on Tax Procedure Law number 315 under the title

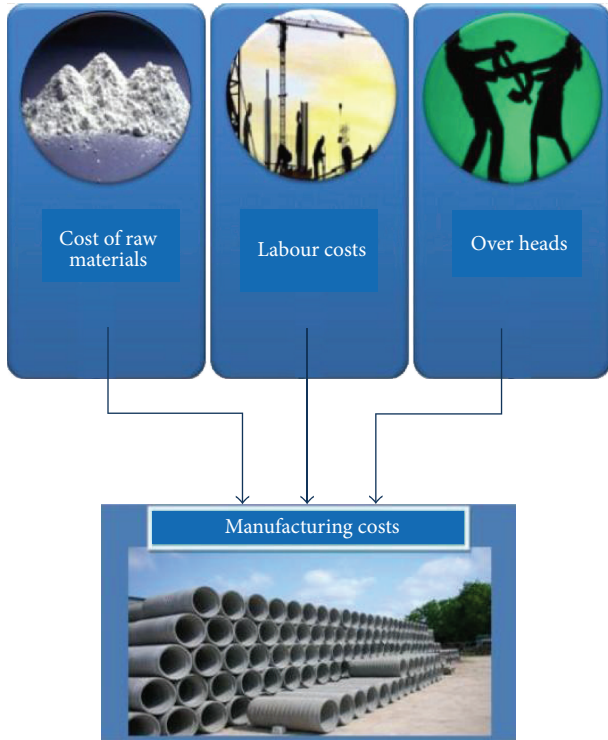


FIGURE 1: Cost of manufacturing process in construction industry.

of Plant and Land Regulations introduces service life of cement-based retrieval systems and pipes used for sewers and other supplementary materials as 15 years and orders amortization of said assets during this period. When cement-based concrete pipes have an average of 15 years of service life, it is well known that polymer-based concrete pipes are designed for a service life longer than 50 years.

### 3. Formulations

In polymer concrete manufacture,  $PC_t$  requires care in the casting process, attention to curing temperature, composition, and careful choice in type of resins and aggregates. The latter involve several linked characteristics: specific area, interfaces with the matrix, strength and deformability, shape, and size. For example, aggregates with irregular shapes and high surface area improve the anchorage with the matrix. The proportion of thermosetting resin to aggregate as well as different types of aggregate varies in different formulations of  $PC_t$ . In principle, the mix design of  $PC_t$  typically involves an aggregate size gradation to provide the lowest possible void volume that will require the minimum polymeric binder concentration necessary to coat the aggregates and to fill the voids [3]. Several different formulations for polymer concretes are presented in Table 1.

In Portland cement concrete production, the used materials are Portland cement (generally CEM I 42.5), aggregates, water, and additives.

Portland cement concrete mixture proportion for pipe is presented in Table 2. Detailed production procedure has been reported in the literature [4, 6, 17–19].

TABLE 1: Several different formulations [3].

Epoxy resin (wt.%)	Polyester resin (wt.%)	Sand (wt.%)	Catalyst (MEKP) (wt.%)
20.0	—	78.5	1.5
20.0	—	78.0	2.0
—	10.0	88.5	1.5
—	15.0	83.5	1.5
—	18.0	80.5	1.5
—	20.0	77.5	2.5
—	20.0	78.0	2.0

## 4. Results and Discussion

**4.1. Cost Assessment of Several Different Polymer- and Cement-Based Concrete Pipes.** In Table 3, diameters, inner and outer wall thickness, and length and weight specifications are given for the different sizes of polymer-based and cement-based concrete pipes. In the table, when PP denotes polymer-based concrete pipes, CP represents the cement-based concrete pipes. In Table 3, polymer- and cement-based concrete pipes existing with a wide range are the types which are commercially sold the most. In the table, first, the prices of all sizes of the pipes are obtained, and then in order to make comparison, for each pipe code, on the basis of meters, unit prices are calculated, and thus normalized prices are found.

**4.2. Comparison of Polymer- and Cement-Based Concrete Pipes in Terms of Cost Effectiveness.** Assuming that PP5-coded polymer-based concrete pipes and CP5-coded cement-based concrete pipes are used for infrastructure work, recognizing that other expenses remains the same and a change in manufacturing conditions is ignored, we implemented a cost comparison for each pipe depending on their market prices shown in Table 3. We prepared two separate tables for each pipe in order to compare their total costs in pursuit of completion of infrastructure work. Much as the initial set-up cost for 1000 units of PP5 and CP5 is \$103000 and \$14000, respectively, the condition is reversed in the long run. According to the obtained results, considering the useful life of polymer-based concrete pipes depending on its technology, costs are notably reduced. Polymer-based technology results in a service life 3.3 times longer than cement-based technology (service life of polymer-based concrete pipes is designed for a period of time no less than 50 years, whereas cement-based concrete pipes have a useful life of 15 year). Regarding the infrastructure work in which polymer-based concrete pipes are used, relying on its longer service life, the labor costs do not repeat as in cement-based concrete technology; therefore, it presents a significant cost advantage. In light of The previously mentioned facts, with the usage of polymer-based concrete pipe as a construction material, it is probable to avoid aforementioned construction costs. Here, longevity of polymer-based concrete pipes is our main motivation for implementing this study.

In Figure 2, it is obvious that labour cost comprises important part of the construction work. Completed units

TABLE 2: Concrete industries mix design (per m<sup>3</sup>).

Sand (kg)	Rock (kg)	Fly Ash (kg)	Cement (kg)	Water (kg)	WRA (L)
1510	448	73.5	294	98.9	7.06

WRA: Water reducing admixture.

TABLE 3: Cost assessment of several different polymer and cement-based concrete pipes.

Codes	Inside diameter, mm	Outside diameter, mm	Wall thickness, mm	Weight, kg/m	Normalized price
PP1	415	427	12	17	46 \$/m
PP2	515	530	15	26	57 \$/m
PP3	615	633	18	35	68 \$/m
PP4	698	718	20	48	88 \$/m
PP5	797	820	23	62	103 \$/m
PP6	1592	1638	46	243	320 \$/m
PP7	2386	2453	67	542	681 \$/m
PP8	2981	3065	84	843	1039 \$/m
PP9	3974	4085	111	1487	1853 \$/m
CP1	150	178	28	49	3 \$/m
CP2	200	236	36	90	4 \$/m
CP3	300	345	45	133	7 \$/m
CP4	400	450	50	200	10 \$/m
CP5	500	565	65	294	14 \$/m
CP6	600	670	70	389	18 \$/m

Work in process		Finished goods	
\$6000	\$343000		
\$103000			
\$198000			
\$36000			
+\$343000		+\$343000	

FIGURE 2: The cost of goods model (adapted from Jackson et al., 2009) [5].

Work in process		Finished goods	
\$46000	\$254000		
\$34300			
\$198000			
\$36000			
+\$254000		+\$254000	

FIGURE 3: The cost of goods model (adapted from Jackson et al., 2009) [5].

related to manufacturing process are recorded in manufacturing accounts. It is seen in the figure that the total cost of manufacturing process adds up to \$343000. As it is shown in Table 5, the total costs incorporate \$6000, the remaining balance from the previous period, \$103000, cost of raw material, \$198000, direct labour cost, and \$36000, manufacturing overheads.

In Figure 3, except for raw materials, we assume that costs of the other elements remain the same as in Figure 2. In Table 6, the total cost of manufacturing process comes to \$254000, and the cost of raw materials used in the process is \$14000. However, the cost of raw materials used seems far lower when compared to polymeric pipes; the service life of polymeric pipes helps to compensate this reverse condition as shown in Table 4. At the same time, longer service life provides a significant savings at direct labour costs and manufacturing overheads including maintenance and repair costs by preventing recurring outlays.

In Table 7 below, the polymer- and cement-based concrete pipes are compared not only regarding their material cost, but they are also assessed by considering the total cost of the whole manufacturing or installation process. For PP5 and CP5-coded pipes which basically fulfill the same functions, taking their service life into account, total annual cost of them is calculated. According to the results, in spite of the high cost of raw materials, if we consider the entire manufacturing process, the installation which is implemented by using polymer technology is around two and a half times lower in cost.

The following equations show us total cost covered for installation process and the proportions of cost elements within installation process:

$$C_t = C_r + C_d + C_m, \quad (1)$$

where  $C_r$  = cost of raw materials and beginning inventory;  $C_d$  = direct labour cost;  $C_m$  = manufacturing overheads;  $C_t$  = total cost per installation process.

TABLE 4: Comparison of polymer and cement-based concrete pipes.

Code	Price, \$	Amount utilized, m	Total cost, \$	Total cost/year	Annual cost
PP5	103	1000	103000	103000/50	2060 \$/year
CP5	14	1000	14000	14000/15	933 \$/year

TABLE 5: Cost of PP5 construction account.

Description	Item	Amount
Work in the beginning of the period	Beginning inventory of	\$6000
Raw materials used	+ Raw material used	\$103000
The amount of direct labor cost incurred	+ Direct Labor	\$198000
Manufacturing overhead incurred	+ Manufacturing overhead	\$36000
The cost of goods manufactured period	= Cost of goods manufactured	= \$343000

TABLE 6: Cost of CP5 construction account.

Description	Item	Amount
Work in the beginning of the period	Beginning inventory of	\$6000
Raw materials used	+ Raw material used	\$14000
The amount of direct labor cost incurred	+ Direct Labor	\$198000
Manufacturing overhead incurred	+ Manufacturing overhead	\$36000
The cost of goods manufactured period	= Cost of goods manufactured	= \$254000

Consider the following:

$$W_t = \left(\frac{C_r}{C_t}\right) + \left(\frac{C_d}{C_t}\right) + \left(\frac{C_m}{C_t}\right) = W_r + W_d + W_m = 1, \quad (2)$$

where  $W_r$  = proportion of cost of raw materials and beginning inventory within total cost of installation process;  $W_d$  = proportion of direct labour cost within total cost of installation process;  $W_m$  = proportion of manufacturing overheads within total cost of installation process;  $W_t$  = proportion of total cost.

By applying the latter formula, we can easily obtain the proportions of cost elements for each installation processes:

$$\begin{aligned} W_{t_{pp5}} &= \left[\frac{103000 + 6000}{343000}\right] + \left[\frac{198000}{343000}\right] + \left[\frac{36000}{343000}\right] \\ &= 32\% + 58\% + 10\% = 1, \\ W_{t_{cp5}} &= \left[\frac{14000 + 6000}{254000}\right] + \left[\frac{198000}{254000}\right] + \left[\frac{36000}{254000}\right] \\ &= 8\% + 78\% + 14\% = 1. \end{aligned} \quad (3)$$

The allocation of annual costs is implemented in accordance with the proportions of cost types within total cost in Table 7. It is apparent that if we consider the long-term

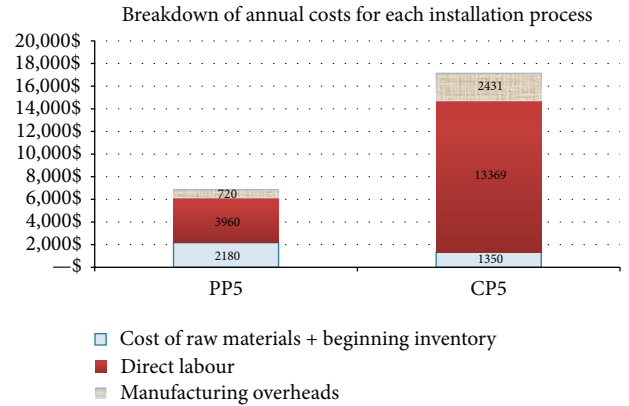


FIGURE 4: Breakdown of annual cost for each installation process using PP5 and CP5-coded pipes.

benefit of the investments, installation implemented by using polymer technology is far more economic than the other choice. In Table 8, the proportions calculated before are used to obtain cost elements per total annual costs for each installation process.

The breakdown of annual cost for each installation process using PP5 and CP5-coded pipes is also displayed in Figure 4.

### 5. Conclusion

Since acquisition cost in construction industry has become a crucial matter today, in terms of minimizing labour, maintenance and repair costs, polymer technology offers a challenging opportunity. In particular, at construction work related to infrastructure, polymer concrete pipe system helps to reduce maintenance, repair, and labour costs significantly by extending the useful life of the investment. Particularly, pipe produced by this technology provides a longer service life with its high technical specifications such as being strong and corrosion resistant.

Scientific researchers have proved for so long that polymer-based concrete pipes have a few times longer service lives compared to cement-based concrete pipes. High material cost of polymer-based concrete pipes should be disregarded as they present a new choice in place of cement-based concrete pipes by reconstruction and maintenance-free service life for a long period of time. In the analysis, according to cost estimation results related to installation processes using CP and PP, the total cost of PP per year is equal to nearly 40% cost of CP. So, in the long run, we can conclude that polymer pipe

TABLE 7: Comparison of installation processes in terms of financial cost.

Code	Price \$	Amount utilized, m	Cost of raw materials, \$	Direct labour, \$	Manufacturing overheads, \$	Beginning inventory, \$	Total cost, \$	Service life, years	Total cost per year, \$
PP5	103	1000	103000	198000	36000	6000	343000	50	6860
CP5	14	1000	14000	198000	36000	6000	254000	15	17150

TABLE 8: Breakdown of annual costs for each installation process.

Type	PP5, \$	$W_{t_{pp5}}$	CP5, \$	$W_{t_{cp5}}$
$C_r$	2180	32%	1350	8%
$C_d$	3960	58%	13369	78%
$C_m$	720	10%	2431	14%
$C_t$	6860	100%	17150	100%

technology is far more cost effective compared to cement-based technology. It is also apparent that the cost analysis is very useful, essential, and demanded by all industries while a new material research is being done.

## References

- [1] E. A. Bobadilla-Sánchez, G. Martínez-Barrera, W. Brostow, and T. Datashvili, "Effects of polyester fibers and gamma irradiation on mechanical properties of polymer concrete containing  $\text{CaCO}_3$  and silica sand," *Express Polymer Letters*, vol. 3, no. 10, pp. 615–620, 2009.
- [2] O. Gencil, W. Brostow, G. Martínez-Barrera, and M. S. Gok, "Mechanical properties of polymer concretes containing different amount of hematite or colemanite," *Polimery*, vol. 57, no. 4, pp. 17–24, 2012.
- [3] G. Martinez-Barrera, E. Viguera-Santiago, O. Gencil, and H. E. Hagg Lobland, "Polymer concretes: a description and methods for modification and improvement," *Journal of Materials Education*, vol. 33, no. 1-2, pp. 37–52, 2011.
- [4] H. Binici, M. Y. Durguna, T. Rızaoğlu, and M. Koluçolak, "Investigation of durability properties of concrete pipes incorporating blast furnace slag and ground basaltic pumice as fine aggregates," *Scientia Iranica*, vol. 19, no. 3, pp. 366–372, 2012.
- [5] S. R. Jackson, R. B. Sawyers, and J. G. Jenkins, *Managerial Accounting: A Focus on Ethical Decision Making*, 5th edition, 2009.
- [6] V. Rostami, Y. Shao, and A. J. Boyd, "Durability of concrete pipes subjected to combined steam and carbonation curing," *Construction and Building Materials*, vol. 25, no. 8, pp. 3345–3355, 2011.
- [7] A. Frank, G. Pinter, and R. W. Lang, "Prediction of the remaining lifetime of polyethylene pipes after up to 30 years in use," *Polymer Testing*, vol. 28, no. 7, pp. 737–745, 2009.
- [8] M. Hultman, M. J. Robson, and C. S. Katsikeas, "Export product strategy fit and performance: an empirical investigation," *Journal of International Marketing*, vol. 17, no. 4, pp. 1–23, 2009.
- [9] U. Ergun and B. E. Karamaras, "Comparison of two contemporary approach to management accounting: activity-based costing and theory of constraints," *Muhasebe Bilim Dünyasi Dergisi*, vol. 4, no. 1, 2002.
- [10] Z. J. Acs and D. B. Audretsch, "Innovation, market structure and firm size," *The Review of Economics and Statistics*, vol. 64, no. 4, pp. 567–574, 1987.
- [11] R. Kanit, O. Ozkan, and M. Gunduz, "Cost assessment of concrete and steel types for office buildings: an exploratory study," *Building and Environment*, vol. 42, no. 9, pp. 3404–3409, 2007.
- [12] S. Mortezania and F. Othman, "Cost analysis of pipes for application in sewage systems," *Materials and Design*, vol. 33, pp. 356–361, 2011.
- [13] G. Cassar and J. Craig, "An investigation of hindsight bias in nascent venture activity," *Journal of Business Venturing*, vol. 24, no. 2, pp. 149–164, 2009.
- [14] S. Yükcü, *Cost Accounting in Terms of Management*, Anadolu Matbaacilik, İzmir, Turkey, 1998.
- [15] S. Sevgener and R. Hacırüstemoğlu, *Management Accounting*, Alfa Basım Yayın Dağıtım, İstanbul, Turkey, 2000.
- [16] Ministry of Finance of the Republic of Turkey, Tax Procedure Law, no. 315.
- [17] C. Berryman, J. Zhu, W. Jensen, and M. Tadros, "High-percentage replacement of cement with fly ash for reinforced concrete pipe," *Cement and Concrete Research*, vol. 35, no. 6, pp. 1088–1091, 2005.
- [18] T. Haktanir, K. Ari, F. Altun, C. D. Atis, and O. Karahan, "Effects of steel fibers and mineral filler on the water-tightness of concrete pipes," *Cement and Concrete Composites*, vol. 28, no. 9, pp. 811–816, 2006.
- [19] L. Hui and L. Yongbiao, "Fabricating technology for concrete pipes," *IERI Procedia*, vol. 1, pp. 124–130, 2012.

## Research Article

# Manufacture of Partially Biodegradable Composite Materials Based on PLA-Tires Powder: Process and Characterization

**Carlos Rolando Rios-Soberanis,<sup>1</sup> Shuchi Wakayama,<sup>2</sup> Takenobo Sakai,<sup>2</sup>  
José de los Ángeles Rodríguez-Laviada,<sup>1</sup> and Emilio Pérez-Pacheco<sup>3</sup>**

<sup>1</sup> *Centro de Investigación Científica de Yucatán, Unidad de Materiales, Calle 43, No. 130, Colonia Chuburná de Hidalgo, CP 97200 Mérida, YUC, Mexico*

<sup>2</sup> *Tokyo Metropolitan University, Mechanical Engineering Department, 1-1 Minami-Ohsawa, Hachioji-shi, Tokyo 192-0397, Japan*

<sup>3</sup> *Instituto Tecnológico Superior de Calkiní en el Estado de Campeche, Avenida Ah Canul SN por Carretera Federal, CP 24900 Calkiní, CAM, Mexico*

Correspondence should be addressed to Emilio Pérez-Pacheco; [eperez@itescam.edu.mx](mailto:eperez@itescam.edu.mx)

Received 21 February 2013; Accepted 16 April 2013

Academic Editor: Osman Gencel

Copyright © 2013 Carlos Rolando Rios-Soberanis et al. This is an open access article distributed under the Creative Commons Attribution License, which permits unrestricted use, distribution, and reproduction in any medium, provided the original work is properly cited.

This research work focuses on the processability and mechanical characterization of blends of polylactic acid (PLA) and tire (elastomeric part). Wasted tires used as filler in the PLA matrix were reduced by two different processes (thermal shock and pyrolysis) in order to acquire the solid residuals in powder to be characterized and compared. Elastomeric solids obtained from scraped tires were used as filler in the PLA matrix and mixed in a Brabender 60 cc mixer at different concentrations ranging from 0% to 60% of filler volume fraction. The blend was laminated, and then samples were obtained in order to undertake mechanical properties at tension and Izod impact tests. A fully detailed analysis on the solid powders by Differential Scanning Calorimeter (DSC), thermogravimetric analysis (TGA), infrared analysis (IR), and scanning electron microscopy analysis (SEM) identified them as a rich source of carbon. Blends were characterized thermally and mechanically showing a direct effect due to the tire nature (thermoset rubber) and concentration. Fracture mechanisms were also identified.

## 1. Introduction

In recent years, there has been widespread interest in the manufacture of products from recycled materials. Among the advantages of doing this is the fact that material recycling makes the technology more economically and environmentally attractive [1]. Particularly among the waste materials in the advancement of civilization, waste tires are a major concern, because the amount of waste tires is increasing more and more due to the increasing demand for tires, and because of their short lifetime, it is therefore necessary to develop methods for recycling waste tires.

A number of approaches have been proposed to make use of the large amount of waste rubber; one of them is like biopolymer. Biopolymers are expensive and have either property or processing limitations [2]. Most durable bioresins available in the markets are based on PLA. Biopolymers are

made from PLA blended with polymers like polycarbonate (PC), polypropylene (PP), acrylonitrile butadiene styrene (ABS), high impact polystyrene (HIPS), polyethylene terephthalate (PET), and poly(methyl methacrylate) (PMMA). Fillers, fibers, and additives are also added to the blends to prevent degradability, increase processability, reduce brittleness and speed crystallization. In order to overcome disadvantages, such as poor mechanical properties of polymers from renewable resources, or to offset the high price of synthetic biodegradable polymers, various blends and composites have been developed over the last decade [3–5]. Until the last decade, the main uses of PLA have been limited to medical applications such as implant devices, tissue scaffolds, and internal sutures because of its high cost, low availability and limited molecular weight [6]. However, recently PLA has been widely used in new developments in composite materials technology, since it has been viewed as a promising

material to reduce the societal solid waste disposal problem [7]. Blends of PLA with various nonbiodegradable polymers have been also investigated [8–10]. Some of these blends were found to be immiscible resulting in fairly poor mechanical properties. Polymer blends containing biodegradable and a nonbiodegradable components have received much interest because of the ease with which their physical properties and degradation characteristics can be tailored. On the other hand, recycling of rubber tires is not possible by simply melting and reshaping them due to the thermosetting nature of the molecular structure: the crosslinking. Spent tyres, however, comprise valuable material that could be recycled if a proper technique can be developed as it has been demonstrated [11–13]. Just like most of organic compounds, tires decompose with heat by pyrolysis that consists in the decomposition of the organic part by heating (about 400°C) in absence of oxygen [14]. In this process, the type and composition of the final products depend on the properties of the organic material, the temperature, pressure of operation, time of the applied method, and the type of gaseous ambient (Ar, N<sub>2</sub>, etc.). Another consequence is that the recovered carbon black is physically different from the original one used as filler in the tires manufacturing. Such dissimilitude is directly related to morphology and structure as well as the particle size and distribution. The powder tire was obtained from scrapping the elastomeric surface of the tire in small flake-like particles (Figure 1).

The scraped elastomeric material is considered as waste, and there is not a specific final use for it, and if it is wrongly disposed can cause contamination. Every week, hundreds of kilograms of such material are produced in flake-like forms and smaller particles that could be used as filler in PLA matrix composites. The aim of this work was to investigate the manufacture and mechanical characterization of PLA-matrix-based composites filled with different contents of wasted tire flakes. One advantage of the elastomeric fillers is that they can be easily dispersed in thermoplastic polymers.

## 2. Materials

The material matrix studied is based on a commercially available Poly(lactic acid) polymer 2002D (Table 1). The tire powder was recollectored from local companies dedicated to repair old tire with several damage on its surface.

## 3. Experimental Procedures

Two processes were carried out in order to obtain solid residues from tire to characterize them. The first one consisted in a pyrolytic process which applies indirect heat in an environment free of flame and oxygen. Several pieces of scraped tire were placed in crucibles and then sited in a furnace at 700°C for 1 hr in the presence of nitrogen (N<sub>2</sub>) atmosphere, and after this period of time, the crucibles were cooled down to room temperature and the carbonized samples were manually pulverized with a pestle and mortar. The second one was by thermal shock caused by the rapid change in extreme temperatures. Again, elastomeric pieces in



FIGURE 1: Obtaining of flake-like particles from wasted tires.

TABLE 1: Physical properties of Poly(lactic acid) polymer.

Physical properties	Poly(lactic acid) polymer
Specific gravity	1.25
Melt index, g/10 min (190°C/2.16 K)	4–8
Clarity	Transparent

crucibles were heated in the furnace, this time at 400°C during 10 min. After this brief period of time, the samples were immediately immersed in liquid nitrogen (125 mL). After the vaporization of N<sub>2</sub>, the residue was manually pulverized. Thermal shock was analyzed at 400°C, because at higher temperature, the tire rubber initiates full decomposition. It was found that 10 min in the furnace were enough to ensure the breakage of the bonds to obtain a powder residue. Experimental diagram is shown in Figure 2. PLA/tire blends were made in concentrations from 100/0% to 40/60%. PLA, used as matrix, was placed in an oven at 60°C during 4 hrs previous to mixing in order to eliminate humidity due to the high hydrophilic character of PLA. Scrap tire was sieved to get a uniform size of particles around 2 mm.

**3.1. Fourier Transform Infrared (FTIR).** The FTIR spectroscopy analyses were performed on all powder samples in order to characterize qualitatively the organic compounds of the solids by using transmission technique. The specimens were prepared by grinding the solid powder residue with 200 mg potassium bromide (KBr) powder and then pressing the mixture into a tablet. The FTIR spectrum of the powder complexes was measured at room temperature with a Thermo Nicolet (Nexus 670-FTIR) spectrometer in a spectral range of 4000 to 400 cm<sup>-1</sup>.

**3.2. Thermal Analysis.** These analyses were carried out to understand the thermal behavior under degradation when samples are heated to high temperatures. A Perkin-Elmer TGA-7 thermogravimetric analyzer (TGA) was used to investigate the thermal stability of the elastomeric section of the tire and the PLA/tire blends within a temperature range from 30 to 800°C in a nitrogen atmosphere analyzed at a heating rate of 10°C/min. DSC was achieved in a DSC-7 Perkin Elmer, with about 7 mg samples of rubber tire, and each concentration blends at a range of 40–200°C and heat rate of 2°C/min. A second run was done to observe the thermal event of crystallization.

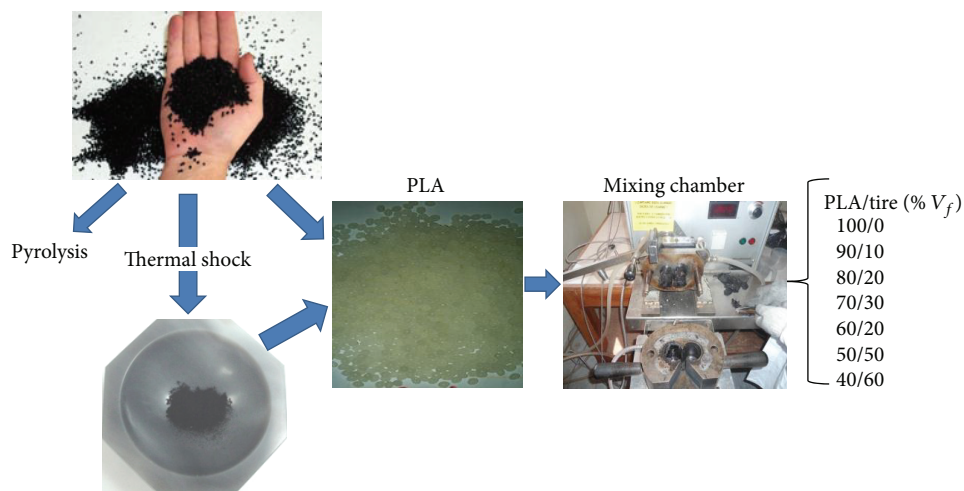


FIGURE 2: Experimental diagram.

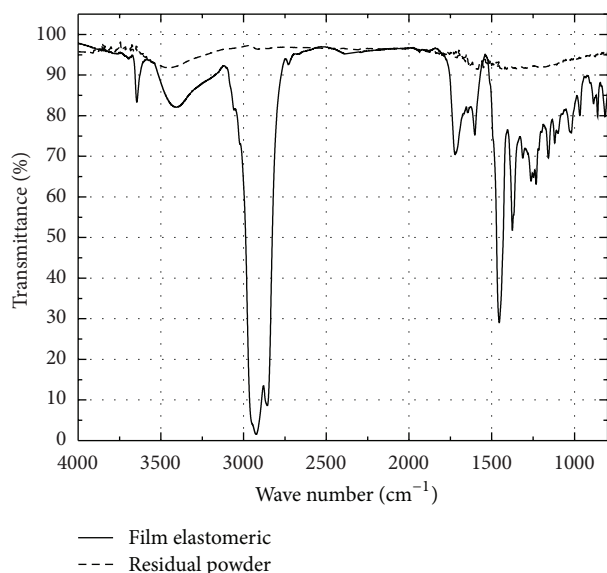


FIGURE 3: FTIR spectrum of the film obtained after extraction and the solid residue.

**3.3. Particle Size and Distribution.** A Coulter LS100 equipment capable of measuring particle sizes between  $0.1 \mu\text{m}$  and  $900 \mu\text{m}$  with ultrasonic sound was used to determine the particle sizes and distribution of the residual powder.

**3.4. Scanning Electron Microscopy (SEM).** Microscopic analysis was performed on the powder in order to examine the morphology of the particles. A small amount of the uncoated powder pellets was mounted on a metallic slide, and the examination was performed with a scanning electron microscopy JEOL JSM 6360 LV electron probe microanalyzer at 15 kV in low vacuum. Fractured surfaces of samples after rupture in tension mode were also scanned.

**3.5. Mechanical Properties.** The mechanical properties for tensile loadings were determined according to ASTM D882-12 standard [15]. A Shimadzu Universal testing machine, model AG-I equipped with a 5 kN load cell and a crosshead speed of 0.5 mm/min was used.

The impact test was carried out by Izod with a 1 Joule hammer. The Izod notched impact strength was determined from specimens measuring  $63.5 \times 12.7 \times 4$  mm using an unnotched Izod impact instrument according to ASTM D256-10 [16].

## 4. Results and Discussion

**4.1. Solid Powder Residue Characterization.** According to FTIR (Figure 3) analyses, it was found that for pyrolyzed samples organic bands do not appear, because at high temperature, tires suffer a complete depolymerization; therefore organic compounds are eliminated, and the remaining are mainly inorganic compounds.

On the one hand, solid powder obtained by thermal shock process was purified with tetrahydrofuran (THF) in order to carry out an extraction of possible organic residuals. The extracted liquid was taken to evaporation. The residual solution developed a yellow film of an elastomeric appearance; therefore, the powder and the film were both characterized separately by FTIR. Figure 3 represents both spectrums where it is possible to observe that the solid residue, after the extraction, exhibits an identical pattern to that found in samples treated by pyrolysis at  $750^\circ\text{C}$  with almost no signals for organic compounds. On the other hand, the spectrum of the film is similar to that displayed by isoprene with bands corresponding to the vibrations of the group  $-\text{CH}_2-$  at 2924, 2856, 1455, and  $1375 \text{ cm}^{-1}$ , as well as vibration stretching of polyisoprene groups  $\text{C}=\text{C}-$  and  $-\text{CH}$  at 1644 and  $813 \text{ cm}^{-1}$ , respectively. The bands of lesser intensity to these correspond to signals of other compounds and butadiene-styrene residues. This result implies that a tire

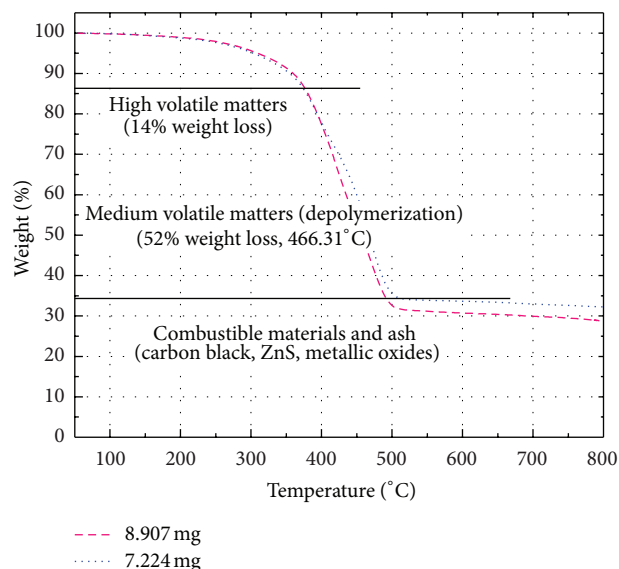


FIGURE 4: The TGA thermogram of the elastomeric part of the tire.

treated with pyrolysis followed by thermal shock avoids total degradation of the polymeric chain breaking only the sulphur bonds [17].

Thermal analysis curves of the elastomeric part of the wasted tire used in this study for a heating rate of  $10^{\circ}\text{C}/\text{min}$  are shown in Figure 4. The thermogram shows different regions for the whole temperature range between 30 and  $800^{\circ}\text{C}$ . These differences are the consequence of the degradation of each major constituent of rubber tires, such as natural rubber, butadiene rubber, styrene-butadiene rubber, as well as minor constituents such as oil, plasticizers, additives and moisture. In the temperature range between 80 and  $350^{\circ}\text{C}$  all the minor constituents are lost, as they are normally volatile materials such as low molecular weight oligomers, plasticizers, emulsifications, oils and waxes, and antioxidants. The degradation process of major constituents or their combinations occurs between 340 and  $550^{\circ}\text{C}$ . It was previously indicated that the maximum mass loss of styrene-butadiene rubber occurs at 350 and  $500^{\circ}\text{C}$ , maximum degradation of natural rubber at  $373^{\circ}\text{C}$ , and for butadiene rubber at  $372$  and  $460^{\circ}\text{C}$ . Finally, in the last degradation phase, above  $500^{\circ}\text{C}$  only about 34% of the original weight of the sample is left, corresponding to decomposition products mainly containing Zn and carbon atoms such as oxidized no-volatile materials, carbon black, and graphite [18, 19]. However, in the case of rubber combinations like those used in tires, it is observed that the mass loss for each peak in the thermogram curves is dependent on the composition of the mixture. In spite of the relative homogeneity of the scrap tire used in this work, different compositions as a function of the relative amount of each elastomer are observed. We obtained similar values to those reported by Stefani et al. for temperatures and mass losses (for the same heating rates), indicating that the analyzed tire rubber has a similar composition [18].

In order to examine the uniformity or disparity in the dimensions of the solid powder obtained by two different

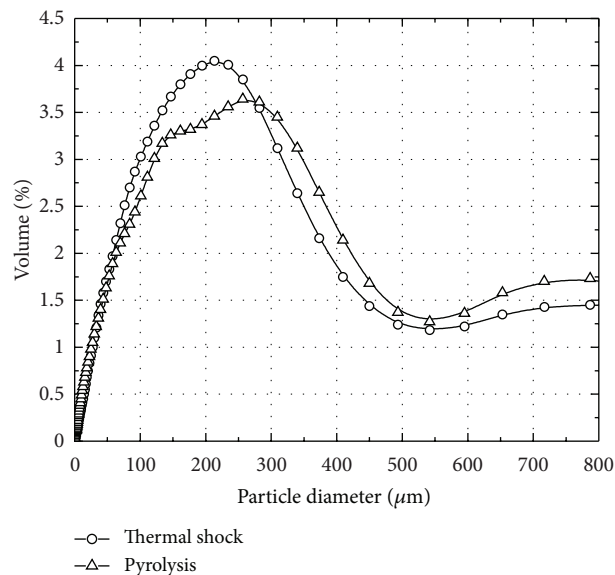


FIGURE 5: Distribution of the particle size.

processes, distribution of the particle size was studied. The results are presented in Figure 5 where the curves for pyrolysis process are compared to the curve acquired for thermal shock process. It is possible to observe the similarity in the two curves that initiate with an exponential augmentation for small particle sizes from 0 to about  $180\ \mu\text{m}$  then a maximum appears at about 210 and  $250\ \mu\text{m}$ . Finally, the curves go down towards stabilization at about  $600\ \mu\text{m}$  and continue to low levels of bigger particles. Invariably the particle sizes in any process are identical; this could be attributed to the manual pulverization with a pestle and mortar by using the same conditions such as pressure force and time for powdering the solids obtained.

Scanning electron microscope was used to examine the appearance of the solid powder obtained from solid reduced by pyrolysis and thermal shock, respectively (see Figure 6), where the difference in the surface area is noticeable.

Thermal shock particles (Figure 6(b)) seem to be covered by a “whitened” rubber surface due to the remaining organic residue (elastomer) as proved before by FTIR analysis. This rubber keeps the particles of the residue united originating the shape observed in the granules. Additionally, the granules size is in agreement with the information obtained by the distribution of the particle size. It was found a similarity in the granules dimensions regardless the process used to obtain the powder. However, particles obtained by thermal shock process exhibited lower amount of large solids.

**4.2. PLA/Tire Material Characterization.** Thermal analyses (DSC and TGA) are presented in Figure 7 where three thermal events ( $T_g$ ,  $T_c$ , and  $T_m$ ) are observed. As seen in Figure 7(a), glass transition ( $T_g$ ) occurred around  $55$ – $59^{\circ}\text{C}$  for all samples corresponding to PLA, while melting ( $T_m$ ) occurred with two endothermic peaks. A multiple melting behavior is a common phenomenon observed in

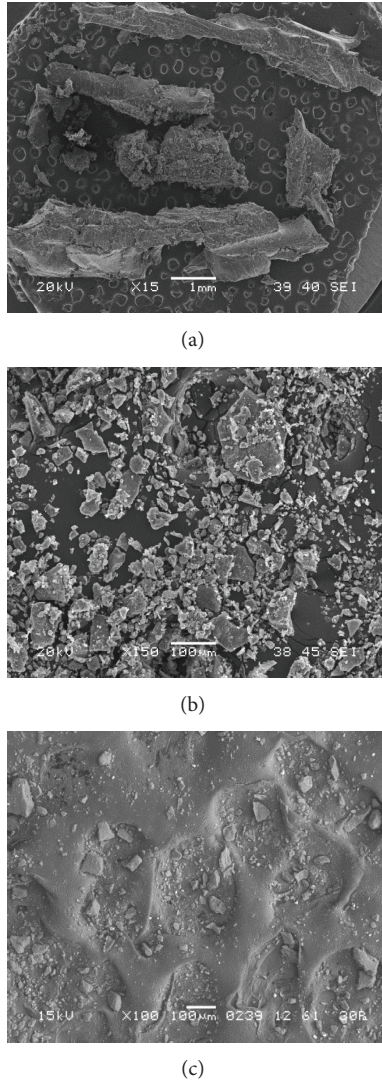


FIGURE 6: Micrographs of solids: (a) scraped tire, (b) thermal shock, and (c) pyrolysis.

polymorphic polymers (several crystalline structures) as PLA which is detected as double melting peaks that have been proposed [20–22] to arise from  $\alpha$ - and  $\alpha'$ -crystalline forms of the polymer.  $\alpha'$  and  $\alpha$  peaks appeared at around 148 and 159°C, respectively, and a slight diminution in those values was found for concentration of 80% of PLA and lower. Same trend was observed for  $T_c$ , a displacement to lower value as the concentration of PLA diminishes. It seems that the elastomer from tire slows down the formation and amount of crystals. On the other hand, apparently  $T_g$  did not exhibit such variation staying at about 58°C. The TGA results shown in Figure 7(b) exhibited a difference in thermal decomposition influenced by tire concentration, so there was a clear divergence in heat resistance. It is clear that with the augmentation of tire concentration, amount of solid residues will be higher due to the presence of minerals in the tire.

Typical stress-strain curves for PLA/tire blends are presented in Figure 8 and numerical results are in Table 2. PLA

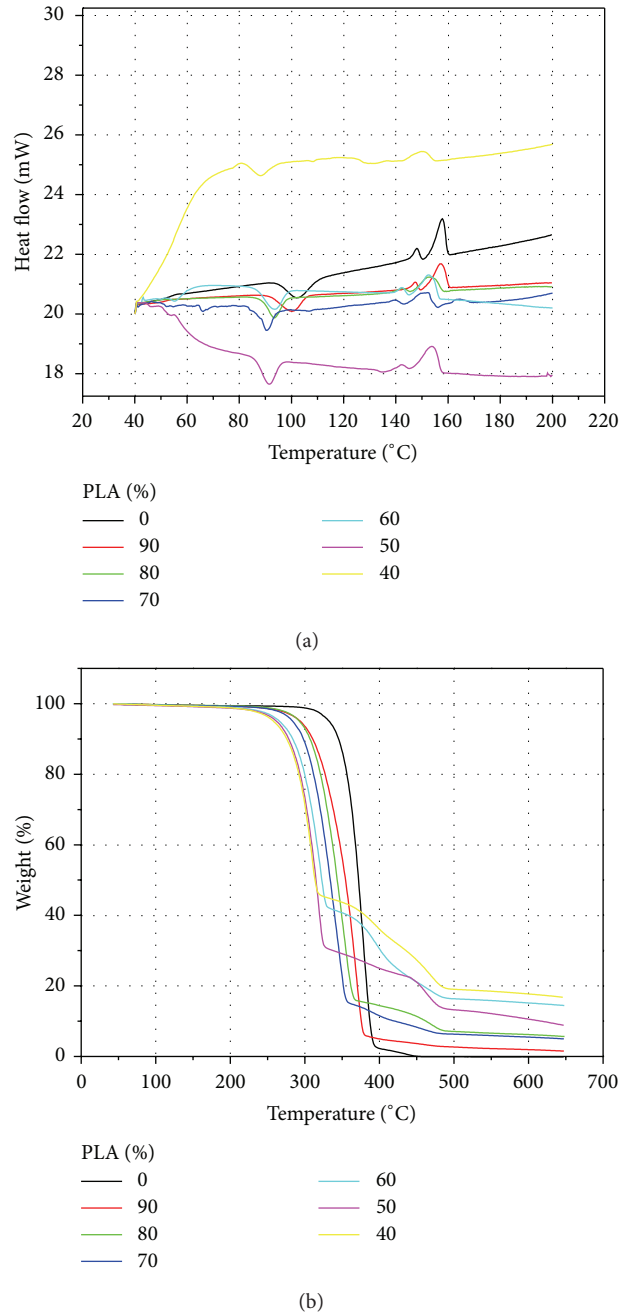


FIGURE 7: Thermal analyses: (a) DSC and (b) TGA.

TABLE 2: Mechanical properties of composite material.

PLA (%)	Strength (MPa)	Strain (%)	E (MPa)
100	27.6	3.2	1403.03
90	2	0.2	1249.8
80	0.9	0.46	1181.4
70	1.1	1.08	880.1
60	1.0	1.7	272.6
50	0.9	2.2	218.9
40	0.8	2.3	245.1

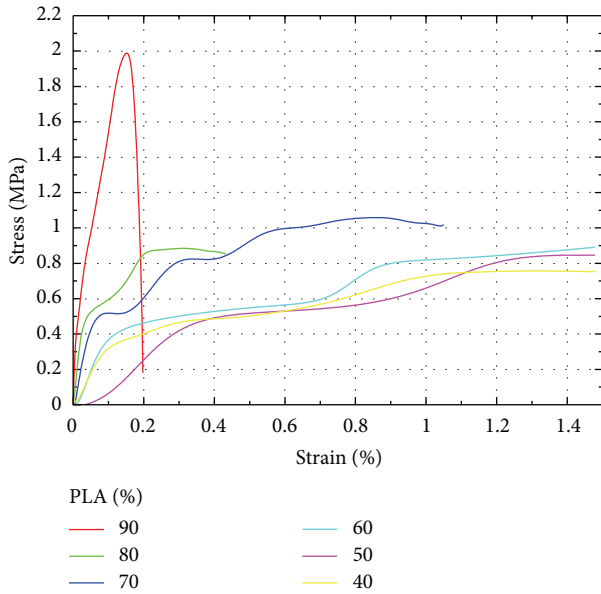


FIGURE 8: Tensile properties of PLA/tire blends.

shows tensile strength of 27.6 MPa and modulus of 1403 MPa. With the first addition of 10 wt% of scraped tire, an important decrement of tensile strength (2 MPa) is achieved. Elastic modulus ( $E$ ) is also reduced but not drastically to 1249 MPa. Eventually, with the increment of tire content, the system is governed by a rubber behavior. On the other hand, fracture behavior of the specimens in tensile mode changed from brittle fracture of the neat PLA to ductile fracture of the blends. In previous works [5, 23–26] where flexible and tough materials are blended with PLA, a substantial amount of elongation (strain at break  $\sim 710\%$ ) is achieved; however, with rubber obtained from tire this behavior is not allowed due to the crosslinked system.

Figure 9 presents results of Izod notch impact tests where it can be seen that, with the first addition of 10% of elastomeric filler, the impact resistance has a diminution of about 60% in comparison with PLA; absorbed energy exhibited similar tendency. A gradual enhancement in the impact resistance and absorbed energy is obtained with the increment of tire concentration. Significant variation is found when volume fraction of elastomeric particles reaches 60% with similar values to virgin PLA.

PLA is similar to many polymers that can undergo plastic flow mechanisms, initiated by dispersed rubber domains. Scraped tire flakes induce energy dissipation mechanisms in the matrix which retard crack initiation and propagation and ultimately result in a material with improved toughness.

The morphology of tensile fracture surfaces was studied by SEM as shown in Figure 10. Photographs at PLA 100% and 90% indicate a brittle behavior exhibiting a smooth longitudinal fracture surface without visible plastic deformation. However, at higher concentrations empty spaces as voids are originated by rubber pull-outs at the scanned surface. PLA/tire 40%–60% blend had the highest elongation at break, and its matrix experienced plastic deformation in the stress

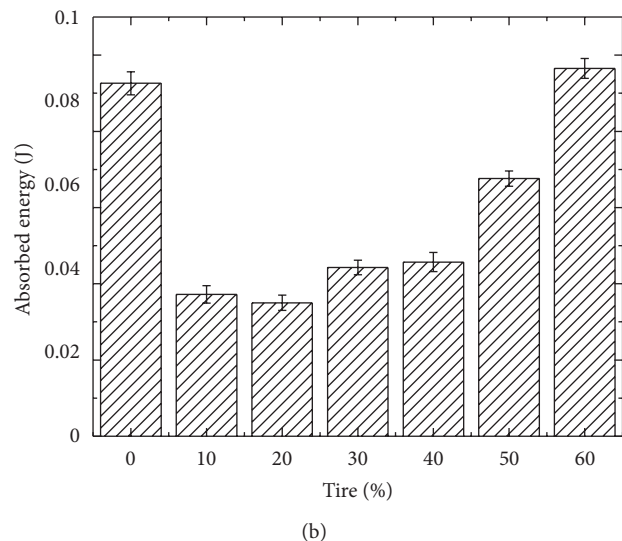
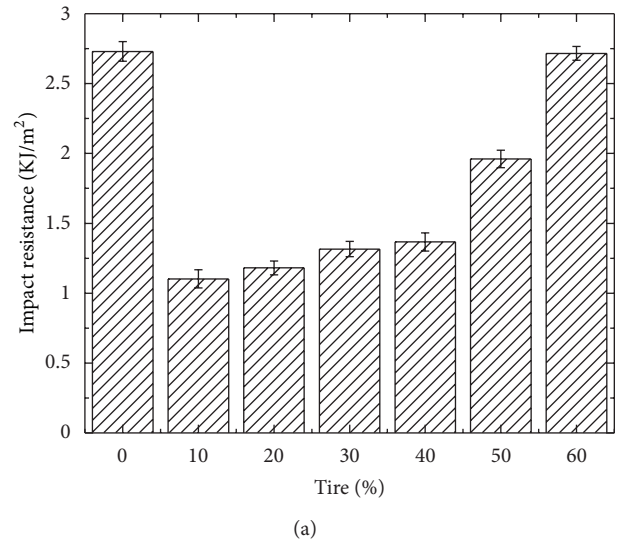


FIGURE 9: Impact test (a) resistance and (b) absorbed energy.

direction. For lower concentration of tire samples whose elongations are smaller at break, their SEM micrographs evidently suggest the toughening mechanism.

Debonding of the rubber particles from the PLA matrix under tensile stress is clearly observed at higher concentrations of tire. These cavities were formed during tension when the stress was higher than the bonding strength at the interface between the PLA matrix and elastomeric inclusions. Scraped rubber debonds from the PLA matrix at the interface, and so cavities arose. These cavities were enlarged in the stress direction along with the deformation of the matrix. Since rubber has different elastic properties compared with PLA matrix, its particles act as stress concentrators under tensile stress. Although a good dispersion of scraped tire into PLA matrix is observed, it is clear that the adhesion is not strong in any of the composites taken the material to an early ductile fracture. There is evidence of immiscibility between both PLA and the elastomeric material.

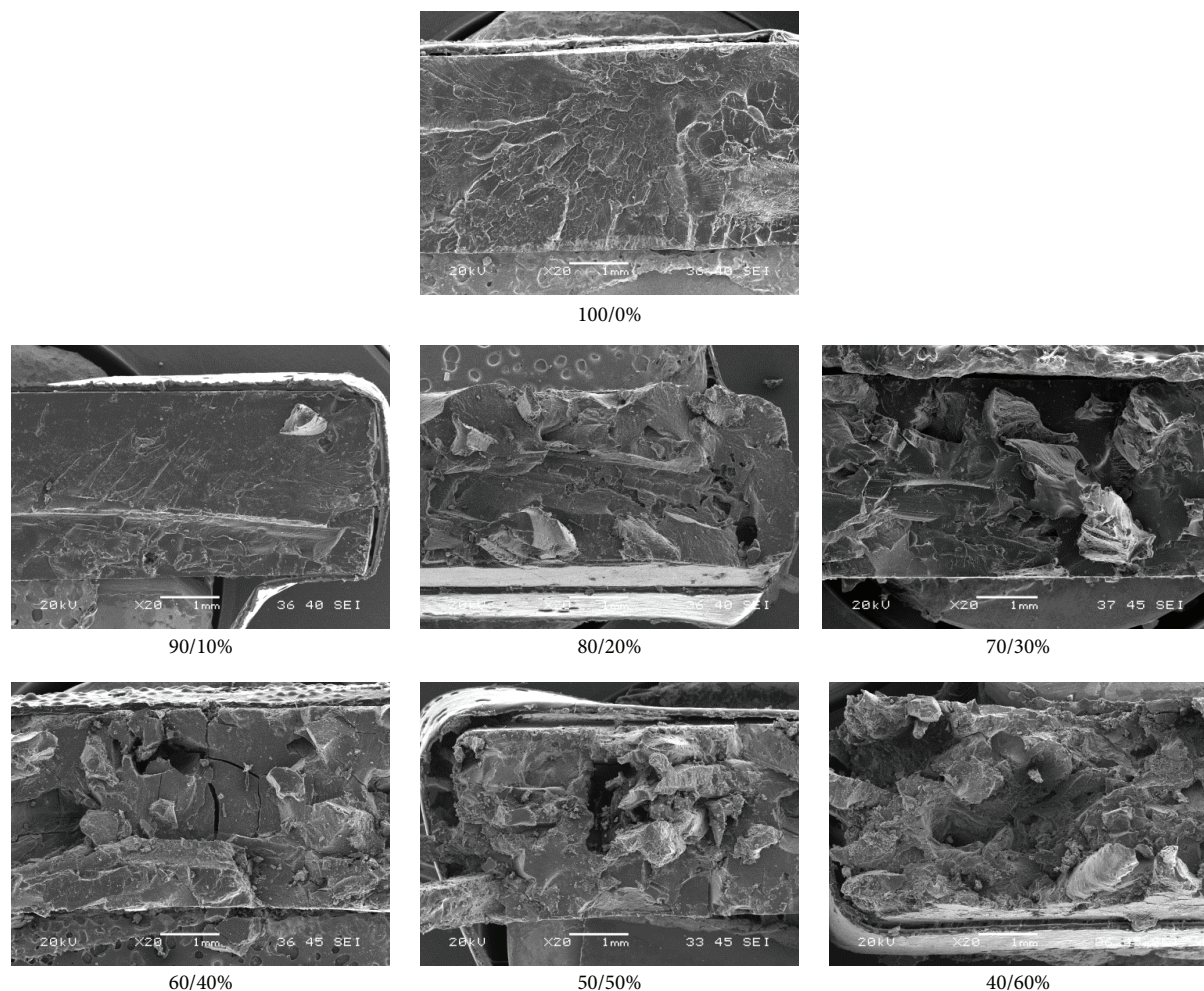


FIGURE 10: Fractured surfaces of PLA/tire blends.

## 5. Conclusions

Physicochemical characterization of the solid residues obtained from scraped tires by means of two reduction processes, pyrolysis and thermal shock, was performed in order to compare efficiency and viability of both processes as an option for wasted tires control and to be used as fillers in PLA blends. Differences in components, morphology, and amount of residual solids were found. Scraped tires, in the form of elastomeric flakes, were chosen as filler into PLA matrix. An effect in thermal events in PLA was found to be caused by the increment of elastomeric content in blends. Mechanical properties were found to be affected as well by the addition of filler into PLA. An enhancement in toughness is only obtained at high values of tire concentration equal to virgin PLA values. Finally, it is important to point out some features that can affect the transference of elastic toughness from the rubber to the PLA matrix: the rubber must be distributed as small domains (usually  $0.1\text{--}1.0\ \mu\text{m}$ ) in the matrix polymer and it must have good interfacial adhesion to PLA. SEM micrographs exhibited the poor interfacial adhesion between tire and PLA.

A further investigation has to be done in the interphase level and intent surface modifications in order to augment

the adhesion. It is also recommendable to understand the mechanisms of degradation of partially biodegradable materials such as PLA/tire composite in order to understand the environmental factors that affect any possible application.

PLA/tire composites displayed good mechanical performance that makes them a good prospectus for collision and impact applications. A good example for that is the automotive industry, where the application of impact absorbers materials was doubled in the form of different cover parts over the last few years.

## Conflict of Interests

The authors affirm that there is no conflict of interests, and they have no financial support from any company, and the authors do not have a direct financial relation with the commercial identities mentioned in the submitted paper.

## Acknowledgment

The authors are grateful to the Mexican Council for Science and Technology (CONACYT) for the provision of Grant 60204/CM0042.

## References

- [1] N. Ayrilmis, U. Buyuksari, and E. Avci, "Utilization of waste tire rubber in the manufacturing of particleboard," *Materials and Manufacturing Processes*, vol. 24, no. 6, pp. 688–692, 2009.
- [2] O. Martin and L. Avérous, "Plasticization and properties of biodegradable multiphase systems," *Polymer*, vol. 42, no. 14, pp. 6209–6219, 2001.
- [3] A. K. Bledzki, A. Jaszkiwicz, and D. Scherzer, "Mechanical properties of PLA composites with man-made cellulose and abaca fibres," *Composites A*, vol. 40, no. 4, pp. 404–412, 2009.
- [4] N. E. Suyatma, A. Copinet, L. Tighzert, and V. Coma, "Mechanical and barrier properties of biodegradable films made from chitosan and poly(lactic acid) blends," *Journal of Polymers and the Environment*, vol. 12, no. 1, pp. 1–6, 2004.
- [5] L. Jiang, M. P. Wolcott, and J. Zhang, "Study of biodegradable polylactide/poly(butylene adipate-co-terephthalate) blends," *Biomacromolecules*, vol. 7, no. 1, pp. 199–207, 2006.
- [6] L. T. Lim, R. Auras, and M. Rubino, "Processing technologies for poly(lactic acid)," *Progress in Polymer Science*, vol. 33, pp. 820–852, 2008.
- [7] M. Ajioka, K. Enomoto, K. Suzuki, and A. Yamaguchi, "The basic properties of poly(lactic acid) produced by the direct condensation polymerization of lactic acid," *Journal of Environmental Polymer Degradation*, vol. 3, no. 4, pp. 225–234, 1995.
- [8] L. Zhang, S. H. Goh, and S. Y. Lee, "Miscibility and phase behavior of poly(D,L-lactide)/poly(*p*-vinylphenol) blends," *Journal of Applied Polymer Science*, vol. 70, no. 4, pp. 811–816, 1998.
- [9] A. J. Nijenhuis, E. Colstee, D. W. Grijpma, and A. J. Pennings, "High molecular weight poly(L-lactide) and poly(ethylene oxide) blends: thermal characterization and physical properties," *Polymer*, vol. 37, no. 26, pp. 5849–5857, 1996.
- [10] A. Mohamed, S. H. Gordon, and G. Biresaw, "Polydactic acid/polystyrene bioblends characterized by thermogravimetric analysis, differential scanning calorimetry, and photoacoustic infrared spectroscopy," *Journal of Applied Polymer Science*, vol. 106, no. 3, pp. 1689–1696, 2007.
- [11] D. Raghavan, H. Huynh, and C. F. Ferraris, "Workability, mechanical properties, and chemical stability of a recycled tyre rubber-filled cementitious composite," *Journal of Materials Science*, vol. 33, no. 7, pp. 1745–1752, 1998.
- [12] F. A. Aisien, F. K. Hymore, and R. O. Ebebele, "Potential application of recycled rubber in oil pollution control," *Environmental Monitoring and Assessment*, vol. 85, no. 2, pp. 175–190, 2003.
- [13] M. Sienkiewicz, J. Kucinska-Lipka, H. Janik, and A. Balas, "Progress in used tyres management in the European Union: a review," *Waste Manage*, vol. 32, pp. 1742–1751, 2012.
- [14] M. Miranda, F. Pinto, I. Gulyurtlu, and I. Cabrita, "Pyrolysis of rubber tyre wastes: a kinetic study," *Fuel*, vol. 103, pp. 542–552, 2013.
- [15] *ASTM D882-12 Standard Test Method for Tensile Properties of Thin Plastic Sheeting*, American Society for Testing Materials, Philadelphia, Pa, USA.
- [16] *ASTM D256-10 Standard Test Methods for Determining the Izod Pendulum Impact Resistance of Plastics*, American Society for Testing Materials, Philadelphia, Pa, USA.
- [17] S. Galvagno, S. Casu, M. Martino, E. Di Palma, and S. Portofino, "Thermal and kinetic study of tyre waste pyrolysis via TG-FTIR-MS analysis," *Journal of Thermal Analysis and Calorimetry*, vol. 88, no. 2, pp. 507–514, 2007.
- [18] P. M. Stefani, D. Garcia, J. Lopez, and A. Jimenez, "Thermogravimetric analysis of composites obtained from sintering of rice husk-scrap tire mixtures," *Journal of Thermal Analysis and Calorimetry*, vol. 81, pp. 315–320, 2005.
- [19] R. Mis-Fernandez, J. A. Azamar-Barrios, and C. R. Rios-Soberanis, "Characterization of the powder obtained from wasted tires reduced by pyrolysis and thermal shock process," *Journal of Applied Research and Technology*, vol. 6, pp. 95–104, 2008.
- [20] X. Chen, J. Kalish, and S. H. Hsu, "Structure Evolution of a  $\alpha'$ -Phase Poly(lactic acid)," *Journal of Polymer Science*, vol. 49, pp. 1446–1454, 2011.
- [21] T. Tábi, I. E. Sajó, F. Szabó, A. S. Luyt, and J. G. Kovács, "Crystalline structure of annealed polylactic acid and its relation to processing," *eXPRESS Polymer Letters*, vol. 4, pp. 659–668, 2010.
- [22] X. Cao, A. Mohamed, S. H. Gordon, J. L. Willett, and D. J. Sessa, "DSC study of biodegradable poly(lactic acid) and poly(hydroxy ester ether) blends," *Thermochimica Acta*, vol. 406, no. 1-2, pp. 115–127, 2003.
- [23] T. Semba, K. Kitagawa, U. S. Ishiaku, and H. Hamada, "The effect of crosslinking on the mechanical properties of polylactic acid/polycaprolactone blends," *Journal of Applied Polymer Science*, vol. 101, no. 3, pp. 1816–1825, 2006.
- [24] H. A. Schneider, "Glass transition behavior of compatible polymer blends," *Polymer*, vol. 30, pp. 771–779, 1989.
- [25] M. Shibata, S. Oyamada, S. I. Kobayashi, and D. Yaginuma, "Mechanical properties and biodegradability of green composites based on biodegradable polyesters and lyocell fabric," *Journal of Applied Polymer Science*, vol. 92, no. 6, pp. 3857–3863, 2004.
- [26] R. C. Willemse, A. Speijer, A. E. Langeraar, and A. Posthuma De Boer, "Tensile moduli of co-continuous polymer blends," *Polymer*, vol. 40, no. 24, pp. 6645–6650, 1999.